Towards the Statistical Evaluation of Phase-Changing Flows: The Development of a Framework for Large-Scale Interface-Resolved Simulations

Zur Erlangung des akademischen Grades eines

DOKTORS DER INGENIEURWISSENSCHAFTEN (Dr.-Ing.)

von der KIT-Fakultät für Maschinenbau des
Karlsruher Instituts für Technologie (KIT)

angenommene

DISSERTATION

von

M.Sc. Lorenz Weber
geb. in Malsch

Tag der mündlichen Prüfung:	12.12.2025
Hauptreferent:	Prof. Dr.-Ing. Andreas G. Class
Korreferenten:	Prof. Dr.-Ing. Hans-Jörg Bauer
	Prof. Dr. Luca Brandt

Kurzfassung

Diese Arbeit präsentiert die Entwicklung und Anwendung einer Methodik, die die numerische Untersuchung siedender Strömungen ermöglicht. Aufgrund seiner Komplexität ist das Siedephänomen noch nicht vollständig untersucht und Gegenstand der aktuellen Forschung. Häufig sind experimentelle Messungen siedender Strömungen schwer umsetzbar, weshalb grenzflächenauflösende Simulationen einen vielversprechenden Ansatz darstellen, um ein tieferes Verständnis zu erlangen. Des Weiteren weisen Simulationen mit der Reynolds-Zeitmittelung Genauigkeitsprobleme auf, da empirische Modelle zur Blasengrößenverteilung in siedenden Strömungen nur eingeschränkt anwendbar sind. In dieser Hinsicht könnten Blasenstatistiken aus grenzflächenauflösenden Simulationen zur Verbesserung dieser Modelle eingesetzt werden. Jedoch sind grenzflächenauflösende Simulationen von Siedephänomen in der Umsetzung aufgrund ihres hohen rechnerischen Aufwands und der Notwendigkeit spezialisierter Lösungsmethoden anspruchsvoll. Im Hinblick auf diese Schwierigkeiten soll eine effiziente und konsistente Methodik zur grenzflächenauflösenden Simulation siedender Strömungen entwickelt werden, die eine statistische Auswertung lokaler Blasenereignisse ermöglicht. In dieser Arbeit wird die "Accurate Conservative Diffuse Interface" (Abk. ACDI, engl. genaue konservative diffuse Grenzfläche) Methodik zur numerischen Beschreibung der Phasengrenzfläche verwendet. Gegenüber anderen Methoden zur Simulation von Phasengrenzflächen zeichnet sich die ACDI-Methodik durch eine Vielzahl numerischer Vorteile aus. Allerdings wurde ACDI bisher nicht auf komplexe Siedevorgänge angewandt. Um dies zu ermöglichen, wird eine Reihe von notwendigen numerischen Verfahren entwickelt. Dazu zählen unter anderem: (i) das Untersuchen der Transportgleichungen, wobei zusätzliche Beiträge in der Impulsbilanz identifiziert wurden, die jedoch oft vernachlässigt werden; (ii) die Entwicklung eines Drucklösungsverfahrens, das die Verwendung von "Fast Fourier Transformations" (Abk. FFT, engl. schnelle Fourier-Transformation) ermöglicht; und (iii) die Modellierung des Phasenübergangs für die ACDI-Methode. Schließlich wird die Simulationssoftware einer Reihe einschlägiger Literaturtests unterzogen. Diese Tests reichen von einfachen, eindimensionalen Grenzflächensimulationen bis hin zu komplexen Simulationen von Blasen im dreidimensionalen Raum. Hier kann gezeigt werden, dass die zusätzlichen Beiträge der Impulsbilanz eine wichtige Rolle bei dem genauen Simulieren des Drucksprungs durch den Phasenübergang spielen. Zusätzlich werden mit diesen Beiträgen präzisere Vorhersagen über die Blasendynamik ohne Phasenübergang erhalten. Der Drucklöser zeigt im Vergleich zu bisherigen FFT-Verfahren

den Vorteil, dass durch den Phasenübergang zusammen mit hohen Dichteunterschieden keine Druckoszillationen entstehen. Die numerischen Tests zeigen außerdem, dass das entwickelte Modell des Phasenübergangs verlässliche Ergebnisse liefert und keine simulationsabhängigen Parameteranpassungen erfordert. Durch den Vergleich mit experimentellen Daten wird gezeigt, dass die Simulationssoftware ein geeignetes Werkzeug darstellt, um technisch relevante Strömungen zu simulieren. Hierfür wird auch die Skalierbarkeit des Simulationscodes auf Hochleistungsrechnern nachgewiesen. Als eine technisch relevante Strömung wird Blasensieden in einer turbulenten Rechteckkanalströmung simuliert und ausgewertet. Diese Anwendung der ACDI-Methodik ist in der Literatur neu. Für die Auswertung der so entstandenen Blasendaten wird ein spezielles Verfahren entwickelt, bei dem Blasenzellen konstruiert und gruppiert werden. Dieses Verfahren verwendet das Voronoi-Diagramm, um eine konsistente Definition einer Blasenzelle zu ermöglichen, die für die Ermittlung volumengemittelter Daten erforderlich ist. Der Gruppierungsschritt hat die einzigartige Eigenschaft, dass auch instantane Blasenstatistiken ausgewertet werden können. Die Blasengruppierung hat auch den Vorteil, dass die Stichprobengröße für eine lokale Blasenstatistik drastisch erhöht wird. Besonders wichtig ist diese Eigenschaft für Daten grenzflächenauflösender Simulationen, da die Ausführung der Software rechnerisch aufwendig ist. Zusammengefasst hat diese Arbeit zur Bereitstellung eines geeigneten Softwarepakets geführt, das künftig zur weiteren Untersuchung von siedenden Strömungen verwendet werden kann.

Abstract

The development and application of a framework for the numerical investigation of boiling phenomena is presented in this thesis. The phase-change mechanism of boiling is a highly complex physical phenomenon that, to date, is not fully understood and is subject to ongoing research. Since experimental measurements of boiling phenomena are challenging to implement, interface-resolved simulations present a promising approach to gain deeper insights. Furthermore, lower-order simulations lack accuracy due to the fundamental challenge of modelling the polydisperse nature of boiling flows. Bubble statistics from interface-resolved simulations could help to address this challenge. However, interface-resolved simulations of boiling flows involve high computational costs and advanced methods, which make them far from straightforward to implement. In light of these challenges, this thesis aims to develop an efficient and sophisticated framework for interface-resolved simulations of boiling flows that also allows for the consistent evaluation of statistical bubble data. The gas-liquid interface is represented by the *accurate conservative diffuse interface* (ACDI) method. The ACDI method is deemed computationally advantageous over other interface-capturing methods in numerous applications. However, the application of ACDI to simulate complex boiling flows has not yet been explored. For this application, a range of necessary modifications is proposed in this thesis. These modifications include: (i) analyzing the system of transport equations, revealing that additional terms are required to achieve consistency in boiling flow scenarios; (ii) developing a pressure solution scheme that enables the use of *fast Fourier transformations* (FFT); and (iii) modelling the mass transfer between the gas and the liquid phase. These developments are compared to numerous benchmarks in the literature through an extensive testing campaign. The testing campaign ranges from one-dimensional interface simulations to complex simulations of three-dimensional bubble dynamics. It is found that the proposed terms in the momentum transport equation are crucial for accurately capturing the *recoil pressure* jump at interfaces subjected to phase change. Even in the absence of phase change, the accuracy improves significantly when using the proposed system of equations. Notably, the developed FFT pressure solver eliminates spurious pressure oscillations commonly encountered in the presence of high density ratios and phase change. In the testing campaign, the developed phase change model reliably yields accurate results without simulation-dependent parameter adjustments. Comparisons with experimental data demonstrate that the framework developed in this thesis is a suitable tool for efficiently simulating technically relevant boiling flows. It is shown that good code scalability

on high-performance computing systems is achieved, which is essential for conducting large-scale simulations. In a final simulation, a novel application of the ACDI method for simulating nucleate boiling in a subcooled turbulent duct flow is presented. A grouped Voronoi analysis is proposed for the statistical evaluation of the resulting bubble data. This Voronoi analysis is found to provide a consistent definition of a bubble cell, which is required to derive statistics of volume-averaged quantities. In this thesis, the grouping of bubble cells is proposed, which allows the definition of instantaneous local bubble statistics. Moreover, grouping drastically increases the sample size for any local bubble statistics, constituting an important feature given that interface-resolved simulations are computationally costly. Overall, this thesis has led to a sophisticated software package that can be used to further understand boiling flow phenomena.

Acknowledgments

The first person I would like to express my gratitude to is Prof. Dr.-Ing. Andreas Class, who supervised me during my doctoral studies. Throughout my years as a doctoral student, you have guided me scientifically and helped me grow as a researcher. Thank you for all the time and effort you invested in my education.

The majority of the work presented in this thesis was carried out at the Karlsruhe Institute of Technology. However, a significant part of the presented research originates from a collaboration with the Royal Institute of Technology (KTH) in Stockholm. Thank you, Prof. Luca Brandt, for making this collaboration possible. I am deeply grateful for your constant advice and support. Thank you for introducing me to the world of diffuse interface modelling - I learned so much. I also would like to thank Dr. Aritra Mukherjee for patiently introducing me to the simulation software FluTAS. Thank you, Prof. Marica Pelanti for the discussions on phase change modelling. Thank you, Prof. Alessio Roccon for all the interesting talks on numerical methods and diffuse interface modelling. Thank you, Dr. Yohei Sato for our fruitful discussions on simulating boiling flows. Additionally, I am thankful for the time and effort invested by Prof. Hans-Jörg Bauer and Prof. Xu Cheng as members of the examination board.

My research visit to KTH was partially funded by the German Academic Exchange Service (DAAD), which is gratefully acknowledged. Furthermore, I would like to thank the Karlsruhe House of Young Scientists (KHYS) for financially supporting an extension of the research stay. Moreover, I gratefully acknowledge the computing time provided on the high-performance computer HoreKa by the National High-Performance Computing Center at KIT (NHR@KIT). Regarding the computational resources, I also acknowledge support by the state of Baden-Württemberg through bwHPC.

Throughout my doctoral studies, I feel very fortunate to have been surrounded by so many great colleagues who really made me enjoy my time in the office. Thank you, Dr. Jorge Yanez, Dr. Philipp Marthaler, Shenhui Ruan, Biao Lyu, Dr. Abdalla Batta, Dr. Karsten Litfin, Prof. Leo Bühler, and more for making me feel welcome at KIT, and for all the nice coffee breaks, lunch breaks, and afterworks. I am also grateful for the colleagues and friends I met at the Fluid Mechanics Department at KTH. Thank you, Parvathy, Victor, Pol, Harry, Adalberto, Martin, Ronith, Arash, Zhenyang, Sharihar, and many others for making the research visit unforgettable.

Outside of work, I would like to thank all my friends from Karlsruhe and Stockholm, from my Bachelor's and Master's studies, and from the ASK sailing club for the fun times and your support. I am especially thankful for my sister, Judith, and the rest of my direct and extended family for all your love and for helping me become who I am today.

A special place in this acknowledgement is reserved for my partner, Dr. Clare Tazzeo. The years as a doctoral researcher are not always easy, but since we are sharing our lives, everything feels doable and more enjoyable. Thank you for all your love and support throughout these years. I am looking forward to seeing where life is taking us next.

Lastly, mom and dad, I am beyond grateful for everything you have done for me. Thank you for believing in me, for cheering me up when I needed it, and for all the time we spend together.

"There is nothing like looking, if you want to find something. You certainly usually find something, if you look, but it is not always quite the something you were after."

J.R.R. Tolkien, *The Hobbit*, 1937

To my family, Ingrid, Armin, and Judith

Contents

Acronyms and symbols

Acronyms

AB	Adams-Bashforth
AC	Allen-Cahn
ACDI	Accurate Conservative Diffuse Interface
CDI	Conservative Diffuse Interface
CFD	Computational Fluid Dynamics
CFL	Courant-Friedrichs-Lewy
CH	Cahn-Hillard
CPU	Central Processing Unit
CSF	Continuum Surface Force
DNS	Direct Numerical Simulation
EB	Energy-Based
FFT	Fast-Fourier Transformation
FT	Front Tracking
GPU	Graphics Processing Unit
HE	Heater Exit
HPC	High Performance Computing
HS	Heater Start
ITES	Institute for Thermal Energy Technology and Safety
KIT	Karlsruhe Institute of Technology

LES	Large Eddy Simulation
LHS	Left-Hand side
LS	Level-Set
MPDJ	Momentum-based Pressure treatment for Density Jumps
MUSIG	Multiple Size Group
NSE	Navier Stokes Equation
NSD	Nucleation Site Density
PDE	Partial Pifferential Equation
PDF	Probability Density Function
PPE	Pressure Poisson Equation
RANS	Reynolds-Averaged Navier-Stokes
RHS	Right-Hand Side
RMS	Root-Mean-Square
SCC	Scientific Computing Center
SEM	Synthetic Eddy Method
TKE	Turbulent Kinetic Energy
VOF	Volume Of Fluid
WENO	Weighted EssentiallyNon-Oscillatory

Latin symbols and variables

Symbol	Unit	Description
a_i	W m^{-1}K^{-1}	Thermal conductivity of i-th phase ($a_i = \lambda_i \rho_i^{-1} c_{p,i}^{-1}$)
$\mathcal{B}_c$	[c] s^{-1}	Temporal rate of change for a scalar quantity c
$\vec{\mathcal{B}}_c$	[c] s^{-1}	Temporal rate of change for a vector quantity c
$\vec{\mathcal{C}}$	N m^{-3}	Momentum correction terms

C_{CFL}	-	Safety factor for the time step constraint
C_Θ	-	Non-dimensional wall-normal phase field gradient limiter
$C_{O\parallel}$	-	Model factor for outflow-parallel force
$c_{p,i}$	J kg^{-1} K^{-1}	Specific heat capacity (at constant pressure) of i-th phase
D	m	Bubble diameter
$\vec{E}_i$	N m^{-3}	Surface energy contributions of i-th phase
$\mathbb{E}(X)$	$[X]$	Expected value of random variable X
$\mathcal{E}$	m^2 s^{-3}	Dissipation
$\vec{\mathcal{F}}$	kg s^{-1} m^{-3}	Differential mass flux
$\vec{f}_{ST}$	N m^{-3}	Surface tension force
Fr	-	Froude number, where Fr $= u_{\text{ref}}/\sqrt{\lvert\vec{g}\rvert\ell}$
$\vec{g}$	m s^{-2}	Gravitational acceleration
Gr	-	Grashof number, where Gr $= \ell\lvert\vec{g}\rvert\rho_1^2\mu_1^{-2}(\rho_2/\rho_1 - 1)$
G	kg s^{-1}m^{-2}	Mass flux
h_i	J kg^{-1}	Specific enthalpy of i-th phase
$\vec{I}_i$	N m^{-3}	Phase interaction forces of i-th phase
$\vec{j}$	W m^{-2}	Anti-trapping current
k	m^2 s^{-2}	Turbulent kinetic energy
L	J kg^{-1}	Temperature-dependent latent heat
L_{sat}	J kg^{-1}	Latent heat at saturation temperature
ℓ	m	Size quantity for computational domain
$\mathcal{M}_i$	kg s^{-1}m^{-3}	Interfacial mass transfer density of i-th phase
$\mathcal{M}$	kg s^{-1}m^{-3}	Interfacial mass transfer density of phase 1 (short for $\mathcal{M}_1$)
M	kg mol^{-1}	Molecular weight
$\vec{n}$	-	Interface normal unit vector

Nu	-	Nußelt number, where Nu $= \ell \frac{\partial T}{\partial x}\big\vert_{\text{wall}} / \Delta T$
N_b	-	Bubble count
p	N m^{-2}	Pressure
Pr	-	Prandtl number, where Pr $= c_p \mu \lambda^{-1}$
$\vec{q}$	W m^{-2}	Generic heat flux
$\vec{\mathcal{R}}$	m s^{-1}	Regularization term
R_g	J mol^{-1}K^{-1}	Universal gas constant
Re	-	Reynolds number, where Re $= \ell u_{\text{ref}} \rho / \mu$
r	m	Radius
$s(X)$	$[X]$	Standard deviation of random variable X
S	s^{-1}	Strain rate tensor
t	s	Time
Δt_ϕ	s	Time step constraint due to CDI/ACDI
T	K	Relative temperature $T = T_{\text{abs}} - T_{\text{sat}}$
T_{abs}	K	Absolute temperature
T_{sat}	K	Saturation temperature
ΔT_{PC}	K	Phase change induced temperature increment
$\vec{u}$	m s^{-1}	Volume-averaged mixture velocity
$\vec{u}_i$	m s^{-1}	Velocity of the i-th phase
u_τ	m s^{-1}	Friction velocity
U_O	m s^{-1}	Characteristic outflow velocity
U_b	m s^{-1}	Bulk velocity
$\vec{v}$	m s^{-1}	Density-averaged (barycentric) mixture velocity
We	-	Weber number, where We $= \rho u_{\text{ref}}^2 \ell / \sigma$
w	-	weight factor

Δx	m	Grid spacing
$\vec{x}$	m	Position vector
X	-	Random number, independently sampled from a uniform continuous distribution

Greek symbols and variables

Symbol	Unit	Description
α_i	-	Volume fraction of i-th phase
β	-	Growth constant
γ	-	Model constant
Γ	m s^{-1}	Interface regularization speed
Γ^*	-	Non-dimensional interface regularization speed
δ	-	Kronecker delta function
ϵ	m	Interface thickness
ϵ^*	-	Non-dimensional interface thickness
ε	-	Small number
ζ	-	Outflow weighting factor
η	-	Sharpening factor
θ	-	Non-dimensional scaling factor for the phase change temperature increment
Θ	$^\circ$	Contact angle
Θ'	$^\circ$	Local contact angle
κ	m^{-1}	Interface curvature
λ	W m^{-1} K^{-1}	Mixture heat conductivity
λ_i	W m^{-1} K^{-1}	Heat conductivity of the i-th phase
Λ	m^{-3}	Bubble concentration

μ	kg m^{-1} s^{-1}	Mixture dynamic viscosity
μ_i	kg m^{-1} s^{-1}	Dynamic viscosity of i-th phase
ξ	N m^{-2}	Chemical potential
Ξ	-	Unique bubble tag
π	-	Mathematical constant
ρ	kg m^{-3}	Mixture density
ρ_i	kg m^{-3}	Density of the i-th phase
σ	N m^{-1}	Surface tension coefficient
τ	N m^{-2}	Viscous stress tensor
Υ	m^{-1}	Interfacial area concentration
Φ	-	Free energy
ϕ	-	Phase field variable
ϕ'	-	Sharpened phase field variable
Ψ	m	Signed interface distance function (level-set function)
ψ	N m^{-2}	Pressure increment
Ω	not appl.	Computational domain
$\partial\Omega$	not appl.	Boundary of computational domain

1 Introduction

Phase-change phenomena appear in everyday situations and are a crucial part of numerous technical processes. The boiling of water in the daily cooking routine, the evaporation of a refrigerant for the cooling in refrigerators, or, on a larger scale, the production of steam for driving turbines in power plants — all are common examples of heat being transferred while a liquid fluid transitions to a gaseous state (or vice versa). Though commonly encountered, phase-change phenomena are considered highly complex and subject to ongoing research. This thesis proposes a methodology that enables the advanced analysis of phase-changing flow through computer simulations. The subsequent sections of this chapter introduce the study of boiling phenomena, and related simulations (Sec. 1.1), and present a motivation behind the chosen research field (Sec. 1.2). A refined definition of the research objectives is presented in Sec. 1.3 and the chapter concludes in Sec. 1.4 with an outline of the thesis.

1.1 Background and Context

The transition from a liquid to a gaseous state (evaporation), and the reverse of this process (condensation), can be further categorized by the mechanism driving the transition. That is, *concentration-driven* phase change or *heat-driven* phase change (Scapin et al. (2020)). For instance, concentration-driven evaporation occurs when water evaporates from wet clothing into the surrounding air of low humidity. This thesis, however, focuses on heat-driven phase change. An example of this is the boiling of water for cooking, where liquid water is heated until the saturation temperature is reached and vapour bubbles start to form. Refer to Fig. 1.1 for a visualization of boiling.

The heat-driven phase change mechanism exhibits fast evaporation rates, and is capable of enabling highly efficient heat transfer at a constant coolant temperature. These properties make heat-driven phase change interesting for industrial applications, where large amounts of heat must be transferred through small areas. Prominent examples include the cooling of: high-performance computer electronics, power electronics in vehicles, and fusion reactor components (see Mudawar (2011)).

Figure 1.1: Boiling heat transfer on a heated rod in an annular gap. Experimental figure provided by Wefers et al. (2025a) obtained by using the COSMOS-L facility at KIT (refer to Wefers et al. (2025b) for details).

Figure 1.2: Thermal damages on heated metal rods after reaching the critical heat flux (refer to Point C in Fig. 1.3). Figure provided by Wefers et al. (2025a) obtained by using the COSMOS-L facility at KIT (refer to Wefers et al. (2024) for details). Sudden surface temperature increase of up to 10^3K within a few seconds can be identified by a change in surface colour.

1.1.1 Brief history of boiling flow research

The utilization of boiling processes for technical applications was dominated by the generation of steam for steam engines in the 18^{th} to early 20^{th} centuries. Since the beginning of the 20^{th} century, new technologies, such as rocket engines and nuclear reactors, have increased scientific interest in boiling heat transfer (Nishikawa (1987)). However, the applications of boiling processes have always been associated with risks, as they often involve high pressures, large amounts of thermal energy, or high heat fluxes, which can potentially lead to catastrophic accidents. For example, Fig. 1.2 demonstrates the sudden thermal damage on heated rods after exceeding the critical heat flux (refer to Fig. 1.3). The critical heat flux causes a change in the boiling heat transfer mechanism, which, in nuclear power applications, must be avoided at all times. As a result, there has been an increasing interest among the research community to delve into the fluid mechanics of boiling flow phenomena.

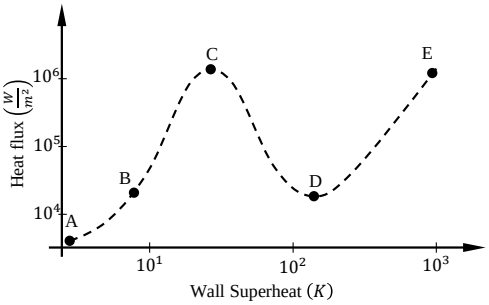

Figure 1.3: Visualization of the boiling regimes. This figure depicts the heat flux from a wall to a fluid, as a function of the surface temperature. Regime A-B: Single-phase heat transfer; no bubbles are forming on the surface. Regime B-C: Start of two-phase heat transfer; liquid partially contacts the surface. Point C: Critical heat flux. Regime C-D: transferred heat flux decreases and surface temperature increases; no liquid contacts the surface. Point D: Leidenfrost point. Regime D-E: Film boiling region. Loosely based on Zuber (1959).

The first notable description of boiling phenomena was published in 1756 by J. G. Leidenfrost (translated publication Leidenfrost (1966)), who described the evaporation behaviour of droplets on hot surfaces. He found that at high surface temperatures, droplets "dance" on the surface and take longer to evaporate entirely. However, there was little other boiling research conducted until the start of the 20^{th} century (Nishikawa (1987)). Among the earliest modern studies, in 1934, Nukiyama measured the wall temperature of different heat fluxes and described a maximum point in the applied heat flux (translation in Nukiyama (1966)). In the subsequent years, researchers identified different boiling regimes, depending on the applied heat flux. For example, the PhD thesis of Zuber (1959) marks a significant milestone in the understanding of boiling regimes. Boiling regimes can be identified on a boiling curve, where the interplay between surface temperature and applied heat flux is visualized (e.g. Fig. 1.3). The nucleate boiling regime, in which bubble growth is observed on a heated wall, is typically located in section B-C of the boiling curve (see Fig. 1.1). Higher wall temperatures lead to the formation of a gas film that separates the liquid from the wall (D-E), which is referred to as film boiling.

Although the majority of studies on boiling in the 20^{th} century remained purely experimental, several simulation-based studies were published in the latter half of the century. The first simulations considered formulations in which two-phase flow is described as a continuous and time-averaged mixture (see Zuber and Findlay (1965), Ishii (1977)). These descriptions are challenging, as they require substantial empirical modelling. Quantitative boiling simulations, involving the instantaneous capturing of the interface, followed significantly later in Juric and Tryggvason (1998), Son and Dhir (1998) and Welch and Wilson (2000).

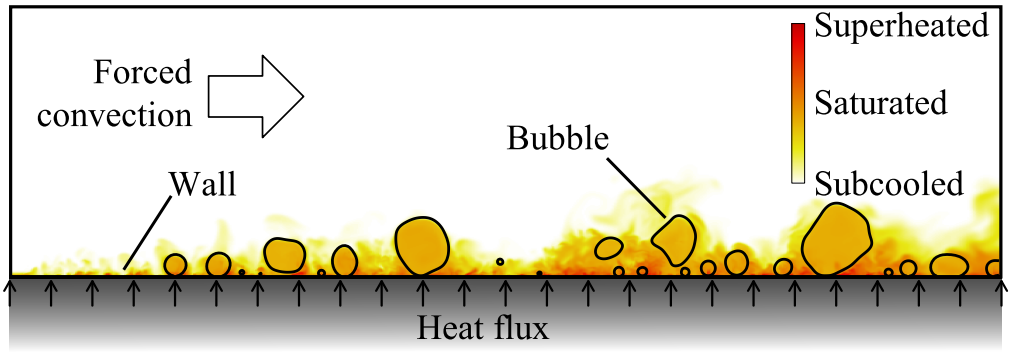

Figure 1.4: Instantaneous visualization of a turbulent boiling flow scenario.

1.1.2 A generic nucleate boiling flow

Fig. 1.4 illustrates a typical scenario in an industrial boiling flow application. Specifically, an instantaneous snapshot of a slice through a nucleate boiling flow is depicted. An external device (e.g. a pump) generates a forced flow from left to right. The bottom boundary represents a solid wall (grey area), at which a heat flux transfers heat from the solid to the fluid (arrows). The heat flux increases the temperature of the fluid. The fluid temperature at which boiling occurs is referred to as the *saturation temperature*. In this figure, the temperature is qualitatively visualized by a colour scale, where white represents the inflow temperature (assumed to be below the saturation temperature in this sketch). Orange hues represent areas where the fluid reaches the saturation temperature, while red hues indicate superheat conditions. In areas where the saturation temperature is met, small impurities in the liquid, or imperfections on the solid surface (i.e., nucleation sites), trigger small bubbles, which subsequently grow through phase change. The transition from the liquid to the gaseous state requires thermal energy (latent heat), which cools the surrounding liquid. The bubbles move within the surrounding liquid and may interact with other bubbles (e.g. merge or break-up). This figure, specifically, depicts a turbulent flow scenario, in which random fluctuations affect the transport of the bubbles and the temperature. As a result, there are many different bubble shapes and sizes. Turbulent flows are highly stochastic processes; accordingly, every snapshot of this same flow would look different.

1.1.3 Time-averaged description of a boiling flow

From an engineering perspective, the instantaneous description of a boiling flow is often neither of interest nor practical. Instead, the description from a time-averaged perspective is often preferred (Ishii and Hibiki (2011)). For example, a design engineer could be interested in the average

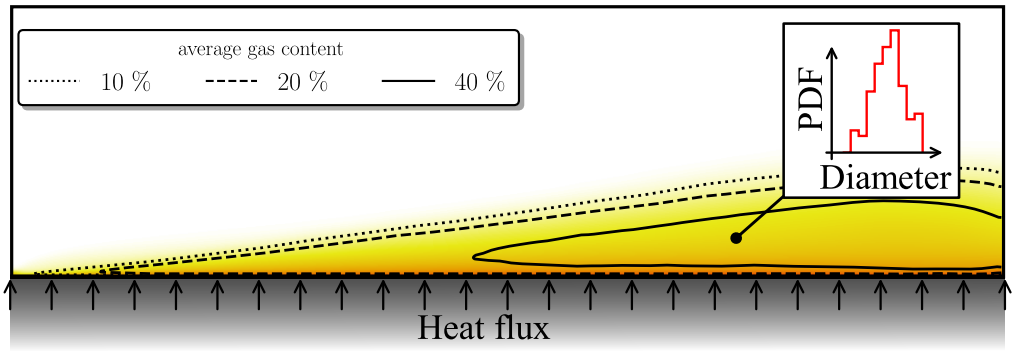

Figure 1.5: Time-averaged representation of Fig. 1.4

temperature expected on a heat-transfer surface or the average gas content in a liquid. A flow description of the latter scenario is depicted in Fig. 1.5. Indeed, Fig. 1.4 and Fig. 1.5 may describe the same flow. By averaging in time, random temperature fluctuations are filtered out and the smooth colour gradient indicates the mean fluid temperature.

With time-averaging, the phase interface between liquid and gas is also lost. Instead, an average gas content remains, which is defined as the probability of finding either gas or liquid in each location (represented by iso-contours of selected probabilities). When describing a bubbly flow by its mean gas content, specific information about the bubbles are not captured. Namely, a time-averaged gas content does not provide information on the size of bubbles in the flow; thus, one cannot discern whether the flow featured many small bubbles or a few very large bubbles. This is problematic, as these two scenarios would result in two very different flows. An enriched description would be to use a Probability Density Function (PDF) to capture this information about the time-averaged distribution of the bubble size. This would allow crucial information on the occurrence frequency of a specific bubble size in a flow to be captured. Sec. 1.2.1 discusses this challenge of accounting for the polydisperse nature of boiling flows in the context of computer simulations.

1.2 Challenges in CFD of boiling flows

The preceding paragraphs outlined the physical basics of boiling flows and highlighted different views for describing a flow, instantaneous or time-averaged. This section will discuss the use of computational fluid dynamics (CFD) for aiding the prediction of boiling flows through numerical simulations. In detail, an overview of CFD methods, from both instantaneous and time-averaged flow perspectives, is provided.

1.2.1 CFD for engineering

As mentioned in Sec. 1.1.3, the time-averaged description of a boiling flow is sufficient for most engineering applications, as time-averaged results are often of interest. To obtain predictions of boiling through computer simulations, adequate mathematical equations need to be formulated. For the mathematical description of a flow, the conservation equations for mass, momentum, and energy (temperature) are averaged in time; these are referred to as the Reynolds-averaged Navier Stokes (RANS) equations. In CFD, solving RANS equations is associated with a low computational cost, making this an interesting approach for industrial applications. However, time-averaging filters out statistical information about the bubbles and the turbulence (see Sec. 1.1.3), and thus, requires mathematical modelling. The modelling of turbulence for RANS simulations is a research field of its own, and will not be discussed here. However, an overview of methods used to model bubble statistics in RANS simulations is provided below.

Relevance of the bubble statistics

The characteristics of a bubble (e.g. the bubble size) impact the behaviour of the flow. The intuitive solution, using average values of the bubble characteristics, is insufficient when non-linear effects are present. For example, Tomiyama et al. (1995) showed that larger bubbles in a duct flow move away from a wall, while smaller bubbles move towards the wall. This highly non-linear behaviour led Krepper et al. (2008) to use different transport velocities for the gas fraction in their simulation depending on the bubble size. Another important consideration for improving the simulation accuracy is the coalescence of smaller bubbles, which is a central process during the life span of a bubble in a boiling flow (Lee et al. (2002)). When Yeoh and Tu (2006) accounted for the coalescence and break-up of bubbles of various sizes, significant improvements in the accuracy of the boiling flow simulations were achieved. In addition, accurate prediction of the interfacial area, a quantity dictated by the bubble's size and shape, largely determines the overall quality of the simulation (Colombo and Fairweather (2016)). All of the presented examples are non-linear effects that depend on the bubble characteristics. Therefore, representing the occurrence probability of a bubble with a certain characteristic (e.g. a certain size) in the simulation software has been implemented to improve the accuracy of the simulation software.

Bubble statistics in CFD

Given that the probability distribution of different bubble characteristics (particularly their size) is essential for obtaining accurate predictions, several methods for representing these statistics have been developed (Shiea et al. (2020)). Fig. 1.6 visualizes three methods to account for

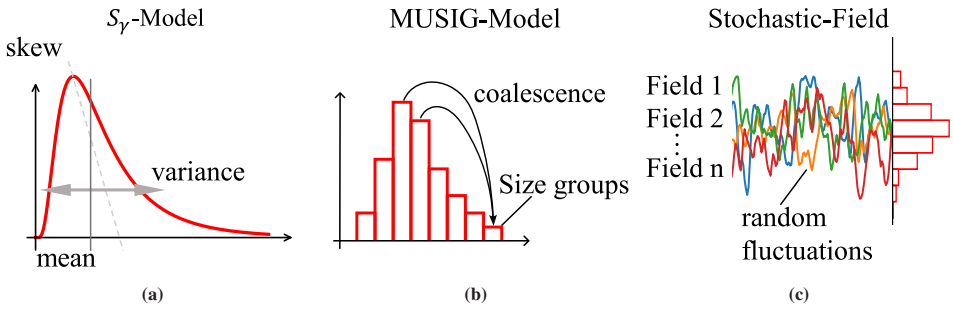

Figure 1.6: Visualization of different methods to represent bubble statistics in CFD.

polydispersity in boiling flow CFD. One possible approach is to apply the the S_γ-Model when assuming the shape of the bubble size PDF (Fig. 1.6a). Here, the PDF is characterized by a number of moments (e.g. first (mean), second (variance), and third (skewness)) for which transport equations are formulated. Kamp et al. (2001) assumed a log-normal distribution and applied this approach to bubbly pipe flows. Using the same PDF, Yun et al. (2012) successfully obtained predictions for subcooled boiling flows. The Multiple Size Group (MUSIG) model is another approach, which was proposed by Lo (1996). In this approach, the PDF is divided into multiple bubble size groups, each with their own transport equation (Fig. 1.6b). In addition, the groups can interact with eachother; for example, to model coalescence, fractions of smaller groups can move to a larger group (and vice versa for bubble break-up). Researchers have successfully employed this approach in boiling flow simulations (e.g. Krepper et al. (2013)). The stochastic fields method is a lesser-used approach (Fig. 1.6c). This method selects representative (field) values from the bubble size PDF for which evolution equations are formulated. The evaluation equations add random fluctuations to the representative fields and the sum of the n representative fields is then used to approximate the local bubble PDF. Raquet (2019) successfully explored the use of this approach for simulating flows subjected to cavitation.

Accuracy of boiling flow CFD

The previous paragraph showed that numerous studies have used PDF methods to simulate boiling flows. In general, the dynamics of bubbles in RANS simulations is still implemented using empirical correlations (e.g. Colombo and Fairweather (2016)). Many parameters in these empirical correlations are resticted to a narrow range of flow conditions and require case-specific adjustments, as highlighted by Krepper et al. (2013). Accordingly, good accuracy of most boiling flow CFD codes is not guaranteed for a wide range of flow conditions, and their predictions must be used with caution (Giustini (2020)). As a result, researchers (e.g. Li et al. (2025)) have emphasized the importance of finding better models to improve the reliability of the simulation

results. For example, models available for bubble break-up and coalescence are often viewed as the limiting factor for using bubble PDF methods (Liao et al. (2011)). In particular, the modelling of the interaction between bubble dynamics and turbulence requires future development (Krepper et al. (2013)).

1.2.2 Interface-resolved simulations

Interface-resolved simulations constitute an alternative approach to predicting boiling flows that does not involve time-averaging. This approach resolves the instantaneous flow field, and thus, the instantaneous location of the phase interface (i.e., Fig. 1.4). Therefore, interface-resolved simulations do not require the modelling of time-averaged quantities. However, the high computational cost of this approach limits its use to academic applications. As a result, this type of simulation is primarily used for enhancing the understanding of the physics of boiling flows (Kharangate and Mudawar (2017)).

Benefits of interface resolved-simulations

There are many benefits of using interface-resolved simulations for predicting boiling flows. Importantly, from resource and safety perspectives, simulations can replace hazardous or expensive experiments. In addition, these simulations grant access to the flow quantities at every time step, and discrete location, in the computational domain. While many quantities are difficult to measure in boiling experiments, numerical simulations can fill this gap, and thus, provide deeper insights into the prevailing physics. The instantaneous velocities, temperature, gas fraction, mass transfer intensity, bubble shape, and pressure, among other quantities, are examples of accessible data that are readily available from interface-resolved simulations.

Computational cost

Studying boiling flows through interface-resolved simulations is typically associated with high computations costs, due to considerable spatial and temporal resolution requirements. In terms of spatial resolution requirements, the accurate simulation of bubble growth requires the resolution of a thin thermal boundary layer around a bubble (Bures et al. (2024)). In addition, temporal resolution requirements arise from the prevailing time scales, for example, in surface tension dominated fluid systems, as presented by Kang et al. (2000). In addition, numerically, some interface capturing methods entail higher computational costs due to the complexity of the algorithms (Mirjalili et al. (2019)). Accordingly, interface-resolved boiling flow simulations

are often regarded as impractical, or sometimes, impossible (Kharangate and Mudawar (2017)). However, the benefits stated in Sec. 1.2.2 make this approach appealing and, therefore, have motivated the development of more efficient simulation frameworks.

1.2.3 Statistical evaluation of bubbly flows

As described in Sec. 1.2.2, interface-resolved simulations can aid in understanding the physical phenomena of boiling flows. Therefore, the results of interface-resolved simulations could be used to derive improved PDF models for RANS-based simulations, enhancing their accuracy (Sec. 1.2.2). However, this would require suitable evaluation methods. For instance, an important link – the definition of a PDF in an instantaneous bubbly flow field (Weber et al. (2023)) – has not yet been developed. In PDF models for RANS simulations, often-used solution quantities include the fraction of the local gas content (see Krepper et al. (2013)), or the volumetric bubble count density (see Yeoh and Tu (2006)), that is occupied by bubbles of, e.g., a certain size. Central questions related to both of these quantities are: How is the related volume around a bubble defined? And, how is the statistical significance guaranteed for every point in space?

1.3 Objectives of the thesis

The objectives of this thesis are to develop a numerical framework that (i) addresses the challenges in contemporary interface-resolved simulations of boiling flows, and (ii) is capable of providing bubble statistics to further understand physical phenomena that could be used to improve RANS-based simulation models.

To address objective (i), a suitable framework for interface-resolved boiling simulations must be developed. The goal of objective (i) is twofold: efficiency and consistency. First, an adequate mathematical description of the interface has to be chosen. Subsequently, all methods for this simulation framework should be selected, or developed, in accordance with these goals and with the interface description method.

To achieve the second objective, a method that allows the consistent statistical evaluation of boiling flow data, obtained from interface-resolved simulations (or experiments), must be developed. This method should provide a clear definition of bubble statistics that ensures statistical significance for all points in space. This also entails connecting the evaluation scheme with the simulation framework.

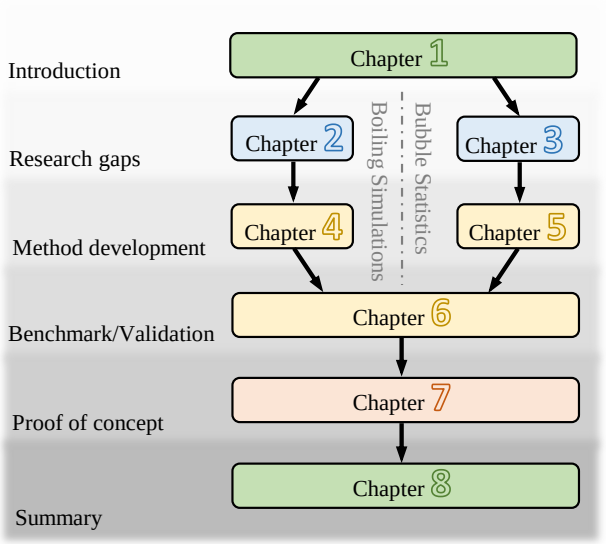

Figure 1.7: Visual structure of the thesis outline (Sec. 1.4). Grey background shading visualizes the cumulative research project progress. Chapters in green boxes represent the opening and closing parts of the thesis. The research gaps are identified in chapter of a blue box. The main scientific contributions are presented in the yellow and orange shaded chapter boxes.

Following the development phase, for both objectives, the framework must be verified through a comprehensive testing and benchmarking campaign. As a final step, a realistic boiling flow scenario should be simulated and evaluated as a proof of concept.

1.4 Thesis outline

The thesis is structured as visualized in Fig. 1.7. In the next two chapters, i.e. Ch. 2 and Ch. 3, the relevant literature for the present work is reviewed and discussed. First, available methods for interface-resolved simulations of boiling flows are reviewed in Ch. 2. Next, tools for the statistical evaluation of bubbly flows are discussed in Ch. 3. Based on the reviewed literature, a suitable flow solver is developed in Ch. 4. Ch. 5 concludes the development phase of this thesis, with a description of the statistical evaluation of bubbly flows. The developments are verified through numerous benchmarks and test cases, the results of which are presented in Ch. 6. As a proof of concept, the simulation of a realistic boiling flow is described and evaluated in Ch. 7. Finally, the findings of this thesis are summarized in Ch. 8.

2 Interface-resolved simulation of boiling flow

This chapter reviews methods for interface-resolved simulations of two-phase flow, with a focus on boiling applications. First, various methods for resolving the phase interface are discussed. This results in the selection of one interface representation method – the *accurate conservative diffuse interface* (ACDI) method – for the simulations in this thesis. All subsequent sections focus on methods tailored to this interface representation method. This chapter consists of a literature review, of which parts are published in Weber et al. (2026); scientific contributions of this thesis are presented in later chapters. Note that in the remainder of this thesis, the following assumptions are made:

- The liquid phase and the gaseous phase are incompressible
- All physical properties of the liquid phase and the gaseous phase are constant
- The saturation temperature is constant

2.1 Interface description

Over the past three decades, a variety of methods have been used for the interface-resolved simulation of boiling flow phenomena. Fig. 2.1 illustrates a classification of some of the most commonly used methods for representing the interface; these can be divided into sharp-interface methods (orange) and diffuse-interface methods (blue).

Sharp interface methods are characterized by an interface that has an exact position and separates the two phases. This class of methods was the first to be used to simulate boiling flows, when Juric and Tryggvason (1998) applied the front-tracking (FT) method to simulate film boiling. In the FT method, the interface is represented by a set of Lagrangian marker points as seen in Fig. 2.2a. In the same year, the level-set (LS) method was introduced by Son and Dhir (1998). The term LS refers to the signed distance function that describes the distance of a point to the interface (Fig. 2.2b). Two years later, Welch and Wilson (2000) introduced the volume of fluid (VOF)

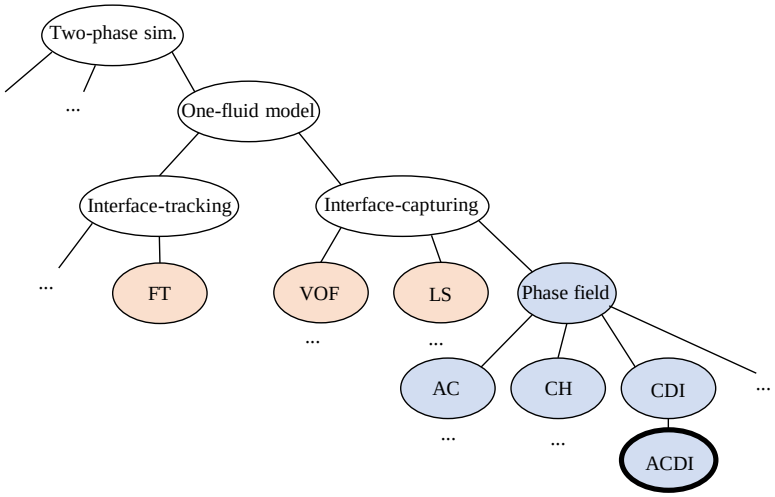

Figure 2.1: Methods for interface-resolved simulations of two-phase flow. The schematic is loosely based on Mirjalili et al. (2017) and Roccon et al. (2023). Blue shades highlight methods that are classified as diffuse-interface methods, while orange shades highlight sharp-interface methods. The thick circle delineates the method – ACDI – that is applied for the simulations in this thesis.

method for simulating film boiling. The VOF method utilizes a colour function that describes the phase fraction from which the interface position can be reconstructed (Fig. 2.2c).

In contrast to sharp interface methods, diffuse interface methods are a class of methods where both phases coexist within a smooth interface region (Fig. 2.2d). Diffuse interface methods were applied to boiling flows later than sharp interface models, and were initially limited to very simple cases. For example, in the first implementations of diffuse interface methods, Jamet et al. (2001) and Sun and Beckermann (2004) conducted one-dimensional simulations of velocity and pressure jumps due to phase change. In the following years, most studies were restricted to two-dimensional domains, as seen in Onuki (2007) for studying boiling with contact angle dynamics or in Laurila et al. (2012) for boiling on heated plates. Since the publication of studies by Badillo (2012) and Badillo (2013), three-dimensional diffuse interface boiling studies have been the norm.

In terms of computational cost, sharp interface methods are often more expensive than diffuse interface methods (e.g. Mirjalili et al. (2019)). This is due to the execution of additional algorithms that are required in sharp interface methods, such as interface reinitialization (LS), interpolation steps (FT), or interface reconstruction (VOF). Diffuse interface methods are considered more efficient, as they usually just require the solution of a single transport equation for the phase indicator. In light of the high computational costs associated with boiling flow simulations, diffuse interface methods are discussed further in the next section.

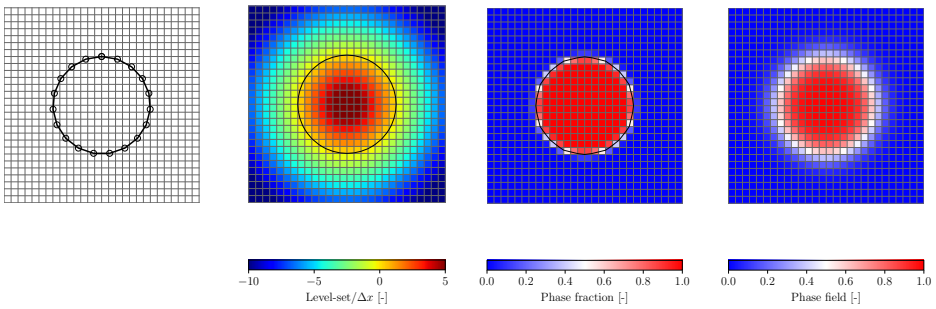

(a) Front tracking **(b)** Level-set **(c)** Volume of fluid **(d)** Phase field

Figure 2.2: Visualization of different methods to represent the phase interface for simulating two-phase flows.

2.2 Phase field models

The term phase field refers to the use of a smooth phase indicator variable to describe the diffuse interface. Historically, the most commonly-used phase field models have been the Allen-Cahn (AC) equation (from Allen and Cahn (1976)) and the Cahn-Hillard (CH) equation (from Cahn and Hilliard (1958)). In both models, an equation is derived to describe the evolution of the phase field. The conservative formulation of the CH equation allows for mass to be conserved. However, it requires a forth-order partial differential equation (PDE) in space to be solved, making it challenging on a numerical level (Tab. 2.1). In contrast, numerically solving the AC equation is simpler, as it exclusively contains second-order derivatives (Tab. 2.1). However, mass is not conserved in the AC equation; this led Sun and Beckermann (2007) and Chiu and Lin (2011) to modify the right-hand side (RHS) of the AC equation to derive a mass-conservative method. This mass conservative second-order equation was first applied to boiling scenarios in 2021 by Haghani-Hassan-Abadi et al. (2021) and Tamura and Katono (2021).

Mirjalili et al. (2020) and Jain et al. (2020) proved that specific parameter choices allow this mass conservative second-order phase field equation to be spatially discretized with central differencing schemes for incompressible and compressible flows, respectively. Their improved scalability potential and low numerical dissipation make central differencing schemes well-suited for simulating complex turbulent flows (see Moin and Verzicco (2016)). Researchers (e.g. Mirjalili et al. (2020)) named this method the *conservative diffuse interface* (CDI) method (Tab. 2.1).

Jain (2022) introduced further improvements to the CDI equation, which led to the name *accurate conservative diffuse interface* (ACDI) method for its higher accuracy and reduced time step constraint. This promising ACDI method has been applied to various phase-change simulations in recent years. For instance, Brown et al. (2023) simulated icing using the ACDI, and Mirjalili et al. (2022a,b) and Salimi et al. (2025) applied the CDI/ACDI to simulate concentration-driven

Table 2.1: Comparison of common phase field methods.

Method	Spatial order of PDE	Mass-conservative
Cahn-Hillard	4^{th}	✓
Allen-Cahn	2^{nd}	✗
Conservative diffuse interface	2^{nd}	✓

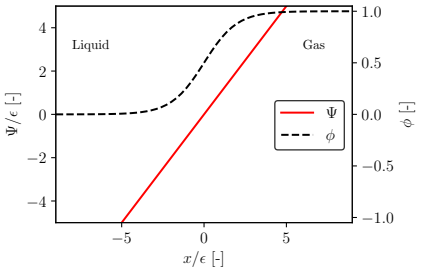

Figure 2.3: Visualization of the equilibrium interface profile of the ACDI method of thickness ϵ (hyperbolic tangent shape). Level-set value Ψ and the phase field variable $\phi \in [0, 1]$ are shown for as a function of the non-dimensional distance from the interface.

evaporation. In terms of boiling, Scapin et al. (2022) and Roccon (2024) used ACDI for simulating nucleate boiling and bubble growth, respectively; however, these simulations were limited to two dimensions. The potential of using ACDI to simulate complex boiling flows in three dimensions has not been explored, to the best of the authors' knowledge. To implement boiling flow simulations, appropriate transport equations must first be described. Accordingly, the following sections – (Sec. 2.3), (Sec. 2.4), and (Sec. 2.5) - will review the literature on the transport equations for mass/phase field, momentum, and energy, respectively, focusing on that related to ACDI.

2.3 Mass and phase field transport using ACDI

The ACDI equation describes the evolution equation of a phase field parameter $\phi \in [0, 1]$. For phase changing flows, Scapin et al. (2022) and Roccon (2024) used the phase field evolution equation

$$\frac{\partial \phi}{\partial t} + \nabla \cdot (\phi \vec{u}) = \frac{\mathcal{M}}{\rho_1} + \nabla \cdot \vec{\mathcal{R}}, \tag{2.1}$$

where $\vec{u}$ is the mixture velocity, ρ_1 is the density of phase 1, and $\mathcal{M}$ is the mass transfer rate. $\vec{\mathcal{R}}$, commonly named the regularization term, maintains the equilibrium interface profile (hyperbolic

tangent shape, see Fig. 2.3). The mass transport of the mixture density $\rho = \rho_1\phi + \rho_2(1-\phi)$ with ρ_i being the density of the i-th phase is then

$$\frac{\partial \rho}{\partial t} + \nabla \cdot (\rho \vec{u}) = \nabla \cdot \vec{\mathcal{F}}. \tag{2.2}$$

The differential mass flux $\vec{\mathcal{F}}$ is defined $\vec{\mathcal{F}} = (\rho_1 - \rho_2)\nabla \cdot \vec{\mathcal{R}}$. In line with the ACDI method by Jain (2022), the regularization term is calculated as

$$\vec{\mathcal{R}} = \Gamma\left[\epsilon\nabla\phi - \frac{1}{4}\left(1 - \tanh^2\left(\frac{\Psi}{2\epsilon}\right)\right)\vec{n}\right]. \tag{2.3}$$

Here, Γ is the regularization speed, ϵ defines the interface thickness, Ψ is the level-set function, and $\vec{n} = \nabla\Psi/|\nabla\Psi|$ is the interface normal unit vector. The regularization speed Γ is directly coupled to the maximum velocity in the domain u_{max}, so that $\Gamma = \Gamma^*|u_{max}|$, with Γ^* being a dimensionless factor. Similarly, ϵ is coupled to the grid spacing Δx through multiplication with a dimensionless factor ϵ^*, i.e., $\epsilon = \epsilon^*\Delta x$. The level-set function Ψ (see Jain (2022)) is defined as

$$\Psi = \epsilon \ln\left(\frac{\phi + \varepsilon}{1 - \phi + \varepsilon}\right). \tag{2.4}$$

In Eq. (2.4), the small number ε ensures stability for regions further away from the interface. Jain et al. (2020) showed that, for central differencing schemes, the time step constraint is

$$\Delta t_\phi = \min_i \left[\frac{1}{\max\left\{\left(\frac{6\Gamma\epsilon}{\Delta x^2}\right) - \left(\frac{\partial u_i}{\partial x_i}\right), 0\right\}}\right]. \tag{2.5}$$

In the CDI studies by Mirjalili et al. (2020) and Jain et al. (2020) it was suggested to use $\epsilon^* = 1$ and $\Gamma^* = 1$. Using the ACDI method through Eq. (2.3) allows thinner interfaces $0.55 \leq \epsilon^* \leq 1$ while $\Gamma^* = 1$, as suggested in Jain (2022).

2.4 Momentum transport

In the context of CDI/ACDI the following balance equation (e.g. Mirjalili and Mani (2021)) is commonly used to describe the momentum transport

$$\frac{\partial \rho \vec{u}}{\partial t} + \nabla \cdot \left(\left(\rho\vec{u} - \vec{\mathcal{F}}\right) \otimes \vec{u}\right) = -\nabla p + \nabla \cdot \tau + \rho\vec{g} + \vec{f}_{ST}. \tag{2.6}$$

In this equation, p is the pressure, and τ, the viscous stress tensor of the mixture, is defined as $\tau = \mu(\nabla\vec{u} + \nabla\vec{u}^T)$, where the mixture dynamic viscosity μ is used. The RHS also features contributions of the gravitational acceleration $\vec{g}$ and the surface tension force $\vec{f}_{ST}$. With the ACDI method, various surface tension models can be applied; these are discussed in Sec. 2.4.1.

Mirjalili and Mani (2021) and Huang et al. (2020) show that the momentum transport of Eq. (2.6) conserves the total kinetic energy. The strategy for deriving Eq. (2.6) is based on the "consistency of mass and momentum transport" (Huang et al. (2020)). This means that the convective transport of momentum in Eq. (2.6) must match the mass transport in Eq. (4.11). In the literature, Eq. (2.6) is the most commonly used momentum transport equation in the CDI/ACDI community.

Note that the momentum transport equation used for diffuse interface methods also remains an ongoing research topic beyond the CDI/ACDI community. For instance, a range of studies (see Gurtin et al. (1996), Lowengrub and Truskinovsky (1998), Boyer (2002), Abels et al. (2012), Souček et al. (2014), Řehoř (2018), ten Eikelder et al. (2023, 2024)) have been published by the CH community. Recently, ten Eikelder and Schillinger (2024) applied an alternative momentum transport equation to simulate bubble dynamics using the CH model. In the study by Souček et al. (2014), it was stated that some derivations might not be consistent for arbitrary magnitudes of the regularization term $\vec{\mathcal{R}}$. However, the applicability of Eq. (2.6) for boiling with ACDI has not been discussed thus far.

2.4.1 Surface tension models

Modelling the surface tension force introduces spurious flow structures, which can significantly impact the simulation accuracy (Scardovelli and Zaleski (1999)). Fig. 2.4 from Kim (2005) depicts such spurious currents around a bubble. The intensity of these flow structures generally increases in the presence of phase change (Tanguy et al. (2014)), due to the interfacial velocity jump. Moreover, spurious flow sometimes interacts with the thermal boundary layer around bubbles in phase change scenarios (Sato and Ničeno (2013)). For CDI/ACDI, two classes of surface tension models are possible (Mirjalili et al. (2023)): (i) continuum surface force (CSF) models (Brackbill et al. (1992)) and (ii) energy-based models (Jacqmin (1999), Kim (2005)). To date, neither of these models has been assessed for simulating boiling flows using the ACDI method.

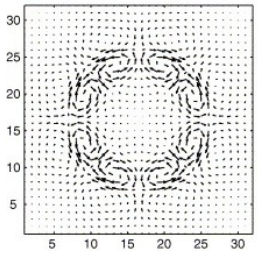

Figure 2.4: Visualization of spurious currents. Reprinted from Kim (2005), Copyright 2004, with permission from Elsevier. The figure qualitatively demonstrates the flow field around a bubble at rest without the influence of gravity.

The continuum surface force

The CSF model from Brackbill et al. (1992) takes the simple form

$$\vec{f}_{ST,CSF} = \sigma\kappa\nabla\phi, \tag{2.7}$$

where $\kappa = \nabla \cdot \vec{n}$ is the interface curvature and σ is the surface tension constant. Although the simple form of Eq. (2.7) is appealing, the CSF is commonly associated with low accuracy (Roccon et al. (2023)). In light of this drawback, alternative formulations have been proposed. For application to flow in porous media, Raeini et al. (2012) proposed

$$\vec{f}^{*}_{ST,CSF} = \sigma\kappa\nabla\phi'. \tag{2.8}$$

This differs from Eq. (2.7) through its use of a sharpened phase indicator ϕ', which is defined as

$$\phi' = \frac{1}{1-\eta}\left[\min\left(\max\left(\phi, \frac{\eta}{2}\right), 1-\frac{\eta}{2}\right) - \frac{\eta}{2}\right] \tag{2.9}$$

The factor η defines the strength of the sharpening. Raeini et al. (2012) proposed to use $\eta = 0.5$ for VOF methods, but did not provide best practice guidlines for phase field methods.

Energy-based surface tension models

Energy-based surface tension models use the chemical potential (denoted ξ) from the AC model (Allen and Cahn (1976)). In the context of CDI/ACDI the following form (e.g. Mirjalili et al. (2023)) of the energy-based model is used

$$\vec{f}_{ST,EB} = \xi\nabla\phi, \quad \xi = \frac{6\sigma}{\epsilon}\left(\frac{\partial\Phi}{\partial\phi} - \epsilon^2\nabla^2\phi\right), \quad \text{and} \quad \Phi = \frac{1}{2}\big[\phi(1-\phi)\big]^2. \tag{2.10}$$

The chemical potential ξ is based on the free energy Φ. Compared to CSF, several studies (Mirjalili et al. (2023), Roccon et al. (2023)) found that this energy-based model has a superior convergence rate for non-phase-change applications. Mathematically equivalent alternative formulations of Eq. (2.10) were proposed to optimize its discrete implementation. For example, Huang et al. (2020) formulated the following "conservative" energy-based model

$$\vec{f}^{*}_{ST,EB} = \frac{6\sigma}{\epsilon}\left(\frac{\partial\Phi}{\partial\phi} - \epsilon^2\nabla^2\phi\right)\nabla\phi = \frac{6\sigma}{\epsilon}\left(\nabla\Phi - \epsilon^2(\nabla^2\phi)\nabla\phi\right). \tag{2.11}$$

Another approach was used by Brown et al. (2024), where $\vec{f}_{ST,EB}$ is expressed in terms of the level-set function Ψ. This level-set variation (Brown et al. (2024)) reads

$$\vec{f}^{**}_{ST,EB} = \frac{6\sigma}{\epsilon}\left(\phi(1-\phi)(1-2\phi)(1-|\Psi|^2) - \epsilon\phi(1-\phi)\nabla^2\Psi\right). \tag{2.12}$$

The benefit of using Eqs. 2.10, 2.11, or 2.12 for simulating boiling flows is yet to be evaluated.

2.5 Energy transport

Several formulations of the energy transport equation have been used in the context of diffuse interface methods. The generic formulation (Jain et al. (2020), Salimi et al. (2025)) for transporting the mixture enthalpy ρh (neglecting viscous dissipation and the contribution pressure) reads

$$\frac{\partial\rho h}{\partial t} + \nabla\cdot(\rho h\vec{u}) = \nabla\cdot(\lambda\nabla T_{\text{abs}}) + \nabla\cdot\left[(\rho_1 h_1 - \rho_2 h_2)\vec{\mathcal{R}}\right], \tag{2.13}$$

where ρh is defined as $\rho h = \rho_1 h_1\phi + \rho_2 h_2(1-\phi)$ and the mixture heat conductivity λ is $\lambda = \lambda_1\phi + \lambda_2(1-\phi)$. The enthalpy of the i-th phase h_i is defined as $h_i = c_{p,i}T_{\text{abs}} + h_{0,i}$, where T_{abs} is the absolute temperature, $c_{p,i}$ is the heat capacity (at constant pressure) and $h_{0,i}$ is the enthalpy of formation at 0 K. Energy transport is often formulated in terms of the transport of the temperature. For instance, Wang et al. (2021) uses a non-conservative formulation

$$\rho c_p\left(\frac{\partial T_{\text{abs}}}{\partial t} + \vec{u}\cdot\nabla T_{\text{abs}}\right) = \nabla\cdot(\lambda\nabla T_{\text{abs}}) - L\mathcal{M}. \tag{2.14}$$

Here, L is the temperature-dependent latent heat defined as $L = f(T_{\text{sat}}) = L_{\text{sat}} + (c_{p,1} - c_{p,2})(T_{\text{abs}} - T_{\text{sat}})$, with L_{sat} being the latent heat at the saturation temperature T_{sat}. Noted that in Eq. (2.14), no term accounts for the differential flux from the diffuse interface model. However, other works (e.g. Mirjalili et al. (2022a)) suggest accounting for this contribution in the equation

for temperature transport. Different variations (e.g., Roccon (2024) and Brown et al. (2023)) of the temperature transport equation have been proposed. A consistent derivation of the temperature transport equation for applying ACDI to boiling flows is not reported yet.

2.5.1 Phase change models

The calculation of the mass transfer rate $\mathcal{M}$ is closely connected to the solution of the energy transport. In recent years, an abundance of phase change models, used to calculate $\mathcal{M}$, have been proposed (see Kharangate and Mudawar (2017) and Liu et al. (2020)). In general, phase change models can be divided into two classes (see Wang et al. (2021)): (i) *heat conduction models*, and (ii) *kinetic models*.

Heat conduction models

Heat conduction models are based on the Rankine-Hugoniot jump conditions (see Gibou et al. (2007)). Therefore, the mass transfer flux $\dot{m}$ times the latent heat L_{sat} is equal to the heat that is transported into the interface (Kharangate and Mudawar (2017)), i.e.

$$\dot{m}L_{\text{sat}} = \left(\lambda_2 \frac{\partial T}{\partial \vec{n}}\bigg|_{\text{phase 2}} - \lambda_1 \frac{\partial T}{\partial \vec{n}}\bigg|_{\text{phase 1}} \right) \quad \text{and} \quad \mathcal{M} = |\nabla \phi| \dot{m} \tag{2.15}$$

This model class is more commonly used than kinetic models, and can be found in numerous studies, including Wang et al. (2021), Tamura and Katono (2021), Roccon (2024), and Haghani-Hassan-Abadi et al. (2021). The prominent advantage of this approach is that Eq. (2.15) is free from empirical or problem-dependent parameters. However, use of this model class entails estimating temperature gradients on both sides of the interface, which can complicate the algorithm (Irfan and Muradoglu (2017)). Therefore, heat conduction models are considered to be more computationally expensive than kinetic models for diffuse interface frameworks.

Kinetic models

Kinetic models were originally based on the kinetic theory of gases (see Schrage (1953)). Further developments (e.g. Tanasawa (1991)) simplified Schrage's model so that $\dot{m}$ has a linear dependency on the vapour temperature, as

$$\dot{m} = \frac{2\gamma}{2-\gamma}\sqrt{\frac{M}{2\pi R_g}}\frac{\rho_1 L_{\text{sat}}(T_{\text{abs}} - T_{\text{sat}})}{\sqrt{T_{\text{sat}}^3}} \tag{2.16}$$

Here, γ is a model constant, M is the molecular mass, and R_g is the universal gas constant. Although the model is simple, γ is a problem-dependent constant (Kharangate and Mudawar (2017)), which is a major drawback of this model. Moreover, other developments, e.g. by Lee (1980), require empirical constants. Rattner and Garimella (2014) and Pan et al. (2016) proposed models that utilize local temperature, which do not require model constants. However, the latter two studies (i) were developed for sharp interface methods, (ii) require sub-iterations for the energy transport, and (iii) are strongly dependent on the time step size (Liu et al. (2020)).

2.5.2 Anti-trapping current

In the context of diffuse interface modelling, researchers have derived transport terms to improve convergence towards the sharp interface limit. Initially, Karma (2001) and Ohno and Matsuura (2009) employed the so-called *anti-trapping current* in their study of dendrite growth. Sun and Beckermann (2010) also utilized an anti-trapping current when studying concentration-driven bubble growth. Badillo (2012) presented an anti-trapping current for boiling flows. Badillo's anti-trapping current reads

$$\vec{j} = -\vec{n}\mathcal{M}L\epsilon\left(\frac{\frac{1}{2}\frac{\lambda}{\lambda_1}\left(\frac{1-\gamma}{\lambda_2/\lambda_1} - \gamma + (1-2\phi)\left(\frac{1-\gamma}{\lambda_2/\lambda_1} + \gamma\right)\right) - 1 + \phi + \gamma}{\phi(1-\phi)}\right). \tag{2.17}$$

According to Badillo (2012), the model constant $\gamma \in [0,1]$ describes the dynamics of the heat flux into the interface. For scenarios where the heat coming from the liquid side to the interface is much larger than that from the gas side, γ is set to zero (Badillo (2013)). In this case, Eq. (2.17) reduces to

$$\vec{j} = -\vec{n}\mathcal{M}L\epsilon\left(\frac{\lambda_1}{\lambda_2} - 1\right). \tag{2.18}$$

As such, $\vec{j}$ is an artificial heat flux and can be added as $+\nabla\cdot\vec{j}$ to the RHS of Eq. (4.21). Within the diffuse interface, adding the anti-trapping current entails that the heat flux is not solely defined by

Fourier's law. However, the anti-trapping current can be explained as a mechanism that accounts for the steep variation in heat conductivities between the gas and the liquid (see Badillo (2012)).

2.6 Numerical Solution

The preceding sections in Ch. 2 discussed the transport equations utilized in the CDI/ACDI method. The remainder of this chapter presents the state of the art for numerically solving these equations.

2.6.1 Spatial discretization

For the spatial discretization of the equations, a staggered grid arrangement is commonly chosen (Fig. 2.5). Eqs. (2.1) and (2.6) can utilize second-order central differencing schemes for approximating spatial derivatives. Specialized schemes may be required for the transport of temperature or enthalpy, as the temperature may exhibit sharp gradients at the phase interface. In these scenarios, the fifth-order WENO scheme from Castro et al. (2011) is commonly used.

For parallel computing, second-order central differencing schemes are preferable. Theey solely require one neighbouring grid point and feature a low numerical dissipation (Moin and Verzicco (2016)). In contrast, WENO schemes like in Castro et al. (2011) require two neighbouring grid points, which increases the communication between processors, and thus, limits the scalability. The complete spatial discretization of the transport equations is a standard technique and will not be reported here (see Zhang et al. (2022) for central differences and Castro et al. (2011) for WENO).

2.6.2 Time-stepping scheme

Many schemes exist for temporal discretization. The explicit Adams-Bashforth (AB) scheme is a simple second-order scheme that has been implemented in numerous studies (e.g. Crialesi-Esposito et al. (2023), Salimi et al. (2025)). In general, the second-order AB scheme (Canuto et al. (1988)) takes the form

$$\frac{c^{n+1} - c^n}{\Delta t^{n+1}} = f_{t,1}\mathcal{B}_c^n + f_{t,2}\mathcal{B}_c^{n-1} \tag{2.19}$$

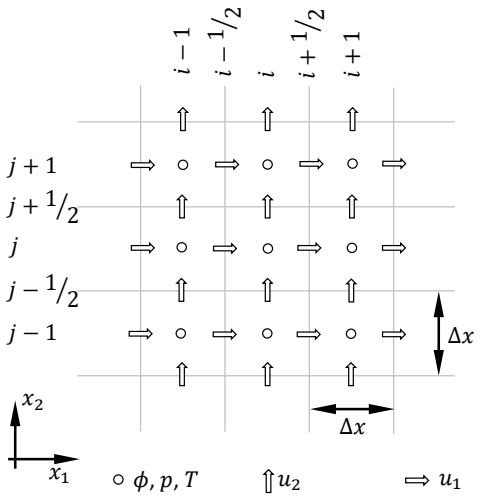

Figure 2.5: Visualization of a two-dimensional staggered grid arrangement taken from Weber et al. (2026). Circles outline the location where scalar fields (e.g., the phase) are defined. The arrows show the location of the velocity components.

In this equation, $\mathcal{B}_c^n$ describes the temporal rate of change at timestep n for a quantity c. That is, the RHS of a PDE of the form $\partial c/\partial t = \mathcal{B}_c$. Furthermore, $\Delta t^{n+1} = t^{n+1} - t^n$ is the time step size between the discrete times t^n and t^{n+1}. The AB coefficients $f_{t,1}$,$f_{t,2}$ are defined as

$$f_{t,1} = 1 + \frac{\Delta t^{n+1}}{2\Delta t^n} \quad \text{and} \quad f_{t,2} = -\frac{\Delta t^{n+1}}{2\Delta t^n}. \tag{2.20}$$

Integrating Eq. (2.1) using Eq. (2.19) (e.g. Salimi et al. (2025)) results in

$$\phi^{n+1} = \phi^n + \Delta t^{n+1}\left(f_{t,1}\mathcal{B}_\phi^n + f_{t,2}\mathcal{B}_\phi^{n-1}\right) \quad \text{with} \quad \mathcal{B}_\phi^n = -\nabla\cdot(\phi^n\vec{u}^n) + \nabla\cdot\vec{\mathcal{R}}^n + \frac{\mathcal{M}^n}{\rho_1} \tag{2.21}$$

For the solution of the momentum equation (Eq. (2.6)), a pressure correction scheme (Chorin (1968)) can be employed to obtain the velocity and pressure. For this purpose, the integration of $(\rho\vec{u})^n$ is divided into two steps: an intermediate momentum $(\rho\vec{u})^* = \rho^{n+1}\vec{u}^*$ and the final momentum $(\rho\vec{u})^{n+1} = \rho^{n+1}\vec{u}^{n+1}$. In Crialesi-Esposito et al. (2023), the momentum equation is integrated by splitting

$$\underbrace{\frac{(\rho\vec{u})^{n+1} - (\rho\vec{u})^*}{\Delta t^{n+1}}}_{\text{Step 2}} + \underbrace{\frac{(\rho\vec{u})^* - (\rho\vec{u})^n}{\Delta t^{n+1}}}_{\text{Step 1}} = \underbrace{f_{t,1}\vec{\mathcal{B}}_{\rho\vec{v}}^n + f_{t,2}\vec{\mathcal{B}}_{\rho\vec{u}}^{n-1} + \rho^{n+1}\vec{g} + \vec{f}_{ST}^{n+1}}_{\text{Step 1}} \underbrace{-\nabla p^{n+1}}_{\text{Step 2}}. \tag{2.22}$$

Note that gravity $\vec{g}$ and the surface tension force $\vec{f}_{ST}$ are excluded from the AB scheme. Using Eq. (2.6), $\vec{\mathcal{B}}^n_{\rho\vec{u}}$ would therefore be $\vec{\mathcal{B}}^n_{\rho\vec{u}} = -\nabla\cdot\left(\rho^n\vec{u}^n\otimes\vec{u}^n\right)+\nabla\cdot\left(\vec{\mathcal{F}}^n\otimes\vec{u}^n\right)+\nabla\cdot\tau^n$. As a result, the first step entails solving

$$(\rho\vec{u})^* = (\rho\vec{u})^n + \Delta t^{n+1}\left[\left(f_{t,1}\vec{\mathcal{B}}^n_{\rho\vec{u}} + f_{t,2}\vec{\mathcal{B}}^{n-1}_{\rho\vec{u}}\right) + \rho^{n+1}\vec{g} + \vec{f}^{n+1}_{ST}\right], \tag{2.23}$$

and the intermediate velocity $\vec{u}^* = (\rho\vec{u})^*/\rho^{n+1}$. The second step is therefore

$$\vec{u}^{n+1} = \vec{u}^* - \frac{\Delta t^{n+1}}{\rho^{n+1}}\nabla p^{n+1}. \tag{2.24}$$

To solve Eq. (2.24), the pressure p^{n+1} must first be computed. The following Sec. 2.6.3 reviews methods to solve for pressure.

2.6.3 Pressure solution

In incompressible flows, the pressure is a quantity that enforces continuity (Ferziger and Perić (2002)). To enforce continuity, the divergence operator can be applied to the second step of Eq. (2.22), which gives

$$\nabla\cdot\left(\frac{\vec{u}^{n+1}-\vec{u}^*}{\Delta t^{n+1}}\right) = \nabla\cdot\left(-\frac{1}{\rho^{n+1}}\nabla p^{n+1}\right). \tag{2.25}$$

Since the divergence of $\vec{u}^{n+1}$ is equal to $\mathcal{M}^{n+1}(1/\rho_1 - 1/\rho_2)$ (e.g. Sun and Beckermann (2004)), Eq. (2.25) can be rewritten as

$$\nabla\cdot\left(\frac{1}{\rho^{n+1}}\nabla p^{n+1}\right) = \frac{1}{\Delta t^{n+1}}\left[\nabla\cdot\vec{u}^* - \mathcal{M}^{n+1}\left(\frac{1}{\rho_1}-\frac{1}{\rho_2}\right)\right]. \tag{2.26}$$

Accordingly, this equation is referred to as the pressure Poisson equation (PPE). Obtaining the pressure from Eq. (2.26) is generally associated with the highest computational cost, as it requires inversion of a matrix. For constant-density single-phase flows, iterative schemes are often employed. Two-phase flows, especially those with large density contrasts, render Eq. (2.26) into an ill-conditioned matrix which reduces the convergence rate (Alsalti Baldellou et al. (2022)) and requires robust preconditions (see Ferronato (2012)).

Density splitting and pressure extrapolation

To overcome this problem, Dodd and Ferrante (2014) introduced a method to turn Eq. (2.26) into a constant coefficient matrix for two-phase flows, on a uniform grid. Their idea is based on the approximation

$$\frac{1}{\rho^{n+1}}\nabla p^{n+1} = \frac{1}{\rho_0}\nabla p^{n+1} + \left(\frac{1}{\rho^{n+1}} - \frac{1}{\rho_0}\right)\nabla p^{n+1} \approx \frac{1}{\rho_0}\nabla p^{n+1} + \left(\frac{1}{\rho^{n+1}} - \frac{1}{\rho_0}\right)\nabla p^{ex}. \quad (2.27)$$

The constant density ρ_0 is chosen $\rho_0 = \min(\rho_1, \rho 2)$, and p^{ex} is the extrapolated pressure from the previous two time steps, i.e., $p^{ex} = (1+\Delta t^{n+1}/\Delta t^n)p^n - (\Delta t^{n+1}/\Delta t^n)p^{n-1}$. Therefore, in Eq. (2.27), the density is divided into a variable part and a constant part (first step), and additionally p^{n+1} is approximated through the extrapolation p^{ex} (second step). Following Frantzis and Grigoriadis (2019), the pressure correction scheme becomes

$$\vec{u}^{**} = \vec{u}^{*} - \Delta t^{n+1}\Big[\Big(\frac{1}{\rho^{n+1}} - \frac{1}{\rho_0}\Big)\nabla p^{ex}\Big], \quad (2.28)$$

$$\nabla^2 p^{n+1} = \frac{\rho_0}{\Delta t^{n+1}}\left[\nabla\cdot\vec{u}^{**} - \mathcal{M}^{n+1}\left(\frac{1}{\rho_1} - \frac{1}{\rho_2}\right)\right], \quad (2.29)$$

$$\vec{u}^{n+1} = \vec{u}^{**} - \frac{\Delta t^{n+1}}{\rho_0}\nabla p^{n+1}, \quad (2.30)$$

where $\vec{u}^{**}$ is a second intermediate velocity after the solution of Eq. (2.23). This method has gained popularity and been used in numerous studies, such as Crialesi-Esposito et al. (2023), Salimi et al. (2025) and Scapin et al. (2020). However, Cifani (2019) demonstrated that for interfacial pressure jumps, the approximation of Eq. (2.27) can lead to pressure oscillations. In the case of surface tension effects, Cifani (2019) proposed a treatment for the forcing term $\vec{f}_{ST}^{n+1}$, which removed the oscillations. Additionally, Cifani (2019) recommended low CFL numbers to achieve satisfactory results.

Interfacial velocity jumps due to phase change also introduce pressure jumps at the interface, known as the *recoil pressure*. Poblador-Ibanez et al. (2025) showed that similar pressure oscillations occur due to recoil pressure and adapted the scheme by Cifani (2019) for terms arising from the convective momentum transport (Trujillo (2021)). In the study by Poblador-Ibanez et al. (2025), significant improvements were achieved, however, start-up oscillations remained.

Method by Juric and Tryggvason (1998)

Juric and Tryggvason (1998) avoid division by density when solving Eq. (2.26). Instead of solving Eqs. (2.24) and (2.25), they arrive at

$$\nabla^2 p^{n+1} = \frac{1}{\Delta t^{n+1}}\left[\nabla\cdot(\rho\vec{u})^* - \nabla\cdot(\rho\vec{u})^{n+1}\right], \tag{2.31}$$

$$\text{and then} \quad \vec{u}^{n+1} = \frac{(\rho\vec{u})^* - \Delta t^{n+1}\nabla p^{n+1}}{\rho^{n+1}}. \tag{2.32}$$

This procedure is appealing, as it obtains a constant coefficient matrix from Eq. (2.31), even for flows with large density ratios. However, shortcomings of this approach are:

- Solving Eq. (2.31) requires $(\rho\vec{u})^{n+1}$, which is generally unknown at this stage
- The velocity field $\vec{u}^{n+1}$ is not guaranteed to have the divergence of $\mathcal{M}^{n+1}(1/\rho_1 - 1/\rho_2)$

FFT-based pressure solution

Turning Eq. (2.26) into a system with constant coefficients (e.g. Eqs. (2.28) or (2.31)) enables the application of fast Fourier transformations (FFT) to accelerate the PPE solution. FFT-based schemes can generally accelerate the PPE solution by one order of magnitude (Buzbee et al. (1970)). The simple example shows how the PPE is reformulated to be efficiently solved with a Gauss elimination scheme (refer to Costa (2018)). Consider a system

$$\nabla^2 p = \text{RHS}. \tag{2.33}$$

On a spatially discrete level in two dimensions, Eq. (2.33) is written as

$$(p_{i-1,j} + p_{i,j-1} - 4p_{i,j} + p_{i+1,j} + p_{i,j+1})/\Delta x^2 = \text{RHS}_{i,j}, \tag{2.34}$$

where i and j refer to the grid indices (see Fig. 2.5). The matrix resulting from Eq. (2.34) has five non-zero diagonals. To reduce the number of diagonals, an FFT can be used. In this section, a hat $\hat{\cdot}$ denotes a variable that has undergone an FFT in the y-direction. Applying the FFT to Eq. (2.34) results in

$$\frac{\text{eig}_j}{\Delta x^2}\hat{p}_{i,j} + (\hat{p}_{i-1,j} - 2\hat{p}_{i,j} + \hat{p}_{i+1,j})/\Delta x^2 = \widehat{\text{RHS}}_{i,j}, \tag{2.35}$$

where eig_j denotes the eigenvalues. The Eq. (2.35) is a tridiagonal matrix that can be solved with a complexity $\mathcal{O}(n)$. After solving the transformed system, a backward transformation

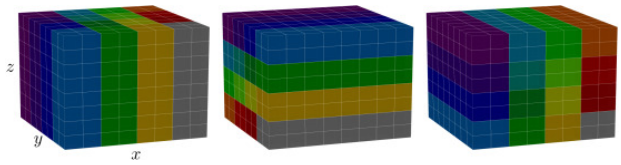

Figure 2.6: Visualization of the pencil-like domain decomposition. Reprinted from Costa (2018), Copyright 2018, with permission from Elsevier. Left: Primary domain decomposition. Middle: transposed domain decomposition to align with direction of first FFT. Right: Transposed domain decomposition to align with direction of second FFT.

(Costa (2018)) must be performed to obtain the pressure p. The extension to three dimensions is straightforward and requires one additional forward and backward FFT. Each FFT has a complexity order of $\mathcal{O}(n\log n)$. Therefore, using an FFT-based pressure solution is favourable for solving large flow problems.

2.6.4 Domain decomposition

This section presents the domain decomposition of the popular FFT-based framework by Costa (2018). In his work, a pencil-like domain decomposition is proposed, where the pencil aligns with the x_3-axis. This situation is illustrated on the left side of Fig. 2.6, where a two-dimensional processor grid decomposes the domain into equally sized subdomains. This x_3-alignment represents the decomposition of all variables during the simulations. The only exception is the solution of the pressure using the FFT. For the forward and backward transformations in the x_1-direction, the data (RHS and p, see previous section) are transposed so that the pencils also align with the x_1-direction (Fig. 2.6, middle). Therefore, the FFT, itself, does not require inter-processor communication. For the second FFT (in x_2-direction), another data transposition is performed, as visualized on the right side of Fig. 2.6.

3 Statistical insights into bubbly flows

The preceding chapter presented an overview of methods that enable the simulation of bubbly two-phase flow. This chapter discusses methods for the post-processing of bubbly flow data. Specifically, methods that allow for the statistical evaluation of bubbles are discussed. Furthermore, the questions stated in Sec. 1.2.3 are explored, namely, (i) how the volume around a bubble can be defined and (ii) how to ensure the bubble evaluation is statistically significant. The methods discussed in this chapter are not limited to simulation data, but can also be applied to post-process experimental data. This chapter consists of a literature review, of which parts are published in Weber et al. (2023); scientific contributions of this thesis are presented in later chapters.

3.1 Box-counting method

When evaluating local statistics of bubbles, the volume associated to which a bubble belongs needs to be defined. The simplest approach is called the box-counting method. The name "box-counting" originates from the process of defining control volumes (boxes) and identifying the bubbles inside each box (e.g., Aliseda et al. (2002)). Subsequently, a statistical analysis of the bubble characteristics can be performed for each box volume. This method has been used to obtain bubble size PDFs (Lau et al. (2013), Laupsien et al. (2019) and Zhao et al. (2021)) and to analyze particle swarms in particle-laden flows (Aliseda et al. (2002) or Laura Villafane-Roca et al. (2016)).

To demonstrate this method, a generic bubble distribution is shown in Fig. 3.1a. Here, the bubbles have an inhomogeneous distribution, with a higher concentration on the right side and a lower on the left. If the local effects are not of interest, the entire domain is defined as a single box (Fig. 3.1a), and all of the bubbles are used to analyze bubble statistics globally (e.g. Laupsien et al. (2019)). This approach is appropriate if the bubble distribution is approximately homogeneous. However, in the case of Fig. 3.1a, where the bubble distribution is inhomogeneous, a decomposition with more boxes (as in Lau et al. (2013) or Zhao et al. (2021)) might be desired to obtain local information. For instance, Fig. 3.1b depicts a possible decomposition into uniform boxes. However, a problem with this decomposition is that the left and middle boxes each only

(a) A generic inhomogeneous bubble distribution

(b) Decomposition into boxes of uniform size

(c) Decomposition into boxes accounting for concentration

Figure 3.1: Visualization of various control volume definitions for a bubble distribution featuring concentration gradients. Bubbles are sketched as circles.

contain one bubble, and thus, constitute poor sample sizes for statistical analysis. To balance the sample distribution between the boxes, the decomposition should account for the bubble concentration. This can be challenging, as the bubble concentration is rarely known a priori (Lau et al. (2016)). The decomposition in Fig. 3.1c could, therefore, be a potential solution. However, a statistic derived from the left box will still be less statistically significant than a statistic derived from the right box. Another drawback of this approach is that quantities like the bubble concentration and the gas fraction are only available as box-averaged values. The bubble concentration or gas fraction associated with each bubble is lost when performing box averaging (Weber et al. (2023)).

3.2 Voronoi analysis

To overcome the problems of the box-counting method (Sec. 3.1), researchers utilized space-filling and auto-adaptive decomposition methods. The Voronoi diagram method, proposed in Voronoi (1908a) and Voronoi (1908b), fulfills these criteria. A Voronoi diagram decomposes an

n-dimensional domain into convex, hexahedral shaped subdomains (bubble cells). By definition, the Voronoi diagram is free from voids or overlaps between the subdomains. As a result, the Voronoi diagram clearly defines a volume around each bubble, which allows a unique bubble concentration and void fraction to be calculated.

The use of cellular models in the context of multi-material flows was initiated by Simha (1952), who analyzed suspensions using an interaction-with-nearest-neighbour model. Later on, Nigmatulin (1979) and Arnold et al. (1989) used polyhedral shapes to study particle flows. In terms of dispersed flows, the term "Voronoi diagram" appeared significantly later, e.g. in Monchaux et al. (2010) and Kidanemariam et al. (2013) for particle-laden flows and even later in Lau et al. (2013) and Kipping et al. (2022) for bubbly flows.

In mathematical terms, a domain that contains a number of bubbles N_b with positions $\vec{x}_1$, $\vec{x}_2$, ..., $\vec{x}_{N_b}$ decomposes the space into N_b bubble cells. The n-th bubble cell $\Omega_{V,n}$ (Voronoi (1908a,b)) is defined as

$$\Omega_{V,n} = \left\{ \vec{x} \quad | \quad |\vec{x} - \vec{x}_n| \leq |\vec{x} - \vec{x}_j| \text{ for } j \neq n, j \in \{1, 2, ..., N_b\} \right\}. \tag{3.1}$$

Eq. (3.1), termed ordinary Voronoi diagram, uses the Euclidean distance to assign each point in the domain to the closest bubble centre. A visualization of the bubble cells is provided in Fig. 3.2.

An advantage of Voronoi diagrams is that each bubble has a single associated bubble cell, and therefore, a unique assigned volume. Thus, quantities like bubble concentration and gas fraction can be related to a single bubble. However, the instantaneous definition of a bubble statistic is not possible, as the sample size is unity. This is not problematic if enough instantaneous data are available, but this can be a drawback if instantaneous data are limited (e.g., for transient flows or computationally expensive simulations), as the local sample size might be small.

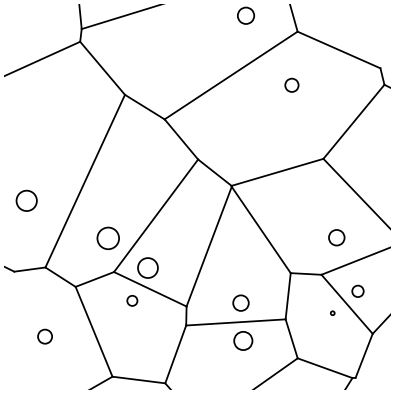

Figure 3.2: Visualization of bubble cells based on an ordinary Voronoi diagram obtained from a random bubble distribution. Figure is taken from Weber et al. (2023).

4 Flow solver developments

Thus far, Ch. 2 and Ch. 3 have provided an overview of the relevant literature regarding the simulation of boiling flows and their statistical evaluation, respectively. This literature review is the basis for deriving and conducting the required method developments. Specifically, the following development goals can be derived from the knowledge gaps identified in Ch. 2:

- The system of transport equations for simulating boiling flows is not consistent throughout the literature. Thus, the clarification and analysis of a suitable mathematical description is needed (see Sec. 2.4 and 2.5)
- The available FFT-based pressure solution schemes shall be improved (see 2.6.3)
- A computationally inexpensive phase change model that avoids the use of empirical parameters is lacking (see Sec. 2.5.1)

Based on these goals, Ch. 4 describes the development of a sophisticated flow solver. The content of this section is published in Weber et al. (2026).

4.1 Improvements to the system of equations

From the governing equations of the liquid and the gas phase, a system of transport equations has to be derived for the artificially diffused interface region. Therefore, these transport equations constitute a modelled system of equations to describe the dynamics of the two-phase flow. As a result, several possible systems of transport equations exist. Depending on the physical application, the accuracy of the result can be affected by the choice of the equations due to their implied assumptions (see Souček et al. (2014)).

In this section, a system of transport equations suitable for boiling flows is discussed. At the beginning of this chapter, the required quantities for describing the two-phase mixture are introduced. For the derivation of a mathematically consistent system of transport equations, the following strategy is used: (i) Identifying the conservation equation for each phase, separately.

(ii) Deriving the mixture equation by summation over both phases. (iii) Augmenting the transport equations with modelling choices for simulating boiling flows.

4.1.1 Mixture quantities

To begin the derivation of the mixture quantities, the i-th phase of the two-phase flow has a volume fraction α_i and a velocity $\vec{u}_i$. The sum of both phases is unity, $\sum \alpha_i = 1$, and both phases are assumed to be incompressible $\nabla \cdot \vec{u}_i = 0$. The partial density $\tilde{\rho}_i$ is defined as

$$\tilde{\rho}_i = \alpha_i \rho_i. \tag{4.1}$$

The volume-averaged mixture properties are

$$\rho = \sum_i \alpha_i \rho_i, \quad \lambda = \sum_i \alpha_i \lambda_i \quad \text{and} \quad \mu = \sum_i \alpha_i \mu_i, \tag{4.2}$$

and the density-averaged mixture properties are

$$\rho c_p = \sum_i \tilde{\rho}_i c_{p,i} \quad \text{and} \quad \rho h = \sum_i \tilde{\rho}_i h_i. \tag{4.3}$$

The decisive factor for the subsequent derivation is the definition of the mixture velocity. One option would be using a density-averaged (barycentric) mixture velocity $\vec{v}$, defined as

$$\vec{v} = \sum_i (\tilde{\rho}_i \vec{u}_i) \rho^{-1}. \tag{4.4}$$

The other option is employing a volume-averaged mixture velocity $\vec{u}$, i.e.,

$$\vec{u} = \sum_i \alpha_i \vec{u}_i. \tag{4.5}$$

Compared to the density-averaged mixture velocity, an advantage of the volume-averaged definition is that, in the absence of phase change, $\vec{u}$ is divergence-free, making it a popular choice in the diffuse interface community (Boyer (2002), Abels et al. (2012), ten Eikelder and Schillinger (2024)). In addition, the CDI/ACDI equations are developed for volume-averaged velocities. Accordingly, a volume-averaged mixture velocity is implemented in this thesis. However, as stated in ten Eikelder and Schillinger (2024), formulations arising from either mixture velocity definition reflect "two sides of the same coin".

Generally, the velocities in both phases differ, which motivates the introduction of a *differential velocity* $\Delta\vec{u}$ to quantify the mismatch. The differential velocity is defined as $\Delta\vec{u} = \vec{u}_1 - \vec{u}_2$ (following Badillo (2012)), and thus the phasic velocities $\vec{u}_i$ can be expressed by using the quantities $\vec{u}$ and $\Delta\vec{u}$ as follows

$$\vec{u}_1 = \vec{u} + \alpha_2 \Delta\vec{u} \quad \text{and} \quad \vec{u}_2 = \vec{u} - \alpha_1 \Delta\vec{u}. \tag{4.6}$$

4.1.2 Mass and phase field transport

The mass transport in each phase is

$$\frac{\partial \tilde{\rho}_i}{\partial t} + \nabla \cdot (\tilde{\rho}_i \vec{u}_i) = \mathcal{M}_i. \tag{4.7}$$

Since mass is conserved, the mass transfer rates have a zero sum, $\sum_i \mathcal{M}_i = 0$. Going forward, the phase field variable ϕ refers to phase "1", which is the gaseous phase. Therefore, $\alpha_1 = \phi$ and $\alpha_2 = (1 - \phi)$. Setting $i = 1$ for Eq. 4.7 and dividing by ρ_1 results in the phase field transport equation

$$\frac{\partial \phi}{\partial t} + \nabla \cdot (\phi \vec{u}_1) = \frac{\mathcal{M}_1}{\rho_1}. \tag{4.8}$$

To eliminate the phasic velocity $\vec{u}_i$, the relations from Eq. (4.6) are implemented. For conciseness, the subscript 1 is dropped from $\mathcal{M}_1$, so that $\mathcal{M}_1 = \mathcal{M}$ and $\mathcal{M}_2 = -\mathcal{M}$. This results in

$$\frac{\partial \phi}{\partial t} + \nabla \cdot (\phi \vec{u}) = \frac{\mathcal{M}}{\rho_1} - \nabla \cdot \big[\phi(1 - \phi)\Delta\vec{u}\big]. \tag{4.9}$$

Multiplying with the reciprocal density, the divergence of $\vec{u}$ can be derived from Eq. (4.7) as

$$\sum_i \left[\frac{\partial \alpha_i}{\partial t} + \nabla \cdot (\alpha_i \vec{u}_i)\right] = \nabla \cdot \vec{u} = \mathcal{M}\left(\frac{1}{\rho_1} - \frac{1}{\rho_2}\right). \tag{4.10}$$

Following the same strategy, but without dividing by the density, leads to the definition of the transport equation of the mixture mass ρ

$$\sum_i \left[\frac{\partial \tilde{\rho}_i}{\partial t} + \nabla \cdot (\tilde{\rho}_i \vec{u}_i)\right] = \frac{\partial \rho}{\partial t} + \nabla \cdot (\rho \vec{u}) = -(\rho_1 - \rho_2)\nabla \cdot \big[\phi(1 - \phi)\Delta\vec{u}\big]. \tag{4.11}$$

4.1.3 Differential velocity closure relation

Thus far, the transport equations for mass and phase field have been derived. However, when attempting to solve Eqs. (4.9) and (4.11), the term $\phi(1-\phi)\Delta\vec{u}$ is encountered. In general, $\Delta\vec{u}$ is not accessible and requires closure. In the presence of phase change, the term could be related to the interfacial velocity jump, but without phase change $\Delta\vec{u}$ is commonly attributed to counteracting numerical diffusion effects. Closure of $\Delta\vec{u}$ can be reached through a term-by-term analogy with the well-known CDI/ACDI transport Eq. (2.1). The regularization term $\vec{\mathcal{R}}$ can be identified as the corresponding term. The analogy yields

$$-\phi(1-\phi)\Delta\vec{u} = \vec{\mathcal{R}} \quad \text{and} \quad -(\rho_1-\rho_2)\big[\phi(1-\phi)\Delta\vec{u}\big] = \vec{\mathcal{F}}, \tag{4.12}$$

and is used for the remainder of this thesis.

4.1.4 Consistent momentum transport

A common strategy for deriving the mixture momentum balance equation is to start by considering each phase separately. This strategy is followed by many, including Boyer (2002), Sun and Beckermann (2004), Badillo (2012), Řehoř (2018), and recently by ten Eikelder et al. (2023) and ten Eikelder et al. (2024).

The (simplified) linear momentum balance equation (ten Eikelder et al. (2024)) for the i-th phase reads

$$\frac{\partial\alpha_i\rho_i\vec{u}_i}{\partial t} + \nabla\cdot(\alpha_i\rho_i\vec{u}_i\otimes\vec{u}_i) = -\alpha_i\nabla p + \nabla\cdot\tau_i + \alpha_i\rho_i\vec{g} + \vec{I}_i + \vec{E}_i. \tag{4.13}$$

Here, $\vec{I}_i$ are the phase interaction forces, which sum to zero $\sum_i \vec{I}_i = \vec{0}$ (see e.g. Sun and Beckermann (2004)). $\vec{E}_i$ is the contribution of the surface energy. For AC and CH models, $\vec{E}_i$ arises from the energy functional (see ten Eikelder et al. (2024)), and according to Sun and Beckermann (2004) the sum of $\vec{E}_i$ is the effect of the surface tension. The stress tensor is $\tau_i = \alpha_i\mu_i(\nabla\vec{u}_i + \nabla\vec{u}_i^T)$ and both phases share the same pressure field p.

LHS analysis

The LHS of the mixture momentum transport equation is obtained by summing Eq. (4.13) over index i for both phases. The quantities $\vec{u}$, $\vec{\mathcal{R}}$, and $\vec{\mathcal{F}}$ are used to simplify the result:

$$\begin{aligned}\sum_i \left[\frac{\partial \alpha_i \rho_i \vec{u}_i}{\partial t} + \nabla \cdot (\alpha_i \rho_i \vec{u}_i \otimes \vec{u}_i)\right] &= \frac{\partial \rho \vec{u}}{\partial t} + \nabla \cdot \left(\rho \vec{u} \otimes \vec{u}\right) - \nabla \cdot \left(\vec{\mathcal{F}} \otimes \vec{u}\right) \\ &- \frac{\partial \vec{\mathcal{F}}}{\partial t} - \nabla \cdot \left(\vec{u} \otimes \vec{\mathcal{F}}\right) + \nabla \cdot \left(\left(\frac{\rho_1}{\phi} + \frac{\rho_2}{1-\phi}\right)\vec{\mathcal{R}} \otimes \vec{\mathcal{R}}\right) \\ &= \frac{\partial \rho \vec{u}}{\partial t} + \nabla \cdot \left(\left(\rho \vec{u} - \vec{\mathcal{F}}\right) \otimes \vec{u}\right) + \vec{\mathcal{C}}.\end{aligned} \tag{4.14}$$

In Eq. (4.14), no assumptions concerning the relevance of terms are made, and thus, the equation is presented in full length. Compared to the commonly used mixture momentum formulation (utilizing a volume-averaged mixture velocity, see Eq. (2.6)), Eq. (4.14) contains additional terms. Specifically, the terms in the second line of Eq. (4.14) are commonly neglected in the mixture momentum formulation. Their corresponding shorthand $\vec{\mathcal{C}}$ is introduced in the last line of Eq. (4.14).

The terms $\frac{\partial \vec{\mathcal{F}}}{\partial t} + \nabla \cdot \left(\vec{u} \otimes \vec{\mathcal{F}}\right)$ are commonly omitted by assuming "relative momenta [...] are negligible when computed relative to the gross motion of the fluid", as stated in Gurtin et al. (1996). This assumption has since been adopted in the derivations of numerous studies, e.g., Abels et al. (2012), Dong (2014a), Řehoř (2018). The strategy of "consistency of mass and momentum transport" proposed by Huang et al. (2020), and employed by Mirjalili and Mani (2021) and Jain et al. (2020), implicitly relies on this assumption. Technically, the term $\frac{\partial \vec{\mathcal{F}}}{\partial t} + \nabla \cdot \left(\vec{u} \otimes \vec{\mathcal{F}}\right) \neq 0$ (ten Eikelder et al. (2023) and ten Eikelder et al. (2024)), and thus, is kept in the present derivation. ten Eikelder and Schillinger (2024) also demonstrated that accurate results for two-phase flows were obtained by keeping $\frac{\partial \vec{\mathcal{F}}}{\partial t} + \nabla \cdot \left(\vec{u} \otimes \vec{\mathcal{F}}\right)$.

The third term in the second line of Eq. (4.14) is also often postulated to be irrelevant and omitted. However, Badillo (2012) explained that it is part of the pressure and Řehoř (2018) added it to the stress tensor τ.

For the remainder of this work, all the terms of Eq. (4.14) are retained, and the relevance of $\vec{\mathcal{C}}$ is evaluated through numerical experiments.

Noted that the LHS can also be expressed in terms of the density-averaged mixture velocity by recognizing that $\rho\vec{v} = \rho\vec{u} - \vec{\mathcal{F}}$. This reformulation reads

$$\frac{\partial \rho\vec{u}}{\partial t} + \nabla\cdot\left(\rho\vec{u}\otimes\vec{u}\right) - \nabla\cdot\left(\vec{\mathcal{F}}\otimes\vec{u}\right) - \frac{\partial\vec{\mathcal{F}}}{\partial t} - \nabla\cdot\left(\vec{u}\otimes\vec{\mathcal{F}}\right) + \nabla\cdot\left(\left(\frac{\rho_1}{\phi} + \frac{\rho_2}{1-\phi}\right)\vec{\mathcal{R}}\otimes\vec{\mathcal{R}}\right) = \frac{\partial\rho\vec{v}}{\partial t} + \nabla\cdot\left(\rho\vec{v}\otimes\vec{v}\right) + \nabla\cdot\left(\left(\frac{\rho_1\rho_2}{\rho\phi(1-\phi)}\right)\vec{\mathcal{R}}\otimes\vec{\mathcal{R}}\right). \tag{4.15}$$

The result of Eq. (4.15) is equivalent to the mixture momentum equation derived in Sun and Beckermann (2004). However, the divergence of $\vec{v}$ is $\nabla\cdot\vec{v} = \nabla\cdot\vec{u} - \nabla\cdot(\rho^{-1}\vec{\mathcal{F}})$; thus, even in the absence of phase change, the divergence is non zero. Occasionally, $\vec{v}$ will be used in subsequent sections due to the compact form of Eq. (4.15).

RHS analysis

It is straightforward to formulate the pressure, gravitation, and interaction forces for the mixture formulation, as

$$\sum_i(-\alpha_i\nabla p + \alpha_i\rho_i\vec{g} + \vec{I}_i) = -\nabla p + \rho\vec{g}. \tag{4.16}$$

However, expressing $\sum_i(\tau_i)$ through mixture quantities is more complicated. Boyer (2002) and ten Eikelder et al. (2024) present complete formulations of $\sum_i(\tau_i)$, whereas Sun and Beckermann (2004) present an approximation. This thesis employs the simple approximation

$$\sum_i(\tau_i) \approx \tau = \mu(\nabla\vec{u} + \nabla\vec{u}^T - 2\nabla\cdot\vec{u}\mathbb{I}). \tag{4.17}$$

By using $-2\nabla\cdot\vec{u}\mathbb{I}$, the spurious pressure contribution[1], that arises from the divergence in normal stress components, is removed (see Juric and Tryggvason (1998), Schreter-Fleischhacker et al. (2024)).

The mixture formulation of $\sum_i \vec{E}_i$ accounts for the effect of surface tension. AC and CH models would use an energy-based expression. However, since no energy functional is known (Mirjalili

[1] Intuitively, a factor of $-2/3$ is expected as it is done for the deviatoric stress tensor in the literature of compressible flow. For diffuse interface simulations of phase change, this factor has a different origin. Here, the correction solely accounts for the artificial viscous stress due to phase change. Consider a 1D case without modification Eq. (4.17): an artificial vicious stress contribution of $\partial_x[2\mu\mathcal{M}(1/\rho_1 - 1/\rho_2)]$ remains in the momentum balance. This spurious contribution is counterbalanced by Eq. (4.17).

et al. (2023)) for the CDI/ACDI equations, the term $\sum_i \vec{E}_i$ is expressed by a force $\vec{f}_{ST}$ to represent surface tension.

The fully closed mixture momentum transport equations is then

$$\frac{\partial \rho \vec{u}}{\partial t} + \nabla \cdot \left(\left(\rho \vec{u} - \vec{\mathcal{F}} \right) \otimes \vec{u} \right) + \vec{\mathcal{C}} = -\nabla p + \nabla \cdot \tau + \rho \vec{g} + \vec{f}_{ST}, \tag{4.18}$$

with

$$\vec{\mathcal{C}} = -\frac{\partial \vec{\mathcal{F}}}{\partial t} - \nabla \cdot \left(\vec{u} \otimes \vec{\mathcal{F}} \right) + \nabla \cdot \left(\left(\frac{\rho_1}{\phi} + \frac{\rho_2}{1-\phi} \right) \vec{\mathcal{R}} \otimes \vec{\mathcal{R}} \right). \tag{4.19}$$

Note that no surface tension model has been selected, yet. Numerical tests in Sec. 6.6.2 will analyze various surface tension models (Sec. 2.4.1) for avoiding spurious currents in boiling flows. As such, Sec. 6.6.2 serves as a best practice guideline for conducting boiling flow simulations with the ACDI method involving surface tension.

4.1.5 Consistent energy transport

The transport equation of the enthalpy of the i-th phase is (see Badillo (2012))

$$\frac{\partial \tilde{\rho}_i h_i}{\partial t} + \nabla \cdot (\tilde{\rho}_i h_i \vec{u}_i) = \nabla \cdot (\alpha_i \lambda_i \nabla T_{\text{abs}}). \tag{4.20}$$

The sum of Eq. (4.20), written in terms of mixture quantities, is

$$\frac{\partial \rho h}{\partial t} + \nabla \cdot (\rho h \vec{u}) = \nabla \cdot (\lambda \nabla T_{\text{abs}}) + \nabla \cdot \left[(\rho_1 h_1 - \rho_2 h_2) \vec{\mathcal{R}} \right]. \tag{4.21}$$

As such, Eq. (4.21) is equivalent to the formulations used in Jain et al. (2020) and Salimi et al. (2025). Moreover, compared to Eq. (2.14), the energy-conservative form of Eq. (4.21) makes it numerically advantageous. However, in contrast to phase field and momentum transport, specialized schemes for the discretization of the convective transport of the enthalpy are required. This is due to the potential presence of interfacial temperature jumps, where WENO schemes (e.g. Castro et al. (2011)) are commonly utilized. Using a WENO scheme for Eq. (4.21), and central differencing schemes for all other transport equations, can lead to inconsistencies. These inconsistencies potentially arise from the transport of physical properties in both the phase field transport Eq. (4.9) and the energy transport Eq. (4.21) (because of ρc_p). To resolve this inconsistency, the transport of physical properties are decoupled from the transport of thermal energy. Therefore, Eq. (4.21) is reformulated below.

For convenience, a relative temperature T is introduced, utilizing the saturation temperature T_{sat} as a reference. Thus, $T = T_{\text{abs}} - T_{\text{sat}}$ and the resulting transport equation is

$$\frac{\partial \rho c_p T}{\partial t} + \nabla \cdot (\rho c_p T \vec{u}) = \nabla \cdot (\lambda \nabla T) - \mathcal{M} L_{\text{sat}} + (\rho_1 c_{p,1} - \rho_2 c_{p,2}) \nabla \cdot (T \vec{\mathcal{R}}). \tag{4.22}$$

In this equation, L_{sat} is the latent heat at saturation temperature, defined as $L_{\text{sat}} = h_1(T_{\text{sat}}) - h_2(T_{\text{sat}})$. Making use of the phase field transport equation (Eq. 4.9), the following equation is obtained

$$\rho c_p \left(\frac{\partial T}{\partial t} + \vec{u} \cdot \nabla T \right) = \nabla \cdot (\lambda \nabla T) - L\mathcal{M} + \Delta \rho c_p \vec{\mathcal{R}} \cdot \nabla T, \tag{4.23}$$

Thus, the transport of ρc_p is decoupled from T. In Eq. (4.23), $\Delta \rho c_p$ is defined as $\Delta \rho c_p = \rho_1 c_{p,1} - \rho_2 c_{p,2}$. As seen in Eq. (4.23), the transport equation of temperature contains the contribution of the regularization term. Although other studies (Scapin et al. (2022), Tamura and Katono (2021), Wang et al. (2021), Haghani-Hassan-Abadi et al. (2021)) did not report this term, this thesis includes $\vec{\mathcal{R}}$ in Eq. (4.23) for consistency with the ACDI model.

To improve convergence, the present model utilizes the anti-trapping current from Badillo (2012) (Eq. (2.18)). Therefore, the final energy transport equation reads

$$\rho c_p \left(\frac{\partial T}{\partial t} + \vec{u} \cdot \nabla T \right) = \nabla \cdot (\lambda \nabla T) + \nabla \cdot \vec{j} - L\mathcal{M} + \Delta \rho c_p \vec{\mathcal{R}} \cdot \nabla T. \tag{4.24}$$

4.1.6 System of transport equations

This section summarizes the final transport equations discussed in the Sec. 4.1.2 - Sec. 4.1.4. The system of equations reads

$$\frac{\partial \phi}{\partial t} + \nabla \cdot (\phi \vec{u}) = \frac{\mathcal{M}}{\rho_1} - \nabla \cdot \vec{\mathcal{R}}, \tag{4.25}$$

$$\frac{\partial \rho \vec{u}}{\partial t} + \nabla \cdot \left(\left(\rho \vec{u} - \vec{\mathcal{F}} \right) \otimes \vec{u} \right) = -\vec{\mathcal{C}} - \nabla p + \nabla \cdot \tau + \rho \vec{g} + \vec{f}_{ST}, \tag{4.26}$$

$$\rho c_p \left(\frac{\partial T}{\partial t} + \vec{u} \cdot \nabla T \right) = \nabla \cdot (\lambda \nabla T) + \nabla \cdot \vec{j} - L\mathcal{M} + \Delta \rho c_p \vec{\mathcal{R}} \cdot \nabla T. \tag{4.27}$$

These equations describe the transport of the phase field variable, the momentum and the thermal energy, respectively.

4.2 Time-stepping scheme

A system of transport equations (Sec. 4.1.6) has now been derived, but the numerical solution still requires spatial and temporal discretization of those equations. In terms of spatial discretization, second-order central differences are used for approximating all derivatives, as described in Sec. 2.6.2. The only exceptions are the terms $\Delta\rho c_p\vec{\mathcal{R}}\cdot\nabla T$ and $\vec{u}\cdot\nabla T$, for which the WENO scheme by Castro et al. (2011) is employed. The spatial discretization of the transport equations is straightforward, and therefore, not discussed further here.

The temporal discretization, discussed in Sec. 2.6.2, must be adapted to the current set of equations. First, the phase field ϕ and the temperature T must be integrated, but the mass transfer $\mathcal{M}$ in this scheme is unknown. Therefore, the integration of ϕ and T is split into two stages. In the first stage, the integration is performed without $\mathcal{M}$ to obtain ϕ and T for an intermediate step denoted by $(\cdot)^*$ (between time step t^n and t^{n+1}). For this strategy, we obtain

$$\phi^* = \phi^n + \Delta t^{n+1}\big(f_{t,1}\mathcal{B}_\phi^n + f_{t,2}\mathcal{B}_\phi^{n-1}\big), \tag{4.28}$$

$$T^* = T^n + \Delta t^{n+1}\big(f_{t,1}\mathcal{B}_T^n + f_{t,2}\mathcal{B}_T^{n-1}\big). \tag{4.29}$$

The rates of change $\mathcal{B}_\phi^n$ and $\mathcal{B}_T^n$, excluding phase change, read

$$\mathcal{B}_\phi^n = -\nabla\cdot(\phi^n\vec{u}^n) + \nabla\cdot\vec{\mathcal{R}}^n, \tag{4.30}$$

$$\mathcal{B}_T^n = -\vec{u}^n\cdot\nabla T^n + \frac{1}{(\rho c_p)^*}\Big(\nabla\cdot(\lambda^n\nabla T^n) + \nabla\cdot\vec{j}^n + \Delta\rho c_p\vec{\mathcal{R}}^n\cdot\nabla T^n\Big). \tag{4.31}$$

In the second stage of the integration, the phase change term $\mathcal{M}^{n+1}$ is added. This splitting procedure enhances the stability of the integration. The second stages of the integration are then

$$\phi^{n+1} = \phi^* + \Delta t^{n+1}\frac{\mathcal{M}^{n+1}}{\rho_1} \quad \text{and} \quad T^{n+1} = T^* + \Delta T_{PC}^{n+1}. \tag{4.32}$$

The temperature increment due to phase change ΔT_{PC}^{n+1} is coupled to $\mathcal{M}^{n+1}$ through the relation

$$\mathcal{M}^{n+1} = -\frac{(\rho c_p)^*\Delta T_{PC}^{n+1}}{L(T^*)\Delta t^{n+1}}. \tag{4.33}$$

In Sec. 4.4, the modelling of phase change and the calculation of ΔT_{PC}^{n+1} from T^* and ϕ^* is discussed.

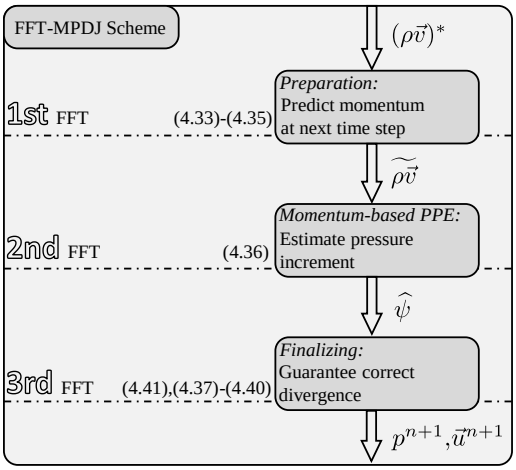

Figure 4.1: Visualization of the three solution stages (darker grey boxes) of the proposed FFT-MPDJ scheme. In- and output quantities of each stage are shown left of the arrows. Corresponding equation number is shown in brackets. The purpose of each solution stage is stated in the boxes.

The velocity field is advanced in time using Eq. (4.18). For the integration, the density-averaged mixture momentum formulation is used for its concise form (see Eq. (4.15)). Similar to Eq. (2.23), the intermediate momentum $(\rho\vec{v})^*$ is obtained by solving

$$(\rho\vec{v})^* = (\rho\vec{v})^n + \Delta t^{n+1}\left[\left(f_{t,1}\vec{\mathcal{B}}^n_{\rho\vec{v}} + f_{t,2}\vec{\mathcal{B}}^{n-1}_{\rho\vec{v}}\right) + \rho^{n+1}\vec{g} + \vec{f}^{n+1}_{ST} - \nabla p^n\right]. \tag{4.34}$$

For convenience, the pressure p^{n+1} is decomposed as $p^{n+1} = p^n + \psi^{n+1}$, and the contribution of p^n is added to the intermediate momentum $(\rho\vec{v})^*$. Here, $\vec{\mathcal{B}}^n_{\rho\vec{v}}$ is calculated from

$$\vec{\mathcal{B}}^n_{\rho\vec{v}} = -\nabla\cdot\left(\rho^n\vec{v}^n\otimes\vec{v}^n\right) - \nabla\cdot\left(\left(\frac{\rho_1\rho_2}{\rho^n\phi^n(1-\phi^n)}\right)\vec{\mathcal{R}}^n\otimes\vec{\mathcal{R}}^n\right) + \nabla\cdot\tau^n, \tag{4.35}$$

and represents the contributions of viscosity and convection.

4.3 FFT-based pressure solution for flows subjected to phase change

Following the intermediate momentum $(\rho\vec{v})^*$ calculation, a suitable pressure solution scheme must be selected. The shortcomings of the commonly-used density splitting and pressure extrapolation schemes, originating from Dodd and Ferrante (2014), were described in Sec. 2.6.3. In contrast,

the pressure solution scheme by Juric and Tryggvason (1998) provides a promising approach, although implementation challenges were identified (Sec. 2.6.3). For this thesis, the *momentum-based* formulation by Juric and Tryggvason (1998) is adopted and modified for the current flow description.

A multi-stage approach is introduced to address the challenges of numerically implementing the scheme by Juric and Tryggvason (1998). Each stage involves solving a constant coefficient Poisson equation, for which efficient FFT schemes can be applied. This solution scheme is visualized in Fig. 4.1. The central part (Stage 2) of the pressure solution is based on Eq. (2.31) from Juric and Tryggvason (1998), whereas Stage 1 and Stage 3 address the implementation challenges related to this method. Specifically, Stages 1 and 3 allow for (i) the prediction of the momentum at time step t^{n+1}, and (ii) ensuring the prescribed divergence of the velocity field after pressure correction. Therefore, the developed scheme has the form:

Stage 1: To prepare for a momentum-based approach, a predicted momentum (marked by a tilde $\widetilde{\cdot}$) must be found. For this, the strategy from Frantzis and Grigoriadis (2019) is adapted as follows

$$\vec{v}^{**} = \vec{v}^{*} - \Delta t^{n+1}\Big[\Big(\frac{1}{\rho^{n+1}} - \frac{1}{\rho_0}\Big)\frac{\Delta t^{n+1}}{\Delta t^{n}}\nabla\psi^{n}\Big], \tag{4.36}$$

$$\nabla^2\widetilde{\psi} = \frac{\rho_0}{\Delta t^{n+1}}\left[\nabla\cdot\vec{v}^{**} - \mathcal{M}^{n+1}\left(\frac{1}{\rho_1} - \frac{1}{\rho_2}\right) + \nabla\cdot\left(\frac{\vec{\mathcal{F}}^{n+1}}{\rho^{n+1}}\right)\right], \tag{4.37}$$

$$\text{and} \quad \widetilde{\rho\vec{v}} = \rho^{n+1}\vec{v}^{**} - \Delta t^{n+1}\frac{\rho^{n+1}}{\rho_0}\nabla\widetilde{\psi}. \tag{4.38}$$

Stage 2: Using the predicted momentum $\widetilde{\rho\vec{v}}$ as an approximation of the momentum $(\rho\vec{v})^{n+1}$ allows Eq. (2.31) to be solved. This *momentum-based* PPE takes the form

$$\nabla^2\widehat{\psi} = \frac{1}{\Delta t^{n+1}}\left[\nabla\cdot(\rho\vec{v})^{*} - \nabla\cdot(\rho\vec{v})^{n+1}\right] \approx \frac{1}{\Delta t^{n+1}}\left[\nabla\cdot(\rho\vec{v})^{*} - \nabla\cdot\widetilde{\rho\vec{v}}\right], \tag{4.39}$$

where $\widehat{\psi}$ refers to the momentum-based pressure estimate for ψ^{n+1}.

Stage 3: This step is applied to guarantee that $\nabla\cdot\vec{u}^{n+1}$ becomes $\mathcal{M}^{n+1}\big(1/\rho_1 - 1/\rho_2\big)$ after the pressure correction. Again, this is similar to the scheme by Frantzis and Grigoriadis (2019), but

instead of an extrapolated pressure gradient, the momentum-based pressure estimate $\widehat{\psi}$ is used. Therefore,

$$\vec{v}^{***} = \vec{v}^{*} - \Delta t^{n+1}\Big[\Big(\frac{1}{\rho^{n+1}} - \frac{1}{\rho_0}\Big)c\nabla\widehat{\psi}\Big], \tag{4.40}$$

$$\nabla^2\psi^{n+1} = \frac{\rho_0}{\Delta t^{n+1}}\left[\nabla\cdot\vec{v}^{***} - \mathcal{M}^{n+1}\left(\frac{1}{\rho_1} - \frac{1}{\rho_2}\right) + \nabla\cdot\left(\frac{\vec{\mathcal{F}}^{n+1}}{\rho^{n+1}}\right)\right], \tag{4.41}$$

$$\vec{u}^{n+1} = \vec{v}^{***} - \frac{\Delta t^{n+1}}{\rho_0}\nabla\psi^{n+1} + \frac{\vec{\mathcal{F}}^{n+1}}{\rho^{n+1}}, \tag{4.42}$$

$$\text{and} \quad p^{n+1} = p^{n} + \psi^{n+1}. \tag{4.43}$$

In Eq. (4.40), $\vec{v}^{***}$ represents the improved prediction velocity, after accounting for $\widehat{\psi}$. Furthermore, the limiter c scales the magnitude of the pressure increment based on the pressure field $\widetilde{\psi}$. This is necessary because the pressure fields $\widehat{\psi}$ and $\widetilde{\psi}$ are not fully independent. They are connected through the prediction momentum $\widetilde{\rho\vec{v}}$. Evidently, for stages 1-3 to be valid, $\widehat{\psi}$ and $\widetilde{\psi}$ cannot deviate largely. Large deviations will cause instabilities in the solution procedure. The limiter c is calculated based on the ratios of the extreme values in $\widehat{\psi}$ and $\widetilde{\psi}$, as

$$c = \min\left(1, \frac{|\min(\widetilde{\psi})|}{|\min(\widehat{\psi})|}, \frac{|\max(\widetilde{\psi})|}{|\max(\widehat{\psi})|}\right). \tag{4.44}$$

Note that the presented limiter is one of many possibilities and does not appear to be a sensitive choice.

The remainder of the thesis refers to this multistage scheme as FFT *Momentum-based Pressure treatment for Density Jumps* (short FFT-MPDJ). Test cases to quantify improvements in solving the pressure when applying the FFT-MPDJ scheme are discussed in Ch. 6.

4.4 Phase change modelling

This work employs a kinetic phase change model due to its computational efficiency. However, as mentioned in Sec. 2.5.1, a drawback of most kinetic models is that their parameters must be adjusted depending on the simulation setup. This drawback is addressed in the subsequent development. In light of its simple formulation, the model by Rattner and Garimella (2014) and Pan et al. (2016) is used as a starting point for the phase change model development. The idea behind their phase change model is that the interface temperature at the next time step is equal to

the saturation temperature, i.e., $T^{n+1} = 0$. Using the definition of the phase change temperature increment $\Delta T_{PC}^{n+1} = T^{n+1} - T^*$ yields the following relation

$$\Delta T_{PC}^{n+1} = (T_{\text{sat}} - T_{\text{abs}}^*) = -T^*. \tag{4.45}$$

The mass transfer $\mathcal{M}^{n+1}$ is then obtained by using the relation in Eq. (4.33). To apply the phase change model to the ACDI method, the following challenges with using Eq. (4.45) are addressed:

- Mass transfer is not limited to the interface region
- Eq. (4.33) strongly depends on the time step size Δt^{n+1} (see Liu et al. (2020))
- Eq. (4.45) does not account for the change in $(\rho c_p)^*$ across the interface. Therefore, the distribution of $\mathcal{M}^{n+1}$ would be significantly concentrated on the liquid side.

These points are addressed in the following section.

4.4.1 A kinetic phase change model suitable for the ACDI method

The strategy for calculating the mass transfer is visualized in Fig. 4.2. Similar to some heat-conduction models (see Mukherjee and Kandlikar (2005) and Mukherjee et al. (2011)), this strategy assumes that the mass transfer is governed by the heat conduction of the liquid phase. The heat penetrating the diffuse interface creates a small superheat, which is used to calculate the phase change rate $\mathcal{M}^{n+1}$.

For the application to the ACDI model, the temperature increment is modified by introducing four non-dimensional factors discussed below. The proposed phase change model reads

$$\Delta T_{PC}^{n+1} = -T^* \theta_t \theta_{pc} \theta_{\rho c_p}^* \theta_\phi^*. \tag{4.46}$$

In Eq. (4.46), factor θ_t accounts for the time step size, factor θ_{pc} is a phase change constant, factor $\theta_{\rho c_p}^* = \theta_{\rho c_p}(\phi^*)$ accounts for the jump in the heat capacities, and factor $\theta_\phi^* = \theta_\phi(\phi^*)$ restricts $\mathcal{M}$ to the interface region.

The factor θ_ϕ^* is a shape function that satisfies $\theta_\phi(\phi = 0.5) = 1$ in the middle of the interface and $\theta_\phi(\phi = 0) = \theta_\phi(\phi = 1) = 0$ in the pure phases (Fig. 4.3). Empirical tests show that shape

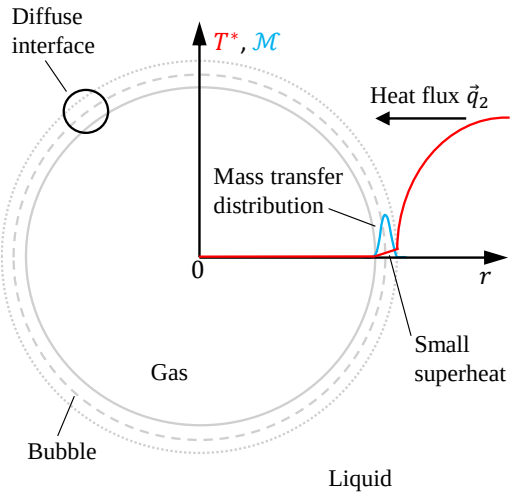

Figure 4.2: Schematic diagram of the developed phase change model. The interface is heated by the thermal energy transported from the liquid side. The mass transfer $\mathcal{M}^{n+1}$ is calculated based on this local superheat.

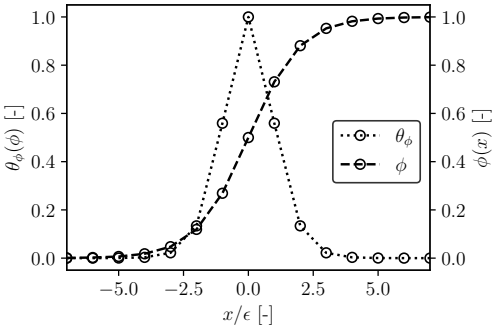

Figure 4.3: Discrete representation of the factor θ_ϕ, plotted over the non-dimensional distance x/ϵ from the interface. Values at cell centres are marked with a circle. The distribution of the phase field ϕ shows the diffuse interface region.

functions with a higher concentration in the middle of the diffuse interface have a more stable performance. As such, in this thesis, the shape function is based on a cosine function

$$\theta_\phi = \frac{1}{2}\Big(1 + \cos\big(2\pi|\phi - 0.5|\big)\Big). \tag{4.47}$$

Fig. 4.3 illustrates the discrete representation of Eq. (4.47), along with the hyperbolic tangent profile of ϕ.

The mass transfer rate $\mathcal{M}$ is decoupled from the time step size by introducing a phase change timescale t_{pc} in the calculation of ΔT_{PC}^{n+1}. For this purpose, the thermal diffusion timescale of the liquid is selected, under the assumption that the liquid heat conduction governs the phase change. This timescale reads

$$t_{pc} = \frac{\Delta x^2}{a_2}, \quad \text{and therefore} \quad \theta_t = \frac{\Delta t^{n+1}}{t_{pc}}. \tag{4.48}$$

Factor $\theta_{\rho c_p}$ dampens the temperature increment towards the liquid side with the ratio of $\rho_2 c_{p,2}$ and $\rho_1 c_{p,1}$ to obtain a balanced distribution of $\mathcal{M}$. The factor $\theta_{\rho c_p}$ is calculated from

$$\theta_{\rho c_p} = \frac{1}{\frac{\rho_1 c_{p,1}}{\rho_2 c_{p,2}} \alpha_1 + \alpha_2}. \tag{4.49}$$

The phase change constant θ_ϕ is empirically optimized to be $\theta_\phi = 0.7$, by comparing the interface growth rate with reference data. It is important to emphasize that this constant is valid for all considered fluid properties and all problem setups (refer to Ch. 6). Note that in Appendix Sec. A.2 and Sec. A.3 the phase change model is extended to arbitrary ϵ^* and to non-cubic grid cells, respectively. These modifications are relevant for Ch. 7, however, they are not in the scope of the main thesis body.

4.4.2 Time step restriction

Analyzing the Eq. (4.46), it is evident that the condition

$$\theta_t \theta_{pc} \theta_{\rho c_p} \theta_\phi < 1 \tag{4.50}$$

must hold. To satisfy this condition, a phase change time step constraint Δt_{pc} is obtained as follows

$$\Delta t^{n+1} < \Delta t_{pc} = \frac{1}{\theta_{pc}} \frac{\lambda_1}{\lambda_2} \frac{\Delta x^2}{a_1}. \tag{4.51}$$

As such, Eq. (4.51) contains the thermal diffusion time scale of the gas. The thermal diffusivity time step constraint has to be satisfied regardless. This means that Δt_{pc} becomes restrictive, only if $\lambda_1 \lambda_2^{-1}$ is small.

4.4.3 Adaptive regularization speed

Selection of the interface regularization speed is closely connected to the phase change timescale. The literature (see Mirjalili et al. (2020) and Jain et al. (2020)) suggests that the regularization speed Γ is coupled to the maximum velocity in the domain through a fixed factor, i.e. a fixed Γ^*. This section shows that this definition can be insufficient for simulating boiling flows, and a solution procedure is proposed.

For boiling flows, the mass transfer rate $\mathcal{M}$ has a strong impact on the interface profile of ϕ. In the absence of phase change, ϕ has the well-known hyperbolic tangent profile in its equilibrium state. For $\mathcal{M} \neq 0$, the velocity divergence causes a constant disequilibrium state that $\vec{\mathcal{R}}$ has to counterbalance. Therefore, too slow regularization speeds can lead to a thickened interface profile, or even a deterioration of the interface profile, and thus, a simulation failure. The latter is the case if the interface regularization time step restriction Δt_ϕ is larger than the phase change constraint Δt_{pc}.

To overcome this problem, a continuous adaptation of Γ^* is proposed so that, at all times, $\Delta t^{n+1} = C_{\text{CFL}} \Delta t_\phi$, where C_{CFL} is the CFL *safety factor*. For completeness, the remaining time step constraints (from Kang et al. (2000)) are listed below. These time step constraints are due to

$$\text{convective transport} \quad \Delta t_{\vec{u}} = \frac{\Delta x}{\max(|u_1| + |u_2| + |u_3|)}, \tag{4.52}$$

$$\text{viscous effects} \quad \Delta t_\mu = \frac{\Delta x^2}{6} \min_i \left(\frac{\rho_i}{\mu_i} \right), \tag{4.53}$$

$$\text{gravity} \quad \Delta t_{\vec{g}} = \sqrt{\frac{\Delta x}{|\vec{g}|}}, \tag{4.54}$$

$$\text{surface tension} \quad \Delta t_\sigma = \sqrt{\frac{\Delta x^2 \min_i \rho_i}{\sigma \max|\kappa|}}, \tag{4.55}$$

$$\text{and heat conduction} \quad \Delta t_\lambda = \frac{\Delta x^2}{6} \min_i \left(a_i^{-1} \right). \tag{4.56}$$

Kang et al. (2000) combined the time step restrictions Eqs. (4.52)-(4.55) into one constraint Δt_Σ by computing

$$\Delta t_\Sigma = 2 \left(\frac{1}{\Delta t_{\vec{u}}} + \frac{1}{\Delta t_\mu} + \sqrt{\left(\frac{1}{\Delta t_{\vec{u}}} + \frac{1}{\Delta t_\mu} \right)^2 + \frac{4}{\Delta t_{\vec{g}}^2} + \frac{4}{\Delta t_\sigma^2}} \right)^{-1}. \tag{4.57}$$

The minimum allowable regularization speed Γ^*_{min} is used as a simulation input, and set to unity for the remainder of the thesis. The corresponding time step constraint $\Delta t_{\phi,min}$ is

$$\Delta t_{\phi,min} = \min_i \left[\max\left\{ \left(\frac{6\Gamma^*_{min}|u_{max}|\epsilon}{\Delta x^2} \right) - \left(\frac{\partial u_i}{\partial x_i} \right), 0 \right\}^{-1} \right]. \tag{4.58}$$

Now, Γ^* can be dynamically adjusted in case of $\Delta t_{\phi,min} > \min(\Delta t_\Sigma, \Delta t_\lambda, \Delta t_{pc})$. By rearranging Eq. (2.5), the updated value of Γ^* is obtained as

$$\Gamma^* = \frac{\Delta x^2}{6|u_{max}|\epsilon} \left[\frac{1}{\min(\Delta t_\Sigma, \Delta t_\lambda, \Delta t_{pc})} + \min_i \left(\frac{\partial u_i}{\partial x_i} \right) \right]. \tag{4.59}$$

In the case of $\Delta t_{\phi,min} < \min(\Delta t_\Sigma, \Delta t_\lambda, \Delta t_{pc})$, the regularization speed is set to $\Gamma^* = \Gamma^*_{min}$. Over the simulation runtime, the time step size Δt^{n+1} is continuously updated based on

$$\Delta t^{n+1} = C_{\text{CFL}} \min(\Delta t_{\phi,min}, \Delta t_\Sigma, \Delta t_\lambda, \Delta t_{pc}). \tag{4.60}$$

For all numerical experiments and simulations in Ch. 6 and Ch. 7, a C_{CFL} value of 0.4 was found to be sufficient.

4.5 Contact angle treatment for the CDI method

For the simulation of two-phase flows involving wall boundaries, it is often necessary to model the wettability phenomenon. This phenomenon is modelled by prescribing a contact angle at the three-phase contact point where the wall (solid), the liquid, and the gaseous phases meet. This work does not consider the effect of contact angle hysteresis (e.g. Yue (2020)). Thus, a static contact angle treatment is implemented.

Fig. 4.4 depicts important considerations in the modelling of the static contact angle boundary conditions for CDI. Here, a small bubble, represented by a diffuse interface, is schematically depicted on a hydrophilic wall. The grey solid, dashed, and dotted lines represent the iso-contours of three phase field values (e.g., 0.9, 0.5, and 0.1, respectively), of which the corresponding contact angles Θ are labelled . In addition, the computational grid is displayed for part of the near-wall region, including the ghost points, which are used for the phase field boundary condition. The wall-normal regularization fluxes $\vec{\mathcal{R}}_\perp$ on the domain boundary are depicted by orange arrows.

The first consideration is the definition of a contact angle Θ for small bubbles. From Fig. 4.4, it is evident that $\Theta_{0.1} \neq \Theta_{0.5} \neq \Theta_{0.9}$. When prescribing a contact angle Θ, a local contact angle Θ' must first be calculated. Utilizing the local values of the level-set value Ψ and the curvature κ,

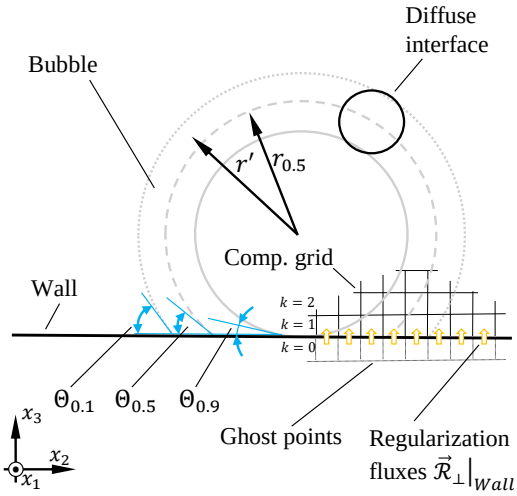

Figure 4.4: Visualization of important aspects when modelling the wettability for diffuse interface bubbles.

a simple geometric relation can be derived for small bubbles in three dimensions. Assuming that both principal radii of the curvature are equal, the local radius r' is $r' = 2/\kappa$, and the radius at $\phi = 0.5$ is $\Psi + r'$. The discrete local angle $\Theta'_{i,j}$ is

$$\Theta'_{i,j,k} = \arccos\left(\cos\Theta\left[\frac{2 + \kappa_{i,j,k}\Psi_{i,j,k}}{2}\right]\right) \tag{4.61}$$

In Eq. (4.61), the indices i, j, and k represent the discrete location in the grid and align with the x_1, x_2 and x_3 axes of Fig. 4.4. The same approach is followed by Brown et al. (2024) for two-dimensional problems. The curvature κ is assumed to have a zero-gradient boundary condition on a wall and therefore $\Theta'_{i,j,1/2} \approx \Theta'_{i,j,1}$ (see Fig. 4.4 for index definition).

For phase field methods, two formulations of the static contact angle treatment (see Ding and Spelt (2007)) are often utilized: (i) the *surface-energy formulation*, and (ii) the *geometric formulation*. Here, the geometric formulation of the boundary condition is used to apply the contact angle $\Theta'_{i,j,1/2}$. Enforcing a static contact angle translates to prescribing a Neumann-type boundary condition for the phase field variable. In line with Ding and Spelt (2007), the wall-normal phase field gradient $\vec{n}_\perp \cdot \nabla\phi$ is calculated as

$$\vec{n}_\perp \cdot \nabla\phi = -\tan\left(\Theta' - \pi/2\right)|\vec{n}_\parallel \cdot \nabla\phi| \tag{4.62}$$

The magnitude of the wall-parallel gradient $|\vec{n}_\parallel \cdot \nabla\phi|$ is approximated using the second-order central difference approximation (e.g. Liang et al. (2019) or Zarareh et al. (2021)) of the two

wall-adjacent layers of grid points. For a wall-normal vector aligning with the x_3 direction, this reads

$$\left(\vec{n}_\perp \cdot \nabla\phi\right)_{i,j,1/2} \approx -\frac{\tan\left(\Theta'_{i,j,1/2} - \pi/2\right)}{4\Delta x} \begin{vmatrix} 3\phi_{i+1,j,1} - 3\phi_{i-1,j,1} - \phi_{i+1,j,2} + \phi_{i-1,j,2}) \\ 3\phi_{i,j+1,1} - 3\phi_{i,j-1,1} - \phi_{i,j+1,2} + \phi_{i,j-1,2}) \\ 0 \end{vmatrix} \tag{4.63}$$

The boundary value of the ghost point $\phi_{i,j,0}$ becomes

$$\phi_{i,j,0} = \phi_{i,j,1} + \max\left(-C_\Theta \phi_{i,j,1} \quad , \quad \Delta x \left(\vec{n}_\perp \cdot \nabla\phi\right)_{i,j,1/2} \right) \tag{4.64}$$

Compared to the boundary condition in the studies by Ding and Spelt (2007), Liang et al. (2019), and Zarareh et al. (2021), Eq. (4.64) is augmented with a limiter constant C_Θ. This limiter is required to avoid nonphysical boundary values when using very small contact angles Θ (see Ch. 7). Avoiding nonphysical boundary values is essential for computing a level-set value $\Psi_{i,j,0}$ from $\phi_{i,j,0}$, which is required for calculating the curvature κ. For super-hydrophilic behaviour, a value of $C_\Theta = 0.3$ is found to provide satisfactory results (see Ch. 7).

To complete the wettability modelling, a treatment for the wall-normal regularization fluxes $\vec{\mathcal{R}}_\perp\big|_{\text{wall}}$ on the wall must be defined (orange arrows in Fig. 4.4). The definition of the regularization term $\vec{\mathcal{R}}$ (Eq. (2.3)) indicates that for contact angles $\Theta \neq 90°$, the flux is $\vec{\mathcal{R}}_\perp\big|_{\text{wall}} \neq 0$. This is problematic, as it violates mass conservation, which can lead to significant mass losses over the duration of the simulation, as seen in Shen and Li (2024). Other researchers (see Huang et al. (2022) or Scapin et al. (2022)) used Lagrange multipliers to balance the mass conservation. These Lagrange multipliers redistribute the lost mass in the simulation to enforce the conservation constraint. To avoid such redistribution of mass, a simple boundary treatment for $\vec{\mathcal{R}}$ is introduced, instead. Here, employing a homogeneous Dirichlet boundary condition on wall boundaries results in

$$\vec{\mathcal{R}}_\perp\big|_{\text{wall}} = \vec{0} \tag{4.65}$$

The boundary condition allows mass to always be conserved. This boundary condition is not new, and was first introduced by Sato and Ničeno (2012) in the context of the conservative level-set method. In their study, a similar resharpening term is used for the reinitialization of the level-set value. More recently, this approach was applied to the CDI method by Brown et al. (2024) and Weber et al. (2024a).

4.6 Outflow boundary treatment

When the long-term behaviour of a bubbly flow is of interest, a sophisticated outflow boundary treatment for bubbles leaving the domain is often necessary. The most simple outflow condition assumes a homogeneous Dirichlet boundary condition for the pressure p and a homogeneous Neumann boundary condition for the velocity $\vec{u}$. However, a typical bubbly flow scenario may involve bubbles featuring small Weber numbers We that are advected towards the outflow boundary. The We defines the ratio of inertial effects to surface tension. Therefore, small We entail a high surface tension effect. Instabilities arise when the interfacial pressure jump comes in contact with the outflow boundary, potentially causing simulation failure (Sato and Ničeno (2013)). With a sophisticated boundary treatment, these instabilities would not occur.

The literature on boundary treatments for small Weber number bubbles is limited. Researchers either choose to remove bubbles before they touch the outflow boundary (Sato and Ničeno (2013)), or are limited to high Weber number simulations (Bozonnet et al. (2021)). Furthermore, using an FFT-based pressure solver restricts the choice of boundary conditions, as discussed in Costa (2018). Therefore, methods that require non-homogeneous boundary conditions (e.g., Dong (2014b)) are not possible.

Recently, Dhruv (2024) proposed a forcing-based outflow treatment, which allows the use of homogeneous Neumann and Dirichlet boundary conditions for velocity and pressure, respectively. Dhruv (2024) claims that his treatment also ensures stable simulations for small Weber number bubbles. The method is capable of handling a range of simulation settings (see, e.g., film boiling in a two-dimensional pool in Sec. 6.7). However, a more restrictive scheme is required for forced convection nucleate boiling flow (see Sec. 7). Accordingly, to satisfy this requirement, a more restrictive variation of the method by Dhruv (2024) is presented below.

Fig. 4.5a visualizes this more restrictive outflow treatment. The computational domain (box) features an inflow and an outflow boundary (grey boundaries) through which the fluid can enter and leave the domain. The convection enforced by the inflow boundary transports the bubbles. The domain is divided into two regions: (i) the outflow region of length ℓ_O, where outflow treatment is enabled, and (ii) the region of interest, in which outflow treatment is disabled. The flow may feature vortices in the region of interest; however, in the outflow region, the flow is straightened to ensure stable transport of bubbles through the outflow boundary.

The region of interest is separated from the outflow region by introducing an outflow weighting factor ζ. In line with Dhruv (2024), this factor ζ is calculated as

$$\zeta = \frac{2}{1 + \exp\left[4(\ell_\perp - x_\perp)/\ell_O\right]} \tag{4.66}$$

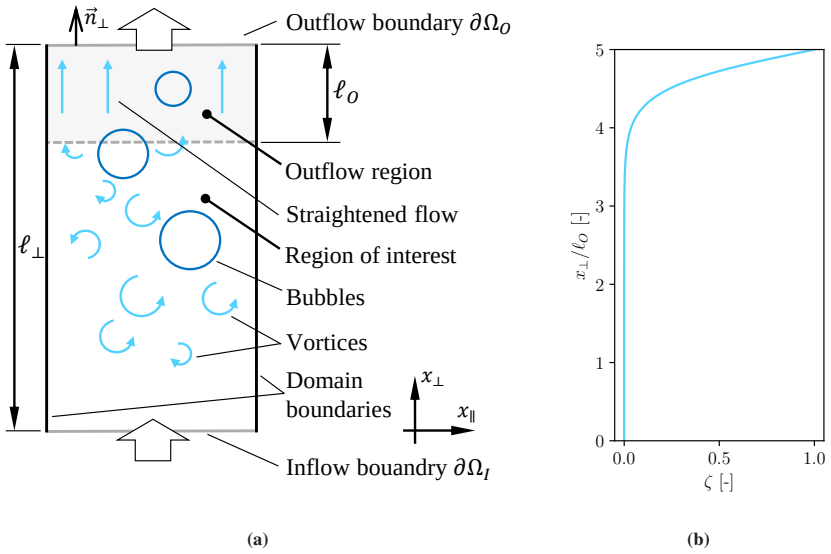

Figure 4.5: (a) Sketch of the outflow boundary treatment for a forced convection inflow-/outflow simulation setup. (b) The outflow weighting factor ζ is shown for a non-dimensional domain length.

Here, $\ell_\perp$ refers to the length of the domain in the direction normal to the outflow boundary. The corresponding coordinates in the directions normal and parallel to the outflow are $x_\perp$ and $x_\parallel$ (see Fig. 4.5a). Fig. 4.5b shows the values of ζ along the non-dimensional length. It can be seen that ζ vanishes in the region of interest and becomes order unity within the outflow region of length ℓ_O.

The treatment in the outflow region has two purposes: (i) decreasing the surface tension, and (ii) straightening the flow. First, the surface tension force is multiplied by $(1-\zeta)$, which continuously decreases the surface tension and results in an interfacial pressure jump of zero at the outflow (see Dhruv (2024)). The outflow-modified surface tension force $\vec{f}_{ST,O}$ becomes

$$\vec{f}_{ST,O} = (1-\zeta)\vec{f}_{ST}. \tag{4.67}$$

Next, the flow field is straightened by introducing a force $\vec{f}_O$. The outflow force is decomposed into a perpendicular and a parallel component $\vec{f}_O = \vec{f}_{O\perp} + \vec{f}_{O\parallel}$ in relation to the outflow boundary $\partial\Omega_O$. The parallel component $\vec{f}_{O\parallel}$ straightens the flow and the perpendicular component $\vec{f}_{O\perp}$ unifies the outflow velocity.

The parallel component of the force is defined as

$$\vec{f}_{O\parallel} = -\zeta\rho\Bigg(\underbrace{C_{O\parallel}\frac{\vec{u}_\parallel}{\Delta t}}_{\text{straightening}} + \underbrace{U_O\frac{\partial \vec{u}_\parallel}{\partial x_\perp}}_{\text{convection}} \Bigg) \tag{4.68}$$

This force $\vec{f}_{O\parallel}$ has two terms. The first term removes momentum in the direction parallel to the outflow at each time step. This process is governed by a constant $0 < C_{O\parallel} < 1$, which regulates the the amount of momentum that is removed. The second part, adapted from Dhruv (2024), accounts for the convective transport of the momentum out of the domain, with the characteristic outflow velocity U_O.

The perpendicular component $\vec{f}_{O\perp}$ unifies the flow field. The idea is that the perpendicular flow field remains within a defined range of magnitudes. Therefore, $\vec{f}_{O\perp}$ is active for velocities that are outside of this range $U_O C_{O\perp} \leq \vec{n}_\perp \cdot \vec{u}_\perp \leq U_O$. For forced convection flows, back flows at the outflow are suppressed when $0 < C_{O\perp} < 1$. The perpendicular component is calculated as

$$\vec{f}_{O\perp} = -\zeta\rho\Bigg(\underbrace{\frac{\Delta\vec{u}_\perp}{\Delta t}}_{\text{unifying}} + \underbrace{U_O\frac{\partial \vec{u}_\perp}{\partial x_\perp}}_{\text{convection}} \Bigg) \tag{4.69}$$

with

$$\Delta\vec{u}_\perp = \begin{cases} (\vec{u}_\perp - \vec{n}_\perp U_O C_{O\perp}) & \text{if} \quad U_O C_{O\perp} > \vec{n}_\perp \cdot \vec{u}_\perp \\ (\vec{u}_\perp - \vec{n}_\perp U_O) & \text{if} \quad U_O < \vec{n}_\perp \cdot \vec{u}_\perp \\ \vec{0} & \text{else.} \end{cases} \tag{4.70}$$

Here, the convection term, adapted from Dhruv (2024), is also utilized. To define the outflow velocity U_O, the bulk velocity at the inflow boundary $\partial\Omega_I$ is calculated as

$$U_O = (1 + C_I)\frac{\int_{\partial\Omega_I} \vec{u}\cdot\vec{n}_\perp dA}{\int_{\partial\Omega_I} dA} \tag{4.71}$$

Thus, the outflow velocity is set based on the inflow bulk velocity as well as a safety margin $C_I > 0$. Two aspects must be considered when selecting a value for C_I: First, the value for C_I defines the range of admitted fluctuations for $\vec{u}_\perp$, and, therefore, should be kept to a minimum. Second, for phase changing flows, the volume change $(\rho_1^{-1} - \rho_2^{-1})\int_\Omega \mathcal{M} dV$ has to be taken into account[2], so that U_O remains larger than the outflow bulk velocity.

[2] Another possibility could be to define U_O with the velocities on $\partial\Omega_O$. But since $\frac{\partial}{\partial t}(\rho_1^{-1} - \rho_2^{-1})\int_\Omega \mathcal{M} dV \neq 0$ also $\frac{\partial U_O}{\partial t} \neq 0$. To eliminate possible fluctuations in U_O, the definition of Eq. (4.71) is chosen.

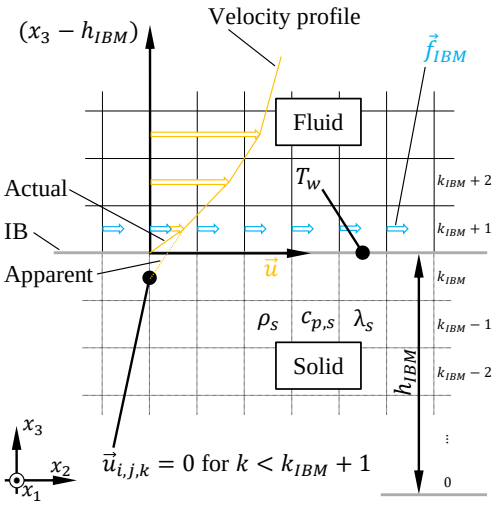

Figure 4.6: Schematic diagram of the IBM from Breugem and Boersma (2005). The solid subdomain consists of k_{IBM} layers of grid points. The immersed boundary (IB) is located on the cell edge at $k = k_{IBM} + 1/2$. During the simulation, the velocities in the solid are set to zero. Therefore, the erroneous (apparent) velocity gradient has to be corrected for the wall-adjacent fluid points. This is done by introducing the IBM forces $\vec{f}_{IBM}$.

Accordingly, for the simulations in Ch. 7, the parameters are chosen to be $C_{O\parallel} = 0.2$, $C_I = 0.4$ and $C_{O\perp} = 0.1$.

4.7 Implementing an immersed boundary method

An immersed boundary method (IBM) refers to a methodology that allows representing a solid region within the computational grid of a fluid simulation. Therefore, the fluid-solid boundary is *immersed* in the computational grid. The need to implement an immersed boundary method (IBM) for the simulation of boiling flows is based on heat transfer phenomena. Typically, nucleate boiling is caused by the transfer of heat from a solid wall into a fluid. To accurately capture this heat transport interplay between solid and fluid (called *conjugate heat transfer*), the simulation of both the fluid and the solid is required (see e.g. Urbano et al. (2019)). Conjugate heat transfer can be simulated through coupled subdomains (e.g. Urbano et al. (2019)) or IBM (e.g. Sato and Niceno (2015)). In this thesis, the IBM approach is applied. This section describes the IBM utilized for the developed flow solver and focuses on the specific details regarding its implementation.

The IBM by Breugem and Boersma (2005) is utilized (see Fig. 4.6) for the developed flow solver. Theirs is an improved version of the IBM proposed by Fadlun et al. (2000), designed for situations where the cell edge coincides with the immersed boundary (IB). This no-slip condition

is enforced by introducing a force field $\vec{f}_{IBM}$, which corrects the errors made when calculating the contribution of the viscous stress tensor (therefore referred to as *Stress IBM*). The error is visualized in Fig. 4.6, where the *apparent* velocity gradient (dotted) is compared with the *actual* velocity gradient at the IB.

Generally, the x_3-derivative of the viscous stress tensor for the grid index i, j, k in the x_2-direction (see Fig. 4.6) is

$$\left.\frac{\partial \tau}{\partial x_3}\right|_{2,i,j,k} = \frac{1}{\Delta x}\left(\mu_{i,j+1/2,k+1/2}\frac{u_{2,i,j,k+1}-u_{2,i,j,k}+u_{3,i,j+1,k}-u_{3,i,j,k}}{\Delta x} - \mu_{i,j+1/2,k-1/2}\frac{u_{2,i,j,k}-u_{2,i,j,k-1}+u_{3,i,j+1,k-1}-u_{3,i,j,k-1}}{\Delta x}\right) \tag{4.72}$$

At each time step, the velocity vector $\vec{u}_{i,j,k} = (u_{1,i,j,k}, u_{2,i,j,k}, u_{3,i,j,k})^T$ is set to zero for $k \leq k_{IBM}$. Therefore, at $k = k_{IBM} + 1$, Eq. (4.72) yields

$$\left.\frac{\partial \tau}{\partial x_3}\right|_{2,i,j,k} = \frac{1}{\Delta x}\left(\mu_{i,j+1/2,k+1/2}\frac{u_{2,i,j,k+1}-u_{2,i,j,k}+u_{3,i,j+1,k}-u_{3,i,j,k}}{\Delta x} - \mu_{i,j+1/2,k-1/2}\frac{u_{2,i,j,k}}{\Delta x}\right) \quad \text{for} \quad k = k_{IBM}+1. \tag{4.73}$$

However, to impose the no-slip boundary at $k = k_{IBM} + 1/2$, the relation $u_{2,i,j,k} = -u_{2,i,j,k-1}$ is applied to Eq. (4.73). The actual viscous stress contribution is, therefore,

$$\left.\frac{\partial \tau}{\partial x_3}\right|_{2,i,j,k} = \frac{1}{\Delta x}\left(\mu_{i,j+1/2,k+1/2}\frac{u_{2,i,j,k+1}-u_{2,i,j,k}+u_{3,i,j+1,k}-u_{3,i,j,k}}{\Delta x} - \mu_{i,j+1/2,k-1/2}\frac{2u_{2,i,j,k}}{\Delta x}\right) \quad \text{for} \quad k = k_{IBM}+1 \quad \text{and} \quad u_{2,i,j,k} = -u_{2,i,j,k-1}. \tag{4.74}$$

The x_2-component of the IBM force $\vec{f}_{IBM}$ is obtained from the difference between Eq. (4.73) and Eq. (4.74), i.e.

$$f_{2,IBM} = -\mu_{i,j+1/2,k-1/2}\frac{u_{2,i,j,k}}{\Delta x^2}. \tag{4.75}$$

As such, Eq. (4.75) is equal to the result presented by Breugem and Boersma (2005). The zero-gradient pressure condition at the IB is enforced as the solid is excluded from the FFT pressure solution.

4.7.1 Conjugate heat transfer

To complete the treatments required for the present IBM, the conjugate heat transfer is discussed in this subsection. In the solid region of the computational domain, the heat transport is governed entirely by the heat conduction equation

$$\rho_s c_{p,s} \frac{\partial T}{\partial t} = \nabla \cdot \left(\lambda_s \nabla T \right), \tag{4.76}$$

where ρ_s, $c_{p,s}$, and λ_s are the solid's density, heat capacity, and heat conductivity, respectively. Usually, these quantities all exhibit a jump in magnitude across the IB, which requires an additional treatment to accurately calculate the heat exchanged between the fluid and solid. This jump of physical properties renders a standard central-difference approximation of the temperature gradient erroneous. For this purpose, an auxiliary variable, the surface temperature T_w, is introduced. Generally, the heat flux $q_{3,i,j,k_{IBM}+1/2}$ from the solid side must be equal to that coming from the liquid side (in the wall-normal direction). This equality leads to

$$q_{3,i,j,k_{IBM}+1/2} = 2\lambda_{i,j,k_{IBM}} \frac{T_{w,i,j} - T_{i,j,k_{IBM}}}{\Delta x} = 2\lambda_{i,j,k_{IBM}+1} \frac{T_{i,j,k_{IBM}+1} - T_{w,i,j}}{\Delta x}, \tag{4.77}$$

and thus,

$$T_{w,i,j} = \frac{\lambda_{i,j,k_{IBM}} T_{i,j,k_{IBM}} + \lambda_{i,j,k_{IBM}+1} T_{i,j,k_{IBM}+1}}{\lambda_{i,j,k_{IBM}} + \lambda_{i,j,k_{IBM}+1}}. \tag{4.78}$$

For the grid points where $k = k_{IBM}$ and $k = k_{IBM} + 1$, Eq. (4.77) must be utilized to calculate the heat flux at $k = k_{IBM} + 1/2$. This strategy for correcting the heat flux in the IB can also be found in Bureš and Sato (2022), and Torres (2023).

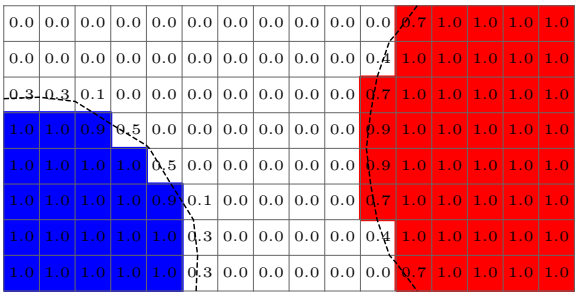

Figure 4.7: Flood-fill algorithm (as in Smith (1979)) applied to the VOF method. Numbers in cells represent the phase fraction of the VOF method. The bubble is clearly defined by connected grid points above a phase fraction threshold value (here 0.5). Grid points assigned to bubbles '1' and '2' are coloured blue and red, respectively. The sharp interface front is depicted by the black dashed line.

4.8 Bubble tagging method

Connecting the interface-resolved simulation with the statistical analysis of bubbles requires a sophisticated methodology. Due to data storage limitations, the trivial solution to frequently save three-dimensional grid data for all flow quantities is, at most, limited to very small grid sizes. For the present application to large-scale boiling flow simulations, efficient online bubble data processing routines are necessary. This need becomes more pronounced when evaluating bubble trajectories. For trajectories, a high output frequency is required to obtain highly accurate connectivity between instantaneous data sets. As such, the present section presents a suitable tagging algorithm for the preprocessed storage of data related to single bubbles for diffuse interface methods.

The flood-fill algorithm is a commonly used tagging algorithm for bubbles (e.g. Herrmann (2010)). Flood-fill algorithms were developed for image processing to fill connected areas of a specific property (see Lieberman (1978) or Smith (1979)). In the context of interface-resolved simulations, this entails assigning a unique tag number to all grid points that belong to the same bubble. A bubble is usually defined as all connected grid points that are above a phase fraction threshold value. Applying the flood-fill method to sharp interface methods is straightforward. For instance, Fig. 4.7 visualizes the application of the flood-fill algorithm in the VOF method, where each grid point is tagged depending on its assignment to a bubble (visualized with the colours blue and red). As shown in the figure, the bubbles have a clear definition and are easily distinguished due to the sharpness of the interface.

In contrast, applying the flood-fill algorithm to diffuse interface methods is more challenging (Fig. 4.8). Unlike sharp interface methods, the definition of the phase field threshold value ϕ_{thr} is

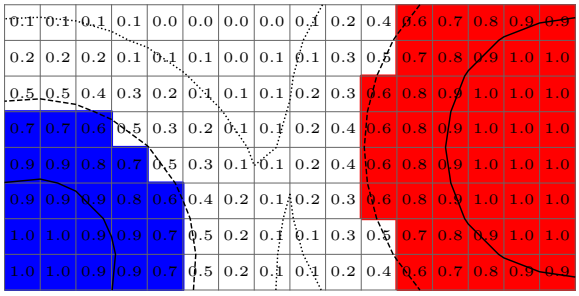

(a) $\phi_{thr} = 0.5$

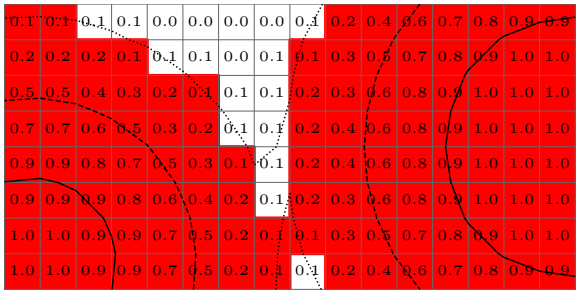

(b) $\phi_{thr} = 0.1$

Figure 4.8: Flood-fill algorithm applied to the ACDI ($\epsilon^* = 1$) method for two different threshold values ϕ_{thr}. Grid points assigned to bubbles '1' and '2' are coloured blue and red, respectively. Higher thresholds result in missing interface information (a), whereas lower values result in unphysical coalescence events (b). The dotted, dashed and solid lines represent the iso-contours corresponding to $\phi = 0.1$, $\phi = 0.5$, and $\phi = 0.9$, respectively. Numbers refer to the phase field value of ϕ.

not unique for diffuse interface methods. This is demonstrated in Fig. 4.8a, where the flood-fill algorithm is applied to the same bubble as in Fig. 4.7, using $\phi_{thr} = 0.5$. Although the same cells are tagged in Fig. 4.8a and Fig. 4.7, information related to half of the interface thickness is lost when the flood-fill algorithm is applied to the ACDI method. Nathan and Jain (2025) presented a method to account for this mass loss due to the truncated tagging of cells with the ACDI method. However, the possibilities of accounting for truncated information are limited, as information about other quantities (e.g. temperature, mass transfer rate, etc.) cannot be recovered. The value of ϕ_{thr} could be decreased to capture additional interface information. Fig. 4.8b shows the result for $\phi_{thr} = 0.1$. With this threshold value, the majority of the interface is captured, but at the expense of detecting an unphysical coalescence event.

This problem can be addressed by using the flood-fill algorithm in combination with propagation steps. The proposed workflow is as follows. First, bubbles are tagged with a unique number,

based on a threshold value ϕ_{thr}. The threshold value is set large enough to not detect unphysical coalescence events. In subsequent steps, all non-tagged grid cells inherit the largest tag number of their direct neighbours (top, bottom, front, back, left, and right). This propagation step can be repeated depending on ϕ_{thr} and the desired accuracy. Fig. 4.9 visualizes this procedure for $\phi_{thr} = 0.3$, with two propagation steps. In Fig. 4.9a, both bubbles receive a tag number based on connected regions where $\phi > \phi_{thr} = 0.3$ (coloured blue and red). In the first propagation step (Fig. 4.9b), the tag is propagated into the non-tagged interface. Fig. 4.9c visualizes a second repetition of this step. Now, both tags are directly neighbouring each other, but a coalescence event is not detected.

In principle, the propagation step can be repeated an arbitrary number of times. If ϕ_{thr} is larger, a higher number of repetitions is required to capture the same information about the interface. On the other hand, when ϕ_{thr} is set too high, very small bubbles will not be detected. For boiling flows, this can be problematic, as small seed bubbles are used to initiate bubble growth. Therefore, high values of ϕ_{thr} entail losing early-stage information of the bubble growth for boiling simulations. Accordingly, a threshold $\phi_{thr} = 0.3$ with two propagation steps is used in the following sections of this thesis.

After running this algorithm, each grid cell carries an identifier $\Xi_{i,j,k}$. Here, $\Xi_{i,j,k} \in \{0, 1, 2, ..., N_b\}$ is an integer-valued array, where zero refers to no assignment to a bubble, and the numbers from one to N_b each refer to one bubble.

4.8.1 Bubble geometry

Employing the tagging methodology described above, scalar and vector quantities (e.g. a sum, bubble-average, or minimum and maximum values) can be calculated with ease. In terms of bubble geometry, the bubble surface, volume, and contact line length are quantities of interest for boiling flows. However, defining the bubble geometry for diffuse interfaces is not obvious. Two possibilities are considered

- Utilizing the phase field ϕ to obtain a diffused geometry
- Using the iso-contour of $\phi = 0.5$ to obtain a sharp geometry.

For larger bubbles, the difference between the definitions is negligible. However, for small bubbles (typically seen at nucleation sites of boiling flows), the difference is significant. In the extreme case, a small bubble might not even reach $\phi = 0.5$ at its centre. Consequently, both definitions lead to different results for the smaller bubbles in the computational domain.

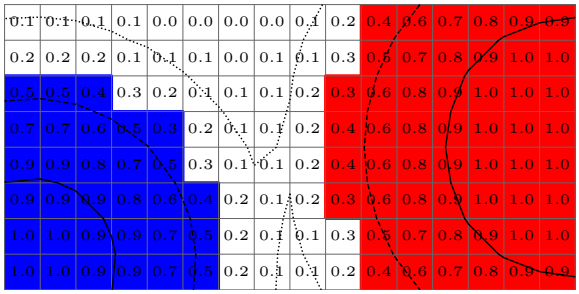

(a) $\phi_{thr} = 0.3$, initial tagging

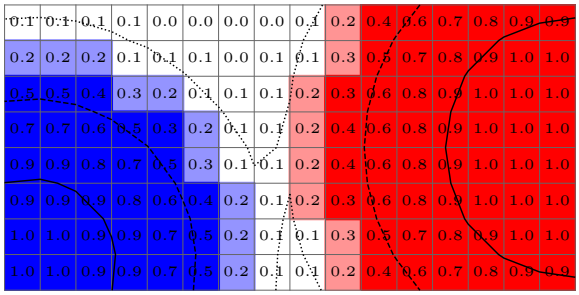

(b) $\phi_{thr} = 0.3$, first propagation

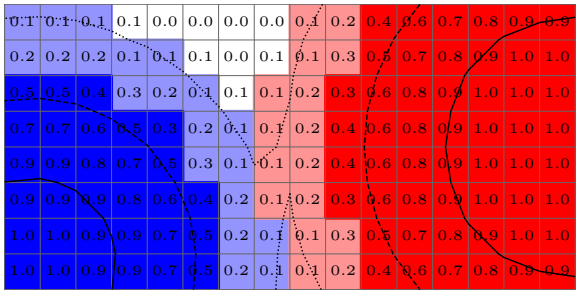

(c) $\phi_{thr} = 0.3$, second propagation

Figure 4.9: Demonstration of the original tagging algorithm with $\phi = 0.3$ and two propagation steps for capturing more interface information. The tagged cells resulting from the propagation steps are coloured using lighter hues of blue and red. Bubbles are represented with the ACDI method and $\epsilon^* = 1$.

In this thesis, the iso-contour of $\phi = 0.5$ is used to define the bubble geometry. A sharpening step improves the approximation of this geometry. Such a sharpening method has already been discussed for the surface tension model by Raeini et al. (2012) in Sec. 2.4.1. Recalling Eq. (2.9), the sharpened interface profile ϕ' is calculated as

$$\phi' = \frac{1}{1-\eta}\left[\min\left(\max\left(\phi, \frac{\eta}{2}\right), 1-\frac{\eta}{2}\right) - \frac{\eta}{2}\right] \tag{4.79}$$

Clearly, the sharpening factor $\eta \in [0,1]$ should be set as high as possible. However, to avoid detecting bubbles of size zero, η cannot be larger than two times the tagging threshold value ϕ_{thr}. Therefore, the sharpening factor is set to $\eta = 2\phi_{thr}$ for evaluating the bubble geometry.

Using ϕ', the n-th bubble volume BV_n is

$$\mathrm{BV}_n = \sum_i \sum_j \sum_k \delta(n, \Xi_{i,j,k}) \Delta x^3 \phi'_{i,j,k}, \tag{4.80}$$

where δ is the Kronecker delta function that evaluates to unity if both arguments are identical. The bubble surface area can be calculated by integrating $|\nabla\phi'|$, as shown in Tiwari et al. (2013). The n-th bubble surface, BS_n, is therefore obtained from

$$\mathrm{BS}_n = \sum_i \sum_j \sum_k \delta(n, \Xi_{i,j,k}) \frac{\Delta x^2}{2} \begin{vmatrix} \phi'_{i+1,j,k} - \phi'_{i-1,j,k} \\ \phi'_{i,j+1,k} - \phi'_{i,j-1,k} \\ \phi'_{i,j,k+1} - \phi'_{i,j,k-1} \end{vmatrix}. \tag{4.81}$$

Following the same strategy, the n-th contact line length CL_n is calculated as

$$\mathrm{CL}_n = \sum_i \sum_j \delta(n, \Xi_{i,j,k}) \frac{\Delta x}{2} \begin{vmatrix} \phi'_{i+1,j,1/2} - \phi'_{i-1,j,1/2} \\ \phi'_{i,j+1,1/2} - \phi'_{i,j-1,1/2} \\ 0 \end{vmatrix}, \tag{4.82}$$

where it is assumed that the solid contact surface coincides with the lower domain boundary in the x_3-direction. The corresponding dry spot area DS_n is then

$$\mathrm{DS}_n = \sum_i \sum_j \delta(n, \Xi_{i,j,k}) \Delta x^2 \phi'_{i,j,1/2}. \tag{4.83}$$

In both Eq. (4.82) and Eq. (4.83), the value of $\phi'_{i,j,1/2}$ corresponds to the linear interpolation of $\phi'_{i,j,0}$ and $\phi'_{i,j,1}$ onto the cell edge (i.e. the contact surface). The accuracy evaluations of BV_n, BS_n, CL_n, and DS_n for different bubble sizes are found in Sec. 6.9.

4.9 Summary and algorithm

After deriving the equation to describe the momentum transport, additional forces were introduced in Sec. 4.6 and Sec. 4.7. The full momentum transport equation now reads

$$\frac{\partial \rho \vec{u}}{\partial t} + \nabla \cdot \left(\left(\rho \vec{u} - \vec{\mathcal{F}} \right) \otimes \vec{u} \right) + \vec{\mathcal{C}} = -\nabla p + \nabla \cdot \tau + \rho \vec{g} + \vec{f}_{ST,O} + \vec{f}_{O} + \vec{f}_{IBM}. \tag{4.84}$$

Accordingly, the time-stepping scheme is adjusted so that the intermediate momentum (refer to Eq. (4.34)) is calculated as

$$(\rho \vec{v})^{*} = (\rho \vec{v})^{n} + \Delta t^{n+1} \left[\left(f_{t,1} \vec{\mathcal{B}}^{n}_{\rho \vec{v}} + f_{t,2} \vec{\mathcal{B}}^{n-1}_{\rho \vec{v}} \right) + \rho^{n+1} \vec{g} + \vec{f}^{n}_{O} + \vec{f}^{n+1}_{ST,O} - \nabla p^{n} \right]. \tag{4.85}$$

To accurately account for the viscous stress contribution of the IBM treatment, the force $\vec{f}_{IBM}$ is incorporated into $\vec{\mathcal{B}}_{\rho \vec{v}}$ (compare with Eq. (4.35)) as follows

$$\vec{\mathcal{B}}^{n}_{\rho \vec{v}} = -\nabla \cdot \left(\rho^{n} \vec{v}^{n} \otimes \vec{v}^{n} \right) - \nabla \cdot \left(\left(\frac{\rho_1 \rho_2}{\rho^{n} \phi^{n} (1 - \phi^{n})} \right) \vec{\mathcal{R}}^{n} \otimes \vec{\mathcal{R}}^{n} \right) + \nabla \cdot \tau^{n} + \vec{f}^{n}_{IBM}. \tag{4.86}$$

The detailed order in which the set of equations is solved is presented in Algorithm 1 (from Weber et al. (2026)). Comparing Algorithm 1 with the aims stated at the start of Ch. 4, it can be noted that:

- The solved equations are derived using a consistent derivation strategy throughout the transported quantities, and additional contributions of $\vec{\mathcal{R}}$ are identified for the momentum balance equations (see $\vec{\mathcal{C}}$ in Eq. (4.84))
- The FFT-based pressure solution is improved by utilizing the developed FFT-MPDJ solver (see Sec. 2.6.3)
- A simple and efficient phase change model is developed to calculate the mass transfer rate $\mathcal{M}^{n+1}$ (see Sec. 4.4)
- The coupling of the phase change model with the ACDI method is stabilized by using a scheme that dynamically adjusts the interphase regularization speed Γ^{*}

Algorithm 1 Chronological order for solving the System of transport equations, taken from Weber et al. (2026)

Set initial conditions $\phi(t=0)$, $T(t=0)$, $p(t=0)$, and $\vec{u}(t=0)$
Set the physical properties $\rho_i, c_{p,i}, \lambda_i, \mu_i, \lambda_s, \rho_s, c_{p,s}$
Calculate initial Ψ using Eq. (2.4)
Calculate $\vec{\mathcal{R}}$ from Eq. (2.3)
while $t < t_{end}$ **do**
    Obtain intermediate phase field value ϕ^* from Eq. (4.28)
    Update physical properties ρ^*, c_p^*
    Obtain intermediate temperature T^* from Eq. (4.29)
    Calculate ΔT_{PC}^{n+1} using Eq. (4.46)
    Obtain $\mathcal{M}^{n+1}$ using Eq. (4.33)
    Final states of ϕ^{n+1} and T^{n+1} through Eq. (4.32)
    Calculate $\Psi^{n+1}, \vec{n}^{n+1}, \kappa^{n+1}$
    Update the physical properties $\rho^{n+1}, c_p^{n+1}, \lambda^{n+1}, \mu^{n+1}$
    Calculate prediction momentum $(\rho\vec{v})^*$ from Eq. (4.85)
    Update $\vec{\mathcal{R}}^{n+1}$ with Eq. (2.3)
    Approximate $(\rho\vec{v})^{n+1}$ with $\widetilde{\rho\vec{v}}$ by Eq. (4.36) - Eq. (4.38)
    Obtain pressure estimate $\widehat{\psi}$ by solving Eq. (4.39)
    Find final p^{n+1} and $\vec{u}^{n+1}$ through Eq. (4.40) - Eq. (4.43)
    Update time step size Δt^{n+1} with Eq. (4.60)
    if $\Delta t_{\phi,min} > \min(\Delta t_\Sigma, \Delta t_\lambda, \Delta t_{pc})$ **then**
        Γ^* with Eq. (4.59)
    else
        Use Γ^*_{min}
    end if
end while
End of simulation

5 Development of a statistical evaluation method

Thus far, the first objective of this thesis – the development of a suitable method for simulating boiling flows – was addressed in the preceding chapter. These simulations can provide instantaneous data about each bubble in the computational domain (Ch. 4). This chapter addresses the second objective of this thesis: the statistical analysis of the bubble data. Considering the shortcomings of other available evaluation methods (see Ch. 3), the Voronoi diagram is implemented for its more favourable properties, including the unique definition of a *bubble cell* that it provides. In this chapter, improvements to the Voronoi method will be proposed, specifically regarding the statistical significance of each point in the computational domain. The content of this chapter is published in Weber et al. (2023).

5.1 Conceptualization

Voronoi diagrams are a useful tool for defining a bubble cell, however, the local bubble count of each instantaneous snapshot is unity. Accordingly, the statistical significance of local bubble statistics can be low when there are few snapshots. To address this challenge, several Voronoi cells are grouped so that a *bubble cluster* is formed. This grouping step (hereby called clustering) allows for a bubble to be defined, even from instantaneous snapshots (Fig. 5.1). Furthermore, by grouping bubbles into clusters of equal bubble count, the statistical significance (sample size) is uniformly distributed in space.

The workflow that emerges when the Voronoi diagram and clustering step are combined is straightforward. Fig. 5.2 depicts a visualization of the chronological order of the data processing steps. Three work steps are required before bubble statistics can be analyzed: (i) data pre-processing, (ii) Voronoi diagram, and (iii) clustering.

The data pre-processing step depends on the source of the data. Data can be derived from experiments (e.g., shadowgraph as in Laupsien et al. (2019), x-ray scans as in Lau et al. (2016), etc.) or simulations. The purpose of this step is to obtain information about the bubble location

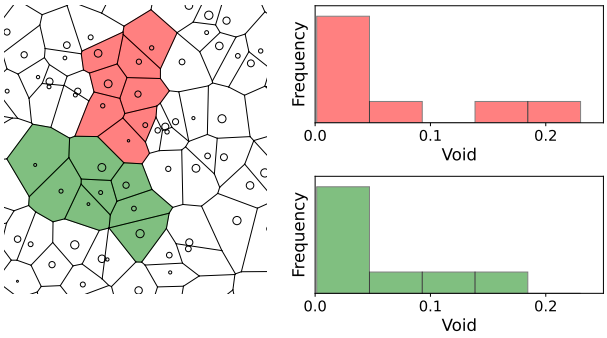

Figure 5.1: Schematic diagram of bubbly flow field (left), where the Voronoi diagram decomposes the domain, so that each bubble is assigned one cellular region. Two bubble clusters are visualized by the red and green regions. Each cluster contains the same number of bubbles. Within the cluster, an instantaneous void fraction PDF is defined (right). Figure is taken from Weber et al. (2023).

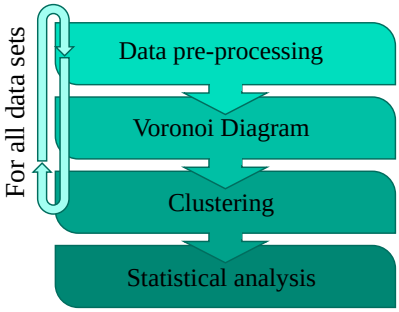

Figure 5.2: Workflow for the processing of data for the statistical evaluation, adapted from Weber et al. (2023).

and quantities of interest (size, surface, velocity, etc). In the present application to boiling flow simulations, the data pre-processing step occurs during the simulation runtime, with the data being obtained through bubble tagging (see Sec. 4.8).

Note that Weber et al. (2023) presents an extension of the data pre-processing step, which allows data sets to be stacked. This extension can be used if one instantaneous dataset does not contain enough bubbles. However, this is not the case for boiling flows.

In the second step of the workflow, the Voronoi diagram is constructed to define the bubble cells. The definition of the n-th Voronoi cell $\Omega_{V,n}$ is already provided in Eq. (3.1). The region $\Omega_{V,n}$

occupies the volume $V_{V,n}$. The cell-averaged gas content is denoted $\hat{\alpha}$. Using $V_{V,n}$ together with the bubble volume BV_n (see Sec. 4.8.1), the relation

$$\hat{\alpha}_n = \frac{\mathrm{BV}_n}{V_{V,n}} \tag{5.1}$$

is found. Applying the same strategy, the bubble concentration Υ and the interfacial area concentration Λ is defined by

$$\hat{\Upsilon}_n = \frac{1}{V_{V,n}}, \tag{5.2}$$

and

$$\hat{\Lambda}_n = \frac{\mathrm{BS}_n}{V_{V,n}}. \tag{5.3}$$

Analogously to $\hat{\alpha}$, the symbol $\hat{\cdot}$ refers to the volume average over a Voronoi cell Ω_V.

5.2 Constrained K-Means clustering

In the third step of the workflow, the K-Means algorithm is employed to group the bubbles into clusters. The original K-Means algorithm (see MacQueen (1967)) clusters a number of observations (here: bubbles) into K clusters based on the squared Euclidean distance from the observations to the cluster centre. Formally, the clustering algorithm assigns each of the N_b bubbles to one of the K clusters. The clustering function f^{CNK} expresses this assignment as

$$f^{CNK} : \{1, 2, ..., N_b\} \rightarrow \{1, 2, ..., K\}. \tag{5.4}$$

Using the function f^{CNK} the i-th cluster region $\Omega_{C,i}$ is defined

$$\Omega_{C,i} = \bigcup_{n=1}^{N_b} \begin{cases} \Omega_{V,n} & \text{if } f^{CNK}(n) = i \\ \emptyset & \text{else} \end{cases}. \tag{5.5}$$

Calculating a cluster-averaged value for $\Omega_{C,i}$ requires the definition of a weight factor w_n for all volume-averaged quantities (i.e. α, Υ, and Λ). Thus, the weight $w_{n,i}$ is the volumetric contribution of the n-th bubble to the i-th cluster volume $V_{C,i}$. Therefore

$$w_{n,i} = \begin{cases} \frac{V_{V,n}}{V_{C,i}} & \text{if } f^{CNK}(n) = i, \\ 0 & \text{else.} \end{cases} \tag{5.6}$$

Subsequently, a cluster-averaged value is indicated by $\hat{\cdot}$. For example, the cluster-averaged void fraction $\hat{\alpha}$ is

$$\hat{\alpha}_i = \sum_{n}^{N_b} w_{n,i} \alpha_n \, , \forall \vec{x} \in \Omega_{C,i}. \tag{5.7}$$

Note that $\hat{\alpha}$ represents an instantaneous value. The corresponding time-averaged value $\overline{\hat{\alpha}}$ is obtained by averaging over S instantaneous data sets as

$$\overline{\hat{\alpha}} = \frac{1}{S} \sum_{s=1}^{S} \hat{\alpha}_s. \tag{5.8}$$

The original K-Means clustering algorithm (see MacQueen (1967)) does not restrict the number of observations (here: bubbles) in one cluster. Therefore, the number of bubbles assigned to each point in space can vary. Instead, this work utilizes the constrained K-Means algorithm by Bennett et al. (2000), which allows for constraints on cluster size. Note that the above bubble cluster analysis remains the same when using the constrained K-Means clustering algorithm.

Specifically, with the constrained K-Means clustering algorithm, lower N_{min} and upper N_{max} boundaries can be set for the number of bubbles in one cluster. The values for N_{min} and N_{max} are chosen by setting a target cluster size N_{trgt}. For each data set, one of three settings is selected:

- $N_{min} = N_{trgt}$ and $N_{max} = N_{trgt} + 1$
- $N_{min} = N_{trgt} - 1$ and $N_{max} = N_{trgt}$
- $N_{min} = N_{max} = N_{trgt}$

The setting that results in the most clusters of size N_{trgt} is selected.

The choice of N_{trgt} itself is always based on the database and the goals of the evaluation. Low values of N_{trgt} (smaller clusters) reduce the spatial expansion of the clusters, and thus, the spatial uncertainty of the results. In contrast, larger values of N_{trgt} increase both the spatial uncertainty and the sample size for each point in space. Therefore, a case-specific choice must be made for an appropriate balance between spatial uncertainty and statistical significance.

This methodology is demonstrated in Fig. 5.3, where 32 bubbles are randomly distributed in a quadratic domain. The cluster size is restricted by setting $N_{min} = N_{max} = N_{trgt} = 8$. Each Voronoi cell is coloured based on its assignment to one of the four clusters. Additionally, all Voronoi cells are of finite size due to the truncation at the boundary of the domain.

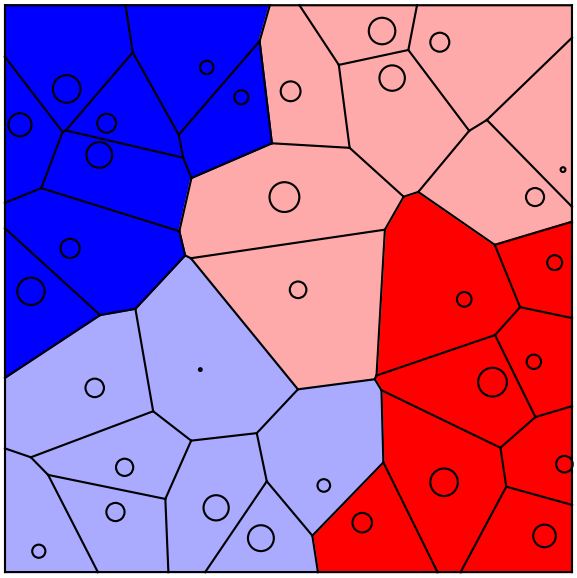

Figure 5.3: 32 bubbles and their corresponding Voronoi cells, grouped into four clusters with eight bubbles each through the constrained K-Means algorithm by Bennett et al. (2000). Each Voronoi cell is coloured based on its assignment to one of the four clusters. Figure adapted from Weber et al. (2023).

Overall, the developments in this chapter constitute an essential tool for evaluating local bubble statistics. The significant features of this approach are (i) the consistent definition of an instantaneous bubble statistic, and (ii) a substantially improved sample size. The latter feature is important for Ch. 7 due to the reduced amount of instantaneous datasets arising from the high computational cost.

6 Validation and Benchmark Simulations

Based on the methods development in Ch. 4 and Ch. 5, a comprehensive testing campaign is conducted. This testing campaign serves as the basis for the application to a technically relevant boiling flow, which is discussed later in (Ch. 7). This chapter provides a description and analysis of the testing campaign, which will focus on evaluating:

- Accuracy of the pressure solution, using the FFT-MPDJ scheme from Sec. 4.3
- Accuracy of the phase change model developed in Sec. 4.4.1
- Impact of the additional momentum contributions derived in Sec. 4.1.4
- Performance of various surface tension models
- Performance of the wettability model from Sec. 4.5
- Capability of simulating realistic, complex boiling flows
- Accuracy of the proposed bubble tagging method of Sec. 4.8
- Accuracy of the statistical evaluation framework of Ch. 5

All physical properties of the fluids used in this chapter are listed in Appendix A.1.

6.1 3D Rising bubble simulation

Simulating the dynamics of rising bubbles is a common benchmark for two-phase flow solvers (see e.g. Dodd and Ferrante (2014), Cifani (2019), Mao et al. (2021), Crialesi-Esposito et al. (2023), and ten Eikelder and Schillinger (2024)). This work adopts the 3D rising bubble simulation setup from Adelsberger et al. (2014), which is depicted in Fig. 6.1. The content of this section is published in Weber et al. (2026).

The setup consists of a box with wall (no-slip) boundaries at all faces (Fig. 6.1). Before initiating the simulation, the centre of a bubble with diameter D_0 is placed at $\vec{x} = (D_0, \quad D_0, \quad D_0)$. Subsequently, the bubble motion due to gravity[3] $\vec{g} = (0, \quad 0, \quad -0.98)$ ms^{-2} is analyzed.

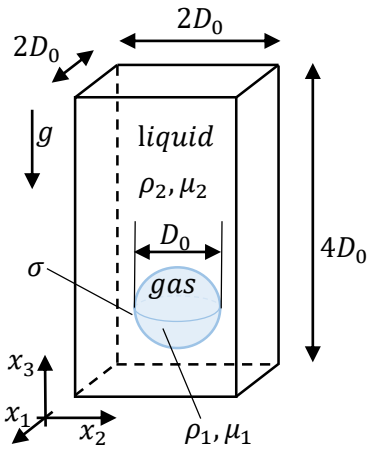

Figure 6.1: Visualization of the rising bubble simulation, taken from Weber et al. (2026).

Fluid	ρ_2/ρ_1	Re	We	Fr
Fluid$_D$	10	35	1	1
Fluid$_E$	1000	3.5	0.125	1

Table 6.1: Non-dimensional numbers corresponding to the fluid properties by Adelsberger et al. (2014) (see Appendix Tab. A.1)

For this simulation, two sets of physical properties are used, those of Fluid$_D$ and Fluid$_E$ (see Tab. A.1). Temperature transport and phase change are not considered in this benchmark. Thus, the relevant non dimensional numbers are the Reynolds number $\mathrm{Re} = \rho_1 u_{\mathrm{ref}} l_{\mathrm{ref}} \mu_1^{-1}$, the Weber number $\mathrm{We} = \rho_1 u_{\mathrm{ref}}^2 l_{\mathrm{ref}} \sigma^{-1}$, and the Froude number $\mathrm{Fr} = u_{\mathrm{ref}} / \sqrt{|\vec{g}| l_{\mathrm{ref}}}$ as in Crialesi-Esposito et al. (2023). These numbers quantify the ratio of inertial forces to viscous, surface tension, and gravitational forces, respectively. The utilized reference quantities are

$$l_{\mathrm{ref}} = D_0, \quad t_{\mathrm{ref}} = \sqrt{\frac{l_{\mathrm{ref}}}{|\vec{g}|}}, \quad u_{\mathrm{ref}} = \sqrt{l_{\mathrm{ref}} |\vec{g}|}, \quad p_{\mathrm{ref}} = \frac{u_{\mathrm{ref}} \mu_2}{l_{\mathrm{ref}}}. \tag{6.1}$$

Quantities marked with an asterisk indicate non-dimensionalization, through the reference quantities from Eq. (6.1). The values of the non-dimensional numbers for each fluid are listed in Tab. 6.1. As seen in Tab. 6.1, surface tension is more relevant for the Fluid$_E$, and laminar flow is expected for both fluids.

[3] The gravitational acceleration on earth is 9.81 ms^{-2}. However, in order to comply with the boundary conditions given in Adelsberger et al. (2014), a *virtual* gravity of 0.98 ms^{-2} has been selected.

The quantities of interest are the location of the bubble centre, the bubble sphericity (defined as $\mathrm{BS}(t=0)/\mathrm{BS}(t)$), and the rise velocity. In Adelsberger et al. (2014), these quantities are reported in a comprehensive database using three different flow solvers:

- DROPS: A level-set code, using finite elements proposed in Gross and Reusken (2011)
- NASt3D: A level-set code, using finite differences, proposed in Croce et al. (2010)
- OpenFOAM: A VOF code, using the finite volume method (see OpenFOAM (2013))

In the following, this benchmark case serves two purposes: (i) evaluating the pressure solver, and (ii) evaluating the additional contribution of the regularization terms to the momentum balance equation. For each test, four simulations are carried out using two grid spacings for both sets of fluid properties. The considered grids are based on uniform cubic cells of length $\Delta x = D_0/32$ and $\Delta x = D_0/64$.

6.1.1 Pressure solver comparison

As shown in Dodd and Ferrante (2014), the pressure solution scheme has a significant impact on bubble motion. Therefore, conducting a rising bubble benchmark is an important case when modifying a pressure solution scheme. In the present section, the proposed FFT-MPDJ solver (Sec. 2.6.3) is compared to the pressure solution scheme by Frantzis and Grigoriadis (2019) (Sec. 2.6.3). In the study by Frantzis and Grigoriadis (2019), their scheme is validated against several benchmark simulations and subsequently adopted in other studies (e.g. Crialesi-Esposito et al. (2023)). Ideally, the FFT-MPDJ solver yields the same results for this non-phase-change benchmark. Note that for all simulations, the additional momentum contribution $\vec{\mathcal{C}}$ is neglected.

Fig. 6.2a and Fig. 6.2b visualize this comparison between both pressure solvers for Fluid_D and Fluid_E, respectively. The quantities considered in this comparison are the bubble location (top), sphericity (middle), and bubble velocity (bottom). In the comparison, using Fluid_D, negligible differences occur between the FFT-MPDJ solver (red lines) and the solve by Frantzis and Grigoriadis (2019) (green lines). At the higher density ratio (Fluid_E), a slight difference is observed for the sphericity of the bubble (Fig. 6.2b). However, the bubble location and velocity show high agreement when using Fluid_E.

A further analysis of the differences between the solution schemes is conducted by comparing the pressure distribution. For this purpose, the pressure along a line parallel to the x_3-axis is considered, which cuts through the centre of the bubble. This pressure distribution should approximately exhibit the hydrostatic pressure, with an interruption of the pressure at the location of the upward-moving bubble. At $t = 0$, the pressure field is initialized as uniform zero.

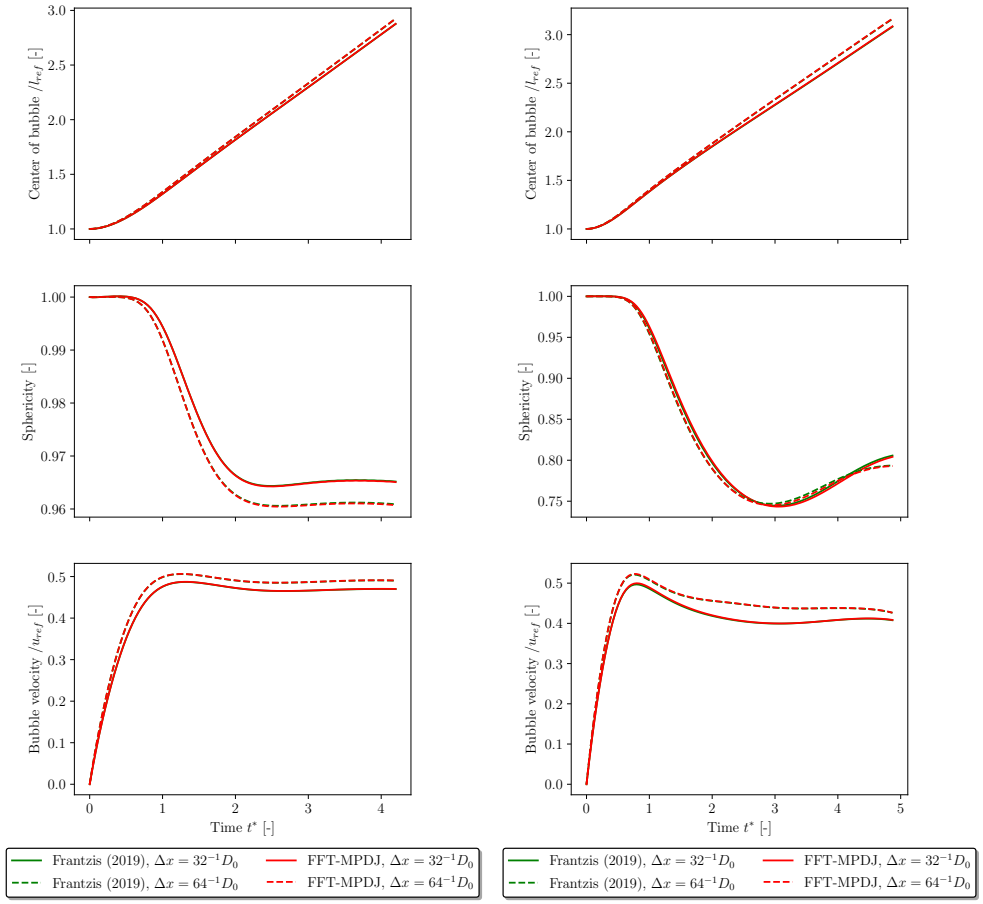

(a) Results for Fluid$_D$ ($\rho_2/\rho_1 = 10$)

(b) Results for Fluid$_E$ ($\rho_2/\rho_1 = 1000$)

Figure 6.2: Comparison of results from the rising bubble benchmark by Adelsberger et al. (2014) for two different fluids. The FFT-MPDJ is compared with the pressure solution scheme by Frantzis and Grigoriadis (2019). Figure adapted from Weber et al. (2026).

In Fig. 6.3, the evolution of the pressure obtained from both pressure solvers are visualized 32 times during the simulation. In the solution scheme by Frantzis and Grigoriadis (2019) (left), the pressure distribution requires a large fraction of the observation period to adjust to the hydrostatic pressure field. In contrast, when using the FFT-MPDJ (right) scheme, the pressure field adapts much faster, i.e., almost within the first output time interval. Minor impacts on the bubble dynamics can be expected to result from these differences (see Fig. 6.2b).

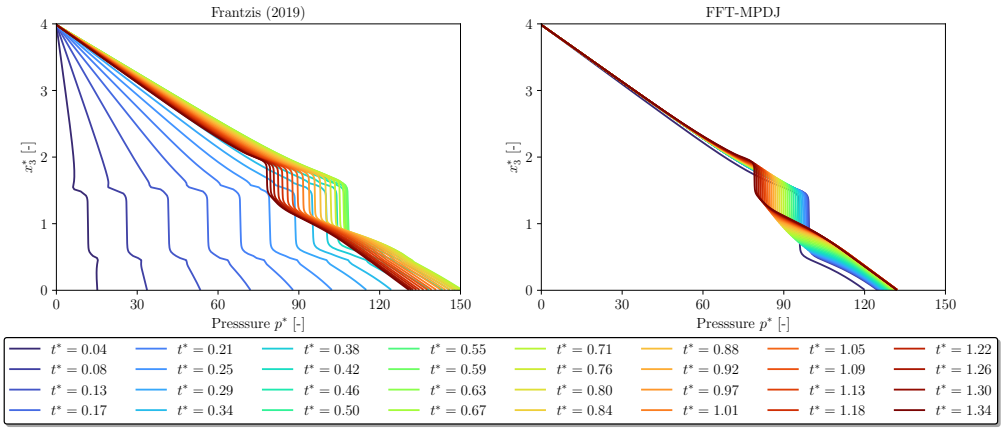

Figure 6.3: Pressure distribution over time for two different pressure solution schemes, taken from Weber et al. (2026). Comparison between the FFT-MBDJ (right) scheme with the scheme by Frantzis and Grigoriadis (2019) on the left.

6.1.2 Relevance of momentum contributions Eq. 4.19

In the second test, the FFT-MPDJ scheme is utilized, and the impact of the additional momentum contribution $\vec{\mathcal{C}}$ is studied. The common assumption that relative momenta are negligible (see Gurtin et al. (1996)) suggests that the impact of $\vec{\mathcal{C}}$ is minor. This assumption is tested in the following by carrying out each simulation, including and excluding $\vec{\mathcal{C}}$.

The results of this test are shown in Fig. 6.4a and Fig. 6.4b, corresponding to Fluid_D and Fluid_E, respectively. In both figures, black lines represent the results of Adelsberger et al. (2014), which are used as reference data to indicate the quality of the present results. Red lines refer to the simulations obtained when $\vec{\mathcal{C}}$ is included (Eq. 4.19), while green coloured data refer to the simulations where $\vec{\mathcal{C}}$ is excluded. For both fluid properties, a clear improvement is observed when the additional momentum contributions, arising from the regularization terms, are included. The improvements are most visible in the sphericity (middle) and the bubble velocity (bottom) of the high-density-ratio fluid (Fig. 6.4b). Including $\vec{\mathcal{C}}$ helps to improve the accuracy of the results significantly, in relation to the sharp interface reference data (black lines). For the lower density ratio fluid (Fig. 6.4a), slight but consistent improvements are visible across all quantities.

6.1.3 Discussion

In Sec. 6.1.1, it is demonstrated that the proposed FFT-MPDJ scheme yields the same results for bubble dynamics as the scheme in Frantzis and Grigoriadis (2019). As such, the FFT-MPDJ

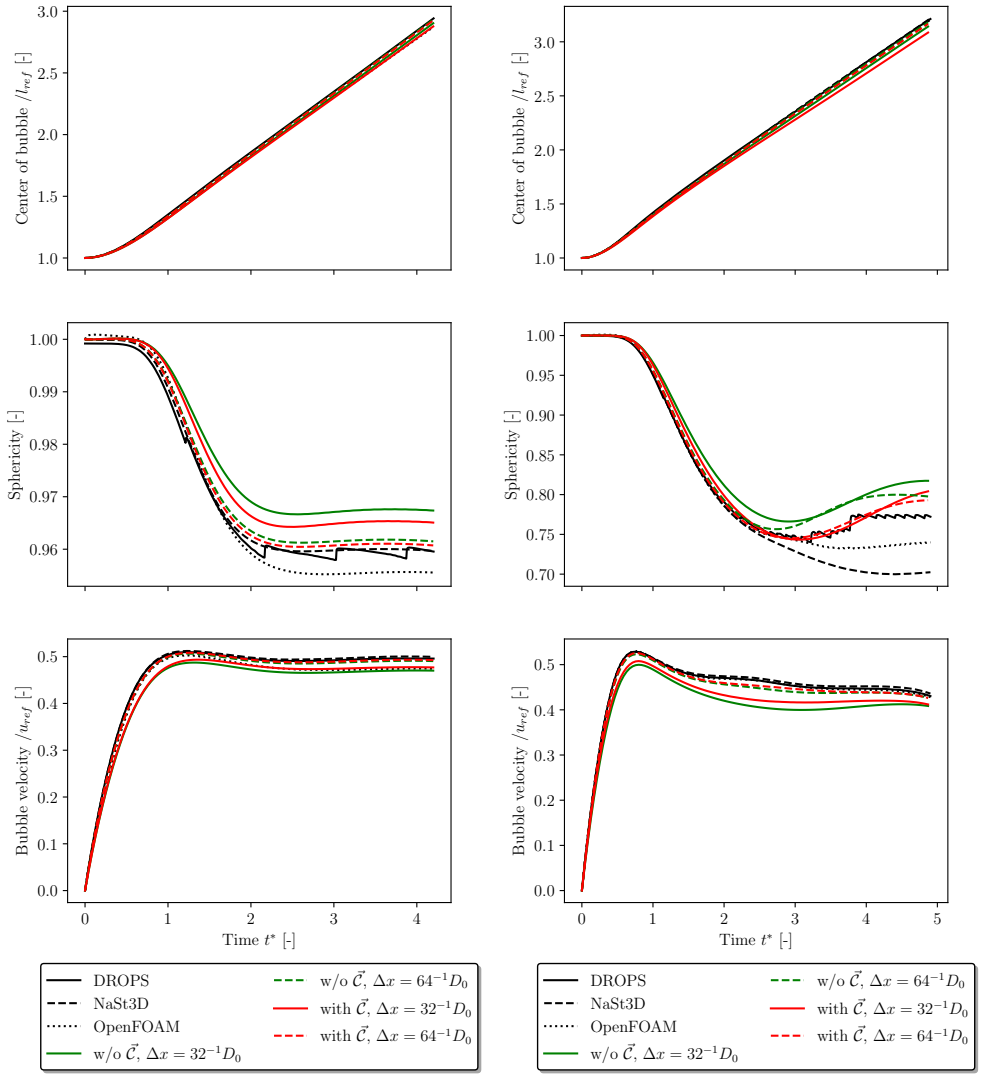

(a) Results for Fluid$_D$ ($\rho_2/\rho_1 = 10$)

(b) Results for Fluid$_E$ ($\rho_2/\rho_1 = 1000$)

Figure 6.4: Evaluation of additional momentum contribution $\vec{\mathcal{C}}$ for two sets of fluid properties. Figure adapted from Weber et al. (2026).

scheme is capable to accurately simulate the dynamics of bubbles subjected to gravity. Furthermore, the FFT-MPDJ scheme exhibits advantageous properties over the scheme by Frantzis and Grigoriadis (2019) for adapting the pressure field to the flow at high-density ratios. When quantifying the effect of including the additional momentum contributions (see Eq. (4.19)), consistent improvements are seen for all quantities. However, the improvements, although significant, are minor.

6.2 Contact angle simulation

In this test simulation, a contact angle Θ is prescribed for a bubble in contact with the wall. The results of this simulation can be used to verify the wettability model described in Sec. 4.5. Specifically, two quantities are of interest: (i) the accuracy of the contact angle boundary treatment, and (ii) the integral mass loss during the simulation runtime.

At $t = 0$, a hemisphere-shaped bubble of radius $r_0 = 1$ mm is placed on a wall (see Fig. 6.5a). The computational domain has the size $6r_0 \times 6r_0 \times 3r_0$. Periodic boundary conditions are applied in the x_1 and x_2-directions, whereas wall boundary conditions are applied to the top and bottom boundaries in the x_3-direction. The bubble is placed at the centre of the bottom boundary face in the x_3-direction. Gravity is neglected, $\vec{g} = \vec{0}$, and the properties of saturated water at atmospheric pressure are applied (see Tab. A.1). Phase change phenomena are neglected.

The influence of grid resolution on the results is analyzed using a coarse grid with $\Delta x = r_0/10$ and a fine grid with $\Delta x = r_0/20$. For both grid spacings, the contact angles $\Theta = 45°$ (hydrophilic) and $\Theta = 135°$ (hydrophobic) are applied employing the contact angle boundary treatment from Sec. 4.5. The simulations are run until a steady state solution is reached, where the motion of the bubble vanishes.

In Fig. 6.5, the initial condition is shown, along with the steady-state solution on the fine grid for both contact angles. For the shape of the steady-state solution, a simple analytical shape is derived. This shape corresponds to a sphere cap that has the same volume as the initial hemisphere but intersects the wall at a contact angle Θ. The steady-state shapes are compared to the analytical shape in Fig. 6.6. The initial shape is the same for both grids, regardless of contact angle. However, the steady-state solution deviates from the analytical solution for coarse grids. In particular, a slight deviation is seen for $\Delta x = r_0/10$, at the contact angle $\Theta = 45°$. However, the overall agreement for both grid spacings is satisfactory.

Furthermore, the mass loss during the simulation runtime is evaluated. For this, the integral mass in the domain is considered, that is, $\int \rho(t) dV$. To obtain the relative mass loss, the mass at $t = 0$ is used as the reference quantity. In Fig. 6.7, the relative mass loss is plotted for 150 output files

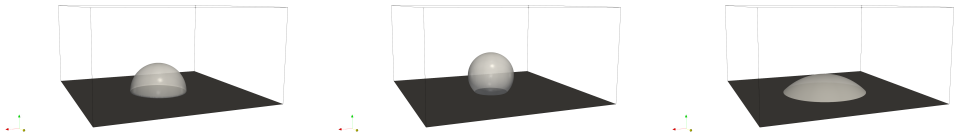

(a) Initial condition **(b)** Steady state, $\Theta = 45°$ **(c)** Steady state, $\Theta = 135°$

Figure 6.5: Three-dimensional visualization of the initial condition and the steady state solutions for two contact angles. Results correspond to the fine grid.

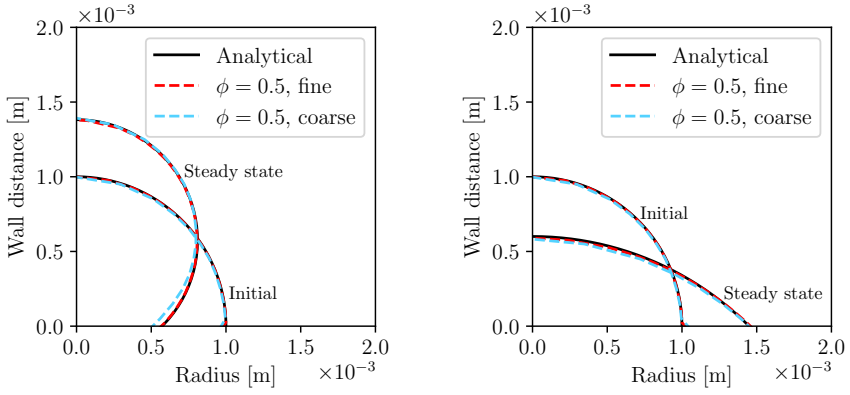

(a) $\Theta = 45°$ **(b)** $\Theta = 135°$

Figure 6.6: Geometric comparison of the steady state solution with the analytical solution. Results are presented in cylindrical coordinates, where the centerline axis aligns with the bubble centerline.

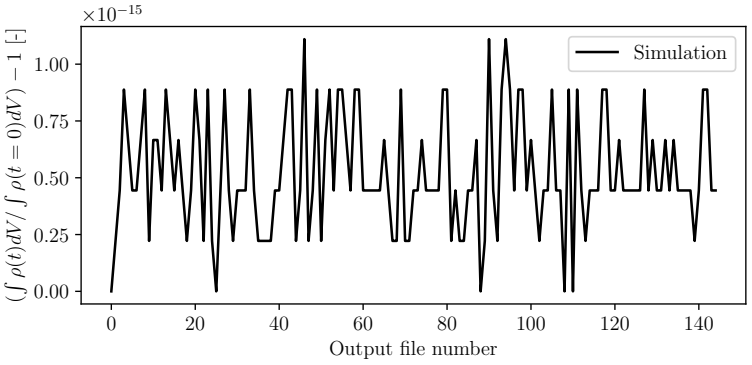

Figure 6.7: Relative loss of mass during the simulation runtime, normalized with the mass at $t = 0$.

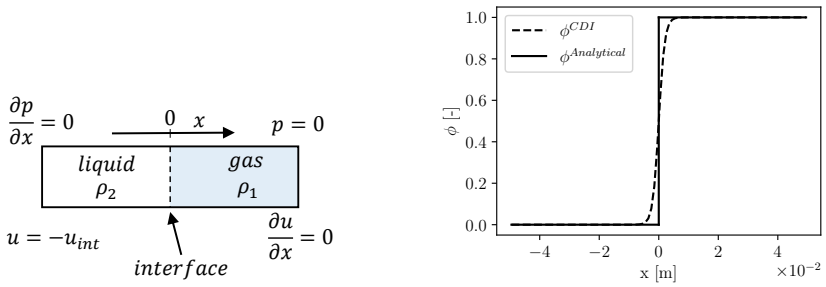

(a) Schematic of the simulation setup, taken from Weber et al. (2026)

(b) Constant phase field profile in reference frame from Weber et al. (2026).

Figure 6.8: Basic simulation settings for the prescribed evaporation simulation.

during the simulation ($t_{tot} = 0.234$ s), corresponding to $\Delta x = r_0/20$ and $\Theta = 135°$. The figure shows that mass was conserved to machine precision.

6.3 1D prescribed evaporation

Mass transfer has been neglected in the previous two test simulations. Now the focus shifts to phase-changing flows. A simple, yet essential test is the simulation of evaporation at a one-dimensional interface (see Sun and Beckermann (2004)). The central quantity of interest in this test is the interfacial pressure jump. With this quantity, two features of the developed solver can be assessed: (i) the FFT-MPDJ solution scheme, and (ii) the identified momentum contribution $\vec{\mathcal{C}}$. The content of this section is taken from Weber et al. (2026).

Fig. 6.8a depicts a schematic of the simulation setup. A feature of this simulation setup is that the coordinate system follows the interface with a velocity u_{int}. Consequently, the phase field variable ϕ is invariant in time and follows the equilibrium hyperbolic tangent profile. The (constant) phase field profile is visualized in Fig. 6.8b. Using $u = \phi u_1 + (1-\phi)(u_1 + \Delta u)$, and recalling that $\nabla \cdot u = \mathcal{M}(\rho_1^{-1} - \rho_2^{-1})$, the interfacial velocity jump can be prescribed by setting

$$\mathcal{M} = \Delta u |\nabla \phi| \left(\frac{1}{\rho_1} - \frac{1}{\rho_2} \right)^{-1} \tag{6.2}$$

For a given velocity jump Δu, the interface velocity u_{int} (see Sun and Beckermann (2004)) is calculated as

$$u_{\text{int}} = -\frac{\Delta u}{\rho_2/\rho_1 - 1} \tag{6.3}$$

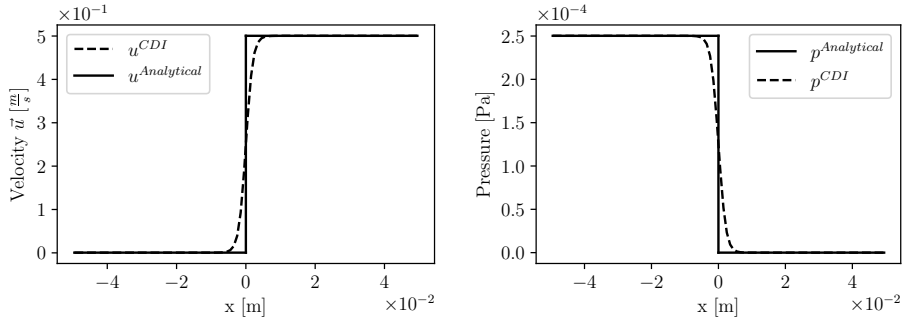

(a) Velocity jump, taken from Weber et al. (2026)

(b) Pressure jump, taken from Weber et al. (2026)

Figure 6.9: Velocity (a) and pressure (b) distribution for a constant velocity jump $\Delta u = 0.5\ \mathrm{ms}^{-1}$. Solid lines represent the analytical solution and dashed lines represent the numerical phase field solution.

Since the liquid is placed on the left side of the computational domain (see Fig. 6.8a), the Dirichlet boundary condition (left) has to be set to $-u_{\mathrm{int}}$ to account for the interface displacement. Due to the momentum difference, a pressure jump Δp_{th}, called *recoil pressure*, is induced. The analytical jump (Sun and Beckermann (2004)) reads

$$\Delta p_{\mathrm{th}} = -u_{\mathrm{int}}^2 \rho_2 \left(\frac{\rho_2}{\rho_1} - 1 \right) \tag{6.4}$$

For known ϕ (and thus ρ) and u, an exact expression for the regularization term $\vec{\mathcal{R}}$ can be obtained integrating Eq. (4.11) to yield

$$\vec{\mathcal{R}} = \frac{\rho u + u_{\mathrm{int}} \rho_2}{\rho_1 - \rho_2} \tag{6.5}$$

Therefore, the only calculated solution quantity is the pressure distribution. This test simulation has the advantage that, for high density ratios, the velocity jump (and therefore the role of the regularization terms) is large compared to u_{int}. Again, two aspects of the flow solver can be tested: (i) the FFT-MPDJ solution method, and (ii) the contributions of the additional regularization terms. For all simulations, the densities are set to $\rho_1 = 0.001$ kg m^{-3} and $\rho_2 = 1$ kg m^{-3}, and the computational domain consists of 100 cells of size $\Delta x = 1$ mm.

6.3.1 Pressure solver comparison

In the first simulation, the pressure solver of Frantzis and Grigoriadis (2019) is compared to the FFT-MPDJ scheme. For this comparison, the velocity jump is set to $\Delta u = 0.5\ \mathrm{ms}^{-1}$ = constant. The analytical velocity profile, along with its phase field representation, is shown in Fig. 6.9a.

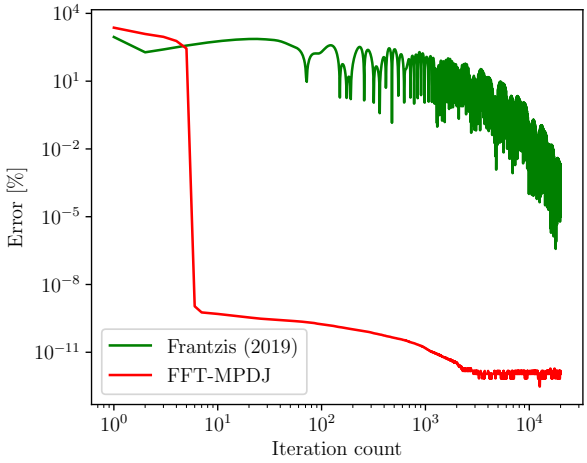

Figure 6.10: Deviation from Δp_{th} in percent over the simulation runtime (taken from Weber et al. (2026)) in the scheme by Frantzis and Grigoriadis (2019) versus the proposed FFT-MPDJ scheme.

Similarly, the analytical pressure distribution is calculated using Eq. (6.4), which is shown in Fig. 6.9b. The results using either pressure scheme are represented by the dashed black line. The quantity of interest, is the accuracy and number of iterations at which the pressure schemes approach the solution of Eq. (6.4). As pointed out in Poblador-Ibanez et al. (2025), commonly used density splitting schemes, like those of Frantzis and Grigoriadis (2019) or Dodd and Ferrante (2014), are associated with pressure oscillation problems.

The accuracy of the pressure jump calculation versus the number of iterations is shown in Fig. 6.10. The measure of error is calculated from

$$\text{Error} = \frac{\Delta p(t) - \Delta p_{\text{th}}}{\Delta p_{\text{th}}} 100\% \tag{6.6}$$

The result obtained when implementing the method by Frantzis and Grigoriadis (2019) is represented by the green line, whereas the red line represents the FFT-MPDJ scheme. The figure shows how the scheme by Frantzis and Grigoriadis (2019) results in severe oscillations and only achieves acceptable errors after 10^4 iterations. In contrast, the proposed FFT-MPDJ scheme reduces the error to $10^{-8}\%$ in less than ten iterations. This highlights a significant advantage of the FFT-MPDJ solver over the available density-splitting-based FFT schemes.

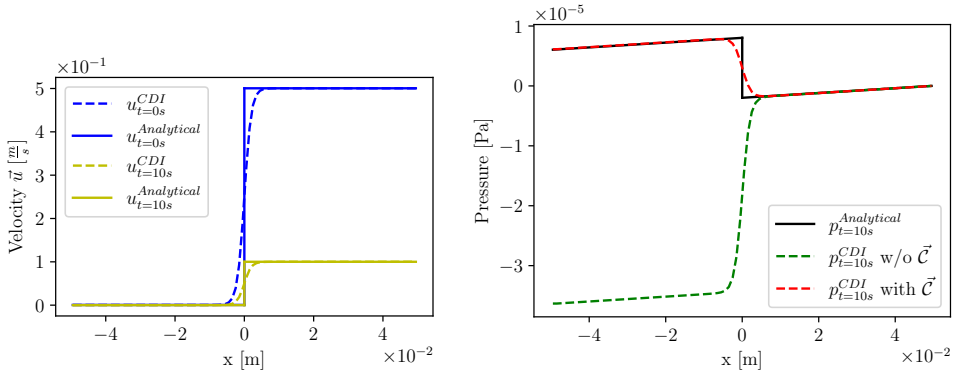

(a) Velocity jump, taken from Weber et al. (2026)

(b) Pressure jump, taken from Weber et al. (2026)

Figure 6.11: Analytical solution in comparison to the phase field simulation results. Velocity distribution at the start and end of the simulation for a time-dependent velocity jump (a). Pressure distribution at simulation end ($t = 10$ s) is visualized in (b), where the effect of the additional momentum contribution $\vec{\mathcal{C}}$ is visualized.

6.3.2 Relevance of momentum contributions Eq. 4.19

To analyze the influence of the identified momentum contributions in Eq. (4.19), a variable velocity jump is prescribed. In this section, the velocity jump is set to $\Delta u = \Delta u(t) = [0.5 - 0.04t]$ ms^{-1}. As such, the velocity jump reduces over the simulation run time, from $\Delta u = 0.5$ ms^{-1} at $t = 0$s down to $\Delta u = 0.1$ ms^{-1} at $t = 10$s. The velocity profiles at the start ($t = 0$ s) and end ($t = 10$ s) of the simulation are shown in Fig. 6.11a. As in Sec. 6.3.1, the analytical pressure jump is obtained from Eq. (6.4). Due to the changing velocity jump, an additional slope in the pressure gradient (Fig. 6.11b) is expected on both sides of the interface, according to $\partial p/\partial x = \rho_2 \partial u_{\text{int}}/\partial t$. The analytical pressure distribution at $t = 10$ s is shown in Fig. 6.11b, represented by the black solid line. In the same figure, the resulting pressure distributions after including (dashed, red) and excluding (green, dashed) the momentum contribution $\vec{\mathcal{C}}$ are illustrated. Excluding $\vec{\mathcal{C}}$ results in an erroneous pressure jump, which exhibits an incorrect magnitude and sign. It is evident from Fig. 6.11b that the additional momentum contributions presented in Eq. (4.19) are responsible to obtain correct recoil pressure distributions in time-dependent phase-change scenarios.

6.4 1D Stephan problem

The Stefan problem is a well-known benchmark test for assessing the accuracy of a phase change model. The content of this section is published in Weber et al. (2026). This benchmark is characterized by a wall at a fixed temperature T_{wall}, which transfers heat to a gaseous layer. The

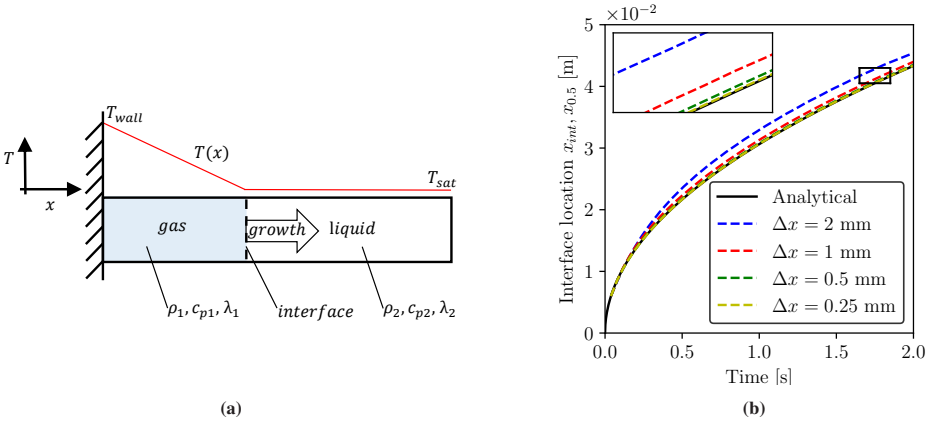

Figure 6.12: (a) Visualization of the Stefan problem. (b) Interface locations obtained with different grid spacings (dashed) in comparison with the analytical solution (black solid). Both figures are taken from Weber et al. (2026).

gas layer thickens due to phase change, pushing the liquid phase away from the wall. This situation is depicted in Fig. 6.12a. An analytic solution for the interface location (see, e.g., Perez-Raya and Kandlikar (2016)) can be obtained as follows

$$x_{\text{int}}(t) = 2\beta\sqrt{a_1 t} \quad \text{, and} \quad \beta \exp(\beta^2)\text{erf}(\beta) = \frac{c_{p,1}(T_{\text{wall}} - T_{\text{sat}})}{L(T_{\text{sat}})\sqrt{\pi}}. \tag{6.7}$$

In Eq. (6.7), β is a growth constant that is numerically calculated from the transcendental equation. As such, the analytic distance of the interface from the wall x_{int} depends on the problem parameters and physical fluid properties, and has a square-root dependency on time t.

The following simulations consider the properties of the Fluid$_A$. These fluid properties, taken from Dongliang Sun and Chen (2014), are listed in Tab. A.1. Setting $T_{\text{wall}} - T_{\text{sat}} = 10$ K, a growth constant of $\beta \approx 0.3064$ is calculated. The length of the one-dimensional domain is $\ell = 0.05$ m and is discretized using uniform grid cells of sizes $\Delta x = 2$ mm, 1 mm, 0.5 mm, and 0.25 mm. The simulation is initialized with the interface ($\phi = 0.5$) located at $x_{0.5} = 6$ mm and a linear temperature profile in the gaseous phase (corresponding to $t \approx 38.34$ ms).

Fig. 6.12b visualizes the interface location versus the simulation runtime. For coarse cell sizes, the growth of the gas layer is visibly over-predicted. With reduced grid spacing, the simulated interface location $x_{0.5}$ approaches the analytic solution. Convergence of simulation results with varied grid spacing to the analytical interface location is quantified through the error measure

$$\text{Error} = \sqrt{\frac{\sum_t \left(x_{\text{int}} - x_{0.5}\right)^2}{\sum_t x_{\text{int}}^2}}. \tag{6.8}$$

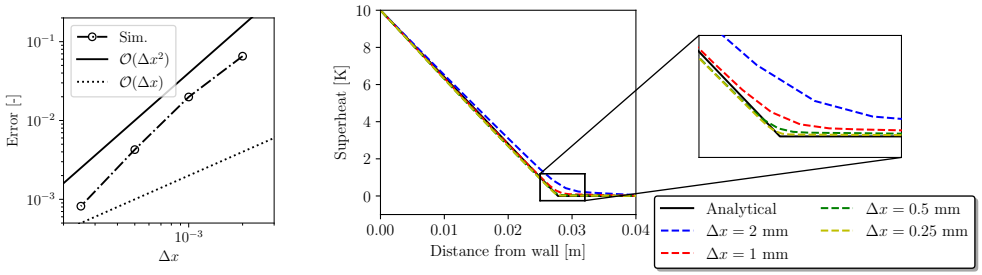

(a) Error measure

(b) Temperatures at $t = 0.823$ s

Figure 6.13: (a) Error measure for the interface location of the analytical solution compared to the simulations with various grid spacings. (b) Temperature profiles compared to the analytical profile. Both figures are taken from Weber et al. (2026).

Fig. 6.13a depicts the error, quantified through Eq. (6.8). The error is reduced with decreasing grid spacing at approximately a second-order rate. At time $t = 0.823$ s, the temperature profiles obtained using different grid sizes are visualized in Fig. 6.13b. Aligning with Fig. 6.12b, larger deviations are observed for the coarser grids, while the two fine grid spacings yield good agreements with the analytical solution.

Dongliang Sun and Chen (2014) achieved good agreement with the analytic solution for the same problem parameters, starting from $\Delta x = 2$ mm, by using a VOF (sharp interface) approach. In comparison, at least twice the resolution is required in this thesis to obtain reasonable agreement. This confirms the trend that diffuse interface methods require higher resolution to achieve a similar accuracy (see the study by Mirjalili et al. (2019)).

6.5 1D sucking interface problem

The sucking interface problem (e.g., Welch and Wilson (2000)) is another one-dimensional benchmark test for evaluating phase change models. The content of this section is published in Weber et al. (2026). Fig. 6.14 shows the characteristic problem setup of this benchmark. Different from the Stefan problem, the wall and the gaseous phase remain at saturation temperature. For the sucking interface, the liquid phase has a superheated far-field temperature T_∞, which leads to a transport of heat towards the interface, resulting in phase change. Therefore, the gaseous layer grows, and a thermal boundary layer develops in the liquid phase. As in the Stefan problem, a known analytical solution (refer to Perez-Raya and Kandlikar (2016)) exists for the sucking interface problem,

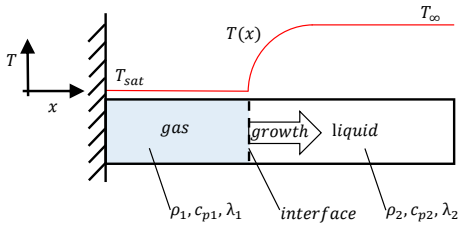

Figure 6.14: Schematic visualization for the sucking interface problem, adapted from Weber et al. (2026).

$$x_{\text{int}}(t) = 2\beta\sqrt{a_1 t}. \tag{6.9}$$

where x_{int} is the analytical interface distance from the wall. The growth constant β is calculated as

$$\exp(\beta^2)\text{erf}(\beta)\left[\beta - \frac{(T_\infty - T_{\text{sat}})c_{p,1}\lambda_2\sqrt{a_1}\exp\left(-\beta^2\frac{\rho_1^2 a_1}{\rho_2^2 a_2}\right)}{L_{\text{sat}}\lambda_1\sqrt{\pi a_2}\,\text{erfc}\left(\beta\frac{\rho_1\sqrt{a_1}}{\rho_2\sqrt{a_2}}\right)}\right] = 0, \tag{6.10}$$

for the sucking interface problem. The thermal boundary layer in the liquid phase (for $x > x_{\text{int}}$) has the following analytic profile:

$$T(x,t) = T_\infty - \left[\frac{(T_\infty - T_{\text{wall}})}{\text{erfc}\left(\beta\frac{\rho_1\sqrt{a_1}}{\rho_2\sqrt{a_2}}\right)}\right]\text{erfc}\left(\frac{x}{2\sqrt{a_2 t}} + \frac{\beta(\rho_1 - \rho_2)}{\rho_2}\sqrt{\frac{a_1}{a_2}}\right). \tag{6.11}$$

The accuracy of the simulation results largely depends on the resolution of this thermal layer. Accordingly, other studies (e.g. Irfan and Muradoglu (2017) or Sato and Ničeno (2013)) have reported underestimation of the growth rates for larger grid spacings. In the following, two sets of parameters are utilized for the sucking interface problem, using the properties of Fluid$_B$ and saturated Water at atmospheric pressure (see Tab. A.1).

6.5.1 Parameter settings from Irfan and Muradoglu (2017)

The first set of parameters involves the fluid properties of the Fluid$_B$, which originate from a simulation carried out by Irfan and Muradoglu (2017). Irfan and Muradoglu (2017) propose

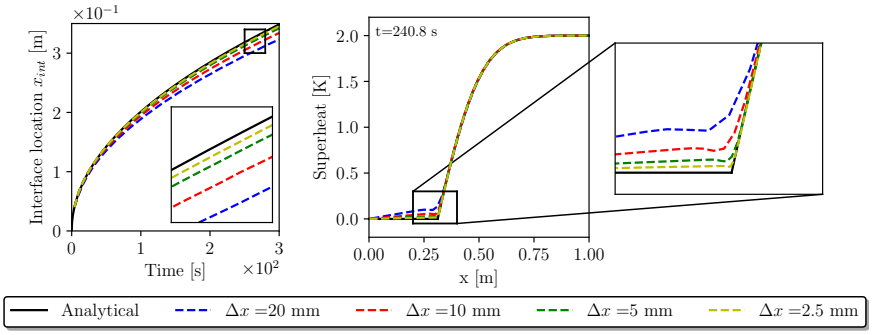

(a) Fluid$_B$, $T_\infty = 2$ K

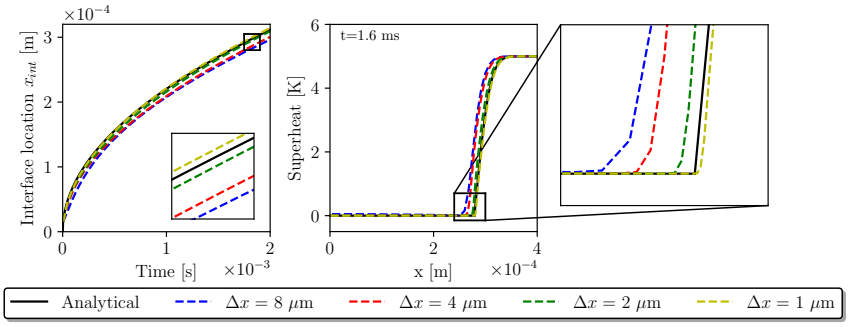

(b) Water, $T_\infty = 5$ K

Figure 6.15: Results for the sucking interface problem. Interface location (left) and temperature profile (right), for two different parameter settings. Simulations with various grid spacings are shown along with the analytical solution. Figures taken from Weber et al. (2026).

using a computational domain of length $\ell = 1$ m and a far field condition of $T_\infty - T_{\text{sat}} = 2$ K. This parameter setting leads to a growth constant value $\beta \approx 0.2689$, calculated from Eq. (6.10). The simulations are initialized using the analytic solution corresponding to the time $t = 4$ s for the interface location ($x_{\text{int}} = 0.0402$ m) and the liquid temperature profile. Four simulations are carried out using the cell sizes $\Delta x = 20$ mm, 10 mm, 5 mm, and 2.5 mm.

The results obtained from these settings are visualized in Fig. 6.15a. On the left of Fig. 6.15a, the resulting interface location is compared to the analytical solution. The figure indicates that the smaller grid spacings, 5 mm, and 2.5 mm, result in a good agreement for the interface location. The right side of Fig. 6.15a depicts the temperature profiles for $t = 240.8$ s. The temperature in the liquid phase is indistinguishable throughout the grid sizes. In the gas layer, however, a significant superheat is observed, especially for the larger grid sizes. This can be explained by the contribution of the anti-trapping current $\vec{j}$ (refer to Eq. (2.18)). Different from most 'real' fluids

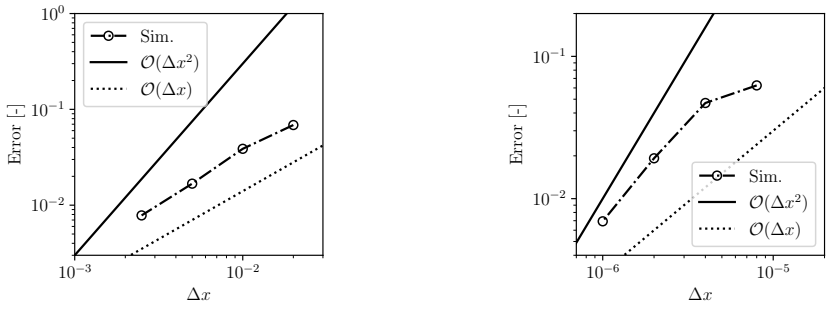

(a) Fluid$_B$, $T_\infty = 2$ K

(b) Water, $T_\infty = 5$ K

Figure 6.16: Error values calculated with Eq. (6.8) for two parameters settings. Figure taken from Weber et al. (2026).

(see Tab. A.1), Fluid$_B$ features $\lambda_1 > \lambda_2$. As a result, $\vec{j}$ is of opposite sign for Fluid$_B$ and causes an additional heat transport into the gas layer.

Fig. 6.16a also shows the convergence of the interface location $x_{0.5}$ to the analytic location x_{int}. The figure shows that the error calculated from Eq. (6.8) reduces with Δx at approximately a first-order rate. Here, the convergence rate is considerably slower than that of the Stefan problem, as it might be affected by the anti-trapping current.

6.5.2 Saturated water at atmospheric pressure

The second set of parameters considers saturated water at atmospheric pressure. Water poses greater challenges for the simulation due to its steeper temperature gradients and higher interface growth constants. Selecting a far-field superheat of $T_\infty - T_{\text{sat}} = 5$ K gives a value of $\beta \approx 0.767$ according to Eq. (6.10). For the simulation, the computational domain of length $\ell = 400$ μm is discretized using uniform cells of size $\Delta x = 8$ μm, $\Delta x = 4$ μm, $\Delta x = 2$ μm, and $\Delta x = 1$ μm. All simulations are initialized using the analytic solution corresponding to $t = 5$ μs.

The resulting interface location is shown on the left of Fig. 6.15b. The two smaller grids fail to accurately capture the interface location during the startup phase. This results in a permanent error for the remainder of the simulation, as shown in Fig. 6.15b. However, in the later stages, the coarser resolutions reproduce the correct growth rate, as they run parallel to the analytical solution.

The temperature distribution depicted in Fig. 6.15b (right) shows the steep gradients characteristic of the properties of water. The close-up reveals that the two smallest grid spacings are capable of resolving the temperature gradient within the fluid region. In addition, the gas layer remains at

saturation temperature for all grid spacings. Note that for water $\lambda_1 < \lambda_2$, thus, the anti-trapping current $\vec{j}$ does not result in additional transport of heat into the gaseous phase.

The convergence rate for the simulation, using properties of water, is also shown in Fig. 6.16b. The Eq. (6.8) is used to quantify the error in the interface location over time. Towards smaller cell sizes, the error convergence rate is significantly higher than that of Fluid$_B$. However, the error convergence is slower compared to that of the Stefan problem.

6.6 Bubble growth in zero gravity

So far, one-dimensional simulations of phase change scenarios have been discussed. Progressing towards realistic applications, the growth of a bubble in the absence of gravity is simulated in this benchmark. Similar to the sucking interface problem, a far-field temperature T_∞ is prescribed. Starting at a nucleation site, a bubble grows. In the liquid phase, a thermal boundary layer develops around the bubbles. The content of this chapter is published in Weber et al. (2026).

Scriven (1959) derived an analytical solution for this spherically symmetric flow, finding an analytic interface location r_{int} of

$$r_{\text{int}}(t) = 2\beta\sqrt{a_2 t}, \tag{6.12}$$

where the transcendental equation determining β is

$$\begin{aligned} &\frac{\rho_2 c_{p,2}(T_\infty - T_{\text{sat}})}{\rho_1\big(L_{\text{sat}} + (c_{p,2} - c_{p,1})(T_\infty - T_{\text{sat}})\big)} \\ &= 2\beta^2 \int_0^1 \exp\left[-\beta^2 \left(\big(1-\chi\big)^{-2} - 2\chi\big(1-\rho_1/\rho_2\big) - 1 \right) \right] d\chi. \end{aligned} \tag{6.13}$$

For this scenario, Scriven (1959) derived an equation describing the thermal boundary layer of the liquid ($r > r_{rint}$) as

$$\begin{aligned} T(r, r_{\text{int}}) &= T_\infty - \frac{2\beta^2\rho_1}{\rho_2 c_{p,2}} \Big(L_{\text{sat}} + (c_{p,2} - c_{p,1})(T_\infty - T_{\text{sat}}) \Big) \\ &\times \int_{1-\frac{r_{\text{int}}}{r}}^1 \exp\left[-\beta^2 \left(\big(1-\chi\big)^{-2} - 2\chi\big(1-\rho_1/\rho_2\big) - 1 \right) \right] d\chi. \end{aligned} \tag{6.14}$$

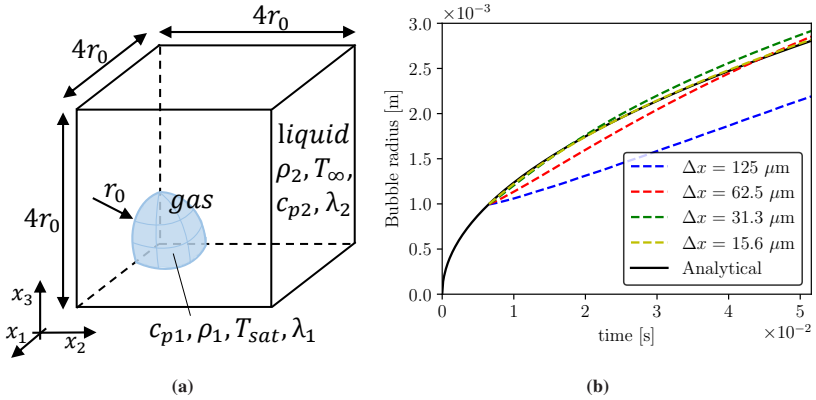

(a) (b)

Figure 6.17: Computational setup (a) and bubble radius evolution for different grid sizes (b). Both figure are taken from Weber et al. (2026).

The computational setup for simulating the bubble growth is visualized in Fig. 6.17a. Making use of the bubble's symmetry, an eighth of the bubble is simulated. Accordingly, an initial bubble of size r_0 is placed in the corner of a cubic domain of size $4r_0$. Symmetry boundary conditions are applied to the boundary faces that intersect with the bubble, and all remaining boundary faces are outflow boundaries. The far-field temperature T_∞ is set to $T_\infty - T_{\text{sat}} = 5$ K, and the properties of saturated water at atmospheric pressure are used. With these parameters, the growth constant is determined to be $\beta \approx 15.073$, thus choosing $r_0 = 1$ mm translates to a physical time of $t = 6.55$ ms (Eq. (6.12)) at simulation start. The temperature field is initialized using Eq. 6.14, and four cell sizes are considered for the simulation, i.e., $\Delta x = 125$ μm, $\Delta x = 62.5$ μm, $\Delta x = 31.3$ μm, and $\Delta x = 15.6$ μm.

6.6.1 Zero surface tension limit

From an analytic point of view (refer to Eqs. (6.12)-(6.14)), surface tension does not influence the growth rate. Therefore, the effect of surface tension is neglected ($\vec{f}_{ST} = \vec{0}$) in the first series of simulations, to isolate the performance of the phase change model.

Fig. 6.17b shows the radius $r_{0.5}$ (where $\phi = 0.5$) of the bubble versus the simulation runtime. The lowest grid resolutions, $\Delta x = 125$ μm and $\Delta x = 62.5$ μm, show significant deviations from the analytical growth rate. Only the finest grid, with $\Delta x = 15.6$ μm, yields an accurate agreement. The temperature distribution at time $t = 51.5$ ms (Fig. 6.18a) illustrates the reason for the strong grid dependence that results from the steep temperature gradients. Only the finest grid is capable

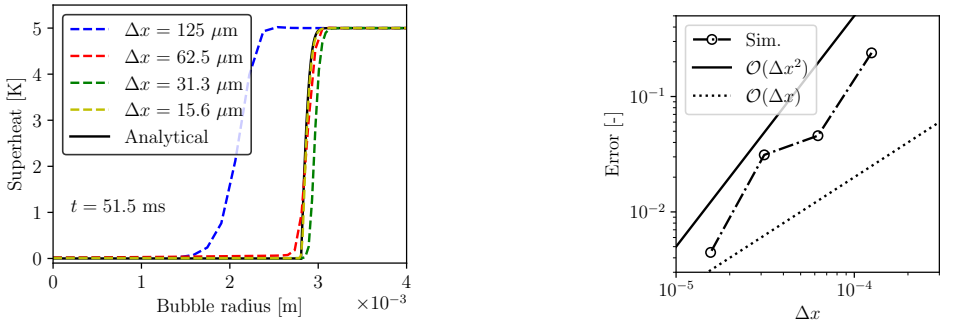

(a) (b)

Figure 6.18: (a) Temperature distribution at time $t = 51.5$ ms for all grid sizes together with the analytical temperature distribution. (b) Error measure for the bubble size evolution using Eq. (6.15). Both figures are taken from Weber et al. (2026).

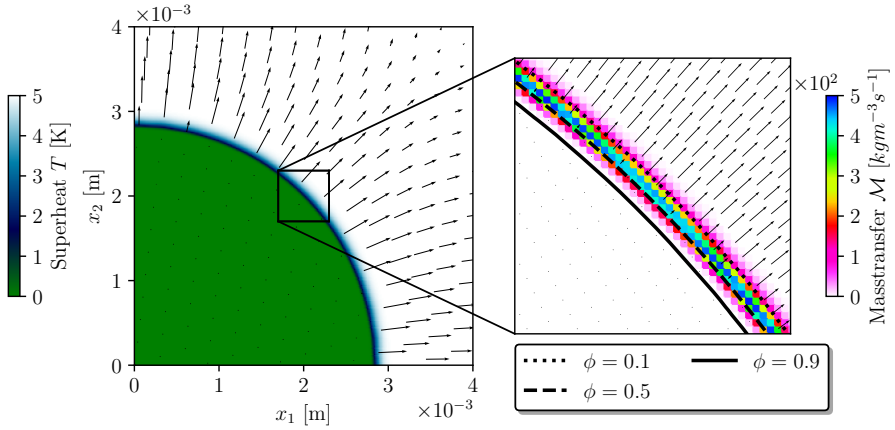

Figure 6.19: The Velocity (qualitative) and temperature distribution is depicted in the left panel. The mass transfer rate $\mathcal{M}$ together with the velocity (qualitative) and iso-contours for three phase field values are visualized in the right panel (closeup). Results correspond to $t = 51.5$ ms and $\Delta x = 15.6$ μm. Figure taken from Weber et al. (2026).

of resolving the very thin thermal boundary layer that is characteristic of the chosen settings. To quantify the accuracy achieved with each grid spacing, the error measure

$$\text{Error} = \sqrt{\frac{\sum_t \left(r_{\text{int}} - r_{0.5}\right)^2}{\sum_t r_{\text{int}}^2}} \tag{6.15}$$

is used. The reduction of error with decreasing grid size is shown in Fig. 6.18b. The error reduces at close to a second-order rate over all grid sizes.

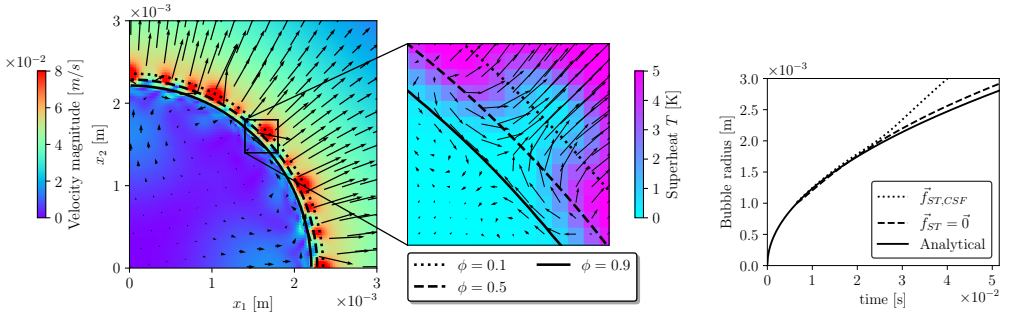

(a) Slice through the bubble centre at $t = 29$ ms

(b) Bubble radius over time

Figure 6.20: Visualization of the effect of using the CSF model for the developed flow solver for simulating bubble growth. Spurious currents are seen on the left of (a),which disturb the thermal boundary layer seen on the right of (a). Thus, the growth rate exhibits an erroneous acceleration (b).Figures are taken from Weber et al. (2026).

The qualitative velocity distribution alongside the temperature field for the smallest cell size, $\Delta x = 15.6$ μm, is shown in the left panel of Fig. 6.19. The pictured two-dimensional distribution represents a slice through the bubble centre. Here, the thin thermal boundary layer surrounding the bubble is visible. The velocity exhibits a jump at the phase interface, while the gaseous phase remains at rest. The right side of Fig. 6.19 zooms in on a section of the interface, which depicts the distribution of the mass transfer rate $\mathcal{M}$ in relation to three iso-contour lines of the phase field (black). The distribution of $\mathcal{M}$ is smooth, however, a slight shift towards the liquid side is observed.

6.6.2 Evaluation of surface tension models

In Sec. 2.4.1, various surface tension models have been presented, and their inherent spurious currents have been discussed. Thus far, no study has assessed surface tension models for simulating boiling flows with the ACDI method. This knowledge gap is addressed in the present section.

At first, the impact of spurious currents on the present methodology is highlighted. In Fig. 6.20a, an instantaneous snapshot is presented using the generic CSF model (Eq. (2.7)) and $\Delta x = 31.3$ μm. The left side of Fig. 6.20a shows the velocity distribution, which exhibits strong spurious flow structures in both the liquid and gas phases. The impact of the spurious flow on the temperature distribution is visualized in the closeup on the left. The closeup shows that the boundary layer around the bubble is disturbed due to convective transport. As a result, the bubble growth exhibits an erroneous growth rate. This effect on the bubble growth is visualized in Fig. 6.20b, where the

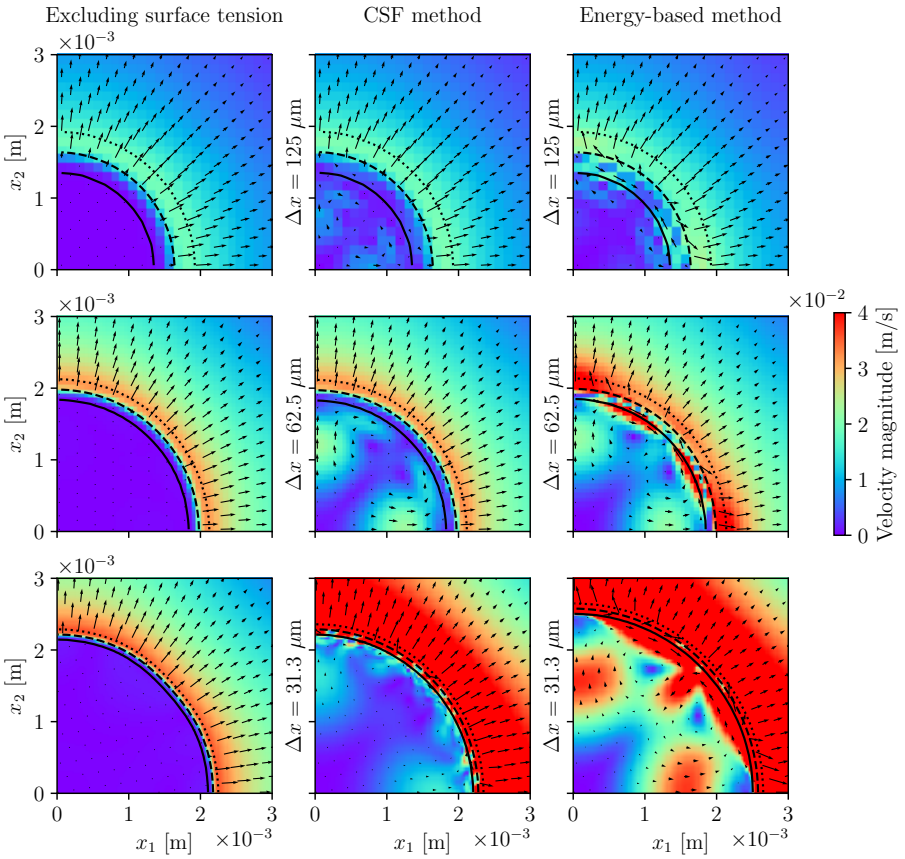

Figure 6.21: Spurious currents using different surface tension treatments and various grid sizes (top $\Delta x = 125$ μm, middle $\Delta x = 62.5$ μm, bottom $\Delta x = 31.3$ μm). The figure corresponds to $t = 29$ ms. Solid lines correspond to the iso-contour of $\phi = 0.9$, dashed lines to $\phi = 0.5$, and dotted lines to $\phi = 0.1$. Figure taken from Weber et al. (2026).

results obtained with the CSF model are compared to the analytical solution and to $\vec{f}_{ST} = \vec{0}$. The figure shows that the bubble growth accelerates as the spurious flow increases.

To further explore the behaviour of spurious currents, simulations are carried out using a range of settings. The standard CSF model (Eq. (2.7)) and the standard energy-based model (Eq. (2.10)) are compared to the zero surface tension simulation. For each setting, three simulations are conducted using the grids $\Delta x = 125$ μm, $\Delta x = 62.5$ μm, and $\Delta x = 31.5$ μm. Instantaneous results for a slice through the bubble at time $t = 29$ ms are visualized in Fig. 6.21. This figure illustrates the direction and magnitude of the flow, thereby highlighting the spurious flow structures. Generally, larger grid sizes appear to result in weaker spurious currents. The energy-based surface tension

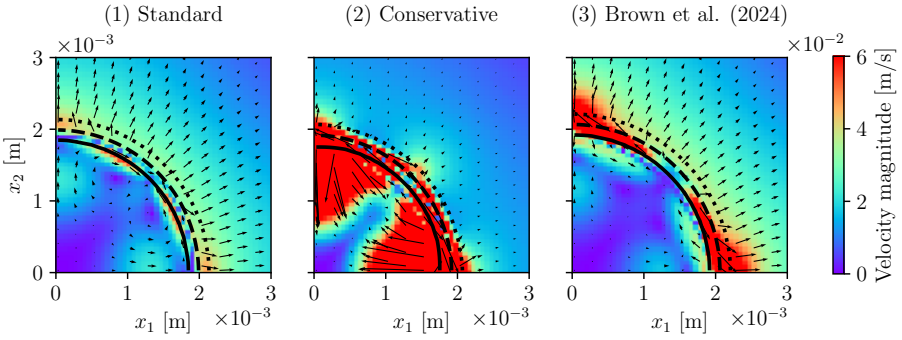

Figure 6.22: Comparison of spurious currents arising from different formulations of the energy-based surface tension model. The standard formulation (e.g. Badillo (2012)) on the left is compared to the alternative formulations from Huang et al. (2020) (middle) and Brown et al. (2024) (right). Figure corresponds to $t = 29$ ms and $\Delta x = 62.5$ μm. Solid lines correspond to the iso-contour of $\phi = 0.9$, dashed lines to $\phi = 0.5$, and dotted lines to $\phi = 0.1$. Figure taken from Weber et al. (2026).

model performs worse than the CSF model at all grid resolutions. However, both surface tension models result in an unacceptable level of spurious flow for smaller grid sizes.

Several alternative formulations have been proposed to improve the energy-based surface tension model (see Sec. 2.4.1). In the following, two alternative formulations are evaluated regarding their capability to reduce spurious flow in boiling flows. Specifically, the *conservative* (Huang et al. (2020)) and *level-set* (Brown et al. (2024)) formulations are compared to the standard energy-based formulation (See Fig. 6.22.) The visualized currents show that both considered alternative formulations result in increased spurious flow. The level-set formulation exhibits similar performance as the standard energy-based method, while the flow structures obtained from the conservative formulation are significantly worse. Energy-based models may demonstrate superior performance in the context of non-phase-change scenarios, however, they result in unacceptable levels of spurious currents for boiling simulations. Accordingly, energy-based models are not considered further in this thesis.

Next, the approach by Raeini et al. (2012) is assessed (refer to Sec. 2.4.1) regarding its performance in simulating boiling flows. Their *sharpened* CSF approach was initially applied to the VOF method. Therefore, the influence of the sharpening factor η on the phase field profile is studied first. Fig. 6.23 visualizes the sharpened phase field profiles ϕ' for two different values of η. Raeini et al. (2012) proposed using $\eta = 0.5$ for VOF. For the current application to ACDI, values of $\eta = 0.5$ and $\eta = 0.75$ are considered (Fig. 6.23). Depending on the location of $\phi = 0.5$ (cell centre, left - cell edge, right), the gradient of ϕ' differs from zero on 2-3 cell edges for $\eta = 0.75$, and 3-4 cell edges for $\eta = 0.5$. Consequently, the pressure gradient arising from the surface tension will be significantly higher in the interface region around $\phi = 0.5$.

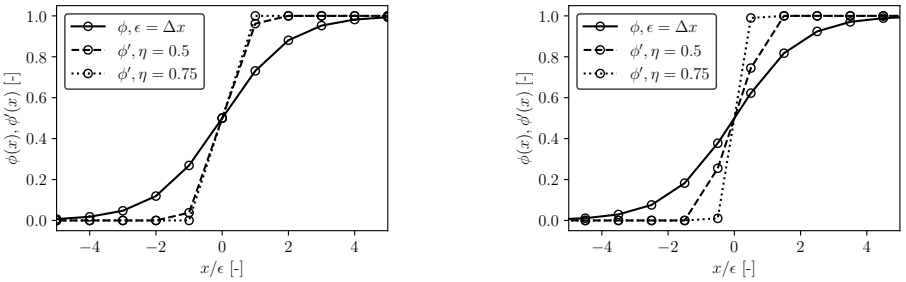

(a) Interface on cell centre

(b) Interface on cell edge

Figure 6.23: Sharpening effect of η on the hyperbolic tangent profile ($\epsilon^* = 1$) using Eq. (2.9). Value of $\eta = 0.5$ is compared to $\eta = 0.75$ for two locations of the interface centre, where $\phi = 0.5$ (cell centre, (a) cell edge, (b)). Figures taken from Weber et al. (2026).

Fig. 6.24 illustrates the impact of the sharpening factor on the spurious currents at two instantaneous snapshots, $t = 29$ ms and $t = 51.5$ ms. Evidently, the sharpened CSF model proposed by Raeini et al. (2012) is capable of significantly reducing spurious currents. Notably, as η increases, the spurious currents are substantially reduced throughout the simulation runtime. However, to ensure a stable simulation, numerical experiments suggest that η should not exceed a value of

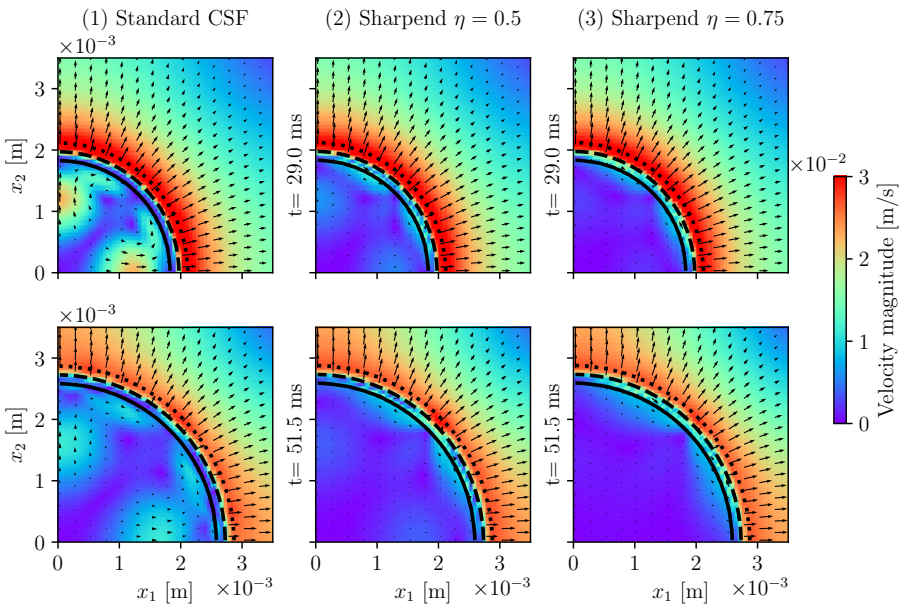

Figure 6.24: Influence of the sharpened CSF model by Raeini et al. (2012) on the formation of spurious currents. The currents are visualized at two times during the simulation, where a resolution of $\Delta x = 62.5$ μm is utilized.

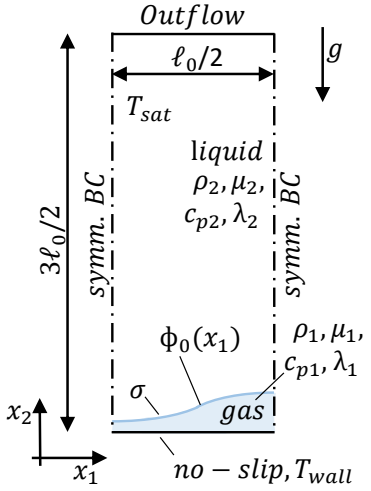

Figure 6.25: Visualization of computational setup for simulating film boiling in two dimensions. Figure taken from Weber et al. (2026).

0.75 (in case $\epsilon^* = 1$). Based on this evaluation, the sharpened CSF model is employed for all subsequent simulations.

6.7 2D film boiling

In this section, a film boiling benchmark simulation in two dimensions is conducted to test the flow solver against a flow configuration with increased complexity. The content of this chapter is published in Weber et al. (2026). In this benchmark simulation, a horizontal wall has a temperature T_{wall} that exceeds the saturation temperature T_{sat}. The liquid phase is separated from the wall by a gas layer, which is growing due to phase change (refer to Fig. 6.25). The gravitational acceleration causes the gaseous film to become unstable, which leads to the formation of a bubble. The bubble detaches from the liquid film and rises upwards.

The length scale ℓ_0 at which the instability in the gaseous film occurs is equal to the Taylor wavelength in two dimensions (see Klimenko (1981)). Therefore ℓ_0 is calculated from

$$\ell_0 = 2\pi \sqrt{\frac{3\sigma}{|\vec{g}|(\rho_2 - \rho_1)}}. \tag{6.16}$$

As such, the two-dimensional Taylor wavelength is 12π-times larger than the capillary length $l_c = \sqrt{\sigma|\vec{g}|^{-1}(\rho_2 - \rho_1)^{-1}}$. Due to the symmetry of the detaching bubbles, it is sufficient to consider a computational domain of size $\ell_0/2$ in the x_1 direction (compare with Fig. 6.25). Therefore, left and right boundaries are symmetry boundaries. In the x_2-direction, the computational domain is truncated to a length of $3\ell_0/2$. In line with the method by by Dhruv (2024), a wall boundary condition is applied at the bottom, with an outflow boundary at the top. The outflow boundary by Dhruv (2024) allows a small Weber number bubbles to leave the domain while keeping homogeneous Neumann and Dirichlet boundary conditions for velocity and pressure, respectively (refer to Sec. 4.6). Following the studies by Welch and Wilson (2000), Guo et al. (2011), Dongliang Sun and Chen (2014) and Wang et al. (2021), properties of Fluid$_C$ are chosen. For these fluid properties, the length scale ℓ_0 is calculated as $\ell_0 = 78.68$ mm. The utilized square grid cell are the following sizes $\Delta x = \ell_0/128$, $\Delta x = \ell_0/256$, and $\Delta x = \ell_0/512$.

The initial interface profile is set to trigger the first detachment of a bubble. For this purpose, the gaseous layer is initialized using a small hump, which follows a sine function. The location of $\phi = 0.5$ (centre of interface) is placed at the location of ϕ_0 defined by Dongliang Sun and Chen (2014) as

$$\phi_0 = \frac{\ell_0}{32} + \frac{\ell_0}{128} \cos\left(\frac{2\pi x_1}{\ell_0}\right), \tag{6.17}$$

The corresponding temperature at $t = 0$ is initialized with a linear profile (similar to the Stefan problem) in the gas phase. Accordingly, in the x_2-direction, the temperature decreases linearly from $T(x_2 = 0) = T_{\text{wall}} - T_{\text{sat}}$ to $T(x_2 = \phi_0) = 0$. Different from Dongliang Sun and Chen (2014), a wall superheat of $T_{\text{wall}} - T_{\text{sat}} = 1$ K is chosen. The reduction is chosen because phase field models appear unable to simulate bubble detachments at higher evaporation rates, as observed by Wang et al. (2021). To capture approximately six bubble detachments, all simulations are run until $t = 4$ s.

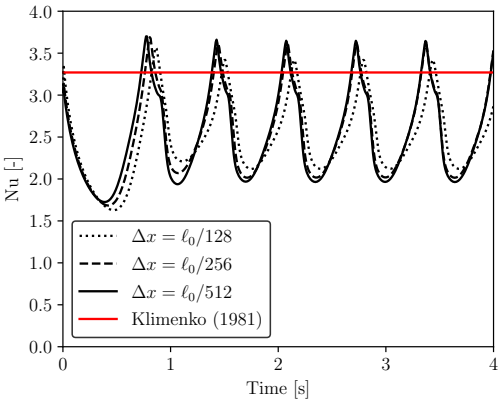

Figure 6.26: Nusselt number evolution for different grids in comparison to the correlation by Klimenko (1981). Figure taken from Weber et al. (2026).

Grid size Δx	$\ell_0/128$	$\ell_0/256$	$\ell_0/512$
$\overline{\mathrm{Nu}}$	2.538	2.583	2.562
$\overline{\mathrm{Nu}}/\mathrm{Nu}_K - 1$	-22.4%	-21.0%	-21.7%

Table 6.2: Time averaged values of Nu in comparison to Eq. (6.19). Table taken from Weber et al. (2026).

The Nusselt number Nu, which quantifies the ratio of the transferred heat including and excluding convection, is the quantity of interest for this benchmark. Dongliang Sun and Chen (2014) defined the instantaneous Nusselt number as

$$\mathrm{Nu} = \frac{l_c}{(T_{\text{wall}} - T_{\text{sat}})} \frac{\int_{\partial\Omega_{\text{wall}}} \frac{\partial T}{\partial x_2}\big|_{x_2=0} dx_1}{\int_{\partial\Omega_{\text{wall}}} dx_1}. \tag{6.18}$$

From Eq. (6.18), it can be seen that Nu is calculated from the average temperature gradient at the wall boundary Ω_{wall}, which is non-dimensionalized by the capillary length l_c and the wall superheat $T_{\text{wall}} - T_{\text{sat}}$. As reference data, the commonly used correlation by Klimenko (1981) is utilized. The Nusselt number of the correlation is denoted Nu_k and can be calculated from

$$\mathrm{Nu}_K = 0.19\mathrm{Gr}^{\frac{1}{3}}\mathrm{Pr}^{\frac{1}{3}}\chi, \text{with} \quad \mathrm{Gr} = \frac{l_c\|\vec{g}\|\rho_1^2}{\mu_1^2}\left(\frac{\rho_2}{\rho_1} - 1\right), \quad \chi = 0.89\gamma^{\frac{1}{3}}, \tag{6.19}$$

where the Prandtl number is $\mathrm{Pr} = c_{p,1}\mu_1\lambda_1^{-1}$ and $\gamma = c_{p,1}(T_{\text{wall}} - T_{\text{sat}})L_{\text{sat}}^{-1}$. This equation represents the simplified correlation for the chosen simulation settings. The evolution of Nu versus time in relation to the empirical value Nu_k is depicted in Fig. 6.26. The figure shows that the largest discrepancies between different grid resolutions occur during the startup phase. After the startup phase, the grid sizes $\Delta x = \ell_0/256$ and $\Delta x = \ell_0/512$ yield the same Nusselt numbers. The results obtained from $\Delta x = \ell_0/128$ exhibit smaller amplitudes compared to the finer grids, however, the bubble cycle frequency remains unchanged.

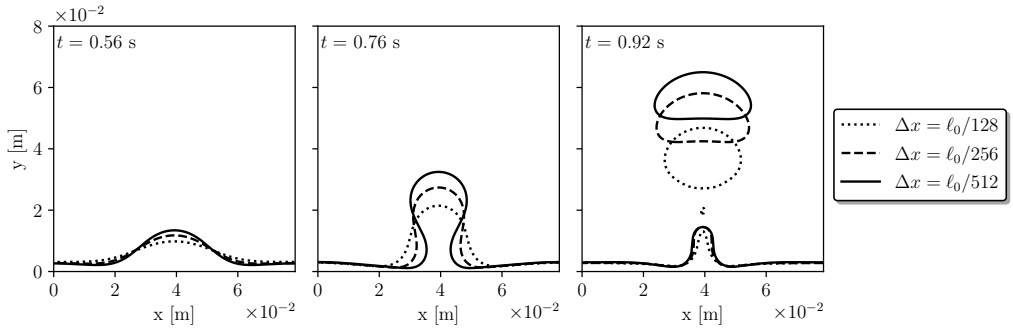

Figure 6.27: Visualization of the interface location during the startup phase using three grid resolutions. Lines represent the iso-contour of $\phi = 0.5$. Figure taken from Weber et al. (2026).

To compare the simulation results with Nu_K, a time-averaged value of Nu is calculated, denoted by an overbar ($\overline{\mathrm{Nu}}$). In Tab. 6.2, the absolute values of $\overline{\mathrm{Nu}}$ and their relative deviation from Nu_K are shown. For all grid sizes, the values for $\overline{\mathrm{Nu}}$ deviate from Nu_K by 21% or more.

Finally, the differences during the startup phase are visualized in Fig. 6.27. Here, the iso-contours of $\phi = 0.5$ are shown at three time steps for all grid sizes. Evidently, the departure of the initial bubble is delayed for coarser grid sizes. Moreover, the shape of the detached bubble (right panel) for $\Delta x = \ell_0/128$ is significantly different from that of the finer grids. The bubble shapes (right panel) of the two finer grids are the same, only differing by the delayed departure for that of $\Delta x = \ell_0/256$. However, Fig. 6.26 shows that the bubble departure times, for the two finer grids, synchronize during the remainder of the simulation.

6.8 Rising bubble subjected to phase change

This benchmark represents the final simulation for validating the flow solver against experimental data. The content of this section is published in Weber et al. (2026). In detail, experimental data from Florschuetz et al. (1969), who studied the growth of vapour bubbles in ethanol under the influence of gravity, are utilized. For this benchmark, the fluid properties of saturated ethanol at atmospheric pressure are used (see Tab. A.1). Furthermore, the experimental results corresponding to a liquid superheat of 3.1 K are chosen. The data from Florschuetz et al. (1969) have been used as a comparison against the numerical results of many studies, including Sato and Ničeno (2013), Badillo (2013), Rajkotwala et al. (2019), Bureš and Sato (2021), Giustini and Issa (2023), and Poblador-Ibanez et al. (2025).

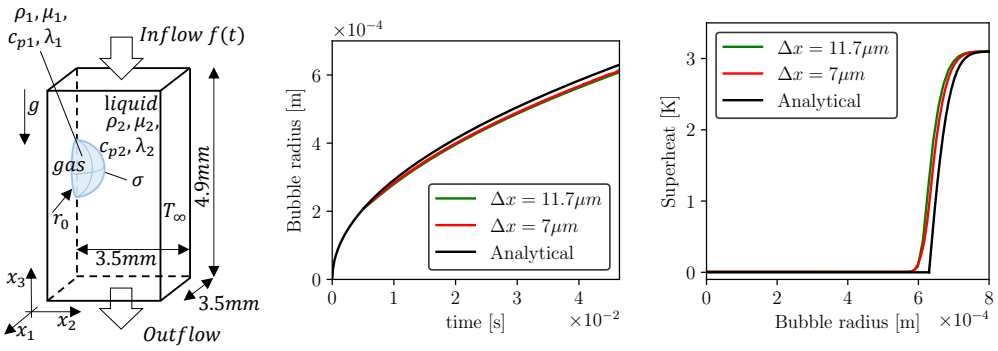

(a) Setup **(b)** Bubble size for $\vec{g} = \vec{0}$ **(c)** Temperatures for $\vec{g} = \vec{0}$

Figure 6.28: (a) Simulation setup. Results of zero-gravity study for grid sizes $\Delta x = 11.6\mu m$ and $\Delta x = 7\mu m$: (b) the bubble size evolution in comparison to Eq. (6.12) and (c) temperature distribution at $t = 46.6$ s in comparison to Eq. (6.14). All figures taken from Weber et al. (2026).

To reduce the computational costs when simulating bubble growth, the rotational symmetry of the flow is exploited. Accordingly, a fourth of the computational domain is simulated, as depicted in Fig. 6.28a. The size of the domain in the x_3-direction is further reduced by selecting a moving coordinate system (as in Rajkotwala et al. (2019) and Giustini and Issa (2023)). As such, the computational domain follows the upward rising bubble. Accordingly, an inflow and outflow boundary condition is applied at the top and bottom, respectively. The inflow velocity is dynamically adjusted to ensure the bubble stays inside the computational domain. Symmetry boundaries are applied to the domain faces that intersect with the bubble. The free-slip condition is implemented at all remaining boundaries. Two grid resolutions are employed, using cubic cells of size $\Delta x = 11.7$ µm and $\Delta x = 7$ µm. At the start of the simulation, a bubble of size $r_0 = 210$ µm is initialized (see Fig. 6.28a). For the initial temperature distribution, the zero-gravity solution by Scriven (1959) is utilized (Eq. (6.14)). For the present parameter settings, a growth constant of $\beta \approx 5.4969$ is determined (physical time at startup is therefore $t_0 = 5.17$ ms). The use of the zero-gravity solution for the initialization is justified by assuming that the effect of gravity is negligible for small bubbles.

At first, gravity is neglected ($\vec{g} = \vec{0}$) to compare the bubble growth with the analytical solution by Scriven (1959). This test provides an opportunity to assess the grid resolution in terms of its capability to resolve the thermal boundary layer around the bubble. The evolution of the bubble size versus time, and the temperature field distribution at $t = 46.6$ s, are shown in Fig. 6.28b and Fig. 6.28c, respectively. It is observed that both grids yield similar results for this test. The growth rate is slightly lower than that of the analytical solution, and minor improvements are achieved by

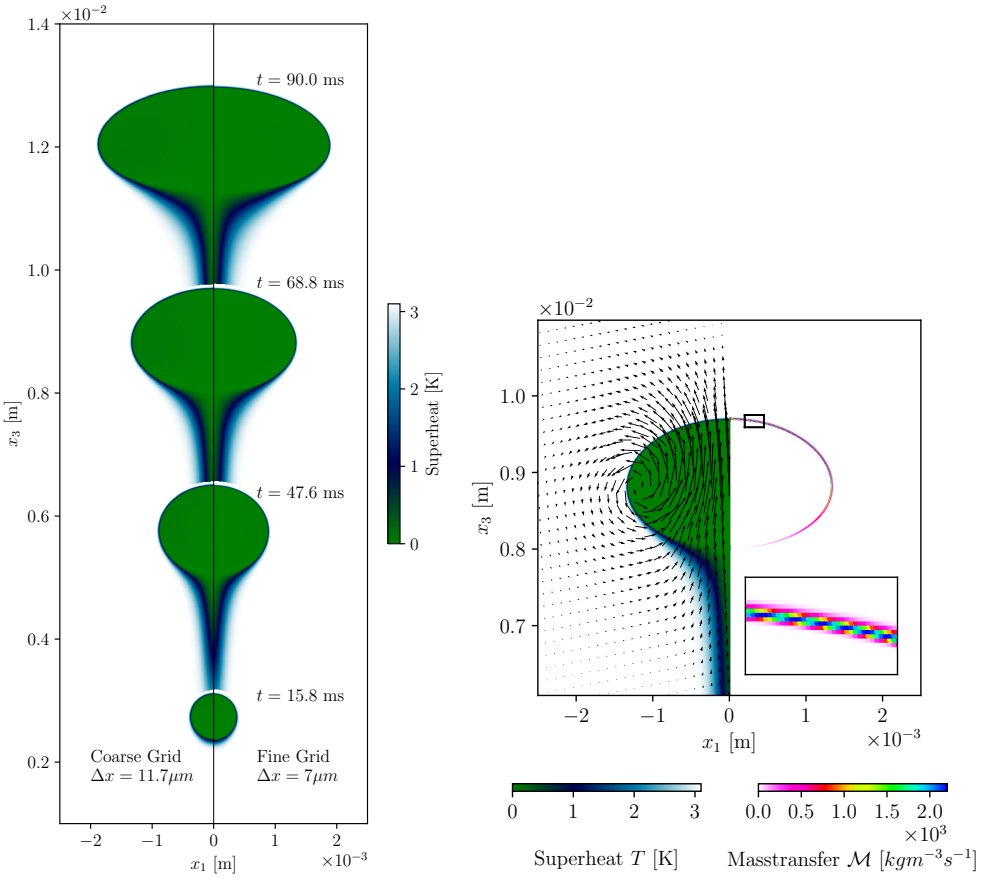

(a) Four temperature fields for both resolutions

(b) Closeup at $t = 68.8ms$ using $\Delta x = 7$ µm

Figure 6.29: Visualization of the simulation results to investigate the growth of bubbles under the influence of gravity. Both figures taken from Weber et al. (2026).

using a fine grid. Overall, the agreement with the solution by Scriven (1959) is satisfactory for both bubble size and temperature. Thus, in the next step, the effect of gravity is considered.

For the following simulations, gravity is set to $\vec{g} = (0, \quad 0, \quad -9.81)$ ms^{-2}, and the simulations are run until $t = 90$ ms. Fig. 6.29a shows the temperature field at four times during the simulation on a plane slicing through the bubble centre. Note that all of the results are transformed back from the moving coordinate system into the laboratory coordinate system. Accordingly, Fig. 6.29a shows the upward-moving bubble, which can be identified by the green area, indicating the saturation temperature. White areas represent areas where $T = 3.1$ K. All of the bubbles exhibit a thin thermal boundary layer at the top and a tail of cooled liquid in their wake. The results

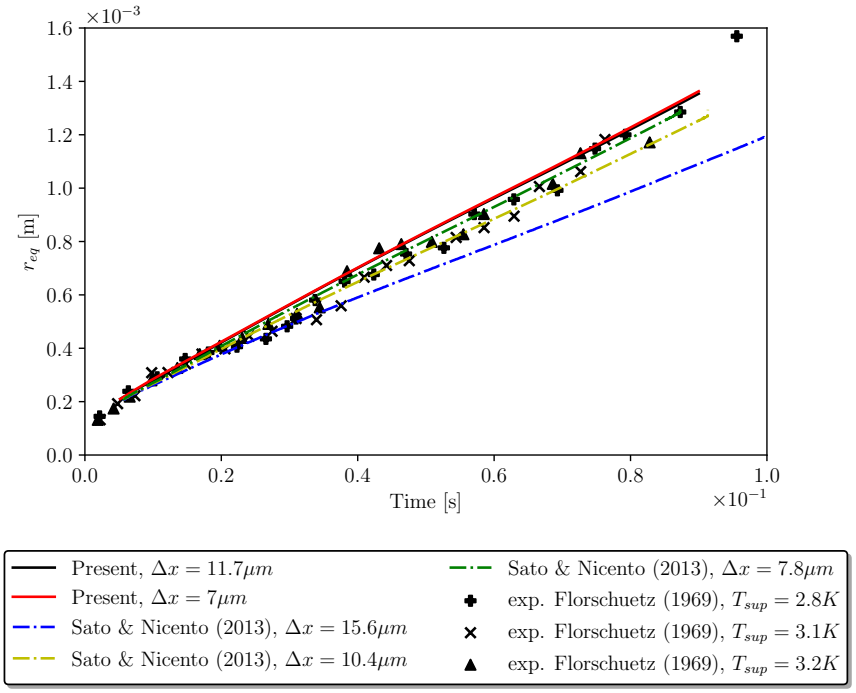

Figure 6.30: Bubble size evolution in the presence of gravity. Comparison of the obtained simulation results to the experimental data from Florschuetz et al. (1969) and the simulation results by Sato and Ničeno (2013). Figure taken from Weber et al. (2026).

obtained when using the coarse and fine grids are presented on the right and left of Fig. 6.29a, respectively. The figure demonstrates that both grids return similar bubble locations, bubble shapes, and temperature distributions. However, the cooling of the liquid wake behind the bubble is slightly less pronounced in the fine grid compared to the coarse grid.

Fig. 6.29b shows a closeup of the bubble at time $t = 68.8$ ms. On the left side, the velocity field (arrows) is shown together with the temperature field. The right side of Fig. 6.29b displays the quantitative distribution of the mass transfer rate $\mathcal{M}$. In addition, the lower right corner of Fig. 6.29b provides a magnified view of the mass transfer rate at the top of the bubble. The figure shows that the mass transfer is concentrated to the top of the bubble, with almost no mass transfer taking place at the bottom of the bubble (due to the cooled liquid wake, see the left half of Fig. 6.29b).

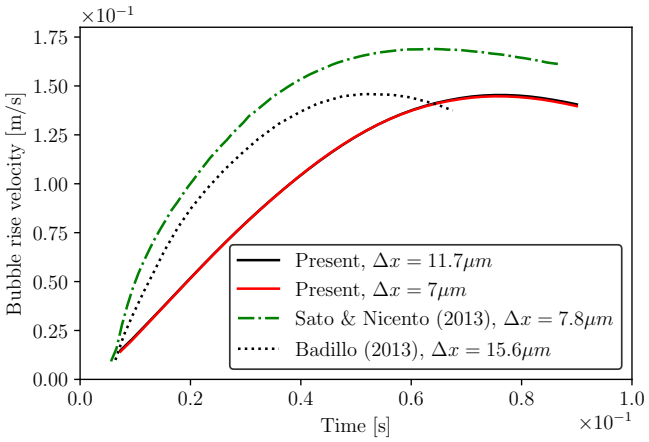

Figure 6.31: Comparison of the rise velocities. The present simulation results are compared to those of Badillo (2013) and Sato and Ničeno (2013). Figure taken from Weber et al. (2026).

To compare the results to data from the literature, an equivalent radius r_{eq} is utilized, as proposed by Florschuetz et al. (1969). The equivalent radius is calculated from

$$r_{eq} = \frac{1}{4}(D_{12} + D_3). \tag{6.20}$$

The bubble diameter in the x_1-x_2 plane is denoted D_{12}, while the bubble expansion in the x_3-direction is D_3. The present simulation results for r_{eq}, with both grid sizes, are visualized in Fig. 6.30. Here, the results are compared to the experimental data by Florschuetz et al. (1969) and the numerical results by Sato and Ničeno (2013). The experimental data show the evolution of bubble size at superheats of $T_\infty - T_{\text{sat}} = 2.8$ K, 3.1 K, and 3.2 K. In general, the present simulation results lie within the scattered experimental data, although more experimental data points are scattered below the simulation data. The present simulation results also show good agreement with those obtained using the finest grid spacing in Sato and Ničeno (2013).

In the next step, the bubble rise velocity is analyzed. In the literature, the rise velocity is reported in the studies by Badillo (2013) and Sato and Ničeno (2013). The results from the simulations in these studies are compared to those of the present simulation in Fig. 6.31. This figure reveals significant differences in the results published in the literature compared to those of the present simulation. While the magnitude of the peak rise velocity in the present simulation agrees with that published in Badillo (2013), the timing of the peak differs. Sato and Ničeno (2013) and Badillo (2012) predict a faster acceleration during the startup phase. This difference could be attributed to a wide range of computational settings reported in the literature. For example, Giustini and Issa (2023) use different boundary conditions than Sato and Ničeno (2013), and

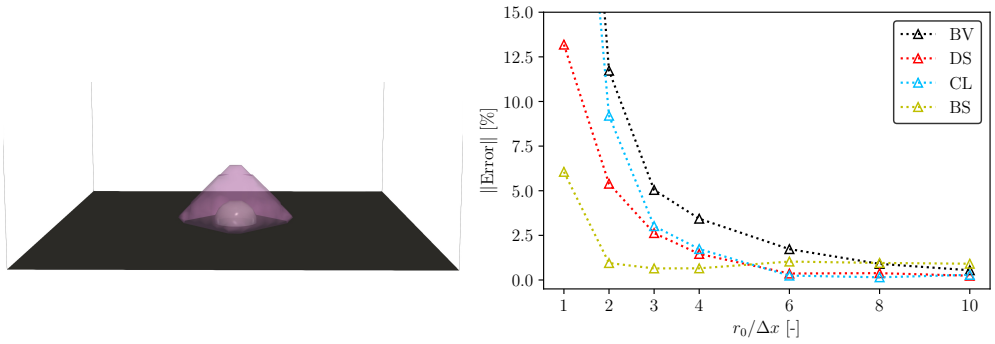

(a) Tagged grid cells (pink) around a bubble of $r_0 = 2\Delta x$

(b) Geometry errors for different bubble resolutions

Figure 6.32: Test simulation evaluating the bubble geometry calculation method, Eqs. (4.80)-(4.83). (a) Simulation setup and visualization of tagged grid cells. (b) Error evaluation by comparing to Eq. (6.22). Cropped error magnitudes for BV and CL at $r_0 = \Delta x$ are 44.5% and 37.3 %, respectively.

Badillo (2013) employs a different domain size. However, more comparison data is needed to investigate the impact of the computational settings. Unfortunately, the rise velocity is not reported by Florschuetz et al. (1969).

The present simulation yields grid-independent results at a grid size of $\Delta x = 11.6$ µm. This is comparable to the grid sizes used in the sharp-interface studies by Sato and Ničeno (2013), Bureš and Sato (2021) and Poblador-Ibanez et al. (2025). In Giustini and Issa (2023), a grid size of $\Delta x = 3.12$ µm is employed, which was not required in the present simulations.

6.9 Bubble Tagging Accuracy

The purpose of this section is to evaluate the accuracy of the bubble geometry calculation. Namely, the accuracy of the bubble volume BV, bubble surface BS, contact line length CL, and dryspot area DS calculations are evaluated (Eq. (4.80), Eq. (4.81), Eq. (4.82), and Eq. (4.83), respectively). In particular, the accuracy of the geometry calculation for bubbles of lower resolution is of interest. That is, for bubbles with radius to grid spacing ratios $r/\Delta x$ in the range of one to ten.

The test setup is straightforward. At $t = 0$, a hemisphere-shaped bubble of radius r_0 is placed on a wall ($\Theta = 90°$). The initial phase field distribution is prescribed as

$$\phi(t=0) = \frac{1}{2}\left[1 + \tanh\left(\frac{r_0 - |\vec{x} - \vec{x}_b|}{2\epsilon}\right)\right], \tag{6.21}$$

where $\vec{x}_b$ is the location of the bubble centre. The grid spacing is $\Delta x = 15.6$ µm, gravity is neglected $\vec{g} = \vec{0}$, and the properties of saturated water at 1.05 MPa are chosen[4]. The simulations are run until the phase field is invariant in time, then the tagging method is applied (Sec. 4.8). Fig. 6.32a visualizes the result of this procedure. The theoretical "sharp" bubble geometry, $\mathrm{BV_{th}}$, $\mathrm{BS_{th}}$, $\mathrm{CL_{th}}$, and $\mathrm{DS_{th}}$, is

$$\mathrm{BV_{th}} = \frac{2\pi}{3} r_0^3, \quad \mathrm{BS_{th}} = 2\pi r_0^2, \quad \mathrm{CL_{th}} = 2\pi r_0, \quad \text{and} \quad \mathrm{DS_{th}} = \pi r_0^2. \tag{6.22}$$

Next, Eq. (6.22) is used as reference data and compared to the results obtained from Eqs. (4.80)-(4.83). This test is carried out for bubbles of the following sizes: $r_0 = \Delta x$, $2\Delta x$, $3\Delta x$, $4\Delta x$, $6\Delta x$, $8\Delta x$, and $10\Delta x$. The deviations of the calculated bubble geometry from the theoretical values are visualized in Fig. 6.32b. For larger bubbles, the error of the calculated geometry is less than 1%. In contrast, for $r_0 = \Delta x$, large errors are observed, exceeding 40% for the bubble volume BV. These deviations drastically reduce with the increasing bubble sizes $r_0 = 2\Delta x$ and $r_0 = 3\Delta x$. Therefore, depending on the desired accuracy, the tagging algorithm can be expected to produce acceptable results from a bubble of size $r_0 = 3\Delta x$.

6.10 Statistical evaluation of synthetic bubble data

Thus far, a comprehensive benchmarking campaign has been conducted to verify the flow solver developments presented in Ch. 4. The remainder of Ch. 6, focuses on testing the statistical evaluation methodology from Ch. 5. The content of this section is published in Weber et al. (2023).

This section aims to demonstrate the application of the K-Means clustering of bubble cells obtained from a Voronoi diagram. This assessment uses synthetic bubble data to be able to quantify the errors by comparing to analytical solutions. The analysis is conducted in two dimensions, however, the extension to three dimensions is straightforward. Furthermore, the accuracy in terms of systematic and statistical errors is assessed. As a result, a better understanding of the statistical evaluation methodology is obtained.

[4] Note that this test is insensitive to the grid spacing and fluid parameters as long as $\sigma \neq 0$. However, the fluid properties might influence the time required to reach a steady phase field distribution.

6.10.1 Generation of synthetic bubble data

A cubic domain of size ℓ in which bubbles are distributed is considered. The bubble data is generated by adding randomness to (i) the bubble location and (ii) the bubble size. All results are non-dimensionalized using ℓ.

First, a number of bubbles N_b are randomly distributed by prescribing a preferential concentration. Globally, the bubble concentration is N_b/ℓ^3. However, locally, the expectation of the bubble concentration $\mathbb{E}(\Lambda)$ is prescribed as

$$\ell^3\mathbb{E}(\Lambda) = N_b f_1(x_1) f_2(x_2), \tag{6.23}$$

$$\text{where} \quad f_1(x_1) = \left[\frac{6.0162}{\sqrt{2\pi}}\exp\left(-\frac{9}{2}\left(\frac{2x_1}{\ell}-1\right)^2\right)\right] \tag{6.24}$$

$$\text{and} \quad f_2(x_2) = \left[\frac{192}{71}\frac{x_2}{\ell} - \frac{100}{71}\left(\frac{x_2}{\ell}\right)^3\right]. \tag{6.25}$$

A random bubble distribution arising from Eq. (6.23) is obtained by using the inverse transform sampling method, as in Devroye (1986). This function requires the antiderivatives of the PDF f_1 and f_2 so that

$$\frac{dF_1(x_1)}{dx_1} = f_1(x_1), \quad \frac{dF_2(x_2)}{dx_2} = f_2(x_2), \quad F_1(0) = F_2(0) = 0, \quad \text{and} \quad F_1(1) = F_2(1) = 1. \tag{6.26}$$

The inverse of F_1 and F_2 are denoted F_1^{-1} and F_2^{-1}. As such, following Eq. (6.23), a random bubble location $\vec{x}_b$ is obtained from

$$\vec{x}_b = \begin{pmatrix} F_1^{-1}(X_{b,1}) \\ F_2^{-1}(X_{b,2}) \end{pmatrix}, \tag{6.27}$$

where $X_{b,1}$ and $X_{b,2}$ are independent random samples drawn from uniform continuous distribution in the interval $[0, 1]$ (Weber et al. (2023)).

The bubbles each have a randomized bubble radius r, with the expectation $\mathbb{E}(r)$ and the standard deviation $s(r)$. These are prescribed as

$$\frac{\mathbb{E}(r)}{\ell} = 0.006 + 0.002\left(\frac{x_2}{H} - 1\right), \tag{6.28}$$

$$\text{and} \quad \frac{s(r)}{\ell} = 0.00095\sqrt{\left(\frac{x_1}{H} - \frac{1}{2}\right)^2 + \left(\frac{x_2}{H} - 1\right)^2}. \tag{6.29}$$

Note that both $\mathbb{E}(r)$ and $s(r)$ have spatial variations. The bubble radius r_b is chosen by randomly sampling from a shifted Maxwell distribution $f(r)$ (e.g., refer to Sadovskii (2019)). The probability distribution reads

$$f(r) = \sqrt{\frac{2}{\pi}}\frac{(r - C_1)^2}{C_2^3} e^{-\frac{(r-C_1)^2}{2C_2^2}}, \quad r \in [C_1, \infty), \tag{6.30}$$

where

$$C_1 = \mathbb{E}(r) - 2C_2\sqrt{\frac{2}{\pi}} \quad \text{and} \quad C_2 = s(r)\sqrt{\frac{\pi}{3\pi - 8}}, \quad C_1 > 0. \tag{6.31}$$

As a result, the expectation of the bubble volume $\mathbb{E}(BV)$ is calculated from

$$\mathbb{E}(BV) = \int_{C_1}^{\infty} \frac{4\pi r^3}{3} f(r) dr = \frac{4\sqrt{\pi}}{3C_2}\left(2^{\frac{7}{2}}C_2^4 + 9\sqrt{\pi}C_1C_2^3 + 3{\cdot}2^{\frac{3}{2}}C_1^2C_2^2 + \sqrt{\pi}C_1^3C_2\right). \tag{6.32}$$

The local expectation of the gas content $\mathbb{E}(\alpha)$ is then

$$\mathbb{E}(\alpha) = \mathbb{E}(\Lambda)\mathbb{E}(BV). \tag{6.33}$$

The spatial distributions of $\mathbb{E}(\Lambda)$, $\mathbb{E}(r)$, $s(r)$, and $\mathbb{E}(\alpha)$ are visualized in Figs. 6.33a-6.33d. Note that the presented distributions are all arbitrarily selected. However, the distributions aim to imitate features that could be found in a realistic bubbly flow. For instance, the bubble concentration Fig. 6.33a could mimic the local entrainment of bubbles on a free surface due to a water jet. Accordingly, $\mathbb{E}(r)$ and $s(r)$ could be interpreted as the spatial variation of the bubble size due the coalescence and breakup.

6.10.2 Clustering of Voronoi cells

For the present test, 150 random bubble datasets, each containing $N_b = 1024$ bubbles, are generated using the methodology described in Sec. 6.10.1. The target cluster size for the grouped

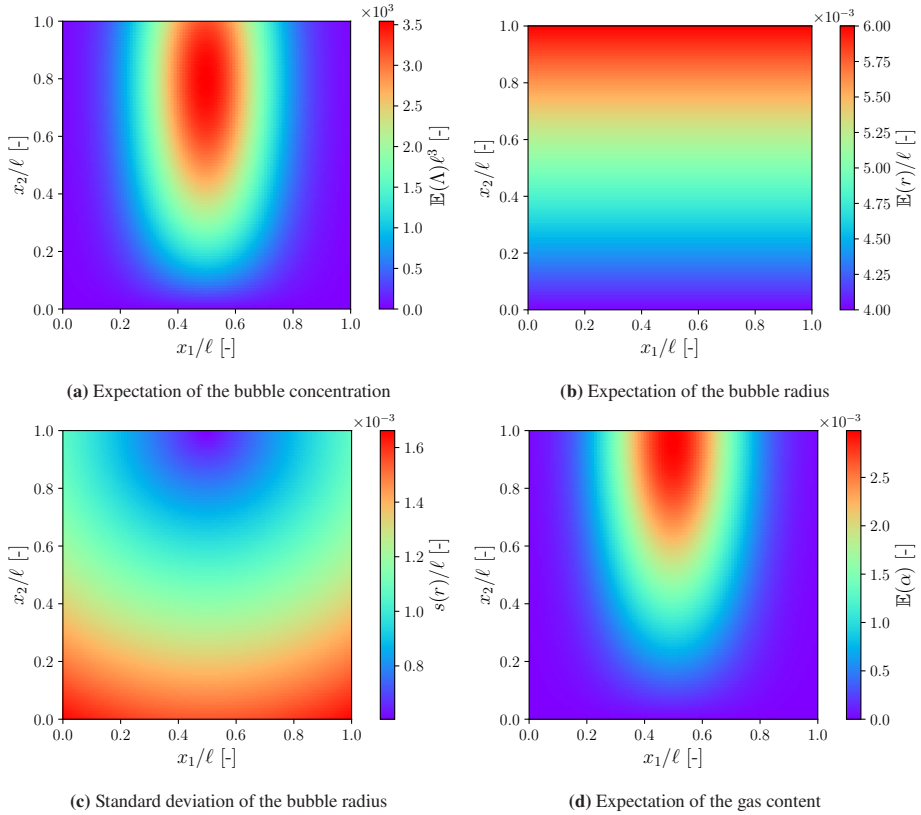

(a) Expectation of the bubble concentration

(b) Expectation of the bubble radius

(c) Standard deviation of the bubble radius

(d) Expectation of the gas content

Figure 6.33: Fictive distributions of bubble characteristics as reference data. Figures adopted from Weber et al. (2023).

Voronoi analysis is $N_{trg} = 8$. As a result, 150×8 bubbles are available at each point in space, for the subsequent analysis.

The stages of the clustered Voronoi analysis are visualized in Fig. 6.34. Here, the analysis is conducted for the gas content. However, the presented analysis could be applied to any quantity related to the bubbles. Fig. 6.34a shows the instantaneous gas content $\hat{\alpha}$ in each cell after applying the Voronoi diagram. The cluster-averaged gas content $\hat{\bar{\alpha}}$ after grouping eight bubbles together is shown in Fig. 6.34b. Averaging the results over all datasets results in the distribution depicted in Fig. 6.34c. At each point in space, a statistical evaluation of the bubble characteristics (here: gas content $\hat{\alpha}$) can be conducted, as shown in Fig. 6.34d.

Following this procedure, the average gas content, the average bubble radius, and the standard deviation of the bubble radius are calculated and compared to the analytical distributions $\mathbb{E}(r)$, $s(r)$, and $\mathbb{E}(\alpha)$. The resulting deviations are shown in Fig. 6.35. The deviation from $\mathbb{E}(r)$ does

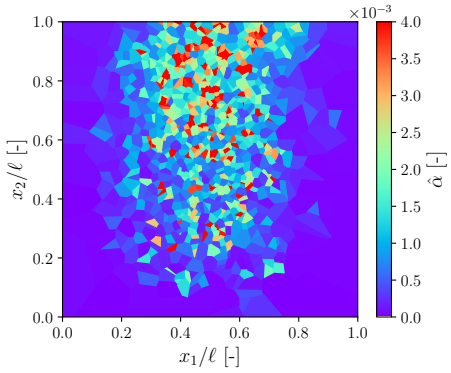

(a) Voronoi cells coloured by their gas content.

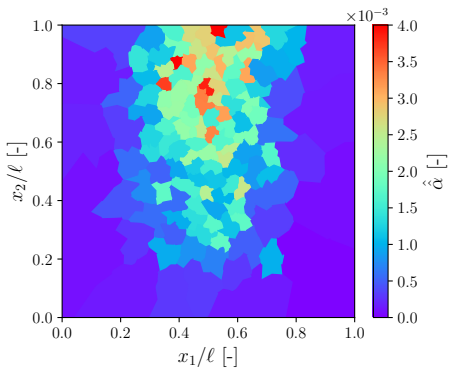

(b) Averaged gas content within clusters.

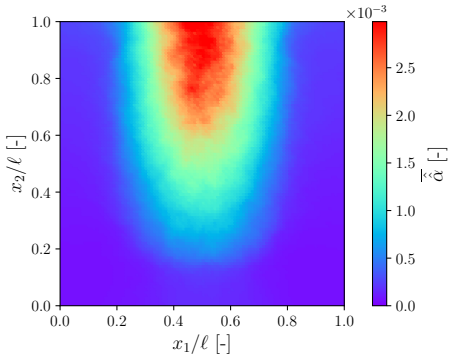

(c) Data averaged over all data sets.

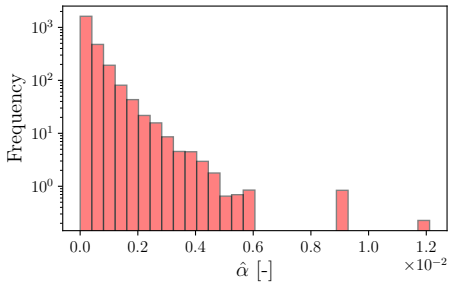

(d) Statical distribution of local gas content at $x_1/\ell = x_2/\ell = 0.3$

Figure 6.34: Results of applying the clustered Voronoi methodology to synthetic snapshot data. Visualization of different stages during the analysis. Figures adopted from Weber et al. (2023).

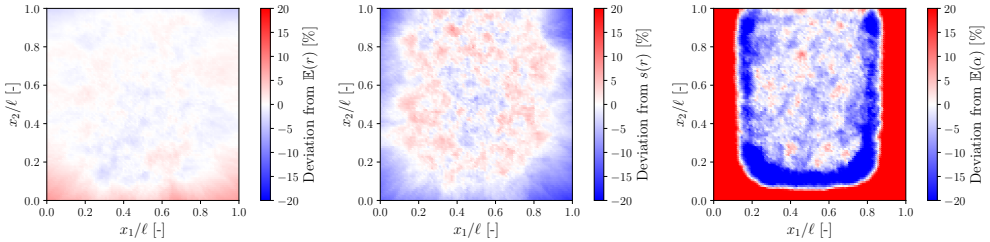

(a) **(b)** **(c)**

Figure 6.35: Deviation of the calculated values for (a) averaged bubble radius, (b) bubble radius standard deviation, and (c) average gas content from $\mathbb{E}(r)$, $s(r)$, and $\mathbb{E}(\alpha)$. Figure taken from Weber et al. (2026).

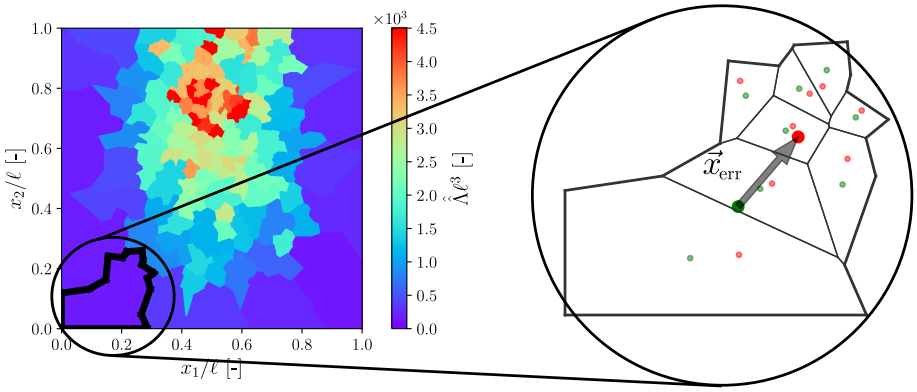

Figure 6.36: Visualization of a cluster-averaged bubble concentration $\hat{\hat{\Lambda}}$ (left). The right side of the figure visualizes a closeup of the lower left cluster. Voronoi cell centroids (small green dots) and bubble centres (small red dots) are visualized. The cluster centroid and average location of the bubbles are marked with a big green and red dot, respectively. The distance between the two is denoted $\vec{x}_{\mathrm{err}}$ (grey arrow). Figure adopted from Weber et al. (2023).

not exceed 5%. Moreover, the analytic standard deviation $s(r)$ shows satisfactory results, not exceeding error magnitudes of 10 %. Only the calculated average gas content appears to exhibit substantial error towards the regions of lower bubble contents (see Fig. 6.33a). In the following, this error in the average gas content calculation (Fig. 6.35c) is analyzed by distinguishing between systematic and statistical errors.

6.10.3 Systematic errors

Based on Fig. 6.35c, it is evident that the calculation of the gas content towards areas of low bubble concentration should be investigated. To examine this, an example cluster is depicted in the lower left corner of Fig. 6.36. Here, the grey arrow visualizes the difference between two definitions of the cluster centre, namely: (i) the centroid of the cluster (big green dot), and (ii) the average location of all bubbles within a cluster (big red dot). The difference between these two locations is denoted $\vec{x}_{\mathrm{err}}$. Evidently, the centre of the *actual* information (i.e., the bubbles) coincides with the big red dot. However, the *apparent* location of information coincides with the cluster centroid, as all points within the cluster are assigned the bubble information. For bubble distributions without a preferential concentration, this mismatch would average to zero after processing many datasets. However, for bubble distributions that feature a concentration gradient, an average error vector $\overline{\vec{x}_{\mathrm{err}}}$ remains, even after processing many datasets. This vector constitutes the first source of the systematic error.

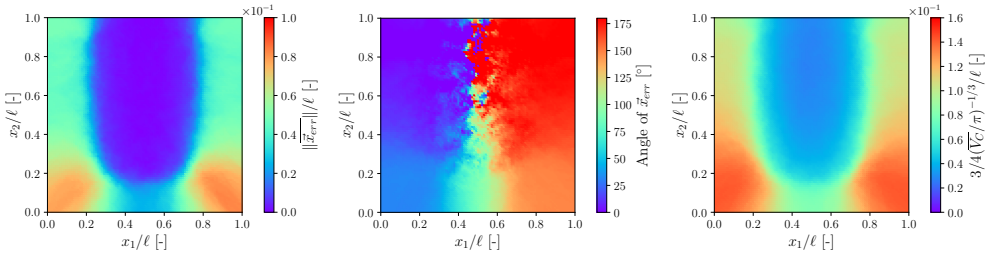

Figure 6.37: Quantification of averaged error vector $\overline{\vec{x}_{\text{err}}}$. Magnitude (a) and direction (b) of the vector are depicted. (c) Equivalent cluster radius $3/4(\overline{V_C}/\pi)^{-1/3}$ shows the clear scaling of the error vector magnitude with the cluster size. Figures adapted from Weber et al. (2023).

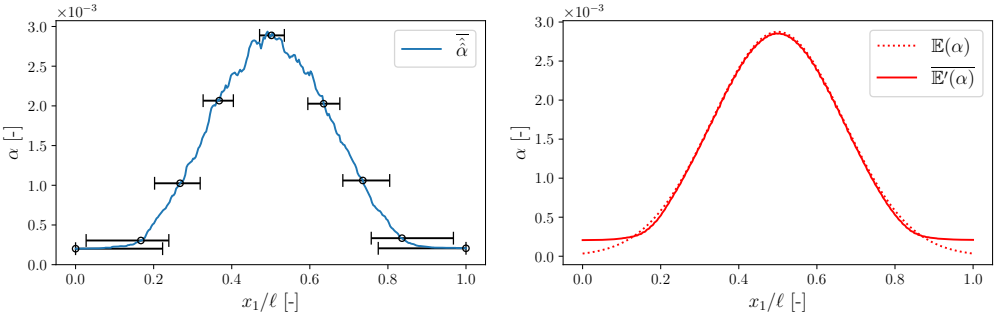

(a) Spatial uncertainty

(b) Difference between $\mathbb{E}(\alpha)$ and $\overline{\mathbb{E}'(\alpha)}$

Figure 6.38: Spatial uncertainties and spatially averaged expectations at $x_2/\ell = 0.85$. Figures adopted from Weber et al. (2023).

The averaged error vector $\overline{\vec{x}_{\text{err}}}$ is quantified in Fig. 6.37. This analysis indicates that the magnitude of $\overline{\vec{x}_{\text{err}}}$ correlates with the cluster size (i.e. correlates with the inverse of the bubble concentration Λ). Furthermore, Fig. 6.37 also depicts the direction of the error vector. Comparing this result with Fig. 6.33a, it can be observed that the direction is correlated with the bubble concentration gradient $\nabla\Lambda$.

Another systematic error arises from the spatial size of the clusters, even if $\vec{x}_{\text{err}} = \vec{0}$. Due to the spatial size of the clusters, or the Voronoi cells themselves, the calculated statistics are always spatially averaged quantities. This fact can be understood as a spatial uncertainty, which is depicted in Fig. 6.38a, where the average gas content $\overline{\hat{\alpha}}$ is shown. The figure corresponds to the data at $x_2/\ell = 0.85$. The average spatial size is depicted by the error bars, at nine locations. In areas of low bubble concentration, the uncertainty is high compared to areas with a high bubble concentration. Also, the equivalent cluster size in Fig. 6.37c represents a measure for the uncertainty.

Furthermore, due to the spatial size of the clusters, the local value of $\mathbb{E}(\alpha)$ cannot be consistently evaluated. Instead, the cluster-averaged gas content returns an approximation for a spatially average expectation $\mathbb{E}'(\alpha)$. For the i-th cluster, the averaged expectation $\mathbb{E}'(\alpha)_i$ is calculated from

$$\mathbb{E}'(\alpha)_i = \frac{1}{V_{C,i}} \int_{\Omega_{C,i}} \mathbb{E}(\alpha) dV \tag{6.34}$$

In Fig. 6.38b, the averaged expectation $\overline{\mathbb{E}'(\alpha)}$ is compared to $\mathbb{E}(\alpha)$, on a line where $x_2/\ell = 0.85$. The differences between $\mathbb{E}(\alpha)$ and $\overline{\mathbb{E}'(\alpha)}$ are insignificant around $x_1/\ell = 0.5$. However, large discrepancies are observed towards the domain boundaries. This means that, in these areas, the cluster size is too large to resolve the gradients of $\mathbb{E}(\alpha)$. This observation is consistent with the errors found in Fig. 6.35. A solution could be to decrease N_{trg}, which would directly decrease the sample size and, thus, increase the statistical error. The statistical error is the content of the following subsection.

6.10.4 Statistical errors

Using the methodology from Ch. 5, the synthetic datasets generated in Sec. 6.10.1 can be processed by assigning the same number of bubbles to each point in the domain. In this case, $N = S \times N_{trg} = 150 \times 8$ bubbles are assigned to each point. For a given point, the observations (here: gas contents) are $\alpha_1, \alpha_2, ..., \alpha_N$. The mean value (see. Eq. (5.8)) of those observations is $\overline{\hat{\alpha}}$, which estimates $\overline{\mathbb{E}'(\alpha)}$. However, $\overline{\mathbb{E}'(\alpha)}$ is unknown for realistic applications. Therefore, the error $|\overline{\hat{\alpha}} - \overline{\mathbb{E}'(\alpha)}|$ has to be estimated to quantify the statistical uncertainty. Rukhin (2007) and Rukhin (2009) derived confidence intervals for weighted sums, which are required for the current application (see weights w in Eq. 5.6). Their confidence intervals are calculated from

$$\overline{\hat{\alpha}} \pm \frac{\mathrm{t}_{C/2\,,\,(N-1)} \sqrt{\sum_{i=1}^{N} w_i'(\alpha_i - \overline{\hat{\alpha}})^2}}{\sqrt{(N-1)\left(N^N \prod_{i=1}^{N} w_i'\right)^{1/(N-1)}}}. \tag{6.35}$$

Eq. (6.35) estimates that $\overline{\mathbb{E}'(\alpha)}$ lies within the interval with a probability of $100\% - C\%$. In this equation, $\mathrm{t}_{C/2\,,\,(N-1)}$ represents a t-value corresponding to a student-t distribution with $N-1$ degrees of freedom. The confidence intervals calculated from Eq. (6.35) are shown in Fig. 6.39. The figure demonstrates how the 99% confidence interval fully covers the averaged expectation $\overline{\mathbb{E}'(\alpha)}$.

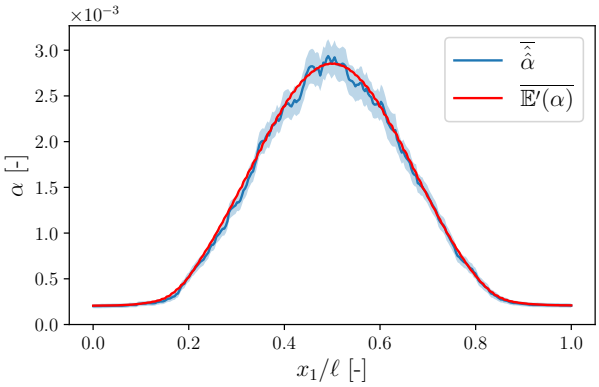

Figure 6.39: Confidence intervals (light blue) of 99%, calculated from the interval proposed in Rukhin (2007). Distribution of $\overline{\mathbb{E}'(\alpha)}$ (red line) and $\overline{\hat{\alpha}}$ (dark blue line) are presented. Figure adopted from Weber et al. (2023).

6.10.5 Discussion

In this section, the grouped Voronoi analysis is tested with randomly generated bubble data. Overall, the results obtained in this section present valuable insights that serve as a best practice guideline. Specifically, inherent uncertainties when defining a local bubble statistic are discussed. For example, it is shown that decreasing the statistical error (larger cluster) increases the spatial uncertainty (and vice versa). In the next step (Ch. 7), this methodology is applied to bubble data obtained from a large-scale boiling flow simulation. For the evaluation of interface-resolved simulations, this bubble data is obtained from the tagging methodology presented in Sec. 4.8 and Sec. 6.9.

7 Boiling Flow Simulation

The preceding chapters presented methodological developments (Ch. 4 and Ch. 5) and a comprehensive testing campaign (Ch. 6). In accordance with the objectives of this thesis (Sec. 1.3), the final step is to simulate a technically relevant boiling flow scenario.

Specifically, the simulation of a turbulent forced convection flow, in the nucleate boiling flow regime (see Fig. 1.3), is conducted. The literature regarding this flow configuration is limited. Nucleate boiling simulations in micro-channels of high-performance electronics have attracted significant attention in recent years, as summarized by Darshan et al. (2024). However, the length-scales in such flows do not allow for turbulence to develop ($Re \leq 200$). Furthermore, many studies consider single nucleation sites, as in Sato et al. (2013), or the PhD thesis of Bhuvankar (2019). In contrast, realistic boiling flows (see Fig. 1.1) feature an abundance of nucleation sites. Notably, in Kaiser et al. (2024), and Sato et al. (2025), full-scale nucleate boiling flows at higher Reynolds numbers are simulated. To the best of the authors' knowledge, no literature has been published on this flow configuration using a phase field method, to date.

For this simulation of a technically relevant boiling flow, the properties of water are considered. At atmospheric pressure, saturated water commonly forms a micro-layer (see Kossolapov (2021) and Wang et al. (2023)). The micro-layer is a thin liquid film between the bubble and the solid wall. Oftentimes, the thickness is not resolved by the computational grid, and subgrid models need to be developed (e.g., Sato and Niceno (2015)). In this thesis, however, the micro-layer is not considered. Thus, water at higher pressures, where the micro region is not present, is chosen for the present simulation (see Kossolapov (2021)). Indeed, technical applications (e.g. power plants) frequently operate at elevated pressure.

In the PhD thesis of Kossolapov (2021), comprehensive experiments are conducted at a pressure of 1.05 MPa, at which no micro-layer is formed. This problem setup is used as reference data in the present thesis. The same experimental data are also considered in the study by Sato et al. (2025). The present simulations are carried out for a Reynolds number of $Re \approx 40.000$.

In the following sections, the simulation setup is described along with minor case-specific developments. Finally, the results are validated by comparing them with the available data from

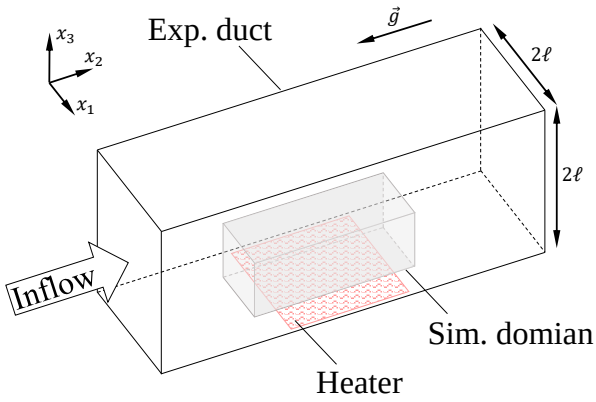

Figure 7.1: Experimental domain (transparent box) in comparison to the simulated domain (grey box). The experimental domain consists of a square duct of height 2ℓ. The simulated domain is located on the heater and is centred on the duct wall.

Kossolapov (2021). Additionally, numerical data are analyzed beyond the experimental measurements.

7.1 Case setup

The chosen reference experiment employs a facility in which boiling is studied in a square duct (see Kossolapov (2021) and Kossolapov et al. (2024)). The inflow length, before the measurement section, is long enough to ensure a fully developed turbulent duct flow. The schematics of their measurement section are depicted in Fig. 7.1. Gravitational acceleration $|\vec{g}| = 9.81$ m s^{-2} points in the opposite direction of the flow, the channel height is $2\ell = 11.78$ mm, and a heated section of 10×10 mm^2 is placed in the centre of the bottom wall. In this chapter, a mass flux of $G = 500$ kg s^{-1}m^{-2}, is considered. In accordance with the experiments, the properties of saturated water at 1.05 MPa are applied, which are listed in Tab. A.1. With these properties, a bulk velocity Reynolds number Re_b, corresponding to the liquid phase at the inlet, is determined as

$$Re_b = \frac{2G\ell}{\mu_2} = 39630. \tag{7.1}$$

Direct numerical simulations corresponding to this Reynolds number ($\approx 40,000$) are conducted in Pirozzoli et al. (2018). According to their results, the bulk velocity Reynolds number in Eq. 7.1 corresponds to a friction Reynolds number $Re_\tau = \ell\rho_2 u_\tau/\mu_2$ of $Re_\tau = 1055$. For the chosen simulation setting, this translates to a friction velocity of $u_\tau = 0.03$ m/s and a friction length

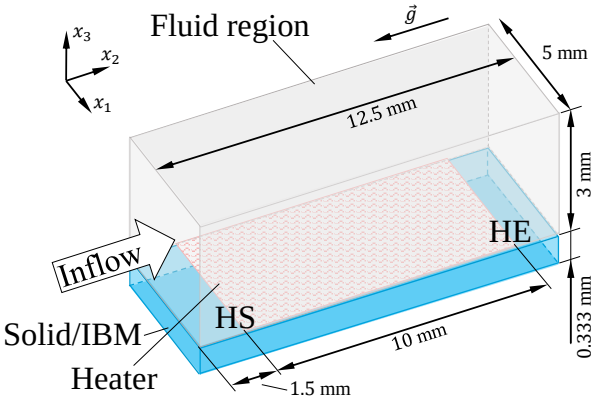

Figure 7.2: Schematic of the computational domain. The solid region (blue part) is represented with an IBM. The grey box represents the fluid region. The locations of the heater start (HS) and heater exit (HE) are indicated with dimensions.

scale of $\ell_\tau = \mu_2 \rho_2^{-1} u_\tau^{-1} = 5.583 \cdot 10^{-6}$ m. Both reference quantities are used in the following analysis to non-dimensionalize results (marked with a plus $(\cdot)^+$ in the exponent).

In the experiments by Kossolapov (2021), the heated section consists of a very thin indium tin oxide layer, which produces heat due to the electrical resistance. For the present simulation, the thin layer cannot be resolved and an alternative heater model must be applied instead (see Sec. 7.4). The heater produces a heat flux of 1 MW/m^2 at the fluid-solid interface.

In the present simulation, only a part of the duct flow is represented (see Fig. 7.1). A detailed visualization, including relevant dimensions, of the computational domain is presented in Fig. 7.2. The solid of the computational domain is chosen thick enough to resolve all temperature fluctuations that penetrate the solid. To match the experiments, the solid domain uses the physical properties of sapphire glass: $\rho_s = 3970$ kg m^{-3}, $c_{p,s} = 750$ J kg^{-1}K^{-1}, and $\lambda_s = 28.5$ W m^{-1}K^{-1}.

An inlet boundary condition is applied to the lower x_2 domain boundary (Fig. 7.2 left, see details Sec. 7.3), whereas the upper x_2 domain boundary (Fig. 7.2 right) uses the outflow boundary condition described in Sec. 4.6. In the x_1 direction, a periodic boundary condition is applied[5]. The solid is simulated using the IBM treatment from Sec. 4.7, and the upper x_3 boundary is a free-slip boundary. In line with the experiments, the inflow temperature T_∞ is set to $T_\infty - T_{\text{sat}} = -10$ K.

[5] The physical duct flow is, of course, not periodic in the x_1 direction. However, this approximation is assumed sufficient for the simulated section.

For the spatial discretization, uniform grid cells of size $\Delta x_1 \times \Delta x_2 \times \Delta x_3 = 15.6 \times 15.6 \times 10.4$ µm^3 are utilized, resulting in a total $320 \times 800 \times 320$ grid cells. The use of non-cubic grid cells has not been discussed, thus far, and requires an extension of the developed phase change model (Sec. 4.4), which is described in the Appendix Sec. A.2 and Sec. A.3. Using non-cubic grid cells also entails a variation in the non-dimensional interface thickness ϵ^* depending on the orientation of the interface in relation to the grid. For this simulation, the interface thickness ϵ is set to $\epsilon = 10.4$ µm. Therefore, the non-dimensional interface-thickness has a dependency on the axis direction: $\epsilon_1^* = 0.66$, $\epsilon_2^* = 0.66$ and $\epsilon_3^* = 1$ in the x_1, x_2, and x_3 directions, respectively. In this regard, the ACDI method by Jain (2022) is advantageous, as it allows stable simulations for $0.5 < \epsilon^* < 1.0$, with no additional time step constraints.

The heated wall is hydrophilic, and thus, a contact angle of $\Theta < 90°$ needs to be enforced. For lower pressures, Kossolapov (2021) estimated an angle of $\Theta \approx 80°$. However, for numerical simulations, a contact angle of around $1°$ is suggested for pool boiling scenarios (see Bureš and Sato (2022)). For this study, the contact angle is set $\Theta = 1°$, which results in satisfactory agreement with the experimental data by Kossolapov (2021).

7.2 Bubble nucleation model

A central part of the boiling flow simulation is the modelling of the nucleation process. The nucleation of bubbles starts at small imperfections on the heated surface. Modelling is required, as these imperfections cannot be resolved and remain at subgrid scale level. Sato and Niceno (2017) proposed a model that randomly distributes nucleation sites on the heated surface. In their model, each nucleation site has an activation temperature based on the active *nucleation site density* (NSD) for that temperature. Information about the active nucleation site density can be obtained from experimental measurements or empirical correlations (e.g., Lemmert and Chawla (1977)).

The thesis by Kossolapov (2021) reports measurements of the active nucleation site density, which are shown in Fig. 7.3a. To utilize this NSD data through the model by Sato and Niceno (2017), a curve fit function is used. The curve fit function has the shape $[A(T_{wall} - T_{\text{sat}})]^B$, which was proposed by Lemmert and Chawla (1977). Note that Lemmert and Chawla (1977) determined $A = 185$ and $B = 1.805$, however, with the experimental data, the curve fit yields $A = 981172$ and $B = 1.22$. This difference is explained by the large variations in the activation frequency of each nucleation site, as measured by Kossolapov (2021). The maximum expected wall superheat is set to 30 K, corresponding to a total of 65060 nucleation sites (see Fig. 7.3b). These nucleation sites are randomly distributed on the heater surface using the method described

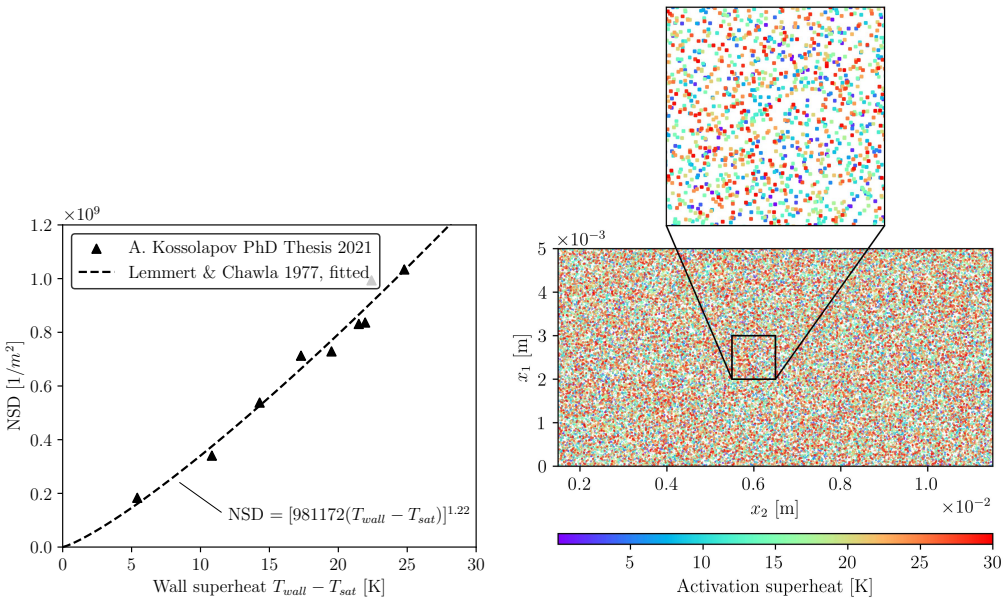

(a) Measurements from Kossolapov (2021) with a curve fit.

(b) Random nucleation site distribution.

Figure 7.3: Nucleation site density used for the present simulation.

in Sato and Niceno (2017). Following their algorithm, all nucleation sites are inspected at every time step if the activation conditions are met. These conditions are:

- The local wall temperature exceeds the activation temperature
- The nucleation site is covered by the liquid phase (see Sato and Niceno (2017))

The second condition is straightforward to implement for sharp interface methods, where a clear separation of liquid and gas is possible. However, diffuse interface methods require an alternative definition of the second nucleation condition, as both phases can locally coexist. To overcome this difficulty, a level-set threshold value Ψ_{thr} is proposed in this work. Recalling that Ψ represents the signed distance to the next interface, a simple definition of Ψ_{thr} is obtained. For the present simulation, it is set to $\Psi_{thr} = -6\Delta x_1$, and, thus, the modified nucleation condition is met if $\Psi < \Psi_{thr}$. That is, the nucleation condition is met if the nearest interface is at a distance of six times the grid size. Note that Ψ_{thr} is negative, as negative level-set values refer to the liquid side of the interface (see Fig. 2.3). Evidently, $|\Psi_{thr}|$ has to be small enough that no unphysical suppression of nucleation events occurs, but large enough to ensure numerical stability. If both nucleation conditions are met, a seed bubble of radius r_0 is placed over the activated nucleation

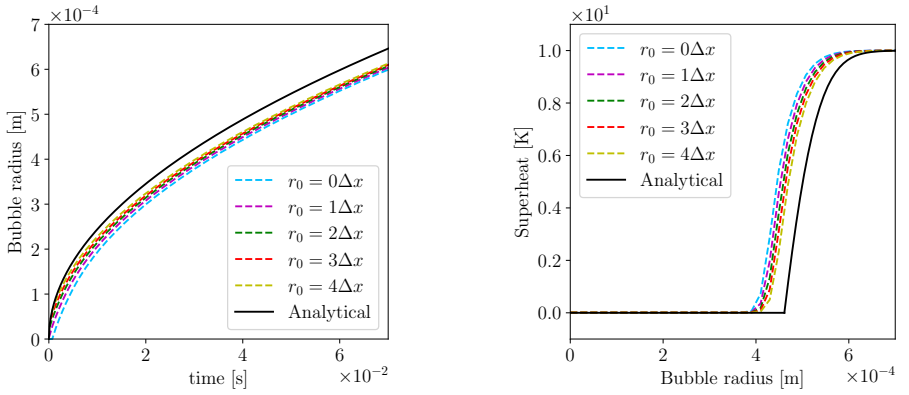

(a) Bubble size

(b) Temperature distribution at $t = 35.7$ ms

Figure 7.4: Impact of the seed bubble size on the bubble growth rate, assuming $T_\infty - T_{\text{sat}} = 10K$. Analytic solution (black line) is taken from Scriven (1959). See Sec. 6.6 for computational details.

site. This seed bubble is initialized with a phase field increment $\Delta\phi$, using the equilibrium profile, as follows:

$$\Delta\phi = \frac{1}{2}\left[1 + \tanh\left(\frac{r_0 - |\vec{x} - \vec{x}_n|}{2\epsilon}\right)\right] \tag{7.2}$$

Here, $\vec{x}_n$ is the centre of the seed bubble, and the phase field is subsequently updated as $\phi + \Delta\phi$. The centre of the bubble is placed slightly above the wall so that it matches the enforced contact angle after nucleation. This wall distance for nucleation can be calculated as $r_0 \cos(\Theta)$.

7.2.1 Seed bubble size r_0

The seed bubble size r_0 is a central simulation setting. Clearly, r_0 has to be as small as possible to capture early-stage information of the bubble growth and to minimize the violation of the mass conservation implied by Eq. 7.2. However, too small bubbles can lead to erroneous growth rates due to poor resolution of the thermal boundary layer around the bubble. Therefore, an optimal value must be found.

To determine an optimal seed bubble size, the results of a simple bubble growth test in the absence of gravity are compared to the analytic solution from Scriven (1959). Assuming a superheat of $T_\infty - T_{\text{sat}} = 10K$ results in a growth constant of $\beta = 2.94$ (refer to Sec. 6.6). Note that the results in this section correspond to uniform cubic grid cells of size $\Delta x = 15.6$ µm. Testing five seed bubble sizes from $r_0 = 0$ to $r_0 = 4\Delta x$ yields the comparisons in Fig. 7.4a and Fig.

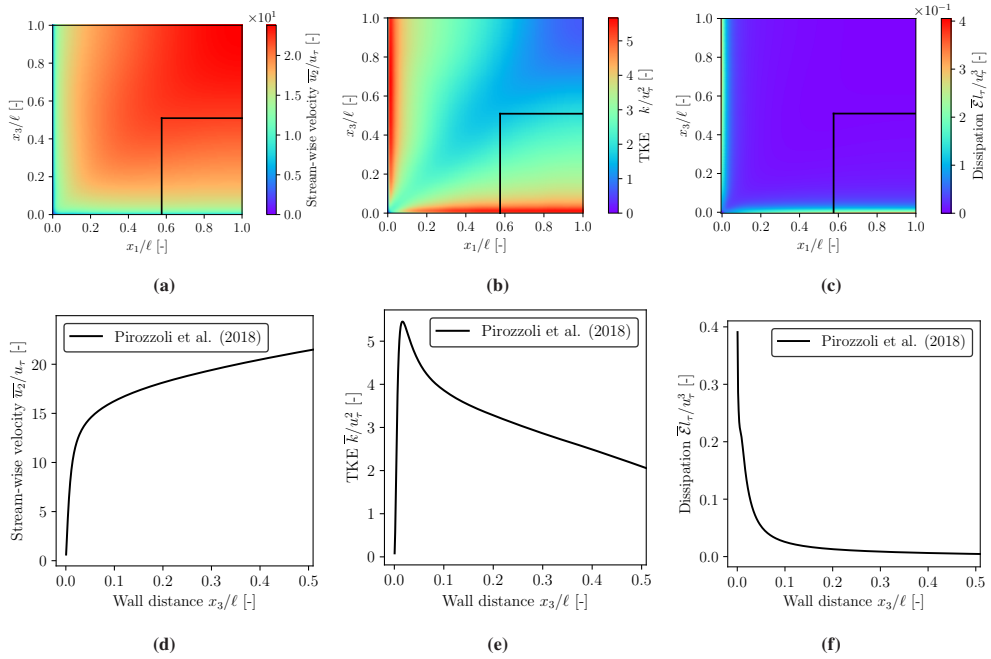

Figure 7.5: Visualization of the DNS database by Modesti (2020) based on the DNS in Pirozzoli et al. (2018). Figs. 7.5a-7.5c depict two-dimensional visualizations of the streamwise velocity, the TKE, and the dissipation. Due to symmetry, a fourth of the duct cross-section is shown. The black box depicts the part of the duct that is resolved in the boiling flow simulation. Figs. 7.5d-7.5f show the lineout data cutting through the centre of the duct ($x_1/\ell = 1$).

7.4b. It can be seen that the growth rate is slightly under-predicted for all seed bubble sizes. The most significant difference is evident at the onset of bubble growth. Here, the growth observed for a seed bubble size of $r_0 = 0$ is significantly delayed in comparison to that of $r_0 = \Delta x$. The improvements achieved among the three largest seed bubbles are marginal.

As a result, the seed bubble size for the boiling flow simulation is chosen to be $r_0 = \Delta x = 15.6$ µm. This seed bubble size allows for a good balance between growth rate accuracy and minimizing r_0.

7.3 Turbulent Inflow

The inflow boundary condition poses an additional difficulty for the computational setup. As seen in Sec. 7.1, a fully developed turbulent duct flow has to be prescribed at the inlet of the computational domain. Therefore, at every time step, an instantaneous velocity field, with the

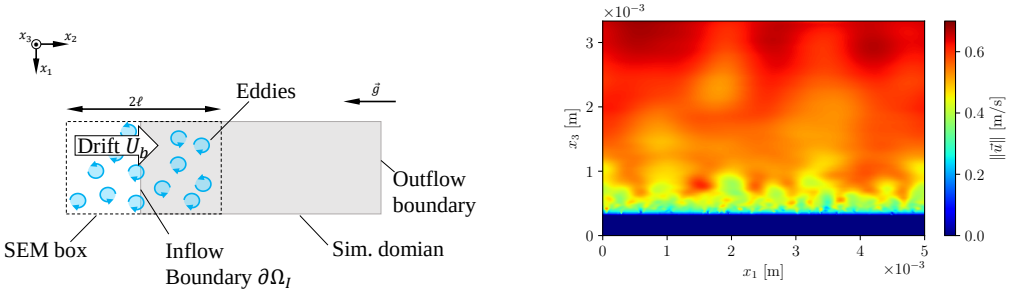

(a) **(b)** Instantaneous flow field on inflow boundary

Figure 7.6: (a) Location of computational domain in relation to SEM box containing the synthetic eddies. Eddies are advected with the bulk velocity U_b. The contribution of each eddy is calculated for the inflow boundary. See Poletto (2015) for further details. (b) Visualization of instantaneous velocity magnitude on the inflow boundary.

properties of the turbulent duct, is required. In terms of a strategy to obtain this information, a precursor duct simulation of the upstream flow at $Re_b \approx 40000$ is too expensive. Moreover, it is expected that boiling generates fluctuations of large amplitude so that the exact inflow turbulence is of weak importance. As a result, a synthetic turbulence approach is utilized, which generates instantaneous velocity fields.

Specifically, the synthetic eddy method (SEM) from the PhD thesis of Poletto (2015) is employed. This method enables the generation of divergence-free velocity fields for both isotropic and anisotropic turbulence. In this work, isotropic turbulence is generated, which requires the following input data: the time-averaged streamwise velocity $\overline{u_2}$, the time-averaged turbulent kinetic energy (TKE) k, and the dissipation $\overline{\mathcal{E}}$. This data is readily available in the database from Modesti (2020), which corresponds to the DNS reported in Pirozzoli et al. (2018). This database is visualized in Fig. 7.5, which shows that $\overline{u_2}$, k, and $\overline{\mathcal{E}}$ are homogeneously distributed along the x_1 direction in the computational domain of the boiling flow. Thus, the values at the centerline of the duct are used as the input data for the SEM (Figs. 7.5d-7.5f) of the boiling flow simulation.

The computational setup with SEM is depicted in Fig. 7.6a. For the present application, $1.5 \cdot 10^5$ eddies are generated in a box of size $5 \times 11.79 \times 3$ mm^3 (corresponding to the x_1, x_2, and x_3 directions). Furthermore, each time step transports the eddies with the bulk velocity[6] U_b in the streamwise direction. Finally, the contribution of each eddy is calculated at each time step on the inflow boundary and used as a Dirichlet boundary condition (refer to Poletto (2015)). An example velocity distribution arising from the chosen SEM is visualized in Fig. 7.6b.

[6] In this simulation, the bulk velocity is $U_b = \int_{\partial\Omega_I} \overline{u_2} dx_3 / \int_{\partial\Omega_I} dx_3 = 0.546$ m/s.

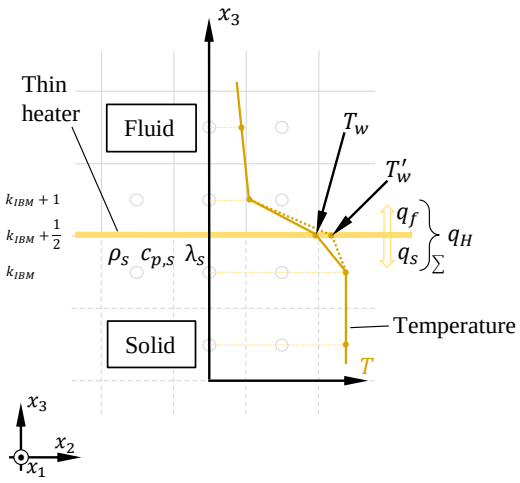

Figure 7.7: Thin heater model visualization. Temperature distribution (dark orange line) is modified at the wall (dotted line) so that the heat flux balance at the fluid-solid interface equals the wall heat flux q_H produced by the heated film.

7.4 Thin heater model

As described in Sec. 7.1, the heater consists of a very thin layer of indium tin oxide. Kossolapov (2021) reports the thickness of this layer to be 0.7 µm, which is more than one order of magnitude smaller than the wall normal grid spacing Δx_3 of the present simulation. As such, a *thin heater model* is utilized, which is described in the following.

The present model is based on the assumption that the thermal resistance of the heater film is negligible, and, thus, the temperature on both sides of the film is equal. Moreover, the model assumes that no heat is stored in the thin film and that negligible heat conduction occurs in the x_1 and x_2 directions.

A schematic of the thin heater is visualized in Fig. 7.7. Here, it can be seen that the heat flux q_H that leaves the heated film is prescribed by modifying the surface temperature T_w. This modified wall temperature is denoted T'_w, and the modified heat flux balance at the interface of the solid and fluid cells is calculated as

$$q_H = 2\lambda_{i,j,k_{IBM}+1} \frac{T_{i,j,k_{IBM}+1} - T'_{w,i,j}}{\Delta x} - 2\lambda_{i,j,k_{IBM}} \frac{T'_{w,i,j} - T_{i,j,k_{IBM}}}{\Delta x}. \tag{7.3}$$

For zero wall heat flux q_H, Eq. (7.3) yields the same result as Eq. (4.78). For the general case, T'_w is calculated from the following relation:

$$T'_{w,i,j} = T_{w,i,j} + \frac{q_H \Delta x}{2(\lambda_{i,j,k_{IBM}} + \lambda_{i,j,k_{IBM}+1})} \tag{7.4}$$

Subsequently, Eq. (7.4) is utilized in Eq. (4.77) to adjust the conjugate heat transfer treatment of the IBM. Furthermore, the heat that is transferred from the wall to the fluid (Eq. (4.77)) has to be accounted for at the contact line in the phase change model. This modification is presented in the appendix Sec. A.4.

7.5 Simplified LES implementation

The presence of turbulence in the boiling flow poses additional spatial resolution requirements for the computational grid. For the full resolution of all turbulent structures, the grid spacing needs to be small enough to resolve the smallest eddies present in the flow. Compared to the grid spacing used in the DNS by Pirozzoli et al. (2018), a satisfactory resolution of the duct flow turbulence can be expected. However, the formation and transport of bubbles is deemed to increase the turbulence. In this case, the turbulent fluctuations closer to the heater are significantly stronger compared to those of the fully developed duct flow. Therefore, a large eddy simulation (LES) model is employed to account for potential turbulence at subgrid level.

The use of LES in two-phase flow simulations is not trivial, as interactions between subgrid turbulence and the phase interface are important. Thus far, numerous studies have proposed turbulent interaction models (e.g., Saeedipour and Schneiderbauer (2019)) or have compared various formulations (e.g., Iberl et al. (2025)). However, Kaiser et al. (2024) reported good results when neglecting interactions between the subgrid turbulence and the phase interface. Accordingly, this simplification is adopted in the present simulation.

In LES, the unresolved turbulent transport of momentum and thermal energy is accounted for by using an eddy diffusivity μ_t and a turbulent heat conductivity λ_t. Accordingly, the modified transport equations for momentum and thermal energy read

$$\frac{\partial \rho \vec{u}}{\partial t} + \nabla \cdot \left(\left(\rho \vec{u} - \vec{\mathcal{F}} \right) \otimes \vec{u} \right) + \vec{\mathcal{C}} = -\nabla p + \nabla \cdot \left[(\mu + \mu_t)(\nabla \vec{u} + \nabla \vec{u}^T - 2\nabla \cdot \vec{u}\mathbb{1}) \right] + \ldots \tag{7.5}$$

and

$$\rho c_p \left(\frac{\partial T}{\partial t} + \vec{u} \cdot \nabla T \right) = \nabla \cdot [(\lambda + \lambda_t) \nabla T] + \nabla \cdot \vec{j} - L\mathcal{M} + \Delta \rho c_p \vec{\mathcal{R}} \cdot \nabla T, \tag{7.6}$$

respectively. Note that in Eq. 7.5 and Eq. 7.6, all solution variables refer to spatially filtered quantities. However, the filter operator is dropped for convenience and for improved readability. Here, a standard Smagorinsky model (see Smagorinsky (1963)) is utilized. Therefore, the eddy diffusivity μ_t is calculated as

$$\mu_t = \rho \left[0.17 \, \Delta \, C(x_3^+) \right]^2 \sqrt{2} \|S\|_F, \tag{7.7}$$

where $\Delta = (\Delta x_1 \times \Delta x_2 \times \Delta x_3)^{1/3}$, and $C(x_3^+)$ is the wall dampening function proposed by van Driest (1956), which reads $C(x_3^+) = 1 - \exp(-x_3^+/25)$. Furthermore, the Smagorinsky constant 0.17 is taken from Lilly (1967), and $\|S\|_F$ refers to the Frobeniusnorm of the rate-of-strain tensor $S = 1/2(\nabla \vec{u} + \nabla \vec{u}^T)$. The turbulent heat conductivity λ_t is obtained by using μ_t and the standard turbulent Prandtl number $Pr_t = 0.9$ (as in Kaiser et al. (2024)). Therefore,

$$\lambda_t = \frac{\mu_t c_p}{Pr_t}. \tag{7.8}$$

7.6 Code scalability

This large-scale flow problem presents an opportunity to assess the scalability potential of the developed simulation software. For this assessment, the software advances the boiling flow for 2000 time steps, by distributing the simulation across a varying number of CPU cores. The average time required to perform one simulation time step is measured. Ideally, a simulation software completes the same number of time steps twice as fast when the number of CPU cores is doubled. This scalability limit is referred to as *strong scaling*. However, the data communication between the CPU cores commonly reduces the speedup.

For this test, 2^7, 2^8, 2^9, and 2^{10} CPU cores are considered. The simulation software is executed on two high-performance computing (HPC) clusters at the Karlsruhe Scientific Computing Center (SCC): (i) the HoreKa cluster, using the CPU partition with Intel Xeon Platinum 8368 hardware, and (ii) the bwUniCluster 3.0 (UC3) cluster, using the Ice Lake CPU partition with Intel Xeon Platinum 8358 hardware. The results of this test are visualized in Fig. 7.8, where the speedup is normalized with the time required when utilizing 2^7 CPU cores.

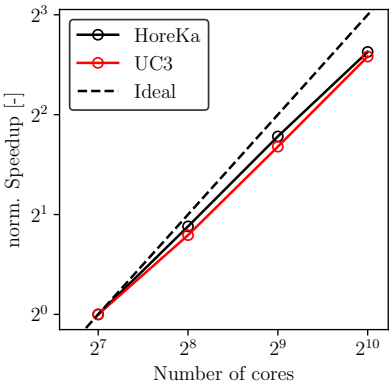

Figure 7.8: Code scalability assessment for two HPC clusters. Speedup is normalized by the time required to execute the test with 2^7 CPU cores. The dashed line represents the strong scaling limit.

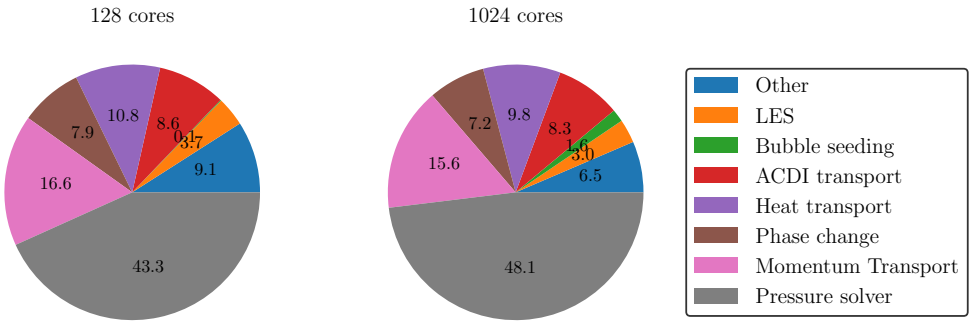

Figure 7.9: Profiler results when using the 2^7 and 2^{10} cores on the HoreKa cluster.

The software exhibits very similar speedup behaviour on both HPC hardware architectures. Increasing the number of CPU cores by a factor of eight results in an overall speedup of 6.2 and 6.0 for HoreKa and UC3, respectively. Additionally, a profiler is used to measure the relative time required to complete the sub-problems during each time step. The results of the profiler analysis are presented in Fig. 7.9. In general, Fig. 7.9 shows that the pressure solution is the most computationally expensive part, requiring 40-50% of the computational time. The relative cost of the pressure solution increases for the results obtained from 2^7 to 2^{10} CPU cores. Utilizing more CPU cores commonly entails increased inter-process communication. This effect is particularly pronounced for the pressure solution, as the FFT requires a transpose of the pressure data (see 2.6.4). For the FFT itself, the highly optimized FFTW library by Frigo and Johnson (2005) is employed. Therefore, potential code optimizations could focus only on other parts of the software. Due to the computational cost of the pressure solution, this optimization potential is limited.

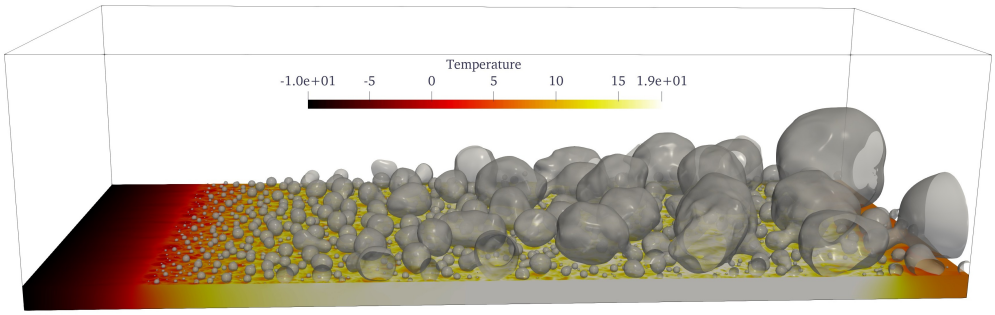

Figure 7.10: Instantaneous snapshot showing the iso-contour of $\phi = 0.5$ and the temperature distribution of the solid.

7.7 Results

With the presented modifications (Sec. 7.2 - Sec. 7.5), the simulation of a turbulent subcooled nucleate boiling flow can be conducted. After reaching a statistically steady flow, the collection of flow data is activated. In Fig. 7.10, an instantaneous snapshot of the statistically steady state is depicted. In this figure, the temperature of the solid region is shown along with the bubbles represented by the phase field iso-surface. It is evident that the flow under investigation exhibits a strongly polydisperse nature, characterized by a wide range of bubble sizes. Furthermore, hot and cold spots are seen on the heater surface, which are visibly correlated with the presence of bubbles. This flow will be investigated in detail in the following.

For the statistical flow analysis, the simulation is run for 6 non-dimensional turnover times[7], during which the statistical information about the flow and the contained bubbles is recorded. The evaluation of the recorded data is divided into three parts. First, available data from the PhD thesis of Kossolapov (2021) is compared to the simulation data. Second, the wall and flow field statistics are discussed. Lastly, the bubbles in the flow are evaluated through a grouped Voronoi analysis.

Although the present simulation resolves the interface, certain physical phenomena (e.g., wettability behaviour or bubble nucleation) are modelled, and thus, introduce uncertainty. As such, minor deviations from the experiments can be expected. However, compared to RANS-based simulations, the amount of modelling is minimal. For example, in this simulation, the dynamics of all bubbles are resolved, allowing the analysis of such data. In the following sections, this fact is emphasized to highlight the importance of interface-resolved boiling simulations.

[7] One turnover time is defined as the length of the heated section (i.e. 10 mm) divided by the inflow bulk velocity U_b.

Table 7.1: Comparison of simulation data to results from Kossolapov (2021). Value range refers to the standard deviation.

Quantity	Unit	Kossolapov (2021)	Present simulation
Wall superheat	K	10.8 ± 1.8	17.5
Contact line density	m^{-1}	490 ± 75	3265.5 ± 86.4
Dry-spot radius	µm	48.7 ± 28.4	25.7 ± 25.0

7.7.1 Comparison with experiments

A range of quantities that are presented in Kossolapov (2021) for the chosen computational settings are listed in Tab. 7.1. These are, the wall superheat averaged over the heated surface, the contact line density, and the dry-spot radius. These quantities are compared to the results obtained in the current simulation. The table shows that the superheat of the wall and the averaged dry-spot radius show slight deviations from the experimental results. A significant difference is seen for the contact line density. This difference means that the simulation features significantly more dry-spots than the experiment. A visualization of the simulation's dry-spots is provided in Fig. 7.11. The white spots in this figure represent the areas in contact with the gaseous phase (dry-spots), which cover, on average, 8.7% of the heated surface. A comparison with the experimental data in Kossolapov (2021) indicates that the simulation data overpredict the amount of dry spots. However, it should be noted that the diffuse interface representation, when combined with super-hydrophilic wetting behaviour, may lead to misinterpretation. As a result, a bubble that touches the wall with the $\phi = 0.5$ contour line is not necessarily fully contacting the wall, as the interface normal vector is pointing almost in the wall-normal direction. As such, the calculated contact line depends strongly on the phase field value that defines the contact line. This dependency on ϕ is depicted in Fig. 7.12. Even a small variation in the contact line definition has an order unity effect on the contact line density. Therefore, the contact line density presented in Tab. 7.1 is regarded as a CDI artifact.

Additionally, the elevated surface temperature observed in the simulation could be a result of the nucleation model. In Fig. 7.13, the dry-spots are shown along with the instantaneous surface temperature. Downstream, the heated surface patches are present where no dry-spots, and thus, no seed bubbles are present. This is an artifact of the inhibition of nucleation arising from large detached bubbles that are transported in proximity to the wall. Therefore, the local level-set value Ψ is above the threshold level-set value Ψ_{thr} (Sec. 7.2) and prevents the nucleation events. As such, the cooling mechanism due to nucleation is missing, and the surface temperature is elevated. However, this artifact has a minor impact, as the difference to the experimental data is in the order of a few Kelvin.

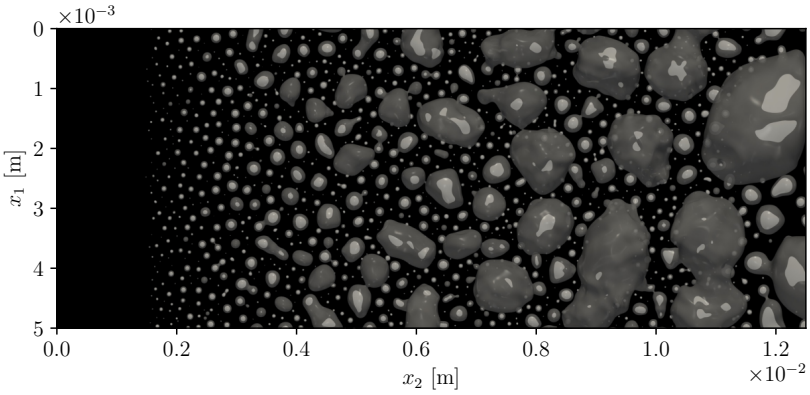

Figure 7.11: Instantaneous dry-spot visualization. Grey areas represent the bubbles projected onto the wall, black areas are covered by the liquid phase ($\phi < 0.5$), white areas are dry-spots ($\phi > 0.5$).

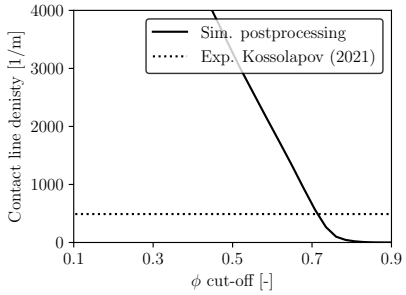

Figure 7.12: Calculated contact line density based on the cut-off phase field value in comparison to the experimental results by Kossolapov (2021).

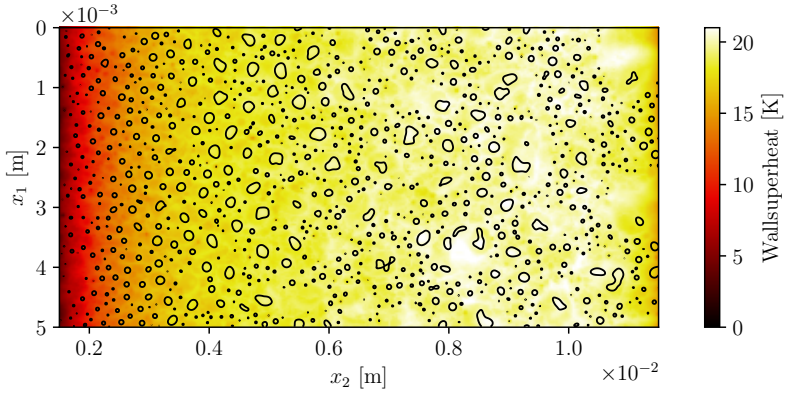

Figure 7.13: Instantaneous heater temperature along with the dry-spot distribution represented by the iso-contour of $\phi = 0.5$ on the heated surface.

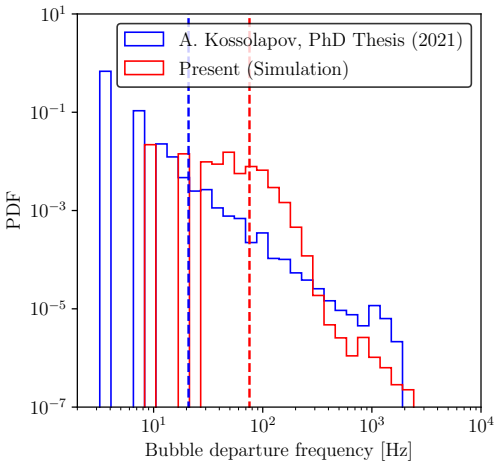

Figure 7.14: Probability distribution of finding a nucleation site with a specific bubble departure frequency. Comparison of simulation results with the experimental data presented in Kossolapov (2021). Dashed lines represent the corresponding mean values.

Furthermore, Kossolapov (2021) measured the bubble departure frequency for each nucleation site. Their study shows that although many different nucleation sites are activated, a large separation among the observed bubble departure frequencies is observed. These frequencies, corresponding to each nucleation site, are also evaluated in the present simulation. The comparison between the experiments and the simulation is visualized in Fig. 7.14. The PDF shows the occurrence probability of finding a nucleation site within a specific range of bubble departure frequencies. The average (dashed line) departure frequency in the simulation is 3-4 times higher than in the experiments. In addition, the low-frequency end of the PDF is missing for the simulation data. However, these observations are influenced by the duration of the simulated time, which leads to under-resolved occurrences of low frequencies. In the simulation, frequencies below 10 Hz are not resolved. It should be noted that excluding the two lowest frequency bars of the experiment would theoretically lead to the same mean value as the simulation (70-80 Hz). Therefore, it is concluded that the simulated departure frequencies exhibit the same features as the experiments. For example, both simulation and experiment find that very few nucleation sites have nucleation events at a frequency that is higher than 10^3 Hz. Further, a large spectrum of frequencies is observed, ranging over two orders of magnitude. And the number of nucleation sites exhibiting departure frequencies within a specific range drastically decreases towards higher frequencies.

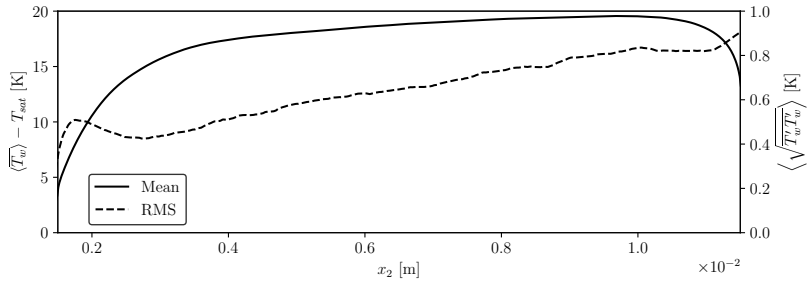

Figure 7.15: Time and spanwise-averaged surface temperature (solid, left axis) together with the spanwise-averaged root-mean-square value of the wall temperature (dashed, right axis).

7.7.2 Heater surface statistics

This section presents data that extend beyond the reported experimental results from Kossolapov (2021). In the analysis, the data is averaged in time (denoted by an overbar $\bar{\cdot}$) and, for some figures, averaged along the spanwise (x_1) direction (denoted by angular brackets $\langle \cdot \rangle$). Further, the Reynolds decomposition, which separates a fluctuation from its mean value, utilizes a prime to denote the fluctuation. Accordingly, an instantaneous value is rewritten as $\phi = \overline{\phi} + \phi'$.

Oftentimes, the wall temperature T_w on the heated surface is a primary quantity of interest. This quantity is shown in Fig. 7.15. Although the temperature exhibits a distinct plateau, a spatial dependency is seen for the mean surface temperature. A maximum $\langle \overline{T_w} \rangle$ of 19.5 K above the saturation temperature is observed at the heater exit (HE). More interestingly, the root-mean-square (RMS) value of the temperature fluctuations is evaluated in this simulation, and is represented by the dashed line. At the heater start (HS), a local peak in the RMS value is observed, which first decreases downstream before rising again. The spatial distribution of the RMS value is visualized in Fig. 7.16a. At HS, the elevated fluctuations are visible as streamwise streaks (e.g., red arrow in Fig. 7.16a). Further, the location of this initial RMS peak coincides with the location of the most active nucleation sites in the computational domain. This indicates a potential correlation between the temperature fluctuations and nucleation site activity.

The location of the highly active nucleation sites is also included in Fig. 7.16b, where the spatial distribution of the dry-spot probability is depicted. The dry-spot probability is calculated using the time-averaged phase field value $\overline{\phi}$, which is interpolated onto the immersed boundary. In Fig. 7.16b, the bubbles appear to have straight sliding paths between $x_2 = 1.5$ mm and $x_2 = 4$ mm, downstream the nucleation (e.g., red arrow in Fig. 7.16b). At $x_2 = 4$ mm, the dry-spot probability shows a maximum value. Comparing with Fig. 7.11, this marks the point after which detached bubbles are observed in the flow. Accordingly, downstream of $x_2 = 4$ mm, the dry-spot probability decreases and becomes irregular. In contrast to the decreasing dry-spot probability,

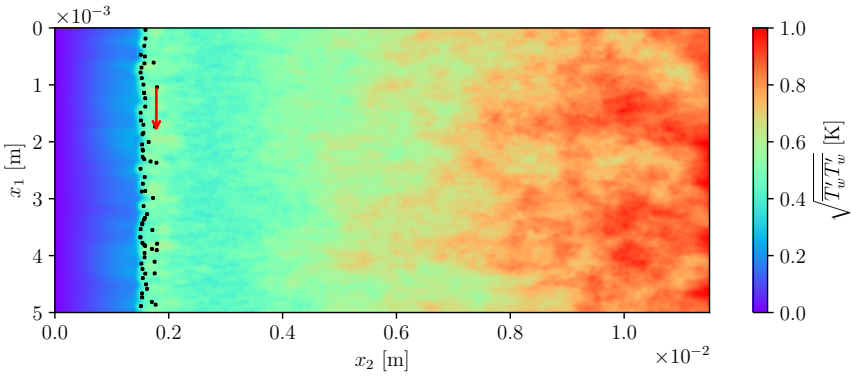

(a) RMS of temperature fluctuations

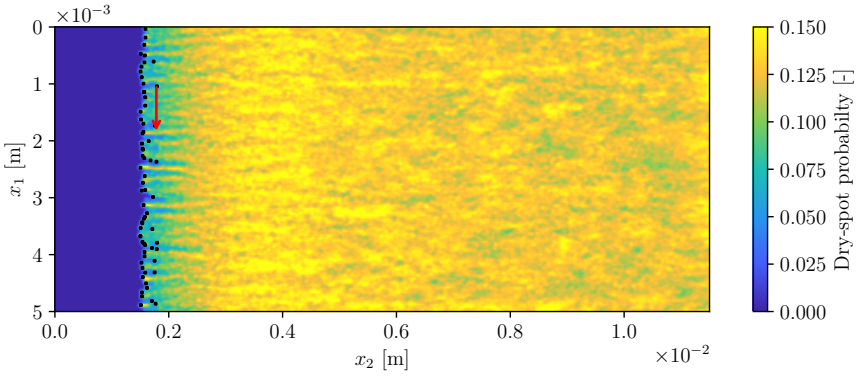

(b) Dry-spot probability

Figure 7.16: Spatial distribution of (a) root-mean-square (RMS) value of the wall temperature fluctuations, and (b) time-averaged dry-spot probability on the solid surface. Black dots represent the location of nucleation sites with more than 400 Hz bubble departure frequency.

an increase in the temperature fluctuations is observed, as in Fig. 7.16a. In this regard, this data could be helpful to investigate the heat transfer mechanisms (evaporation, convection, bubble sliding, etc). For example, the experiments by Kossolapov (2021) showed that up to 60% of the heat is transferred through unknown mechanisms.

7.7.3 Flow field statistics

In this section, time-averaged information about the two-phase flow is discussed. For this purpose, the gas content, the mass transfer distribution, the velocities, and the resolved turbulent kinetic energy (TKE) are presented in the following.

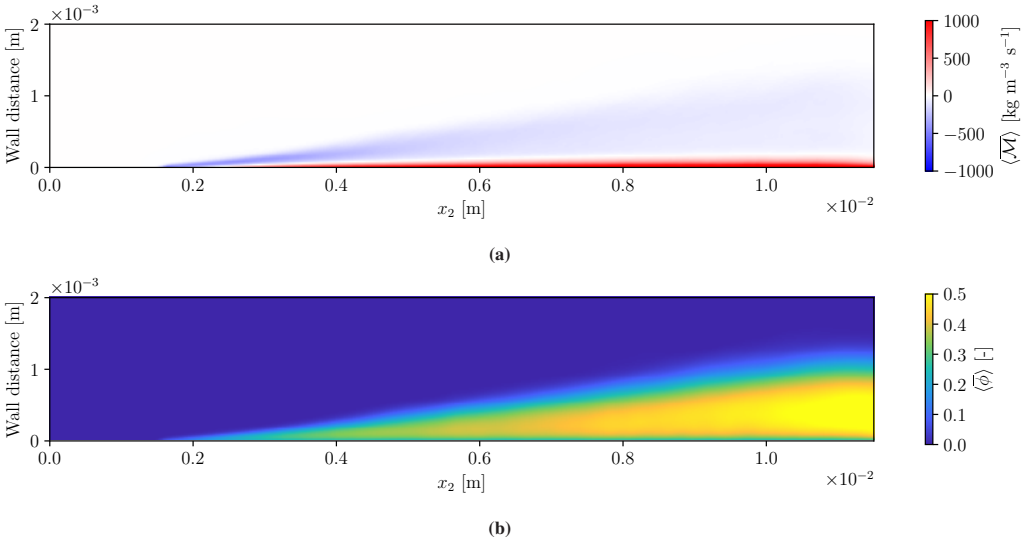

Figure 7.17: Time and spanwise-averaged (a) mass transfer rate (b) gas content.

First, the distribution of the mass transfer is presented in Fig. 7.17a. Areas in which condensation is dominant are shaded blue (negative mass transfer rate $\langle\overline{\mathcal{M}}\rangle$), . Red areas highlight evaporation-dominated areas (positive $\langle\overline{\mathcal{M}}\rangle$). At the HS, condensation is the predominant mechanism. That is, seeded bubbles shrink at first on the heater. In line with Kossolapov (2021), evaporation occurs within a thin layer above the wall. Furthermore, detached bubbles in the bulk of the flow condensate due to the subcooled inflow condition. However, condensation decreases towards the outflow as the fluid is heating up.

The average distribution of the gaseous phase due to evaporation is shown in Fig. 7.17b. This quantity is equivalent to the time and spanwise-averaged phase field variable $\langle\overline{\phi}\rangle$. As such, a constantly growing layer of bubbles is observed from HS ($x_2 = 1.5$ mm) onward in Fig. 7.17b. The gas content increases along the heater, reaching a maximum of $\langle\overline{\phi}\rangle = 0.54$ at HE. Utilizing the gas velocity (see Fig. 7.18b) and the latent heat, it is calculated that 37% of the total wall heat flux input leaves the computational domain as latent heat.

The evolution of the gaseous layer is further visualized in Fig. 7.18a. Here, the profiles of the gas content are shown at three representative locations in the computational domain. The velocity at which the gas content is transported is not equal to the average velocity profile. To quantify the velocity difference between both phases, the phase-averaged (see Ishii and Hibiki (2011)) streamwise velocity is presented in 7.18b. Near the wall, the velocity of the gaseous phase is higher than that of the liquid for all three locations. Accordingly, an increase in the liquid velocity is observed along the length of the heater. In addition, the bulk of the liquid phase is accelerated

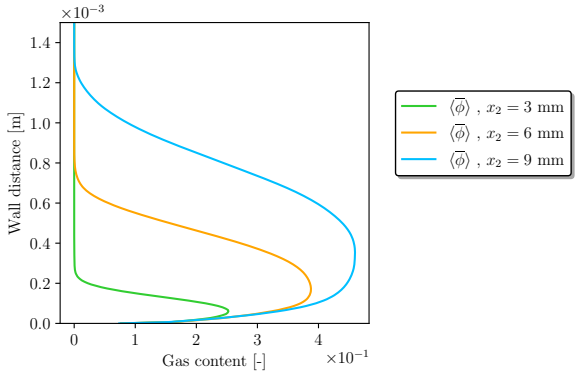

(a) Time and spanwise-averaged gas content

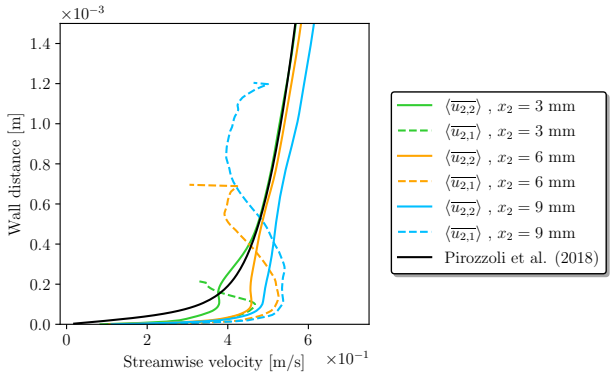

(b) Time and spanwise-averaged liquid (solid lines) and gas (dashed lines) velocities in the streamwise direction

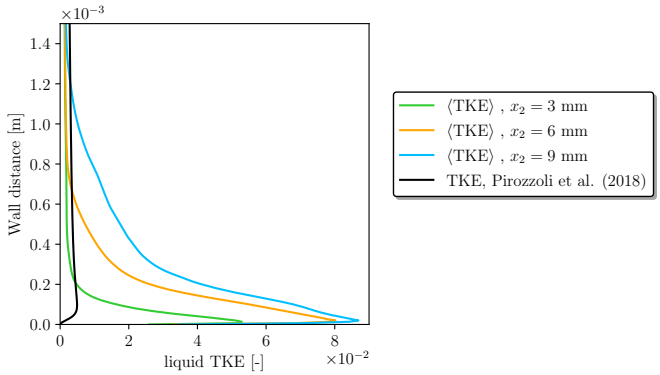

(c) Resolved liquid turbulent kinetic energy (TKE)

Figure 7.18: Time and spanwise-averaged quantities evaluated at three locations in the computational domain: $x_2 = 3$ mm, $x_2 = 6$ mm, and $x_2 = 9$ mm. For reference, the streamwise velocity and the TKE at the inflow from Pirozzoli et al. (2018) are depicted by black solid lines.

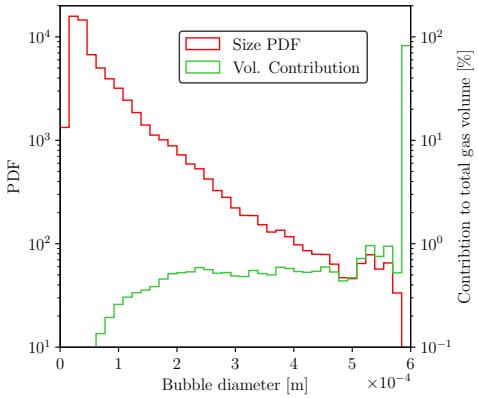

Figure 7.19: Probability distribution of bubble sizes. The last histogram bin on the right also includes all bubble sizes larger than 0.6 mm.

due to the increasing gas content (similar observation as in Kaiser et al. (2024)). Starting at $x_2 = 6$ mm, a clear deviation from the inflow velocity profile of Pirozzoli et al. (2018) is visible. The interplay between the bubbles and the liquid phase causes an increase in the turbulent kinetic energy (TKE), as seen in Fig. 7.18c.

7.7.4 Bubble statistics

In the preceding section, the evaluation of the boiling flow has focused on flow field data. The final stage of the flow analysis, however, aims at evaluating the dispersed data related to single bubbles. The evaluation of this data is divided into two steps. First, bubble statistics accounting for all bubbles in the computational domain are evaluated. Second, the local bubble statistics are assessed using the Voronoi analysis from Ch. 5. Therefore, the spatial evolution of bubble statistics can be studied.

Global bubble statistics

The distributions of bubble sizes and bubble velocities are evaluated on a global level. For every time step, the computational domain contains between 1100 and 1200 bubbles of various sizes. The probability distribution of bubble sizes is provided in Fig. 7.19. The majority of the bubbles have a size of 15-61 µm, corresponding to between one and four times the grid size Δx_1. This bubble size represents the early growth stage of the bubbles after the nucleation event. With larger bubble size, the frequency is much lower. From a bubble count perspective (left axis, PDF),

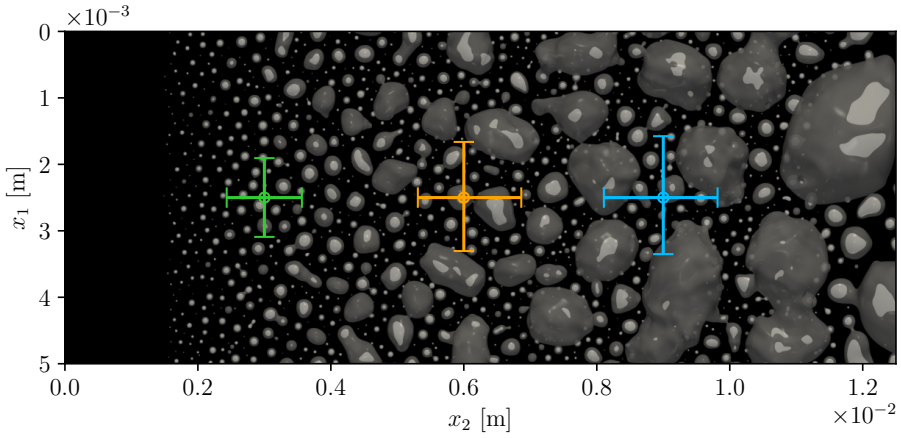

Figure 7.20: Visualization of the evaluation locations for the Voronoi analysis. Bubble clusters are evaluated at $x_2 = 3, 6,$ and 9 mm ($x_1 = 2.5$ mm for all points). Error bars represent the spatial uncertainty calculated from the mean spatial expansion of the bubble clusters. Grey areas represent the bubbles projected onto the wall, black areas are covered by the liquid phase ($\phi < 0.5$), white areas are dry-spots ($\phi > 0.5$).

bubbles of 0.6 mm and larger play a negligible role. In contrast, they dominate the volumetric contribution to the total gas volume, as visualized by the green steps in Fig. 7.19.

Local bubble statistics

Global bubble analysis in the previous section does not allow for an evaluation of the spatial distribution of statistical information. With the aid of the grouped Voronoi framework of Ch. 5, a consistent derivation of local bubble statistics is possible for even a low amount of bubble datasets. It is necessary to use uncorrelated snapshot data for the evaluation of local statistics (refer to Weber et al. (2023)). The required time interval for obtaining uncorrelated datasets is set to a third of the turnover time. For each instantaneous bubble dataset, a Voronoi diagram is constructed in the bubble layer to define the bubble cells, which are grouped into clusters of $N_{trgt} = 16$ bubbles. This procedure is repeated for all uncorrelated bubble datasets of the simulated flow.

For the local evaluation, three representative locations in the flow are used, which are visualized in Fig. 7.20. In this figure, the error bars visualize the inherent spatial uncertainty in local bubble statistics. For these locations, the bubble sizes, the gas content, and the gas content distribution across the bubble sizes are evaluated. The results of this evaluation are presented in Fig. 7.21.

In the first panel (Fig. 7.21a), the spatial evolution of the bubble size PDF is studied. The occurrence frequency of the smaller bubbles is similar across all considered locations. However,

significant differences appear for bubbles larger than 0.3 mm in diameter. For $x_2 = 3$ mm, no bubbles larger than 0.3 mm are seen, whereas a multi-modal distribution is observed for $x_2 = 6$ mm and $x_2 = 9$ mm, with local peaks at 0.6 mm diameter and 1.0 mm diameter, respectively.

In Fig. 7.21c, the probability distribution of the bubble cell-averaged gas content is shown. Similar to Fig. 7.21a, a unimodal shape is only observed at location $x_2 = 3$ mm. Downstream, higher values in the cell gas content become more likely to contribute to the local time-averaged gas content.

The interesting combination of the data from Fig. 7.21a and Fig. 7.21b is the gas content contributions of each bubble diameter class. The distribution of this quantity is shown in Fig. 7.21c. For example, this distribution is the solution quantity of the MUSIG model in RANS-based two-phase flow simulations (see Krepper et al. (2013)). At the first location ($x_3 = 3$ mm), the gas content is dominated by smaller bubbles up to 0.4 mm. Downstream of $x_2 = 6$ mm, two separate peaks in the distribution become apparent. At $x_3 = 9$ mm, a significant separation between small and large bubbles is present, where intermediate bubble sizes do not appear. For this distribution, it is concluded that, at the downstream locations, the growth of all seed bubbles terminates with a coalescence event with a large bubble. The modelling of these coalescence events (e.g., Prince and Blanch (1990)) to predict the distributions shown in Fig. 7.21c constitutes a primary challenge for RANS-based simulation (as in Krepper et al. (2013)). For the present interface-resolved simulation, experimental data for comparison of coalescence would further help the validation of the simulated coalescence events (compare Kaiser et al. (2024)).

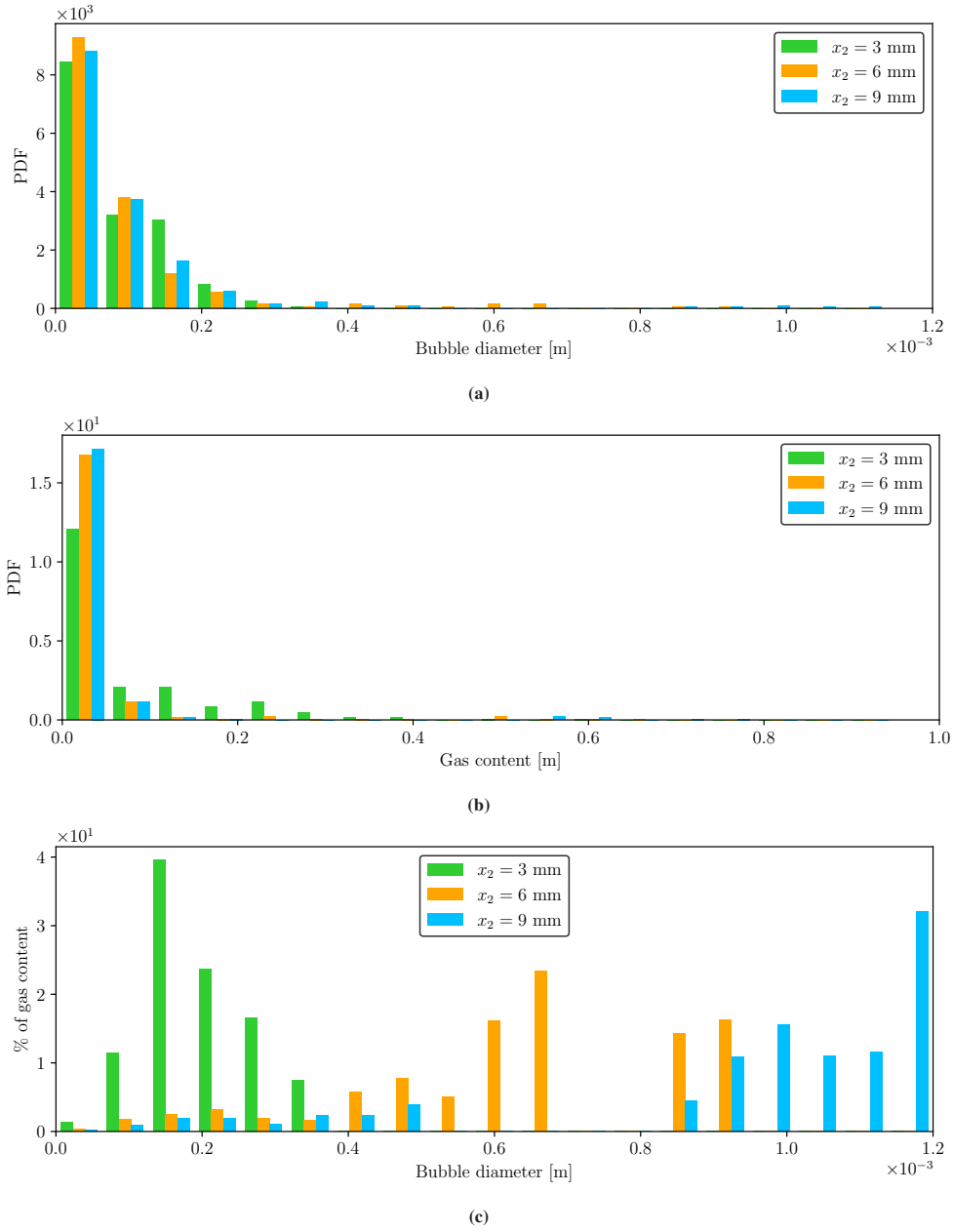

Figure 7.21: Evaluation of local (a) bubble size probability distribution, (b) void fraction probability distribution, and (c) percentage of the total void fraction that is transported by bubbles within a range of diameters.

8 Summary

In this final chapter of the thesis, conclusions (Sec. 8.3) are drawn from the work presented in Ch. 4 to Ch. 7. Furthermore, the major scientific contributions of this thesis are summarized in Sec. 8.2. The chapter closes, in Sec. 8.3, with final remarks concerning future developments and analyses.

8.1 Conclusions

In the introduction of this thesis, a need to conduct large-scale interface-resolved simulations of boiling flows was identified. This need stems from the complexity of boiling flow phenomena, which (i) renders experimental measurements challenging and (ii) limits the accuracy of common models for RANS-based simulations. A potential solution to the latter challenge is using interface-resolved simulations to improve PDF models that represent the polydispersity in RANS-based simulations. For this purpose, an advanced numerical framework was developed that is capable of simulating boiling flows efficiently and allows for the consistent analysis of local bubble statistics.

In Ch. 2, the *accurate conservative diffuse interface* (ACDI) method was identified as a promising interface-capturing method, as it allows for highly efficient calculations. Numerous implementations of the ACDI method exist in open-source codes. However, the ACDI method has not previously been applied to complex boiling flows. Therefore, fundamental developments for this application were required (Ch. 4). These developments include (i) the derivation of a consistent system of transport equations, (ii) the development of an efficient FFT-based pressure solution scheme, suitable for simulating boiling flows, and (iii) the development of a phase change model for the ACDI method.

When deriving the system of transport equations, contributions of the regularization terms, which maintain the equilibrium profile of the phase interface during the simulation, were identified (Ch. 4). For boiling flows, an analogy between the regularization term and the interfacial velocity jump was identified, highlighting that the contribution of the regularization terms is much more significant in boiling scenarios. Interestingly, the derivation of the momentum transport equation revealed commonly neglected contributions of the regularization terms that are

important for accurately simulating boiling flows. Even in the absence of phase change, significant improvements were observed when compared to benchmark simulations in the literature (Ch. 6). It is, therefore, concluded that when simulating boiling flows with the ACDI method, using the presented regularization contributions improves the accuracy.

In addition, for large flow problems, an efficient FFT-based solution scheme is required for solving the computationally expensive pressure Poisson equation. However, for boiling flows involving high density contrasts, existing FFT solution schemes were found to exhibit unacceptable pressure oscillations. In this work, an FFT *momentum-based pressure treatment for density jumps* (MPDJ) was developed to overcome this problem (Ch. 4). In Ch. 6, a series of numerical benchmarks led to the conclusion that the FFT-MPDJ solver (i) suppresses spurious pressure oscillations, (ii) achieves an improved accuracy for interfacial pressure jump calculations, and (iii) allows for a faster pressure adaptation to the flow field during the simulation startup.

The modelling of phase change is required to satisfy both efficiency and robustness in the mass transfer rate calculations. The first requirement was achieved by developing a *kinetic* phase change model for the ACDI method that is free from simulation-dependent parameter adjustments. The second requirement was satisfied by deriving a phase change time step constraint that must match the time step constraint of the ACDI interface regularization. For this purpose, a dynamic adaptation of the non-dimensional regularization speed was employed. This novel strategy was found to return accurate results reliably across all considered computational settings.

Three-dimensional simulations of boiling flow scenarios demonstrated that *energy-based* surface tension models led to more spurious currents than the *continuum surface forcing* (CSF) method (Ch. 6). It is emphasized that this result is counterintuitive, as the literature reports the reverse trend for non-phase change simulations. Accordingly, a comprehensive comparison of surface tension models was conducted to provide a best practice guideline for boiling simulations using the ACDI method. It is concluded that the *sharpened* CSF model by Raeini et al. (2012) returned the lowest spurious currents.

Finally, the simulation framework was successfully validated through an extensive testing campaign involving ten different setups. These tests range from conceptual tests to complex bubble dynamics with phase change. As reported in Ch. 6, good agreement with theoretical and experimental data was obtained. Therefore, it is concluded that the simulation framework is a suitable tool for conducting realistic, large-scale boiling flow simulations.

A proof of concept for the application of the ACDI method to simulating nucleate boiling in a turbulent subcooled flow was pioneered in this thesis (Ch. 7). The considered simulation setup aimed at replicating the experimental results of such a flow of boiling water at high pressures. A

range of results was successfully compared to experimental data, exhibiting satisfactory agreement. In the subsequent analyses of the simulation results, both flow field and bubble statistics were evaluated. It was demonstrated that the presented interface-resolved simulation provides full access to all flow quantities, thus supplementing experiments with data that is otherwise challenging or impossible to measure.

As the developed software can simulate the bubble dynamics of boiling flows, a suitable tool for postprocessing such data was needed and developed. First, in Ch. 3, it was demonstrated that Voronoi diagrams can provide a proper definition of a bubble cell. However, it was also found that when evaluating local bubble statistics, with a single bubble per cell, many instantaneous datasets are required to achieve an acceptable sample size for statistical evaluation. For interface-resolved simulations, this is computationally too expensive. A constrained K-Means clustering algorithm for grouping Voronoi cells was found to solve this problem (Ch. 5). It is, therefore, concluded that grouping the bubble cells (i) allows an instantaneous definition of a bubble statistic, and (ii) ensures a spatially homogeneous distribution of the sample size. Finally, in Ch. 7 it was successfully demonstrated that the proposed grouped Voronoi analysis provides a consistent evaluation of bubble statistics that can be used as reference data for RANS-based simulations.

8.2 Contributions of this work

In this thesis, significant contributions to (i) the efficient interface-resolved simulation of boiling flow phenomena, and (ii) the analysis of the resulting data. In line with the conclusions drawn in Sec. 8.1, the following major contributions to the numerical simulation of boiling flows are summarized in the following

- Derivation and validation of a consistent system of transport equations for applying the *accurate conservative diffuse interface* (ACDI) method to boiling flow scenarios (Ch. 4 and Ch. 6)
- Development, analysis and validation of an efficient and robust phase change model for the application to the ACDI method (Ch. 4 and Ch. 6)
- Development and validation of the FFT-MPDJ pressure solution scheme, which allows the simulation of boiling flows at high density ratios without pressure oscillations (Ch. 4 and Ch. 6)
- Assessment and comparison of various surface tension models regarding their suitability in boiling flow simulations using the ACDI method (Ch. 6)

- Development and implementation of a consistent methodology to access the local bubble statistics through grouped Voronoi cells. This involves the instantaneous definition of a bubble statistic (Ch. 5 and Ch. 6)
- Implementation of a scalable state-of-the-art software capable of simulating turbulent subcooled boiling flows with the ACDI method (Ch. 7)
- Analysis of a turbulent subcooled boiling flow simulation, involving a comparison of the results to experimental data (Ch. 7)

8.3 Outlook

The results presented in this thesis inspire a range of potential future research projects that are beyond the scope of this thesis. A selection of some future study recommendations is provided in the following.

The presented interface-resolved simulation of nucleate boiling in turbulent flows relies on specific model parameters that potentially influence the results. In a future study, the influence of the model parameters could shed more light on the uncertainties of the simulation.

Thus far, the simulation of nucleate boiling on a heated wall has been limited to fluids that do not form a micro-layer. An interesting project could be implementing such a micro-layer subgrid model. This feature could significantly improve the versatility of the simulation software. For example, such a micro-layer model would enable the simulation of water at atmospheric pressures.

Even though all of the numerical schemes in this thesis were carefully selected to ensure an efficient and scalable simulation of boiling flows, they remain computationally costly and time-consuming. In recent years, greater interest in heterogeneous computer systems has led to an increase in the amount of GPU resources offered on HPC clusters. A future study could adapt the developed software for executing computational tasks on GPUs and, thus, decrease the time-to-result significantly. This would enable larger simulations of a longer physical time.

Improving models for RANS-based simulations requires the statistical analysis of a wide range of flow parameters. Accordingly, carrying out further simulations with additional sets of parameters, such as different wall heat fluxes, could provide more insights into the physics of boiling flows.

A Appendix

A.1 Physical fluid properties

All of the fluid properties included in the present work are listed in Tab. A.1. Fluids$_{A-E}$ refer to fictive fluid properties found in the literature. Saturated water (at two different pressures) and saturated ethanol (at atmospheric pressure), used for realistic boiling flow simulations, are also included in this table.

Table A.1: Physical properties used in this thesis, adapted from Weber et al. (2026).

Property	Unit	Fluid$_A$[1]	Fluid$_B$[2]	Fluid$_C$[1]	Fluid$_D$[3]	Fluid$_E$[3]	Water[4]	Water[5]	Ethanol[6]
ρ_1	kg m^{-3}	0.01	0.25	5	100	1	0.597	5.391	1.647
ρ_2	kg m^{-3}	1	2.5	200	1000	1000	958.4	884.84	736.44
μ_1	kg m^{-1} s^{-1}	n/a	n/a	0.005	1	0.1	$1.26 \cdot 10^{-5}$	$1.51 \cdot 10^{-5}$	$1.02 \cdot 10^{-5}$
μ_2	kg m^{-1} s^{-1}	n/a	n/a	0.1	10	10	$2.80 \cdot 10^{-4}$	$1.49 \cdot 10^{-4}$	$4.49 \cdot 10^{-4}$
$c_{p,1}$	J kg^{-1} K^{-1}	200	10	200	n/a	n/a	2030	2741.6	1806
$c_{p,2}$	J kg^{-1} K^{-1}	n/a	10	n/a	n/a	n/a	4216	4413.4	3185
λ_1	W m^{-1} K^{-1}	0.005	0.0035	1	n/a	n/a	0.025	0.035	0.0199
λ_2	W m^{-1} K^{-1}	n/a	0.0015	n/a	n/a	n/a	0.679	0.67	0.1654
L_{sat}	J kg^{-1}	10^4	10^2	10^4	n/a	n/a	$2.26 \cdot 10^6$	$2.78 \cdot 10^6$	$8.499 \cdot 10^5$
T_{sat}	°C	n/a	n/a	n/a	n/a	n/a	100	182	78.2
σ	N m^{-1}	n/a	n/a	0.1	24.5	1.96	0.059	0.0417	0.0174

[1] from Dongliang Sun and Chen (2014)
[2] from Irfan and Muradoglu (2017)
[3] from Adelsberger et al. (2014)
[4] at 1013 hPa, from Sato and Ničeno (2013)
[5] at 1.05 MPa, from Wagner et al. (2000)
[6] at 1013 hPa, from Kleiber and Joh (2013)

Table A.2: A selection of non-dimensional interface thicknesses ϵ^* and their corresponding phase change factors θ_{pc}.

Interface thickness ϵ^*	Phase change constant θ_{pc}
0.55	0.645
$2/3$	0.645
1	0.7
1.1	0.73
2	0.78

A.2 Phase change model for arbitrary interface thicknesses

The phase change model developed in Sec. 4.4.1 is developed for a non-dimensional interface thickness of $\epsilon^* = 1$. However, the ACDI equation of Jain (2022) allows for thinner interfaces in the range of $0.5 < \epsilon^* \leq 1$, with no additional computational cost. Therefore, extending the phase change model in Sec. 4.4.1 to arbitrary interfaces can be of interest. This extension is presented below.

A smaller ϵ^* means that, compared to a situation where $\epsilon^* = 1$, the same amount of phase change must occur within a thinner interface region. Therefore, the mass transfer rate $\mathcal{M}$ needs to be increased. To account for this, an inverse proportionality of ΔT_{PC}^{n+1} to ϵ^* is postulated. This is analogous to using a dependency of $|\nabla\phi|$ on the mass transfer rate $\mathcal{M}$, as in Brown et al. (2023). With the proposed modification factor θ_ϵ, the modified Eq. (4.46) reads

$$\Delta T_{PC}^{n+1} = -T^* \theta_t \theta_{pc} \theta^*_{\rho c_p} \theta^*_\phi \theta_\epsilon, \tag{A.1}$$

where

$$\theta_\epsilon = \frac{1}{\epsilon^*}. \tag{A.2}$$

A slight dependency between ϵ^* and the phase change constant θ_{pc} is observed. For various values of ϵ^*, the corresponding values of θ_{pc} are reported in Tab. A.2. Based on the values of θ_{pc} in this table, a slight non-linear dependency is observed. Therefore, the corresponding value for θ_{pc} must be manually set in accordance with Tab. A.2 before starting the simulation.

All parameters reported in Tab. A.2 are applied to the Stefan problem (see Sec. 6.4) and the sucking interface problem (see Sec. 6.5). The results of these tests are shown in Fig. A.1. For the Stefan problem (Fig. A.1a), the accuracy of the results exhibit clear improvements with lower

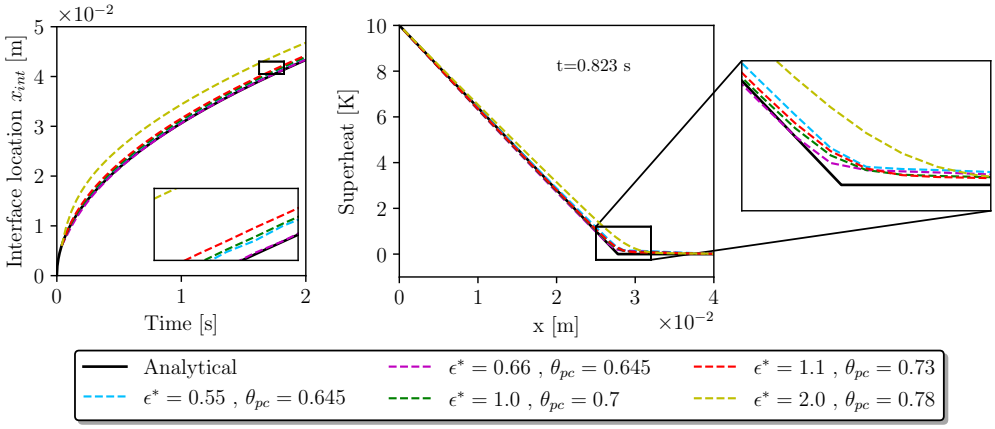

(a) Stefan problem from Dongliang Sun and Chen (2014) with properties of Fluid$_A$ and $\Delta x = 1$ mm

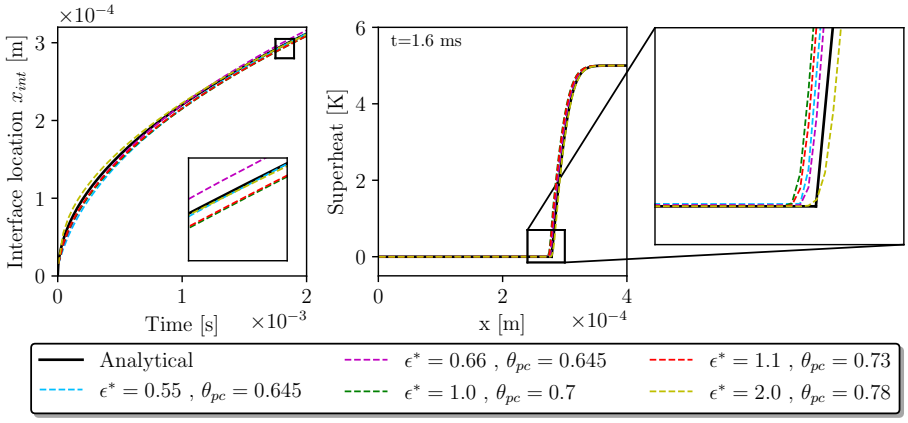

(b) Sucking interface problem with saturated water properties at atmospheric pressure and $\Delta x = 2$ µm

Figure A.1: Effect of interface thickness ϵ^* on the results for two benchmarks. (a) Results obtained for the Stefan problem with the settings reported in Sec. 6.4. (b) Results obtained for the sucking interface problem with the settings reported in Sec. 6.5.

values of ϵ^* until $\epsilon^* = 2/3$. The results of the sucking interface problem (Fig. A.1b) show that ϵ^* has a significant impact on the initial interface speed. The interface speed is significantly slower than the analytical solution for small values of ϵ^* (e.g. 0.55). In contrast, larger values (e.g., 2) lead to an overprediction of the initial interface speed. Combining the findings of both benchmarks, there is no clear recommendation for setting a value of ϵ^*. However, a good balance of accuracy in both benchmarks is achieved for ϵ^* values around 1.

A.3 Phase change model for non-cubic grid cells

The phase change model proposed in Sec. 4.4.1 was developed for uniform cubic grids. Accordingly, all benchmark simulations in Ch. 6 use cubic grids. However, the extension of the phase change model in Sec. A.2 can allow the use of a non-cubic grid. This can be helpful for reducing the number of grid points when refining the grid along one axis only (e.g., Ch. 7).

In non-cubic (uniform) grids, the size of a grid cell is $\Delta x_1 \times \Delta x_2 \times \Delta x_3$, where the index refers to the x_1, x_2, and x_3-directions. The interface thickness ϵ is constant, leading to a spatially varying ϵ^*, depending on the local interface orientation. Simultaneously, when calculating ΔT_{PC}^{n+1} (see Eq. (A.1)), a directional dependency is observed through the factors θ_t, θ_{pc}, and θ_ϵ. Therefore, each grid direction leads to a different temperature increment, $\Delta T_{PC,1}^{n+1}$, $\Delta T_{PC,2}^{n+1}$, and $\Delta T_{PC,3}^{n+1}$. To overcome this problem, the three different increments are weighted based on the local interface orientation. The interface normal vector $\vec{n}$ has the components

$$\vec{n} = \begin{pmatrix} n_1 \\ n_2 \\ n_3 \end{pmatrix} \tag{A.3}$$

The components of $\vec{n}$ are then used as weights to calculate ΔT_{PC}^{n+1} with

$$\Delta T_{PC}^{n+1} = \frac{|n_1|\Delta T_{PC,1}^{n+1} + |n_2|\Delta T_{PC,2}^{n+1} + |n_3|\Delta T_{PC,3}^{n+1}}{|n_1| + |n_2| + |n_3|} \tag{A.4}$$

This modification is now compared to the analytical solution from Scriven (1959) by simulating three-dimensional bubble growth in zero gravity. The properties of saturated water at 1.05 MPa are considered (see Tab. A.1), as in Ch. 7. For a general description of this flow problem, refer to Sec. 6.6. This specific setup uses the parameters described in Sec. 7.2, with $r_0 = 15.6$ µm. The considered cell sizes are

- $15.6 \times 15.6 \times 10.4$ µm^3 with $\epsilon = 2/3\Delta x_1$
- $15.6 \times 15.6 \times 15.6$ µm^3 with $\epsilon = \Delta x_1$
- $15.6 \times 15.6 \times 15.6$ µm^3 with $\epsilon = 0.55\Delta x_1$
- $15.6 \times 15.6 \times 7.8$ µm^3 with $\epsilon = 0.55\Delta x_1$

The results of the bubble radius over time are provided in Fig. A.2. Consistent with Sec. A.2, smaller interface thicknesses lead to less accurate results. However, the grid cell sizes

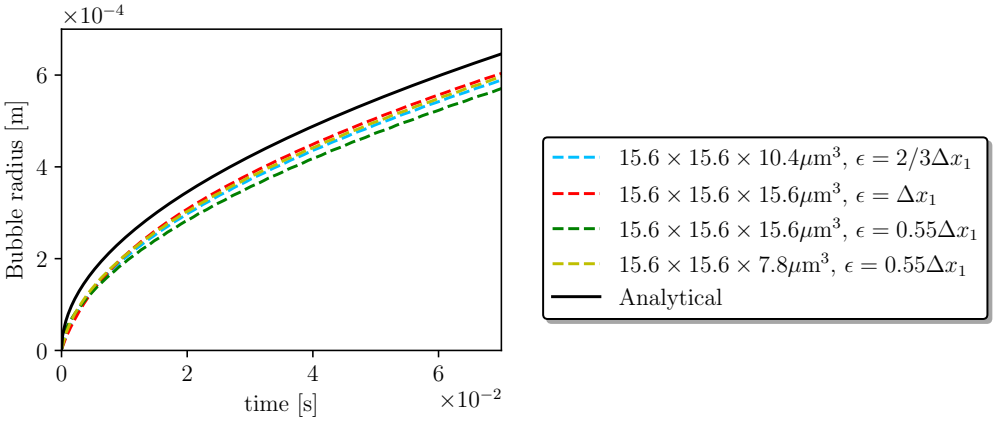

Figure A.2: Bubble size over time for various cubic and non-cubic grid cells and different interface thicknesses.

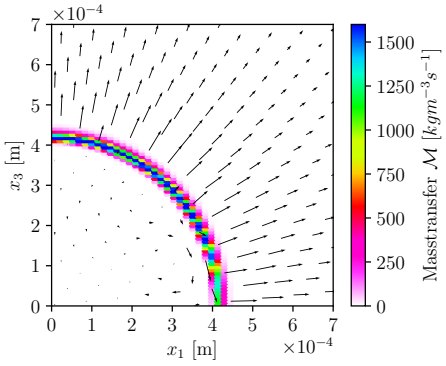

Figure A.3: Visualization of mass transfer rate distribution for non-cubic grid cells on a slice through the growing bubble. Arrows quantitatively depict the velocity field. Figure corresponds to $t = 35.7$ ms and a grid cell size of $15.6 \times 15.6 \times 10.4$ µm^3.

$15.6 \times 15.6 \times 10.4$ µm^3 and $15.6 \times 15.6 \times 7.8$ µm^3 yield very similar results to those of the cubic cells with $\epsilon = \Delta x_1$. All grid sizes result in an underestimation of the analytical growth rate, due to the small initial radius r_0 (see Sec. 7.2.1).

The mass transfer rate distribution for a non-cubic grid cell is shown in Fig. A.3. In this case, the grid cell lengths have the ratio $x_1/x_3 = 2$. As expected, the mass transfer rate $\mathcal{M}$ is significantly larger where the interface normal vector points in the x_3-direction. Accordingly, $\mathcal{M}$ is reduced where $\vec{n}$ points in the x_1-direction. Minor spurious currents are observed inside the bubble, which do seem to affect the overall growth rate. In conclusion, the extension presented in this section enables the use of non-cubic grid cells.

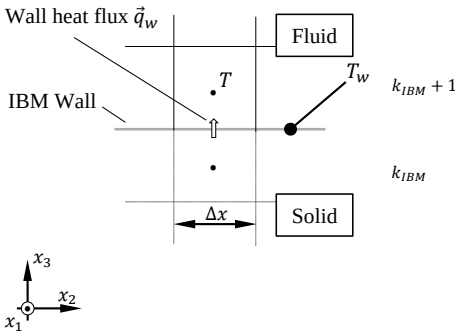

Figure A.4: Wall heat flux that needs to be accounted for in the calculation of ΔT_{PC}^{n+1}.

A.4 Phase change model for conjugate heat transfer

When non-adiabatic walls are used in combination with boiling flow (e.g., Ch. 7), a modified phase change model is needed. Recalling the assumptions of the phase change model development in Sec. 4.4.1, the following inconsistency is observed. Specifically, this inconsistency concerns the assumption that the mass transfer rate is dictated by the heat transport from the liquid side into the interface. For non-adiabatic walls, however, an additional heat flux enters the interface region at the triple contact line (TLC), where the interface is in contact with the solid wall. Therefore, the wall-adjacent fluid points require a modified temperature increment $\Delta T_{PC,w}^{n+1}$. Within the interface region, defined by θ_ϕ, the additional wall heat flux $\vec{q}_w$ (see Fig. A.4) directly translates to phase change. At a grid point with a grid index $k = k_{IBM} + 1$, the energy balance of the additional heat flux and the phase change is

$$2\lambda\theta_\phi \frac{T - T_w}{\Delta x^2} = -\mathcal{M}L. \tag{A.5}$$

Further, it is assumed that the temperature in the diffuse interface is approximately zero, i.e., $T \approx 0$.

Reformulating Eq. (A.5), and adding it to Eq. 4.46, yields

$$\Delta T_{PC,w}^{n+1} = -\theta_t \theta^*_{\rho c_p} \theta^*_\phi (\theta_{pc} \theta_\epsilon T^* + 2\theta^*_\lambda T_w), \tag{A.6}$$

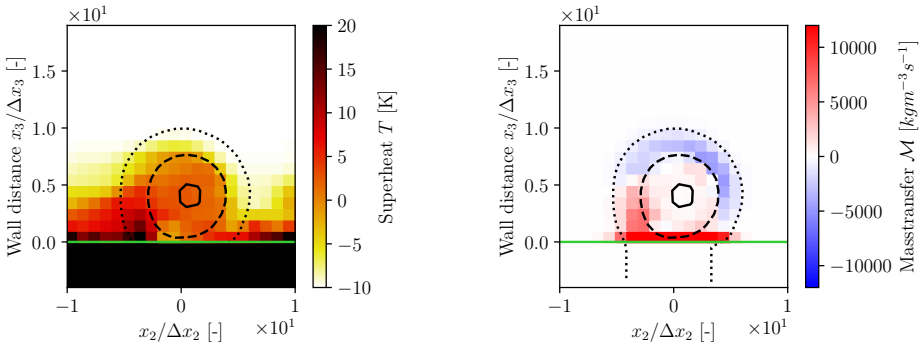

(a) Temperature distribution

(b) Mass transfer distribution

Figure A.5: Visualization of the effect of Eq. (A.6) on a slice through a small bubble sliding on a superheated wall. The green line represents the location of the wall/IBM. Dotted, dashed, and solid lines refer to the iso-contours of the phase field values of $\phi = 0.1$, $\phi = 0.5$, and $\phi = 0.9$.

where θ_λ accounts for the change in the heat conductivity across the diffuse interface, i.e., $\theta_\lambda = (\lambda_1/\lambda_2 - 1)\phi + 1$.

In Fig. A.5, the effect of using Eq. (A.6) is visualized. This figure depicts a representative bubble from the nucleate boiling simulation in Ch. 7. The core of the bubble remains at saturation temperature. Due to the subcooled bulk flow, the top of the bubble condenses. However, on the wall, the mass transfer rate $\mathcal{M}$ is significantly increased to balance the heat that is transported from the wall into the interface region.

List of Figures

List of Tables

List of Publications

Journal articles

Lorenz Weber, Stephan Gabriel, and Andreas G. Class. On the statistical evaluation of bubbly flows using Voronoi cells grouped in clusters with fixed cell count. *Physics of Fluids*, 35(5): 053311, 05 2023. ISSN 1070-6631. doi: https://doi.org/10.1063/5.0145551.

Lorenz Weber, Aritra Mukherjee, Andreas G. Class, and Luca Brandt. A consistent and scalable framework suitable for boiling flows using the conservative diffuse interface method. *Journal of Computational Physics*, 551:114680, 2026. ISSN 0021-9991. doi: https://doi.org/10.1016/j.jcp.2026.114680.

Conference contributions

Lorenz Weber and Andreas G. Class. Methodology for statistical evaluation of bubbly flows using grouped bubble cells. 75th Annual Meeting of the Division of Fluid Dynamics, Indianapolis, IN, USA, Oral presentataion, November 20 - 22 2022.

Lorenz Weber and Andreas G. Class. A field-monte-carlo framework for simulating nucleate-boiling flows. 76th Annual Meeting of the Division of Fluid Dynamics, Washington, DC, USA, Oral presentataion, November 19 - 21 2023.

Lorenz Weber and Andreas G. Class. Development of a two-phase flow solver using an eulerian monte-carlo method. Summer school, Numerical methods for random differential problems, Lausanne, Switzerland, Poster presentataion, June 11 - 14 2024.

Lorenz Weber, Aritra Mukherjee, Marica Pelanti, Andreas Class, and Luca Brandt. Towards the simulation of turbulent, subcooled boiling flow using a conservative diffuse interface method. 5th International Conference on Numerical Methods in Multiphase Flows, Reykjavik, Iceland, Oral presentataion, June 26-28 2024a.

Lorenz Weber, Francesco Secchi, Davide Gatti, Bettina Frohnapfel, and Philipp Schlatter. Feedback-forcing immersed boundaries in spectral element methods: Capabilities and limitations. In *Proceedings of the 14th International ERCOFTAC Workshop on Direct and Large-Eddy Simulation, held at the Friedrich-Alexander University of Erlangen, April 10-14, 2024*, April 2024b.

Lorenz Weber, Aritra Mukherjee, Andreas G. Class, and Luca Brandt. Development of a consistent diffuse interface framework for phase-change at high-density ratios. Italian Society of Applied and Industrial Mathematics (SIMAI) Conference, Trieste, Italy, Oral presentataion, September 1-5 2025.

Bibliography

Helmut Abels, Harald Garcke, and Günther Grün. Thermodynamically consistent, frame indifferent diffuse interface models for incompressible two-phase flows with different densities. *Mathematical Models and Methods in Applied Sciences*, 22(03):1150013, 2012. doi: 10.1142/S0218202511500138. URL https://doi.org/10.1142/S0218202511500138.

Jutta Adelsberger, Patrick Esser, Michael Griebel, Sven Gross, Margrit Klitz, and Alexander Rüttgers. 3D incompressible two-phase flow benchmark computations for rising droplets. In *Proceedings of the 11th World Congress on Computational Mechanics (WCCM XI)*, 01 2014.

A. Aliseda, A. Cartellier, F. Hainaux, and J. C. Lasheras. Effect of preferential concentration on the settling velocity of heavy particles in homogeneous isotropic turbulence. *Journal of Fluid Mechanics*, 468:77–105, 2002. doi: 10.1017/S0022112002001593.

Samuel M. Allen and John W. Cahn. Mechanisms of phase transformations within the miscibility gap of Fe-rich Fe-Al alloys. *Acta Metallurgica*, 24(5):425–437, 1976. ISSN 0001-6160. doi: https://doi.org/10.1016/0001-6160(76)90063-8.

Àdel Alsalti Baldellou, Xavier Álvarez Farré, Andrei Gorobets, Francesc Xavier Trias Miquel, and Asensio Oliva Llena. Efficient strategies for solving the variable Poisson equation with large contrasts in the coefficients. In *Collection of papers presented at the 8th European Congress on Computational Methods in Applied Sciences and Engineering (ECCOMAS Congress 2022)*, 2022.

Gary S. Arnold, Donald A. Drew, and Richard T. Lahey Jr. Derivation of constitutive equations for interfacial force and reynolds stress for a suspension of spheres using ensemble cell averaging. *Chemical Engineering Communications*, 86(1):43–54, 1989. doi: 10.1080/00986448908940362.

Arnoldo Badillo. Quantitative phase-field modeling for boiling phenomena. *Phys. Rev. E*, 86: 041603, Oct 2012. doi: 10.1103/PhysRevE.86.041603. URL https://link.aps.org/doi/10.1103/PhysRevE.86.041603.

Arnoldo Badillo. Phase-Field Simulations of Bubble Growth Under Convective Conditions. *ASME*, Volume 8C: Heat Transfer and Thermal Engineering:V08CT09A064, 11 2013. doi: 10.1115/IMECE2013-65925.

K.P. Bennett, P.S. Bradley, and A. Demiriz. Constrained k-means clustering. Technical Report MSR-TR-2000-65, May 2000. URL https://www.microsoft.com/en-us/research/publication/constrained-k-means-clustering/.

Pramod R Bhuvankar. *A Numerical Study of Heat Transfer in Bubbly Flows*. PhD thesis, Perdue University, 8 2019. URL https://hammer.purdue.edu/articles/thesis/A_Numerical_Study_of_Heat_Transfer_in_Bubbly_Flows/9117032.

Franck Boyer. A theoretical and numerical model for the study of incompressible mixture flows. *Computers & Fluids*, 31(1):41–68, 2002. ISSN 0045-7930. doi: https://doi.org/10.1016/S0045-7930(00)00031-1.

Cyril Bozonnet, Olivier Desjardins, and Guillaume Balarac. Traction open boundary condition for incompressible, turbulent, single- or multi-phase flows, and surface wave simulations. *Journal of Computational Physics*, 443:110528, 2021. ISSN 0021-9991. doi: https://doi.org/10.1016/j.jcp.2021.110528.

J.U Brackbill, D.B Kothe, and C Zemach. A continuum method for modeling surface tension. *Journal of Computational Physics*, 100(2):335–354, 1992. ISSN 0021-9991. doi: https://doi.org/10.1016/0021-9991(92)90240-Y. URL https://www.sciencedirect.com/science/article/pii/002199919290240Y.

W. P. Breugem and B. J. Boersma. Direct numerical simulations of turbulent flow over a permeable wall using a direct and a continuum approach. *Physics of Fluids*, 17(2):025103, 01 2005. ISSN 1070-6631. doi: 10.1063/1.1835771.

Lucy Brown, Suhas Jain, and Parviz Moin. A phase field model for simulating the freezing of supercooled liquid droplets. *SAE International Journal of Advances and Current Practices in Mobility*, 6(3):1150–1157, June 2023. doi: https://doi.org/10.4271/2023-01-1454.

Reed L. Brown, Shahab Mirjalili, Makrand A. Khanwale, and Ali Mani. A mass-conserving contact line treatment for second-order conservative phase field methods based on the generalized Navier boundary condition, 2024. URL https://arxiv.org/abs/2412.16843.

Lubomir Bures, Mattia Bucci, Yohei Sato, and Matteo Bucci. A coarse grid approach for single bubble boiling simulations with the volume of fluid method. *Computers & Fluids*, 271:106182, 2024. ISSN 0045-7930. doi: https://doi.org/10.1016/j.compfluid.2024.106182.

Lubomír Bureš and Yohei Sato. Direct numerical simulation of evaporation and condensation with the geometric VOF method and a sharp-interface phase-change model. *International Journal of Heat and Mass Transfer*, 173:121233, 2021. ISSN 0017-9310. doi: https://doi.org/10.1016/j.ijheatmasstransfer.2021.121233.

Lubomír Bureš and Yohei Sato. Comprehensive simulations of boiling with a resolved microlayer: validation and sensitivity study. *Journal of Fluid Mechanics*, 933:A54, 2022. doi: 10.1017/jfm.2021.1108.

B. L. Buzbee, G. H. Golub, and C. W. Nielson. On direct methods for solving poisson's equations. *SIAM Journal on Numerical Analysis*, 7(4):627–656, 1970. doi: 10.1137/0707049.

John W. Cahn and John E. Hilliard. Free energy of a nonuniform system. I. interfacial free energy. *The Journal of Chemical Physics*, 28(2):258–267, 02 1958. ISSN 0021-9606. doi: 10.1063/1.1744102. URL `https://doi.org/10.1063/1.1744102`.

Claudio Canuto, M. Yousuff Hussaini, Alfio Quarteroni, and Thomas A. Zang. *Temporal Discretization*, pages 94–123. Springer Berlin Heidelberg, Berlin, Heidelberg, 1988. ISBN 978-3-642-84108-8. doi: https://doi.org/10.1007/978-3-642-84108-8_4.

Marcos Castro, Bruno Costa, and Wai Sun Don. High order weighted essentially non-oscillatory weno-z schemes for hyperbolic conservation laws. *Journal of Computational Physics*, 230(5):1766–1792, 2011. ISSN 0021-9991. doi: https://doi.org/10.1016/j.jcp.2010.11.028.

Pao-Hsiung Chiu and Yan-Ting Lin. A conservative phase field method for solving incompressible two-phase flows. *Journal of Computational Physics*, 230(1):185–204, 2011. ISSN 0021-9991. doi: https://doi.org/10.1016/j.jcp.2010.09.021.

Alexandre Joel Chorin. Numerical solution of the Navier-Stokes equations. *Mathematics of Computation*, 22(104):745 – 762, 1968. doi: 10.1090/S0025-5718-1968-0242392-2.

Paolo Cifani. Analysis of a constant-coefficient pressure equation method for fast computations of two-phase flows at high density ratios. *Journal of Computational Physics*, 398:108904, 2019. ISSN 0021-9991. doi: https://doi.org/10.1016/j.jcp.2019.108904.

M. Colombo and M. Fairweather. Accuracy of eulerian–eulerian, two-fluid cfd boiling models of subcooled boiling flows. *International Journal of Heat and Mass Transfer*, 103:28–44, 2016. ISSN 0017-9310. doi: https://doi.org/10.1016/j.ijheatmasstransfer.2016.06.098.

Pedro Costa. A FFT-based finite-difference solver for massively-parallel direct numerical simulations of turbulent flows. *Computers & Mathematics with Applications*, 76(8):1853–1862, 2018. ISSN 0898-1221. doi: https://doi.org/10.1016/j.camwa.2018.07.034.

Marco Crialesi-Esposito, Nicolò Scapin, Andreas D. Demou, Marco Edoardo Rosti, Pedro Costa, Filippo Spiga, and Luca Brandt. Flutas: A GPU-accelerated finite difference code for multiphase flows. *Computer Physics Communications*, 284:108602, 2023. ISSN 0010-4655. doi: https://doi.org/10.1016/j.cpc.2022.108602.

Roberto Croce, Michael Griebel, and Marc Alexander Schweitzer. Numerical simulation of bubble and droplet deformation by a level set approach with surface tension in three dimensions. *International Journal for Numerical Methods in Fluids*, 62(9):963–993, 2010. doi: https://doi.org/10.1002/fld.2051.

M.B. Darshan, M. Magnini, and O.K. Matar. Numerical modelling of flow boiling inside microchannels: A critical review of methods and applications. *Applied Thermal Engineering*, 257, 2024. doi: 10.1016/j.applthermaleng.2024.124464.

Luc Devroye. *General Principles in Random Variate Generation*, pages 27–82. Springer New York, New York, NY, 1986. ISBN 978-1-4613-8643-8. doi: 10.1007/978-1-4613-8643-8_2. URL https://doi.org/10.1007/978-1-4613-8643-8_2.

Akash Dhruv. A vortex damping outflow forcing for multiphase flows with sharp interfacial jumps. *Journal of Computational Physics*, 511:113122, 2024. ISSN 0021-9991. doi: https://doi.org/10.1016/j.jcp.2024.113122.

Hang Ding and Peter D. M. Spelt. Wetting condition in diffuse interface simulations of contact line motion. *Phys. Rev. E*, 75:046708, Apr 2007. doi: 10.1103/PhysRevE.75.046708.

Michael S. Dodd and Antonino Ferrante. A fast pressure-correction method for incompressible two-fluid flows. *Journal of Computational Physics*, 273:416–434, 2014. ISSN 0021-9991. doi: https://doi.org/10.1016/j.jcp.2014.05.024.

S. Dong. An efficient algorithm for incompressible N-phase flows. *Journal of Computational Physics*, 276:691–728, 2014a. ISSN 0021-9991. doi: https://doi.org/10.1016/j.jcp.2014.08.002.

S. Dong. An outflow boundary condition and algorithm for incompressible two-phase flows with phase field approach. *Journal of Computational Physics*, 266:47–73, 2014b. ISSN 0021-9991. doi: https://doi.org/10.1016/j.jcp.2014.02.011.

Jinliang Xu Dongliang Sun and Qicheng Chen. Modeling of the evaporation and condensation phase-change problems with FLUENT. *Numerical Heat Transfer, Part B: Fundamentals*, 66(4):326–342, 2014. doi: 10.1080/10407790.2014.915681. URL https://doi.org/10.1080/10407790.2014.915681.

E.A. Fadlun, R. Verzicco, P. Orlandi, and J. Mohd-Yusof. Combined immersed-boundary finite-difference methods for three-dimensional complex flow simulations. *Journal of Computational Physics*, 161(1):35–60, 2000. ISSN 0021-9991. doi: https://doi.org/10.1006/jcph.2000.6484.

Massimiliano Ferronato. Preconditioning for sparse linear systems at the dawn of the 21st century: History, current developments, and future perspectives. *International Scholarly Research Notices*, 2012(1):127647, 2012. doi: https://doi.org/10.5402/2012/127647.

Joel H Ferziger and Milovan Perić. *Computational methods for fluid dynamics*, volume 586. Springer, 2002.

L.W. Florschuetz, C.L. Henry, and A.Rashid Khan. Growth rates of free vapor bubbles in liquids at uniform superheats under normal and zero gravity conditions. *International Journal of Heat and Mass Transfer*, 12(11):1465–1489, 1969. ISSN 0017-9310. doi: https://doi.org/10.1016/0017-9310(69)90028-3.

C. Frantzis and D.G.E. Grigoriadis. An efficient method for two-fluid incompressible flows appropriate for the immersed boundary method. *Journal of Computational Physics*, 376: 28–53, 2019. ISSN 0021-9991. doi: https://doi.org/10.1016/j.jcp.2018.09.035.

Matteo Frigo and Steven G. Johnson. The design and implementation of FFTW3. *Proceedings of the IEEE*, 93(2):216–231, 2005. Special issue on "Program Generation, Optimization, and Platform Adaptation".

Frédéric Gibou, Liguo Chen, Duc Nguyen, and Sanjoy Banerjee. A level set based sharp interface method for the multiphase incompressible Navier–Stokes equations with phase change. *Journal of Computational Physics*, 222(2):536–555, 2007. ISSN 0021-9991. doi: https://doi.org/10.1016/j.jcp.2006.07.035.

Giovanni Giustini. Modelling of boiling flows for nuclear thermal hydraulics applications—a brief review. *Inventions*, 5(3), 2020. ISSN 2411-5134. doi: 10.3390/inventions5030047.

Giovanni Giustini and Raad I Issa. Modelling of free bubble growth with interface capturing computational fluid dynamics. *Experimental and Computational Multiphase Flow*, 5(4):357–364, 2023.

S. Gross and A. Reusken. *Numerical Methods for Two-phase Incompressible Flows*. Springer Series in Computational Mathematics. Springer Berlin Heidelberg, 2011. ISBN 9783642196867.

D. Z. Guo, D. L. Sun, Z. Y. Li, and W. Q. Tao and. Phase change heat transfer simulation for boiling bubbles arising from a vapor film by the VOSET method. *Numerical Heat Transfer, Part A: Applications*, 59(11):857–881, 2011. doi: 10.1080/10407782.2011.561079. URL `https://doi.org/10.1080/10407782.2011.561079`.

Morton E. Gurtin, Debra Polignone, and Jorge Viñals. Two-phase binary fluids and immiscible fluids described by an order parameter. *Mathematical Models and Methods in Applied Sciences*, 06(06):815–831, 1996. doi: 10.1142/S0218202596000341.

Reza Haghani-Hassan-Abadi, Abbas Fakhari, and Mohammad-Hassan Rahimian. Phase-change modeling based on a novel conservative phase-field method. *Journal of Computational Physics*, 432:110111, 2021. ISSN 0021-9991. doi: https://doi.org/10.1016/j.jcp.2021.110111.

M. Herrmann. A parallel eulerian interface tracking/lagrangian point particle multi-scale coupling procedure. *Journal of Computational Physics*, 229(3):745–759, 2010. ISSN 0021-9991. doi: https://doi.org/10.1016/j.jcp.2009.10.009. URL `https://www.sciencedirect.com/science/article/pii/S0021999109005543`.

Ziyang Huang, Guang Lin, and Arezoo M. Ardekani. Consistent and conservative scheme for incompressible two-phase flows using the conservative Allen-Cahn model. *Journal of Computational Physics*, 420:109718, 2020. ISSN 0021-9991. doi: https://doi.org/10.1016/j.jcp.2020.109718.

Ziyang Huang, Guang Lin, and Arezoo M. Ardekani. Implementing contact angle boundary conditions for second-order phase-field models of wall-bounded multiphase flows. *Journal of Computational Physics*, 471:111619, 2022. ISSN 0021-9991. doi: https://doi.org/10.1016/j.jcp.2022.111619.

Andreas Iberl, Elias Trautner, Markus Klein, and Josef Hasslberger. A-posteriori assessment of mixed models for large eddy simulation of polydisperse multiphase flows. *International Journal of Multiphase Flow*, 189:105231, 2025. ISSN 0301-9322. doi: https://doi.org/10.1016/j.ijmultiphaseflow.2025.105231. URL `https://www.sciencedirect.com/science/article/pii/S0301932225001090`.

Muhammad Irfan and Metin Muradoglu. A front tracking method for direct numerical simulation of evaporation process in a multiphase system. *Journal of Computational Physics*, 337:132–153, 2017. ISSN 0021-9991. doi: https://doi.org/10.1016/j.jcp.2017.02.036.

M Ishii. One-dimensional drift-flux model and constitutive equations for relative motion between phases in various two-phase flow regimes. Technical report, Argonne National Lab., Ill. (USA), 10 1977. URL `https://www.osti.gov/biblio/6871478`.

Mamoru Ishii and Takashi Hibiki. *Thermo-Fluid Dynamics of Two-Phase Flow*. Springer New York, New York, NY, 2011. ISBN 978-1-4419-7985-8. doi: 10.1007/978-1-4419-7985-8. URL `https://doi.org/10.1007/978-1-4419-7985-8`.

David Jacqmin. Calculation of two-phase Navier–Stokes flows using phase-field modeling. *Journal of Computational Physics*, 155(1):96–127, 1999. ISSN 0021-9991. doi: https://doi.org/10.1006/jcph.1999.6332.

Suhas S. Jain. Accurate conservative phase-field method for simulation of two-phase flows. *Journal of Computational Physics*, 469:111529, 2022. ISSN 0021-9991. doi: https://doi.org/10.1016/j.jcp.2022.111529.

Suhas S. Jain, Ali Mani, and Parviz Moin. A conservative diffuse-interface method for compressible two-phase flows. *Journal of Computational Physics*, 418:109606, 2020. ISSN 0021-9991. doi: https://doi.org/10.1016/j.jcp.2020.109606.

D. Jamet, O. Lebaigue, N. Coutris, and J.M. Delhaye. The second gradient method for the direct numerical simulation of liquid–vapor flows with phase change. *Journal of Computational Physics*, 169(2):624–651, 2001. ISSN 0021-9991. doi: https://doi.org/10.1006/jcph.2000.6692.

Damir Juric and Grétar Tryggvason. Computations of boiling flows. *International Journal of Multiphase Flow*, 24(3):387–410, 1998. ISSN 0301-9322. doi: https://doi.org/10.1016/S0301-9322(97)00050-5.

Florian Kaiser, Yohei Sato, and Stephan Gabriel. Subcooled forced convection boiling flow measured using high-resolution techniques at the cosmos-l facility and accompanying cfd simulation employing an interface-tracking scheme. *International Journal of Multiphase Flow*, 174:104772, 2024. ISSN 0301-9322. doi: https://doi.org/10.1016/j.ijmultiphaseflow.2024.104772.

A.M Kamp, A.K Chesters, C Colin, and J Fabre. Bubble coalescence in turbulent flows: A mechanistic model for turbulence-induced coalescence applied to microgravity bubbly pipe flow. *International Journal of Multiphase Flow*, 27(8):1363–1396, 2001. ISSN 0301-9322. doi: https://doi.org/10.1016/S0301-9322(01)00010-6.

Myungjoo Kang, Ronald P Fedkiw, and Xu-Dong Liu. A boundary condition capturing method for multiphase incompressible flow. *Journal of scientific computing*, 15:323–360, 2000. doi: 10.1023/A:1011178417620.

Alain Karma. Phase-field formulation for quantitative modeling of alloy solidification. *Phys. Rev. Lett.*, 87:115701, Aug 2001. doi: 10.1103/PhysRevLett.87.115701. URL `https://link.aps.org/doi/10.1103/PhysRevLett.87.115701`.

Chirag R. Kharangate and Issam Mudawar. Review of computational studies on boiling and condensation. *International Journal of Heat and Mass Transfer*, 108:1164–1196, 2017. ISSN 0017-9310. doi: https://doi.org/10.1016/j.ijheatmasstransfer.2016.12.065.

Aman G Kidanemariam, Clemens Chan-Braun, Todor Doychev, and Markus Uhlmann. Direct numerical simulation of horizontal open channel flow with finite-size, heavy particles at low solid volume fraction. *New Journal of Physics*, 15(2):025031, feb 2013. doi: 10.1088/1367-2630/15/2/025031. URL `https://doi.org/10.1088/1367-2630/15/2/025031`.

Junseok Kim. A continuous surface tension force formulation for diffuse-interface models. *Journal of Computational Physics*, 204(2):784–804, 2005. ISSN 0021-9991. doi: https://doi.org/10.1016/j.jcp.2004.10.032.

Ragna Kipping, Michael Wagner, and Uwe Hampel. On inter-bubble distances and bubble clustering in bubbly flows: An experimental study. *Chemical Engineering Journal*, 431: 133486, 2022. ISSN 1385-8947. doi: https://doi.org/10.1016/j.cej.2021.133486.

Michael Kleiber and Ralph Joh. *VDI-Wärmeatlas*, chapter D3 Stoffwerte von sonstigen reinen Fluiden, pages 357–488. Springer Berlin Heidelberg, Berlin, Heidelberg, 2013. ISBN 978-3-642-19981-3. doi: 10.1007/978-3-642-19981-3_20.

V.V. Klimenko. Film boiling on a horizontal plate — new correlation. *International Journal of Heat and Mass Transfer*, 24(1):69–79, 1981. ISSN 0017-9310. doi: https://doi.org/10.1016/0017-9310(81)90094-6.

Artyom Kossolapov. *Experimental Investigation of Subcooled Flow Boiling and CHF at Prototypical Pressures of Light Water Reactors*. PhD thesis, Massachusetts Institute of Technology. Department of Nuclear Science and Engineering, 9 2021. URL `https://hdl.handle.net/1721.1/151891`.

Artyom Kossolapov, Matthew T. Hughes, Bren Phillips, and Matteo Bucci. Bubble departure and sliding in high-pressure flow boiling of water. *Journal of Fluid Mechanics*, 987:A35, 2024. doi: 10.1017/jfm.2024.405.

Eckhard Krepper, Dirk Lucas, Thomas Frank, Horst-Michael Prasser, and Phil J. Zwart. The inhomogeneous musig model for the simulation of polydispersed flows. *Nuclear Engineering and Design*, 238(7):1690–1702, 2008. ISSN 0029-5493. doi: https://doi.org/10.1016/j.nucengdes.2008.01.004.

Eckhard Krepper, Roland Rzehak, Conxita Lifante, and Thomas Frank. Cfd for subcooled flow boiling: Coupling wall boiling and population balance models. *Nuclear Engineering and Design*, 255:330–346, 2013. ISSN 0029-5493. doi: https://doi.org/10.1016/j.nucengdes.2012.11.010.

Y.M. Lau, K. Thiruvalluvan Sujatha, M. Gaeini, N.G. Deen, and J.A.M. Kuipers. Experimental study of the bubble size distribution in a pseudo-2d bubble column. *Chemical Engineering Science*, 98:203–211, 2013. ISSN 0009-2509. doi: https://doi.org/10.1016/j.ces.2013.05.024.

Yuk Lau, Karolin Müller, Salar Azizi, and Markus Schubert. Voronoï analysis of bubbly flows via ultrafast x-ray tomographic imaging. *Experiments in Fluids*, 57, 02 2016. doi: 10.1007/s00348-016-2118-8.

D. Laupsien, C. Le Men, A. Cockx, and A. Liné. Image processing for bubble morphology characteristics in diluted bubble swarms. *Physics of Fluids*, 31(5):053306, 2019. doi: 10.1063/1.5088945.

Laura Laura Villafane-Roca, M. Esmaily-Moghadam, A. Banko, and J.K. Eaton. A robust method for quantification of preferential concentration from finite number of particles. *Center for Turbulence Research Annual Research Briefs*, pages 123–135, 2016. URL `https://web.stanford.edu/group/ctr/ResBriefs/2016/Reports/012_Villa.pdf`.

T. Laurila, A. Carlson, M. Do-Quang, T. Ala-Nissila, and G. Amberg. Thermohydrodynamics of boiling in a van der Waals fluid. *Phys. Rev. E*, 85:026320, Feb 2012. doi: 10.1103/PhysRevE.85.026320.

T.H. Lee, G.C. Park, and D.J. Lee. Local flow characteristics of subcooled boiling flow of water in a vertical concentric annulus. *International Journal of Multiphase Flow*, 28(8):1351–1368, 2002. ISSN 0301-9322. doi: https://doi.org/10.1016/S0301-9322(02)00026-5.

Wen Ho Lee. A pressure iteration scheme for two-phase flow modeling. *Multiphase transport fundamentals, reactor safety, applications*, 1:407–431, 1980.

Johann Gottlob Leidenfrost. On the fixation of water in diverse fire. *International Journal of Heat and Mass Transfer*, 9(11):1153–1166, 1966. ISSN 0017-9310. doi: https://doi.org/10.1016/0017-9310(66)90111-6.

M. Lemmert and J.M. Chawla. *Heat Transfer in Boiling*, chapter Influence of flow velocity on surface boiling heat transfer coefficient, page 237–247. Academic Press and Hemisphere, New York, NY, USA, 1977.

Junfeng Li, Yanxu Huang, Yunyu Qiu, Shixian Wang, Qunhui Yang, Kai Wang, and Yunzhong Zhu. Prediction of critical heat flux using different methods: A review from empirical correlations to the cutting-edge machine learning. *International Communications in Heat and Mass Transfer*, 160, 2025. doi: 10.1016/j.icheatmasstransfer.2024.108362.

Hong Liang, Haihu Liu, Zhenhua Chai, and Baochang Shi. Lattice boltzmann method for contact-line motion of binary fluids with high density ratio. *Phys. Rev. E*, 99:063306, Jun 2019. doi: 10.1103/PhysRevE.99.063306.

Yixiang Liao, Dirk Lucas, Eckhard Krepper, and Martin Schmidtke. Development of a generalized coalescence and breakup closure for the inhomogeneous musig model. *Nuclear Engineering*

and Design, 241(4):1024–1033, 2011. ISSN 0029-5493. doi: https://doi.org/10.1016/j.nucengdes.2010.04.025. International Conference on Nuclear Energy for New Europe 2009.

Henry Lieberman. How to color in a coloring book. *SIGGRAPH Comput. Graph.*, 12(3):111–116, August 1978. ISSN 0097-8930. doi: 10.1145/965139.807380.

D.K. Lilly. The representation of small-scale turbulence in numerical simulation experiments. In *Proc. IBM Sci. Comput. Symp. on Environmental Science*, pages 195–210, 1967.

Hongli Liu, Jiguo Tang, Licheng Sun, Zhengyu Mo, and Guo Xie. An assessment and analysis of phase change models for the simulation of vapor bubble condensation. *International Journal of Heat and Mass Transfer*, 157:119924, 2020. ISSN 0017-9310. doi: https://doi.org/10.1016/j.ijheatmasstransfer.2020.119924.

S Lo. Application of the musig model to bubbly flows. *AEAT-1096, AEA Technology*, 230(8216): 826, 1996.

J. Lowengrub and L. Truskinovsky. Quasi–incompressible Cahn–Hilliard fluids and topological transitions. *Proceedings of the Royal Society of London. Series A: Mathematical, Physical and Engineering Sciences*, 454(1978):2617–2654, 1998. doi: 10.1098/rspa.1998.0273.

J MacQueen. Multivariate observations. In *Proceedings ofthe 5th Berkeley Symposium on Mathematical Statisticsand Probability*, volume 1, pages 281–297, 1967.

Xiaoyu Mao, Vaibhav Joshi, and Rajeev Jaiman. A variational interface-preserving and conservative phase-field method for the surface tension effect in two-phase flows. *Journal of Computational Physics*, 433:110166, 2021. ISSN 0021-9991. doi: https://doi.org/10.1016/j.jcp.2021.110166.

S. Mirjalili, S. S. Jain, and M. S. Dodd. A mass-conserving pressure-based method for two-phase flows with phase change. In *Center for Turbulence Research Annual Research Briefs*, pages 117–135. Stanford University, Center for Turbulence Research, 2017.

S Mirjalili, M Khanwale, and A Mani. Consistent modeling of scalar transport in multiphase flows using conservative phase field methods. In *Proceedings of the Summer Program 2022*, pages 167–178, 2022a.

Shahab Mirjalili and Ali Mani. Consistent, energy-conserving momentum transport for simulations of two-phase flows using the phase field equations. *Journal of Computational Physics*, 426:109918, 2021. ISSN 0021-9991. doi: https://doi.org/10.1016/j.jcp.2020.109918.

Shahab Mirjalili, Christopher B. Ivey, and Ali Mani. Comparison between the diffuse interface and volume of fluid methods for simulating two-phase flows. *International Journal of Multiphase*

Flow, 116:221–238, 2019. ISSN 0301-9322. doi: https://doi.org/10.1016/j.ijmultiphaseflow.2019.04.019.

Shahab Mirjalili, Christopher B. Ivey, and Ali Mani. A conservative diffuse interface method for two-phase flows with provable boundedness properties. *Journal of Computational Physics*, 401:109006, 2020. ISSN 0021-9991. doi: https://doi.org/10.1016/j.jcp.2019.109006.

Shahab Mirjalili, Suhas S. Jain, and Ali Mani. A computational model for interfacial heat and mass transfer in two-phase flows using a phase field method. *International Journal of Heat and Mass Transfer*, 197:123326, 2022b. ISSN 0017-9310. doi: https://doi.org/10.1016/j.ijheatmasstransfer.2022.123326.

Shahab Mirjalili, Makrand A. Khanwale, and Ali Mani. Assessment of an energy-based surface tension model for simulation of two-phase flows using second-order phase field methods. *Journal of Computational Physics*, 474:111795, 2023. ISSN 0021-9991. doi: https://doi.org/10.1016/j.jcp.2022.111795.

Davide Modesti. Direct numerical simulation dataset of turbulent square duct flow, 2020. Version 1. 4TU.ResearchData. dataset. https://doi.org/10.4121/uuid:3226d808-f354-47b1-b6f8-3a8048215193.

P. Moin and R. Verzicco. On the suitability of second-order accurate discretizations for turbulent flow simulations. *European Journal of Mechanics - B/Fluids*, 55:242–245, 2016. ISSN 0997-7546. doi: https://doi.org/10.1016/j.euromechflu.2015.10.006. Vortical Structures and Wall Turbulence.

R. Monchaux, M. Bourgoin, and A. Cartellier. Preferential concentration of heavy particles: A voronoï analysis. *Physics of Fluids*, 22(10):103304, 2010. doi: 10.1063/1.3489987. URL `https://doi.org/10.1063/1.3489987`.

Issam Mudawar. Two-phase microchannel heat sinks: Theory, applications, and limitations. *Journal of Electronic Packaging*, 133(4), 2011. doi: 10.1115/1.4005300.

A. Mukherjee, S.G. Kandlikar, and Z.J. Edel. Numerical study of bubble growth and wall heat transfer during flow boiling in a microchannel. *International Journal of Heat and Mass Transfer*, 54(15):3702–3718, 2011. ISSN 0017-9310. doi: https://doi.org/10.1016/j.ijheatmasstransfer.2011.01.030.

Abhijit Mukherjee and Satish G Kandlikar. Numerical simulation of growth of a vapor bubble during flow boiling of water in a microchannel. *Microfluidics and Nanofluidics*, 1:137–145, 2005.

Pranav J. Nathan and Suhas S. Jain. Accurate calculation of bubble and droplet properties in diffuse-interface two-phase simulations. *Journal of Computational Physics*, 538:114190, 2025. ISSN 0021-9991. doi: https://doi.org/10.1016/j.jcp.2025.114190.

R.I. Nigmatulin. Spatial averaging in the mechanics of heterogeneous and dispersed systems. *International Journal of Multiphase Flow*, 5(5):353–385, 1979. ISSN 0301-9322. doi: https://doi.org/10.1016/0301-9322(79)90013-2. URL `https://www.sciencedirect.com/science/article/pii/0301932279900132`.

Kaneyasu Nishikawa. Historical developments in the research of boiling heat transfer. *JSME international journal*, 30(264):897–905, 1987. doi: 10.1299/jsme1987.30.897.

Shiro Nukiyama. The maximum and minimum values of the heat q transmitted from metal to boiling water under atmospheric pressure. *International Journal of Heat and Mass Transfer*, 9 (12):1419–1433, 1966. ISSN 0017-9310. doi: https://doi.org/10.1016/0017-9310(66)90138-4.

Munekazu Ohno and Kiyotaka Matsuura. Quantitative phase-field modeling for dilute alloy solidification involving diffusion in the solid. *Phys. Rev. E*, 79:031603, Mar 2009. doi: 10.1103/PhysRevE.79.031603.

Akira Onuki. Dynamic van der Waals theory. *Phys. Rev. E*, 75:036304, Mar 2007. doi: 10.1103/PhysRevE.75.036304.

OpenFOAM, 2013. URL `https://openfoam.org/release/2-2-2/`.

Zhenhai Pan, Justin A. Weibel, and Suresh V. Garimella. A saturated-interface-volume phase change model for simulating flow boiling. *International Journal of Heat and Mass Transfer*, 93:945–956, 2016. ISSN 0017-9310. doi: https://doi.org/10.1016/j.ijheatmasstransfer.2015.10.044.

I. Perez-Raya and S.G. Kandlikar. Chapter three - evaporation on a planar interface – numerical simulation and theoretical analysis of heat and mass transport processes. volume 48 of *Advances in Heat Transfer*, pages 125–190. Elsevier, 2016. doi: https://doi.org/10.1016/bs.aiht.2016.08.005.

Sergio Pirozzoli, Davide Modesti, Paolo Orlandi, and Francesco Grasso. Turbulence and secondary motions in square duct flow. *Journal of Fluid Mechanics*, 840:631–655, 2018. doi: 10.1017/jfm.2018.66.

Jordi Poblador-Ibanez, Nicolás Valle, and Bendiks Jan Boersma. A momentum balance correction to the non-conservative one-fluid formulation in boiling flows using volume-of-fluid. *Journal of Computational Physics*, 524:113704, 2025. ISSN 0021-9991. doi: https://doi.org/10.1016/j.jcp.2024.113704.

Ruggero Poletto. *Divergence free development of the sythetic eddy method in oder to improve synthetic turbulence for embedded LES simulations*. PhD thesis, School of Mechanical, Aerospace and Civil Engineering, The University of Manchester, 3 2015.

Michael J. Prince and Harvey W. Blanch. Bubble coalescence and break-up in air-sparged bubble columns. *AIChE Journal*, 36(10):1485–1499, 1990. doi: https://doi.org/10.1002/aic.690361004. URL https://aiche.onlinelibrary.wiley.com/doi/abs/10.1002/aic.690361004.

Ali Q. Raeini, Martin J. Blunt, and Branko Bijeljic. Modelling two-phase flow in porous media at the pore scale using the volume-of-fluid method. *Journal of Computational Physics*, 213(2): 5653–5668, 2012. ISSN 0021-9991. doi: http://dx.doi.org/10.1016/j.jcp.2012.04.011.

A.H. Rajkotwala, A. Panda, E.A.J.F. Peters, M.W. Baltussen, C.W.M. van der Geld, J.G.M. Kuerten, and J.A.M. Kuipers. A critical comparison of smooth and sharp interface methods for phase transition. *International Journal of Multiphase Flow*, 120:103093, 2019. ISSN 0301-9322. doi: https://doi.org/10.1016/j.ijmultiphaseflow.2019.103093.

Martin R. Raquet. *Stochastische Euler-Euler-PDF-Methodik für das Zwei-Fluid-Modell und Anwendung auf kavitierende Strömungen der Automobilindustrie*. PhD thesis, Karlsruher Institut für Technologie (KIT), 2019. 32.02.01; LK 01.

Alexander S. Rattner and Srinivas Garimella. Simple mechanistically consistent formulation for volume-of-fluid based computations of condensing flows. *Journal of Heat Transfer*, 136(7): 071501, 03 2014. ISSN 0022-1481. doi: 10.1115/1.4026808. URL https://doi.org/10.1115/1.4026808.

Alessio Roccon. Boiling heat transfer by phase-field method. *Acta Mechanica*, pages 1–16, 2024. doi: https://doi.org/10.1007/s00707-024-04122-7.

Alessio Roccon, Francesco Zonta, and Alfredo Soldati. Phase-field modeling of complex interface dynamics in drop-laden turbulence. *Phys. Rev. Fluids*, 8:090501, Sep 2023. doi: 10.1103/PhysRevFluids.8.090501. URL https://link.aps.org/doi/10.1103/PhysRevFluids.8.090501.

Andrew L. Rukhin. Conservative confidence intervals based on weighted means statistics. *Statistics & Probability Letters*, 77(8):853–861, 2007. ISSN 0167-7152. doi: https://doi.org/10.1016/j.spl.2006.12.008. URL https://www.sciencedirect.com/science/article/pii/S0167715207000247.

Andrew L Rukhin. Weighted means statistics in interlaboratory studies. *Metrologia*, 46(3):323, 05 2009. doi: 10.1088/0026-1394/46/3/021. URL https://dx.doi.org/10.1088/0026-1394/46/3/021.

Michael V. Sadovskii. *Statistical Physics*. De Gruyter, Berlin, Boston, 2019. ISBN 9783110648485. doi: doi:10.1515/9783110648485. URL https://doi.org/10.1515/9783110648485.

Mahdi Saeedipour and Simon Schneiderbauer. A new approach to include surface tension in the subgrid eddy viscosity for the two-phase les. *International Journal of Multiphase Flow*, 121: 103128, 2019. ISSN 0301-9322. doi: https://doi.org/10.1016/j.ijmultiphaseflow.2019.103128.

Salar Zamani Salimi, Aritra Mukherjee, Marica Pelanti, and Luca Brandt. A low Mach number diffuse-interface model for multicomponent two-phase flows with phase change. *Journal of Computational Physics*, 523:113683, 2025. ISSN 0021-9991. doi: https://doi.org/10.1016/j.jcp.2024.113683.

Yohei Sato and Bojan Niceno. A depletable micro-layer model for nucleate pool boiling. *Journal of Computational Physics*, 300:20–52, 2015. ISSN 0021-9991. doi: https://doi.org/10.1016/j.jcp.2015.07.046. URL https://www.sciencedirect.com/science/article/pii/S002199911500491X.

Yohei Sato and Bojan Niceno. Nucleate pool boiling simulations using the interface tracking method: Boiling regime from discrete bubble to vapor mushroom region. *International Journal of Heat and Mass Transfer*, 105:505–524, 2017. ISSN 0017-9310. doi: https://doi.org/10.1016/j.ijheatmasstransfer.2016.10.018.

Yohei Sato and Bojan Ničeno. A new contact line treatment for a conservative level set method. *Journal of Computational Physics*, 231(10):3887–3895, 2012. ISSN 0021-9991. doi: https://doi.org/10.1016/j.jcp.2012.01.034. URL https://www.sciencedirect.com/science/article/pii/S0021999112000642.

Yohei Sato and Bojan Ničeno. A sharp-interface phase change model for a mass-conservative interface tracking method. *Journal of Computational Physics*, 249:127–161, 2013. ISSN 0021-9991. doi: https://doi.org/10.1016/j.jcp.2013.04.035.

Yohei Sato, Sreeyuth Lal, and Bojan Niceno. Computational fluid dynamics simulation of single bubble dynamics in convective boiling flows. *Multiphase Science and Technology*, 25(2-4): 287–309, 2013. ISSN 0276-1459.

Yohei Sato, Artyom Kossolapov, Bojan Niceno, and Matteo Bucci. Interface tracking simulation for subcooled flow boiling of water at 10 bar. *Journal of Fluid Mechanics; under review*, 2025.

N. Scapin, A. Shahmardi, W. H. R. Chan, S. S. Jain, S. Mirjalili, M. Pelanti, and L. Brandt. A mass-conserving pressure-based method for two-phase flows with phase change. In *Proceedings of the Summer Program 2022*, pages 195–204. Stanford University, Center for Turbulence Research, 2022.

Nicolò Scapin, Pedro Costa, and Luca Brandt. A volume-of-fluid method for interface-resolved simulations of phase-changing two-fluid flows. *Journal of Computational Physics*, 407:109251, 2020. ISSN 0021-9991. doi: https://doi.org/10.1016/j.jcp.2020.109251.

Ruben Scardovelli and Stéphane Zaleski. Direct numerical simulation of free-surface and interfacial flow. *Annual Review of Fluid Mechanics*, 31(Volume 31, 1999):567–603, 1999. ISSN 1545-4479. doi: https://doi.org/10.1146/annurev.fluid.31.1.567.

Robert W. Schrage. *Chapter I. Introduction*, pages 1–24. Columbia University Press, New York Chichester, West Sussex, 1953. ISBN 9780231877367. doi: doi:10.7312/schr90162-001. URL `https://doi.org/10.7312/schr90162-001`.

Magdalena Schreter-Fleischhacker, Peter Munch, Nils Much, Martin Kronbichler, Wolfgang A Wall, and Christoph Meier. A consistent diffuse-interface model for two-phase flow problems with rapid evaporation. *Advanced Modeling and Simulation in Engineering Sciences*, 11(1): 19, 2024.

L.E. Scriven. On the dynamics of phase growth. *Chemical Engineering Science*, 10(1):1–13, 1959. ISSN 0009-2509. doi: https://doi.org/10.1016/0009-2509(59)80019-1.

Mingguang Shen and Ben Q. Li. Enhanced conservative phase field method for moving contact line problems. *International Journal for Numerical Methods in Fluids*, 96(7):1215 – 1229, 2024. doi: 10.1002/fld.5286.

Mohsen Shiea, Antonio Buffo, Marco Vanni, and Daniele Marchisio. Numerical methods for the solution of population balance equations coupled with computational fluid dynamics. *Annual Review of Chemical and Biomolecular Engineering*, 11(Volume 11, 2020):339–366, 2020. ISSN 1947-5446. doi: https://doi.org/10.1146/annurev-chembioeng-092319-075814.

Robert Simha. A treatment of the viscosity of concentrated suspensions. *Journal of Applied Physics*, 23(9):1020–1024, 1952. doi: 10.1063/1.1702338. URL `https://doi.org/10.1063/1.1702338`.

J. Smagorinsky. General circulation experiments with the primitive equations: I. the basic experiment. *Monthly Weather Review*, 91(3):99 – 164, 1963. doi: https://doi.org/10.1175/1520-0493(1963)091%3C0099:GCEWTP%3E2.3.CO;2.

Alvy Ray Smith. Tint fill. *SIGGRAPH Comput. Graph.*, 13(2):276–283, August 1979. ISSN 0097-8930. doi: 10.1145/965103.807456.

G. Son and V. K. Dhir. Numerical simulation of film boiling near critical pressures with a level set method. *Journal of Heat Transfer*, 120(1):183–192, 02 1998. ISSN 0022-1481. doi: 10.1115/1.2830042.

Ondřej Souček, Vít Průša, Josef Málek, and KR Rajagopal. On the natural structure of thermodynamic potentials and fluxes in the theory of chemically non-reacting binary mixtures. *Acta Mechanica*, 225:3157–3186, 2014.

Y. Sun and C. Beckermann. Diffuse interface modeling of two-phase flows based on averaging: mass and momentum equations. *Physica D: Nonlinear Phenomena*, 198(3):281–308, 2004. ISSN 0167-2789. doi: https://doi.org/10.1016/j.physd.2004.09.003.

Y. Sun and C. Beckermann. Sharp interface tracking using the phase-field equation. *Journal of Computational Physics*, 220(2):626–653, 2007. ISSN 0021-9991. doi: https://doi.org/10.1016/j.jcp.2006.05.025.

Y. Sun and C. Beckermann. Phase-field modeling of bubble growth and flow in a Hele–Shaw cell. *International Journal of Heat and Mass Transfer*, 53(15):2969–2978, 2010. ISSN 0017-9310. doi: https://doi.org/10.1016/j.ijheatmasstransfer.2010.03.036.

Akinori Tamura and Kenichi Katono. Development of a Phase-Field Method for Phase Change Simulations Using a Conservative Allen–Cahn Equation. *Journal of Nuclear Engineering and Radiation Science*, 8(2):021401, 10 2021. ISSN 2332-8983. doi: 10.1115/1.4050209.

Ichiro Tanasawa. Advances in condensation heat transfer. In James P. Hartnett, Thomas F. Irvine, and Young I. Cho, editors, *Advances in Heat Transfer*, volume 21, pages 55–139. Elsevier, 1991. doi: https://doi.org/10.1016/S0065-2717(08)70334-4.

Sébastien Tanguy, Michaël Sagan, Benjamin Lalanne, Frédéric Couderc, and Catherine Colin. Benchmarks and numerical methods for the simulation of boiling flows. *Journal of Computational Physics*, 264:1–22, 2014. ISSN 0021-9991. doi: https://doi.org/10.1016/j.jcp.2014.01.014.

M. F. P. ten Eikelder, K. G. van der Zee, I. Akkerman, and D. Schillinger. A unified framework for Navier–Stokes Cahn–Hilliard models with non-matching densities. *Mathematical Models and Methods in Applied Sciences*, 33(01):175–221, 2023. doi: 10.1142/S0218202523500069.

Marco F.P. ten Eikelder, Kristoffer G. van der Zee, and Dominik Schillinger. Thermodynamically consistent diffuse-interface mixture models of incompressible multicomponent fluids. *Journal of Fluid Mechanics*, 990:A8, 2024. doi: 10.1017/jfm.2024.502.

M.F.P. ten Eikelder and D. Schillinger. The divergence-free velocity formulation of the consistent Navier-Stokes Cahn-Hilliard model with non-matching densities, divergence-conforming discretization, and benchmarks. *Journal of Computational Physics*, 513:113148, 2024. ISSN 0021-9991. doi: https://doi.org/10.1016/j.jcp.2024.113148.

Arpit Tiwari, Jonathan B. Freund, and Carlos Pantano. A diffuse interface model with immiscibility preservation. *Journal of Computational Physics*, 252:290–309, 2013. ISSN 0021-9991. doi: https://doi.org/10.1016/j.jcp.2013.06.021.

A. Tomiyama, A. Sou, I. Zun, N. Kanami, and T. Sakaguchi. Effects of eötvös number and dimensionless liquid volumetric flux on lateral motion of a bubble in a laminar duct flow. In Akimi Serizawa, Tohru Fukano, and Jean Bataille, editors, *Multiphase Flow 1995*, pages 3–15. Elsevier, Amsterdam, 1995. ISBN 978-0-444-81811-9. doi: https://doi.org/10.1016/B978-0-444-81811-9.50005-6.

Loric Torres. *Direct Numerical Simulation of Nucleate Boiling in Microgravity*. PhD thesis, Institut National Polytechnique de Toulouse-INPT, 2023.

Mario F. Trujillo. Reexamining the one-fluid formulation for two-phase flows. *International Journal of Multiphase Flow*, 141:103672, 2021. ISSN 0301-9322. doi: https://doi.org/10.1016/j.ijmultiphaseflow.2021.103672.

A. Urbano, S. Tanguy, and C. Colin. Direct numerical simulation of nucleate boiling in zero gravity conditions. *International Journal of Heat and Mass Transfer*, 143:118521, 2019. ISSN 0017-9310. doi: https://doi.org/10.1016/j.ijheatmasstransfer.2019.118521.

E. R. van Driest. On turbulent flow near a wall. *Journal of the Aeronautical Sciences*, 23(11): 1007–1011, 1956. doi: https://doi.org/10.2514/8.3713.

Georges Voronoi. Nouvelles applications des paramètres continus à la théorie des formes quadratiques. premier mémoire. sur quelques propriétés des formes quadratiques positives parfaites. *Journal für die reine und angewandte Mathematik (Crelles Journal)*, 1908(133):97–102, 1908a. doi: doi:10.1515/crll.1908.133.97. URL `https://doi.org/10.1515/crll.1908.133.97`.

Georges Voronoi. Nouvelles applications des paramètres continus à la théorie des formes quadratiques. Deuxième mémoire. recherches sur les paralléllòedres primitifs. *Journal für die reine und angewandte Mathematik (Crelles Journal)*, 1908(134):198–287, 1908b. doi: doi:10.1515/crll.1908.134.198. URL `https://doi.org/10.1515/crll.1908.134.198`.

Martin Řehoř. *Diffuse interface models in theory of interacting continua*. PhD thesis, Mathematical Institute of Charles University and Interdisciplinary Center for Scientific Computing at Heidelberg University, Czech Republic, Germany, 2018. URL `http://dx.doi.org/10.11588/heidok.00025676`.

W. Wagner, J. R. Cooper, A. Dittmann, J. Kijima, H.-J. Kretzschmar, A. Kruse, R. Mares˘, K. Oguchi, H. Sato, I. Sto¨cker, O. S˘ifner, Y. Takaishi, I. Tanishita, J. Tru¨benbach, and Th. Willkommen. The iapws industrial formulation 1997 for the thermodynamic properties of

water and steam. *Journal of Engineering for Gas Turbines and Power*, 122(1):150–184, 01 2000. ISSN 0742-4795. doi: 10.1115/1.483186.

Ji Wang, Hongbin Wang, and Jinbiao Xiong. Experimental investigation on microlayer behavior and bubble growth based on laser interferometric method. *Frontiers in Energy Research*, Volume 11 - 2023, 2023. ISSN 2296-598X. doi: 10.3389/fenrg.2023.1130459.

Zhicheng Wang, Xiaoning Zheng, Chryssostomos Chryssostomidis, and George Em Karniadakis. A phase-field method for boiling heat transfer. *Journal of Computational Physics*, 435:110239, 2021. ISSN 0021-9991. doi: https://doi.org/10.1016/j.jcp.2021.110239.

Nicolas Wefers, Wilson Heiler, and Stephan Gabriel. Influence of atf coatings on the critical heat flux in a vertical rod bundle during flow boiling of water at low pressure. In *Proceedings of 14th International Topical Meeting on Nuclear Reactor Thermal-Hydraulics, Operation and Safety, Vancouver, BC, Canada, August 25 – 28, 2024*, 2024.

Nicolas Wefers, Wilson Heiler, and Stephan Gabriel. Private Communication, 2025a. Boiling heat transfer experiments in an annular gap using the COSMOS-L facility at Karlsruhe Institute of Technology.

Nicolas Wefers, Daniel Vlček, Wilson Heiler, and Stephan Gabriel. High-speed imaging and analysis of nucleation site density on nuclear fuel claddings. In *Proceedings of NURETH21, Busan, South Korea, August 31 – September 05*, 2025b.

Samuel W.J. Welch and John Wilson. A volume of fluid based method for fluid flows with phase change. *Journal of Computational Physics*, 160(2):662–682, 2000. ISSN 0021-9991. doi: https://doi.org/10.1006/jcph.2000.6481.

G.H. Yeoh and J.Y. Tu. Two-fluid and population balance models for subcooled boiling flow. *Applied Mathematical Modelling*, 30(11):1370–1391, 2006. ISSN 0307-904X. doi: https://doi.org/10.1016/j.apm.2006.03.010. Selected papers from the Third International Conference on CFD in the Minerals and Process Industries.

Pengtao Yue. Thermodynamically consistent phase-field modelling of contact angle hysteresis. *Journal of Fluid Mechanics*, 899:A15, 2020. doi: 10.1017/jfm.2020.465.

Byong-Jo Yun, Andrew Splawski, Simon Lo, and Chul-Hwa Song. Prediction of a subcooled boiling flow with advanced two-phase flow models. *Nuclear Engineering and Design*, 253: 351–359, 2012. ISSN 0029-5493. doi: https://doi.org/10.1016/j.nucengdes.2011.08.067. SI : CFD4NRS-3.

Amin Zarareh, Sorush Khajepor, Stephen B Burnside, and Baixin Chen. Improving the staircase approximation for wettability implementation of phase-field model: Part 1 – static contact

angle. *Computers & Mathematics with Applications*, 98:218–238, 2021. ISSN 0898-1221. doi: https://doi.org/10.1016/j.camwa.2021.07.013.

Wenqiang Zhang, Armin Shahmardi, Kwing so Choi, Outi Tammisola, Luca Brandt, and Xuerui Mao. A phase-field method for three-phase flows with icing. *Journal of Computational Physics*, 458:111104, 2022. ISSN 0021-9991. doi: https://doi.org/10.1016/j.jcp.2022.111104.

Weiyang Zhao, Hang Wang, Ruidi Bai, Wangru Wei, and Hongtao Wang. Bubble characteristics and turbulent dissipation rate in horizontal bubbly pipe flow. *AIP Advances*, 11(2):025125, 2021. doi: 10.1063/5.0035816.

N. Zuber and J. A. Findlay. Average volumetric concentration in two-phase flow systems. *Journal of Heat Transfer*, 87(4):453–468, 11 1965. ISSN 0022-1481. doi: 10.1115/1.3689137. URL `https://doi.org/10.1115/1.3689137`.

Novak Zuber. Hydrodynamic aspects of boiling heat transfer (thesis). Technical report, Ramo-Wooldridge Corp., Los Angeles, CA (United States); Univ. of California, Los Angeles, CA (United States), 06 1959. URL `https://www.osti.gov/biblio/4175511`.